Westfälische
Wilhelms-Universität
Münster

Calibrating finite element head models using EEG/MEG to account for variability in conductivity

Dissertation

wissen.leben
WWU Münster

Vorgelegt von Sophie Schrader
2022

Calibrating finite element head models using EEG/MEG to account for variability in conductivity

Inauguraldissertation zur Erlangung des
Doktorgrades der Naturwissenschaften
- Dr. rer. nat. -
im Fachbereich Mathematik und Informatik
der Mathematisch-Naturwissenschaftlichen Fakultät
der Westfälischen Wilhelms-Universität Münster
als interdisziplinäre Promotion
in Zusammenarbeit mit der Medizinischen Fakultät

Vorgelegt von:

Sophie Schrader
aus Celle

Münster, 2022

Dekan: Prof. Dr. Xiaoyi Jiang
Erstgutachter: Prof. Dr. Christian Engwer
Zweitgutachter: Prof. Dr. Carsten H. Wolters
Drittgutachter: PD Dr. Stefan Rampp

Tag der mündlichen Prüfung:
Tag der Promotion:

Abstract

Accurate source reconstructions of electroencephalography (EEG) or combined EEG and magnetoencephalography (MEG) signals, as well as targeted optimized transcranial electric stimulation (TES) are important for many clinical applications and neuroscientific research. Both are strongly influenced by the conductive properties of the head volume conductor model, most importantly by individual skull conductivity.

The aim of this thesis is to develop an automatic pipeline to calibrate head models with respect to this influential parameter, which is validated in spherical head models and applied to realistic data sets. The algorithm exploits the complementarities of EEG and MEG modalities in reconstructing the underlying source of the somatosensory evoked P20/N20 component. It uses the DUNEuro toolbox for the numerical computation of the EEG/MEG forward solutions with the finite element method (FEM) and can easily be integrated into existing analysis pipelines. A well-controlled spherical head model scenario, for which (quasi-)analytical solutions exist, is used to evaluate the accuracy of the calibration procedure and investigate the influence of various conditions using realistic noise levels and dipole characteristics. Subsequently, realistically shaped volume conductor models are calibrated using different somatosensory experiments and settings.

The results indicate that skull conductivity can be reliably reconstructed by the calibration procedure for sources resembling the generator of the somatosensory evoked P20/N20 component. Additionally, the effect of erroneous assumptions about scalp conductivity on source reconstruction results can be partly counterbalanced by using the individually fitted skull conductivity. Electric stimulation of the median nerve at the wrist resulted in the best signal-to-noise ratio and most accurate results and is therefore the recommended somatosensory stimulation setup.

In this work, we propose an automated procedure to individually fit skull conductivity to create calibrated head volume conductor models which can be used to improve EEG and combined EEG/MEG source analysis, e.g., in presurgical epilepsy diagnosis, and the optimization of TES montages.

Zusammenfassung

Präzise Quellrekonstruktionen von Elektroenzephalografie (EEG) oder kombinierten EEG- und Magnetoenzephalografie (MEG)-Signalen sowie optimierte transkranielle Elektrostimulation (TES) sind für viele klinische und neurowissenschaftliche Forschungsbereiche von großer Bedeutung. Beide Anwendungen werden stark von den Leitfähigkeitseigenschaften des Kopfvolumenleitermodells beeinflusst, vor allem von der individuellen Schädelleitfähigkeit.

Ziel dieser Arbeit ist es, ein automatisches Verfahren zur Kalibrierung von Kopfmodellen hinsichtlich dieses einflussreichen Parameters zu entwickeln, das in sphärischen Kopfmodellen validiert und auf realistische Datensätze angewendet wird. Dabei wird die Komplementarität der EEG- und MEG-Modalitäten ausgenutzt um die zugrunde liegende Quelle der somatosensorisch evozierten P20/N20-Komponente zu rekonstruieren. Der Algorithmus nutzt die DUNEuro-Toolbox zur numerischen Lösung der EEG/MEG-Vorwärtsprobleme mithilfe der Finite-Elemente-Methode (FEM) und kann leicht in bestehende Analyse-Pipelines integriert werden. Ein mehrschichtiges Kugelmodell, für das (quasi-)analytische Lösungen existieren, wird verwendet um die Genauigkeit des Verfahrens zu bewerten und den Einfluss verschiedener Faktoren unter realistischen Bedingungen zu untersuchen. Anschließend werden realistische Volumenleitermodelle unter Verwendung verschiedener somatosensorischer Experimente und Rahmenbedingungen kalibriert.

Die Ergebnisse zeigen, dass die Leitfähigkeit des Schädels mit dem vorgeschlagenen Kalibrierverfahren für Dipole, die der kortikalen Quelle der somatosensorisch evozierten P20/N20-Komponente ähneln, zuverlässig rekonstruiert werden kann. Darüber hinaus kann die Auswirkung falscher Annahmen über die Haut-Leitfähigkeit auf die Ergebnisse der Quellenrekonstruktion teilweise durch die Verwendung der individuell angepassten Leitfähigkeit des Schädels ausgeglichen werden. Die elektrische Stimulation des Medianusnervs am Handgelenk ergab das beste Signal-Rausch-Verhältnis unter den berücksichtigten somatosensorischen Experimenten und wird daher für optimale Ergebnisse empfohlen.

In dieser Arbeit schlagen wir ein automatisiertes Verfahren zur individuellen Anpassung der Schädelleitfähigkeit vor um kalibrierte Kopfvolumenleitermodelle zu erzeugen, die für eine verbesserte EEG- und kombinierte EEG/MEG-Quellenanalyse, z. B. bei der prächirur-

gischen Epilepsiediagnostik, und der Optimierung von TES, verwendet werden können.

Acknowledgments

I would like to express my sincere gratitude to those people who have supported me and contributed to this work in various ways.

First of all, I would like to thank Carsten Wolters for supervising and supporting this thesis, for his scientific insights in the field of neuroscience, for his motivation and his perseverance in grant writing that gave me the opportunity to work on this interesting topic.

I would also like to express my gratitude to Christian Engwer for supervising this thesis, for his valuable impulses and mathematical insights and his constructive feedback.

Also, many thanks to Stefan Rampp for his efforts to make this project possible, his help related to epilepsy data sets, his scientific input and feedback, and for agreeing to review this work. I would also like to thank all other project partners for their collaboration in this interdisciplinary project.

Additionally, I would like to thank Benedikt Wirth for being an examiner of this work.

I would also like to thank Sampsa Pursiainen for his scientific input and his hospitality in Tampere.

I would also like to thank all former and current members of the SIM-Neuro workgroup and the AG Engwer, especially Marios Antonakakis, Ümit Aydin and Tim Erdbrügger for their head model generation pipeline and discussions about realistic data sets and Andreas Westhoff and Jorrit Fahlke for their help with the DUNE/DUNEuro toolboxes.

Moreover, I greatly appreciated the pleasant work environment at the IBB and I would like to thank its former and current directors Christo Pantev and Joachim Gross for creating a stimulating scientific environment for interdisciplinary exchange, Andreas Wollbrink for his invaluable technical support and advice regarding the experimental setups, Jasmin Kula for the support in administrative matters and Karin Wilken, Hildegard Deitermann and Ute Trompeter for their assistance in the EEG/MEG/MRI data acquisition.

Furthermore, I am very grateful to Maria Carla Piastra, Frank Neugebauer and Paul Breutmann for offering their feedback and proofreading different parts of this thesis.

Insbesondere möchte ich meinen Freunden und meiner Familie danken, vor allem Sonja, meinen Eltern und Großeltern für ihre kontinuierliche Unterstützung in all den Jahren, und Michael – für alles.

This thesis was supported by the DFG through the project "Reconstruction of epilepsy-characteristic sources by means of a simultaneous evaluation of EEG- and MEG- data using calibrated realistic head models" (WO1425/7-1). Additional support was provided by the DAAD through a bilateral researcher exchange project (57405052).

Contents

List of Figures

List of Tables

List of Algorithms

1. Introduction

The spatial distribution of electric activity in the head due to neuronal generators in the brain is largely influenced by the conductive and geometric properties of the constitutive tissues. A realistic modeling of the head volume conductor model is therefore essential for many applications in neuroscience. In particular, the impact of volume conduction effects have been emphasized in the contexts of electroencephalography (EEG), combined EEG and magnetoencephalography (MEG) and transcranial electric stimulation (TES) (Bikson et al., 2016; Brette and Destexhe, 2012). Modern imaging techniques such as magnetic resonance imaging (MRI) provide more detailed geometrical information about the head composition and have been used to create realistically shaped individual head models (Céspedes-Villar et al., 2020; Vorwerk et al., 2014). In most cases, literature values are assigned to a set of homogenized tissue compartments (Vorwerk et al., 2014; Wendel et al., 2009). However, depending on the measurement modality, experimental conditions and modeling assumptions, reported values for most tissue types vary considerably (McCann et al., 2019). This is especially the case for skull conductivity, which is assumed to vary largely inter- and intra-individually, e.g., depending on age (Antonakakis et al., 2020; Hoekema et al., 2003; Wendel et al., 2010). Due to its relatively high resistivity compared to the other head tissues, the importance of skull conductivity and the ratio between skull and skin conductivity has been stressed in several sensitivity studies in the context of EEG and TES (Saturnino et al., 2019; Schmidt et al., 2015; Vallaghé and Clerc, 2009; Vorwerk et al., 2019a). Additionally, varying modeling approaches of the skull composition and assigned conductivity parameters were shown to have a strong effect on EEG source reconstruction results (Chen et al., 2010; Montes-Restrepo et al., 2014; Roche-Labarbe et al., 2008).

Due to the large variability of skull conductivity and its strong influence on bioelectric modalities, it has been suggested to individually calibrate head volume conductor models with respect to this influential parameter. Several methods have been proposed for this purpose, some of which rely on single-modality EEG (Akalin Acar et al., 2016; Lew et al., 2009a). Due to its complementary nature and its insensitivity to skull conductivity (Haueisen et al., 1997; Lew et al., 2013), adding MEG to the calibration procedure was suggested in order to increase its robustness (Antonakakis et al., 2019; Baysal and Haueisen, 2004; Fuchs et al., 1998; Gonçalves et al., 2003b; Huang et al., 2007; Wolters et al., 2010). In these studies, the calibration procedure involves the reconstruction of the source underlying the P20/N20 component, i.e., the signal peak approximately 20 ms after the stimulus, of somatosensory evoked potential (SEP) and field (SEF) data sets. This component has been found to be well suited for this purpose due to strong evidence suggesting a mainly lateral, focal single dipolar origin with a rather tangential orientation of the underlying source (Allison et al., 1991; Antonakakis et al., 2020; Götz et al., 2014; Nakamura et al., 1998).

In this work, a novel algorithm to calibrate head volume conductor models is presented that relies on the non-invasive modalities of EEG/MEG. In a procedure that exploits their complementarities, the most influential conductivity parameter, i.e., skull conductivity (Saturnino et al., 2019; Schmidt et al., 2015; Vorwerk et al., 2019a), is estimated in combination with the reconstruction of the underlying source of the somatosensory evoked P20/N20 component. The calibration pipeline relies on solutions of the EEG and MEG forward problems using the finite element method (FEM), and employs an automatic optimization approach to find the optimal skull conductivity in a continuous parameter space. This procedure can easily be integrated into existing analysis pipelines for the evaluation of EEG or combined EEG/MEG data, e.g., in the context of presurgical epilepsy diagnosis (Aydin et al., 2014), or for an improved targeting using individually optimized TES montages (Guler et al., 2016; Huang et al., 2017; Sadleir et al., 2012; Saturnino et al., 2019; Schmidt et al., 2015).

This work is structured as follows. Chapter 2 is devoted to providing general background related to EEG/MEG modalities and the importance of head volume conductor modeling in this context. In the following, the mathematical background related to the theoretical derivation of the EEG and MEG forward problems and their (quasi-)analytical and numerical solutions using the FEM is presented in Chapter 3. In Chapter 4, a novel algorithm to calibrate head volume conductor models with respect to skull conductivity is introduced. This automated procedure is systematically validated and tested in a controlled spherical head volume conductor model in Chapter 5, followed by investigations in more realistically shaped individual head models in Chapter 6. Subsequently, an example clinical application of the pipeline is presented in Chapter 7, which focuses on EEG/MEG source reconstructions in presurgical epilepsy diagnosis. In the following, an overview of software-related aspects is provided in Chapter 8. Finally, a discussion of the findings in this work is presented in Chapter 9, followed by a short summary in Chapter 10.

2. Background of EEG and MEG modalities

Both EEG and MEG are non-invasive functional neuroimaging methods that directly reflect neuronal activity, with an exceptional temporal resolution within the sub-millisecond range. In this chapter, we will provide an overview of the biophysical background of the generation and propagation of electromagnetic signals that can be detected by EEG and MEG. First, the neurophysiological processes related to the generation of EEG and MEG signals are explained in Section 2.1. Second, the geometric and conductive properties of the head tissues are described in Section 2.2. Third, an overview of practical aspects related to the measurement of both modalities is presented in Section 2.3.

2.1. Generators of EEG and MEG signals

In the human brain, there are about 10^{10} neuronal cells that transmit information by generating time-varying electrical currents (Hallez et al., 2007). In their resting state, the intracellular environment of a neuron has a stable membrane potential of approximately -60 mV compared to the extracellular tissue (Hari and Puce, 2017). This potential difference results from an unequal concentration of sodium (Na^+), chloride (Cl^-) and potassium (K^+), which is actively maintained by ion pumps in the cell membrane that transport Na^+ ions outside and K^+ inside the cell (Hallez et al., 2007).

Two main forms of neuronal activity can be distinguished which alter the potential distribution of the neuron, their description mainly follows Hari and Puce (2017). The first form is given by *action potentials* which are short pulses fired by an activated neuron. Action potentials propagate along the axon and reach an amplitude of approximately 100 mV. Their duration is approximately 1–2 ms consisting of a short depolarization followed by a repolarization phase returning to the resting membrane potential. The second form is given by *postsynaptic potentials* which are more protracted potential changes triggered by action potentials of presynaptic neurons. Typically, neurons receive input from other neurons through thousands of synaptic connections at the dendrites and the cell body. Neurotransmitters change the permeability of the postsynaptic membrane and either lead to a depolarization (excitatory postsynaptic potential) or a hyperpolarization (inhibitory postsynaptic potential). Postsynaptic potentials reach magnitudes of only around 10 mV with a duration of approximately 10–30 ms (excitatory) up to 80–100 ms (inhibitory). At the cell body, the inhibitory and excitatory postsynaptic potentials from presynaptic cells are integrated and if a depolarization threshold in the axon hillock is reached, an action potential is induced which then in turn propagates to other neurons (Hallez et al., 2007).

In order to be detectable by EEG or MEG, the strength and duration of the neuronal activity must be sufficiently large. This relates to the number of active neurons as well as their temporal and geometric correlation. The main contribution to EEG and MEG signals stems from pyramidal neurons in layers III, IV and V of the neocortex whose elongated apical dendrites are aligned orthogonally to the cortical surface (Brette and Destexhe, 2012). These intracellular net flows of ions along the dendrites of the pyramidal cells can be considered as current dipoles which represent the primary current. Since the human head is a conducting medium, the primary current is associated with volume (return) currents, as the current returns through the surrounding space closing the loop (Lopes da Silva and Rotterdam, 1982). A schematic representation of a pyramidal cell and the current dipole model is depicted in Figure 2.1. According to the right-hand-rule of electromagnetism, these current flows generate a magnetic field around them. Due to the synchronous activity and spatial alignment of the pyramidal cells, these electromagnetic signals can be detected by EEG and MEG sensors. The direction of the dipole may vary depending on the relative position of

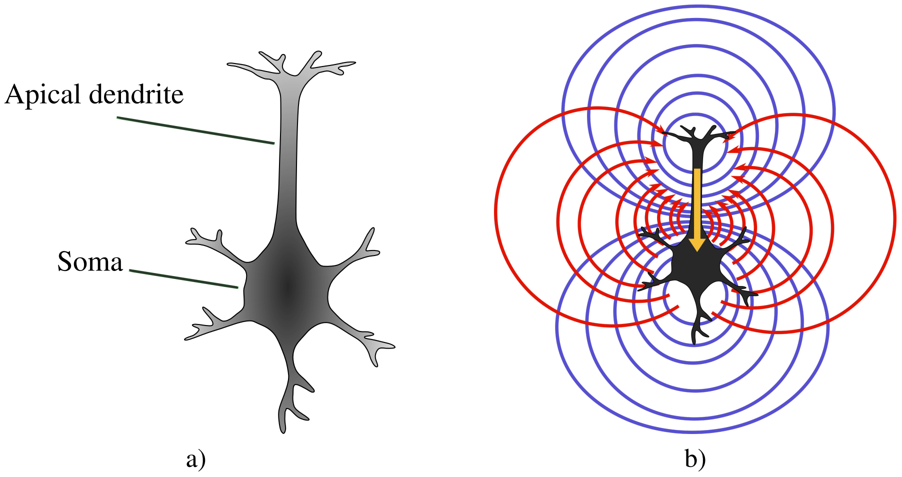

Figure 2.1.: a) Schematic representation of pyramidal cell. b) Current dipole model: The current dipole (yellow arrow) represents the primary current, the volume (return) currents are depicted as red arrows and the blue lines indicate the isopotential lines. Modified from Hari and Puce (2017).

the synapses and the type of postsynaptic potential (excitatory/inhibitory) (Hari and Puce, 2017). Simulation studies suggest that several tens of thousands of pyramidal cells need to be synchronously active in order to be detectable with MEG and EEG (Murakami and Okada, 2006). The electric current distribution related to action potentials is geometrically complex and can be modeled using higher order multipole sources (Brette and Destexhe, 2012). As a result, the signal at a distance (e.g., at the scalp) is dominated by dipolar sources (Brette and Destexhe, 2012). Additionally, action potentials last only about 1%–5% of the duration of postsynaptic potentials and therefore, they are not significantly contributing to the measured EEG and MEG signals (Hari and Puce, 2017).

2.2. Geometric and conductive properties of human head tissues

The current distribution resulting from cortical sources, and therefore also the measured signals by EEG/MEG, depend on the geometric and conductive characteristics of the human head which acts as a passive volume conductor (Hari and Puce, 2017). This influence is especially pronounced for EEG, although MEG studies also suggest an influence of geometry and resistivity, mainly for modeling differences in tissues in the vicinity of the source as opposed to changes in the skull and scalp compartment (Haueisen et al., 1997; Lew et al., 2013; Ramon et al., 2006). In this section, the anatomical characteristics of the human head as well as common approaches and typical simplifications to model the head volume conductor will be presented for the most important tissue compartments, with a focus on skull modeling and conductivity.

Figure 2.2 provides an anatomical overview and presents a schematic representation of the various tissue compartments in the human head. White matter mainly consists of nerve bundles that connect the cortical gray matter (Hallez et al., 2007). The brain itself is enveloped by the three membranes of pia mater, arachnoid mater and dura mater, which form the meninges (Yang and Lei, 2019). The subarachnoid space between the former two is filled with cerebrospinal fluid (CSF). The layered skull consists of compact bone connected by sutures with an enclosed spongiform layer (McCann et al., 2019; Yang and Lei, 2019).

Due to this complex organization, it is clear that simplifications and homogenizations are necessary for the creation of suitable head volume conductor models. Head modeling approaches typically differ in the shape, the number of tissues that are differentiated and the conductivities assigned to each of them. These aspects are closely related, for instance, it has been suggested to counterbalance the omission of the CSF tissue compartment by

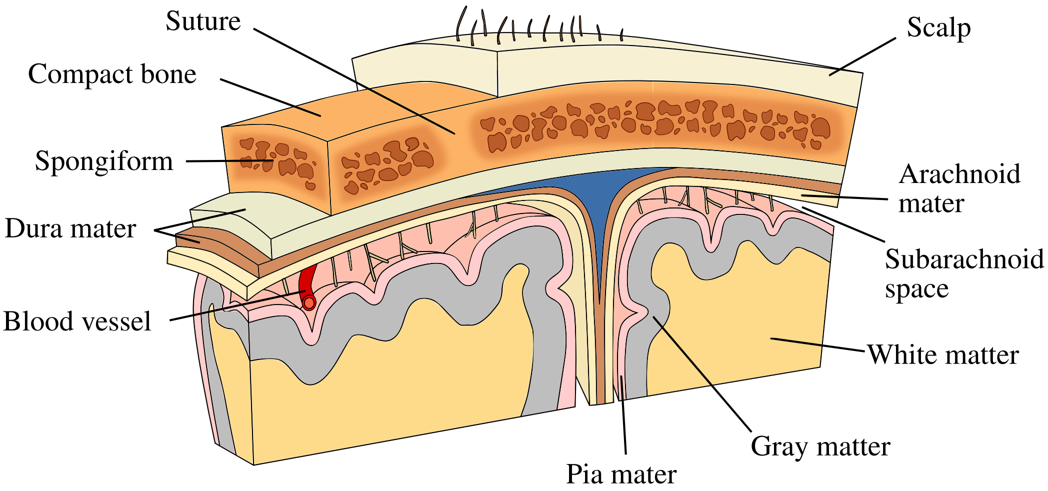

Figure 2.2.: Schematic representation of head tissues. The brain is encased by the meninges: pia mater, arachnoid mater and dura mater. The subarachnoid space located between the former two is filled with cerebrospinal fluid (CSF). The skull consists of an outer and inner layer of compact bone connected by sutures, with a spongiform layer enclosed. The labels are based on McCann et al. (2019) and Yang and Lei (2019), the drawing is modified from Blausen Medical (2014).

adapting the conductivity of the other tissues (Stenroos and Nummenmaa, 2016). Concerning the shape of the head model, in most applications, a standard spherical geometry is used as a simplified model of the human head (Brette and Destexhe, 2012; De Munck and Peters, 1993; Lalancette et al., 2011). For more realistic geometries, template head models can serve as a readily available alternative (Akalin Acar and Makeig, 2013). Commonly used template models consist of individual head models based on imaging modalities (e.g., MRI) which are averaged across multiple subjects (Fillmore et al., 2015; Fuchs et al., 2002; Mazziotta et al., 2001; Valdés-Hernández et al., 2009), or from a single individual (Collins et al., 1998). For an even more accurate modeling, individually segmented realistic head models can be created if imaging data is available (Céspedes-Villar et al., 2020; Von Ellenrieder et al., 2009). Regarding the number of tissues differentiated, in the simplest case, one-compartment (single-shell) head models can be used for MEG analysis (Hämäläinen and Sarvas, 1987; Nolte, 2003). Usually for EEG/MEG analysis, however, there are at least three tissue distinctions, modeling scalp, skull and brain compartments (Fuchs et al., 1998; Kybic et al., 2005; Stenroos et al., 2014). The distinction of further tissue compartments has been suggested for CSF, gray/white matter and compact/spongiform layers (Ramon et al., 2004; Wendel et al., 2008), resulting in up to six different tissues (Vorwerk et al., 2014). In some cases, even more compartments have been taken into account, e.g., air cavities

(Montes-Restrepo et al., 2014). Ramon et al. (2006, 2004) used an eleven-compartment head model additionally including muscle, fat, eyes, spinal cord/cerebellum and soft tissue. The availability and quality of imaging data increases and more sophisticated automated software pipelines for the segmentation of head models are offered, facilitating the generation of individual head models. However, the question of how to best assign conductivity values to these different biological tissues remains an important issue. The segmentation of additional tissue types may therefore not always be worth the effort, if the conductivity of the added compartment is unknown and has to be guessed. Typically, literature values are used to assign conductivities to each tissue compartment. This is problematic as firstly, reported conductivity values for most tissue compartments vary depending on the experimental setup, e.g., measurement modality, temperature, frequency and condition (*in vivo*, *ex vivo*, *in vitro*) (McCann et al., 2019). Secondly, most tissue conductivities vary inter-individually and may even be influenced by subject-specific factors such as pathology and age (McCann et al., 2019). Each major tissue type will be addressed in more detail in the following.

The outer tissue compartment usually referred to as scalp comprises the skin, fat and muscle layers outside the skull and is often assigned a conductivity of 0.43 S/m or 0.33 S/m in case it is assumed to be identical to the brain conductivity (Geddes and Baker, 1967; Gonçalves et al., 2003b; Haueisen et al., 1997; Vorwerk et al., 2014). This is in accordance with the meta-analysis of McCann et al. (2019), reporting a weighted mean of 0.41 S/m based on the reliability assessments of each study that was included.

The brain is usually either modeled as a homogeneous compartment or gray and white matter are distinguished for a more detailed modeling. While the homogeneous tissue compartment is often assumed to have a conductivity of 0.33 S/m, values of 0.33 S/m and 0.14 S/m are commonly used for gray and white matter, respectively, in case they are modeled separately (Gonçalves et al., 2003b; Ramon et al., 2004; Vorwerk et al., 2014). Weighted mean values of 0.38 S/m (whole brain, gray matter) and 0.15 S/m (white matter) were reported in McCann et al. (2019, 2021). Additionally, it has been suggested to take white matter anisotropy into account, as the conductivity along the direction of nerve bundles within the white matter has been reported to be approximately nine times higher compared to the orthogonal direction (Nicholson, 1965). This directional information can be reconstructed based on the characteristics of water diffusion detectable by DTI measurements (Ruthotto et al., 2012; Tuch et al., 2001). Due to the influence of white matter anisotropy on EEG and MEG forward and inverse analysis, which is especially pronounced for deep sources, is has been suggested to incorporate this information into realistic head models, provided it is available (Güllmar et al., 2010; Hallez et al., 2005; Wolters et al., 2006).

If taken into account, the tissues between skull and brain are usually homogenized as the CSF compartment. Often, the fixed conductivity of 1.79 S/m is used for this compartment based on the average of seven CSF samples measured by Baumann et al. (1997) at body temperature using directly applied current (DAC), while observing less than 2.4% deviations. This value is similar to the weighted mean reported by McCann et al. (2019, 2021) of 1.74 S/m. However, as the subarachnoid space filled with CSF is just part of the tissue between skull and brain, it has been suggested to model further tissue types such as dura mater (Ramon et al., 2014) and blood vessels (Fiederer et al., 2016) separately in addition to CSF.

In general, tissue modeling and conductivity attribution is demanding for most head tissues. However, skull conductivity seems especially important due to its high resistivity and considerable influence especially on the electric forward solutions and has therefore been intensely discussed. Sensitivity studies of EEG as well as TES forward and inverse solutions have stressed the importance of skull conductivity and the ratio between skull and scalp conductivity (Saturnino et al., 2019; Schmidt et al., 2015; Vallaghé and Clerc, 2009; Vorwerk et al., 2019a). As a result, many studies suggest that variations in skull modeling and conductivity strongly affect EEG source reconstructions and electric stimulation, e.g., shown in simulations in spherical and realistic head models (Chen et al., 2010; Montes-Restrepo et al., 2014; Roche-Labarbe et al., 2008; Saturnino et al., 2019; Schmidt et al., 2015) and in the context of localizing the irritative zone in presurgical epilepsy diagnosis (Aydin et al., 2017). However, it has also been shown that the role of skull conductivity in EEG and combined EEG/MEG source localizations using minimum-norm estimate (MNE) methods is negligible, although the spread of the source was found to vary slightly (Stenroos and Hauk, 2013). On the other hand, MNE methods have a depth bias favoring superficial sources and may therefore be less reliable for deeper sources (Fuchs et al., 1999; Lin et al., 2006).

There are different approaches how to best model the structure of the skull. Generally, the human skull consists of an outer and inner layer of compact bone encasing a spongiform layer in the middle with local inhomogeneities such as sutures which further complicate the modeling, see Figure 2.2. In the simplest and most common case, the skull is simplified as a homogeneous compartment , either as a spherical shell or realistically shaped, taking local variations in thickness into account (Brette and Destexhe, 2012; Gramfort et al., 2011). This strategy, however, does not account for the inhomogeneous distribution of the spongy and compact bone tissues. Therefore, it has been suggested to individually segment the spongiform bone layer from imaging data if available (Montes-Restrepo et al., 2014; Ramon et al., 2004). This would also take local skull inhomogeneities such as sutures into account, which might form a path of higher conductance (Law, 1993; Ollikainen et al., 1999; Pohlmeier et al., 1997; Tang et al., 2008). In addition, age-related anatomical changes, e.g., related to the fontanels, should not be neglected due to their large impact in neonates and infants (Azizollahi et al., 2016; Lew et al., 2013).

As for the other tissues, usually a standard literature value is assigned to the skull. Typical isotropic values adopted for skull conductivity are 0.0042 S/m (Buchner et al., 1997; Gençer and Acar, 2004; Güllmar et al., 2010) or 0.01 S/m (Cho et al., 2015; Dannhauer et al., 2011; Vorwerk et al., 2014). Different measurement techniques such as DAC (Akhtari et al., 2002; Hoekema et al., 2003; Tang et al., 2008), electrical impedance tomography (EIT) (Abascal et al., 2008; Fernández-Corazza et al., 2018; Nissinen et al., 2015), EEG or combined EEG/MEG (Baysal and Haueisen, 2004; Gonçalves et al., 2003b; Gutierrez et al., 2004) and magnetoacoustic tomography (Li et al., 2016) have been suggested and applied to individually determine this parameter. McCann et al. (2019) reported significantly lower whole skull conductivity values measured by EIT compared to values reported by DAC and EEG/MEG studies. Moreover, a higher conductivity can be observed in *in vivo* samples (McCann et al., 2019), by a factor of approximately 2.5–4 (Wendel and Malmivuo, 2006). In combination with different measurement conditions (e.g., temperature and frequency), highly varying literature values for bulk skull conductivity are reported with a weighted mean of 0.016 S/m (McCann et al., 2019). In addition to measurement characteristics, skull conductivity is assumed to strongly vary inter- and intra-individually, e.g., based on age (Antonakakis et al., 2020; Hoekema et al., 2003; Wendel et al., 2010). Often, the ratio of skull to other tissue conductivity has been discussed, either to soft tissue (scalp and brain) in general, usually assuming their conductivity is the same, or specifically to either brain or scalp tissue. Earlier works indicated a ratio of approximately 1:80 (Rush and Driscoll, 1968), while higher factors of up to 1:15 have been reported more recently (Akalin Acar et al., 2016; Dannhauer et al., 2011; Gonçalves et al., 2003a,b; Lai et al., 2005; Oostendorp et al., 2000; Zhang et al., 2006). The weighted mean of brain-to-skull conductivity ratios reported in McCann et al. (2019) was 50.4 with a standard deviation of 38.9. The disadvantage of a homogeneous isotropic conductivity is that the skull anisotropy resulting from its layered structure is not accounted for, which was found to have a smearing effect on the EEG potentials (Wolters et al., 2006). The spongiform tissue is more conductive than the compact bone layers (Akhtari et al., 2002), therefore the conductivity tangential to the head surface is assumed to be higher compared to the radial direction. This can be modeled by an anisotropic but homogeneous conductivity, i.e., by assigning each skull location a tangential and a radial conductivity value (Hallez et al., 2005; Wolters et al., 2006). This approach would account for the anisotropic nature of skull conductivity, but neglect local inhomogeneities. In case spongiosa is segmented separately, a ratio of approximately 3.6 between spongiform and compact skull conductivity has been suggested (Akhtari et al., 2002). Dannhauer et al. (2011) compared various skull modeling approaches in the context of EEG source analysis and concluded that the modeling of local variations of the skull was more important than modeling the skull conductivity as isotropic or anisotropic.

Due to the emphasized importance of skull conductivity in EEG, combined EEG/MEG and TES applications on the one hand, and largely varying individual measurements reported in literature on the other hand, a subject-based estimation of this parameter has been suggested and is subject of this thesis. In Chapter 4, a novel algorithm based on EEG/MEG to individually estimate skull conductivity will be presented.

2.3. EEG and MEG recordings

In this section, practical aspects related to the measurement of EEG and MEG signals are outlined. Although the underlying electromagnetic activity is identical, the acquisition of EEG and MEG signals poses modality-specific challenges that define the methods' applicability and characteristics.

EEG measures voltage differences via electrodes that are attached to the scalp, typical amplitudes measured from brain activity are in the range of 50–100 µV (Berger, 1929; Hari and Puce, 2017). We will only consider surface EEG in this thesis, however, also intracranial measurements are possible in clinical applications, e.g., in epilepsy diagnosis (Parvizi and Kastner, 2018). The number of sensors may vary, usually a standardized system is used for a better comparison such as the International 10–20 system (21 electrodes), the more dense 10–10 system (81 electrodes) or even higher resolutions (Hari and Puce, 2017; Oostenveld and Praamstra, 2001). These systems imply that the distance between electrodes is, for instance, based on 20% or 10% fractions of lines connecting anatomical landmarks, i.e., the connection between nasion and inion and the one linking the preauricular points. The electrodes are usually integrated in a cap for a more convenient setup and electrode gel and mild skin scraping underneath each electrode can improve the signal quality. EEG relies on a reference as it measures voltage differences and the particular choice of reference impacts its interpretation. Typically, a specific (ideally neutral) electrode is used as a reference, during the preprocessing the signals are often re-referenced using the average over all electrodes (Hari and Puce, 2017).

In MEG, magnetic fields generated by brain activity are detected which are typically in the order of 100 fT (Cohen, 1972; Gross, 2019). These amplitudes are about six orders of magnitude smaller than urban noise and three orders of magnitude smaller than the magnetic field strength generated by the human heart (Gross, 2019; Proudfoot et al., 2014). In order to capture these weak signals, MEG measurements are conducted in a magnetically shielded room and feature highly sensitive sensors. Typically used commercial whole-head systems comprise around 300 sensors which are arranged in a helmet-shaped insulated tank (dewar) in which the subject's head is positioned (Baillet, 2017; Gross, 2019).

Currently, most MEG systems rely on sensor technology based on highly sensitive Superconducting Quantum Interference Devices (SQUIDs) which operate in a state of superconductivity and can pick up signals in the fT range (Cohen, 1972; Gross, 2019). Every SQUID is coupled to a pickup coil located at a typical distance of approximately 2 cm from the subject's head (Cohen, 1972; Hari and Puce, 2017). Each sensor measures the magnetic flux through the surface area of this pickup coil in units of weber, although the output of most MEG systems is indicated as the magnetic flux density or magnetic field, indicated in units of tesla (Cheyne and Papanicolaou, 2017). In most MEG systems, pickup coils are oriented parallel to the head surface, thus measuring the magnetic field component in radial direction to the head surface, perpendicular to the coil surface (Cheyne and Papanicolaou, 2017). Pickup coils can have different shapes, some common designs are depicted in Figure 2.3. While a magnetometer consists of a single coil and therefore does not differentiate between homogeneous and rapidly changing magnetic fields, gradiometers are designed to measure the spatial gradient of the magnetic field in order to increase the signal-to-noise ratio (SNR). A first-order axial gradiometer consists of two coils with a typical distance (baseline) of 4–14 cm that are wound in opposite direction, measuring the changes in field strength along the distance between the coils, typically in the direction radial to the head surface (Hari and Puce, 2017). Consequently, sources that are far away which have a more slowly changing magnetic field are attenuated (Cheyne and Papanicolaou, 2017). Planar gradiometers operate similarly but consist of two coils arranged next to each other, measuring the gradient along the direction parallel to this arrangement (Cheyne and Papanicolaou, 2017). When located over a current dipole source, a bipolar field pattern with minimum and maximum field strengths on both sides of the dipole moment orientation is observed when using magnetometers or axial gradiometers. Planar gradiometers lead to a monopolar pattern with a maximum directly above the source in case the coils are arranged on a line perpendicular to the dipole moment vector (Hari and Puce, 2017). As the output of planar gradiometers depends on their orientation of coils in relation to the dipole moment, typically two planar gradiometers are combined orthogonally in one sensor array (Cheyne and Papanicolaou, 2017; Hari et al., 2018). Due to the small amplitude of the signals of interest, both EEG and MEG recordings are amplified and further preprocessed in order to minimize

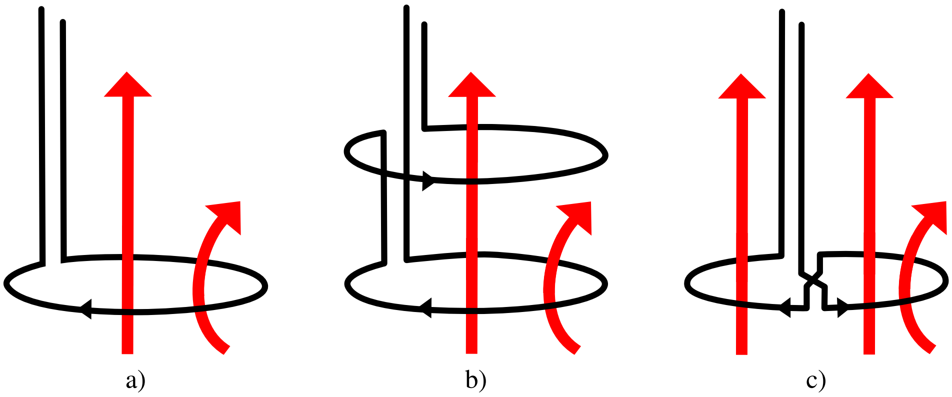

Figure 2.3.: Different designs of MEG sensors: a) magnetometer, b) first-order axial gradiometer and c) first-order planar gradiometer. While a magnetometer consists of only one coil, a first-order axial gradiometer has two coils wound in opposite direction. As a result, it filters out the uniform magnetic field (straight red arrow) that passes through the coils and instead only measures the change in the magnetic field strength between both coils. A planar gradiometer consists of two coils next to each other and measures the spatial gradient in the direction parallel to the coils. Modified from Cheyne and Papanicolaou (2017) and Hari and Puce (2017).

the influence of artifacts both originating from the environment (e.g., power line noise) and from the subject's body (e.g., eye movements) (Hari and Puce, 2017).

There are several technological advancements worth mentioning that may significantly impact research in these fields. Regarding EEG, conventional wet electrodes typically require a large preparation and cleanup time. Recent developments include dry (gel-free) electrode systems that almost achieve a comparable quality and may broaden clinical applications of EEG due to their easy setup and usability (Hinrichs et al., 2020; Lopez-Gordo et al., 2014). Additionally, even though quality of EEG measurements improves in an electromagnetically shielded environment and body movements are usually discouraged, there are also advances in small and wireless portable EEG systems that allow EEG measurements in natural environments outside the laboratory (De Vos et al., 2014; Ratti et al., 2017). This technological progress also offers new possibilities in providing viable neurofeedback therapies, e.g., in the context of attention deficit hyperactivity disorder (ADHD) or epilepsy (Egner and Sterman, 2006; Enriquez-Geppert et al., 2017; Monastra et al., 2002). Related to MEG, a major drawback of SQUID technology is their requirement for extremely low temperatures of approximately 4 K in order to function properly (Gross, 2019). To achieve this, the dewar is filled with liquid helium which needs to be refilled regularly in some systems, although there are also advances in helium recycling (Gross, 2019). As a result, MEG systems typically have rather high acquisition and maintenance costs. Additionally, the fixed arrangement of sensors within the dewar described above is sensitive to head movements and poses restrictions for its applicability, for instance related to different head sizes or children (Gross, 2019; Hari and Puce, 2017). There are several promising alternatives to conventional SQUID technology emerging. Amongst others, high-transition-temperature (high-T_c) SQUIDs can operate at the temperature of liquid nitrogen (77 K) and therefore require less insulation, potentially allowing them to be positioned closer to the scalp (Körber et al., 2016; Öisjöen et al., 2012). In addition, a promising new sensor technology of optically pumped magnetometers (OPMs) is evolving that might overcome the disadvantages of conventional MEG systems, with a similar sensitivity (Borna et al., 2020; Gross, 2019; Tierney et al., 2019). These sensors rely on principles of magnetic resonance and involve a light-vapor (e.g., rubidium) interaction in a cell, which does not depend on expensive cryogenic components (Borna et al., 2020; Labyt et al., 2019). Therefore, they are more flexible in their setup, as they can be placed directly adjacent to the scalp, allowing an integration into wearable systems (Boto et al., 2018; Tierney et al., 2020).

EEG and MEG are closely related, but although the underlying cortical sources are identical, it can be advantageous to combine both modalities. Their mutual acquisition does not only increase the number of sensors and therefore improve the spatial sampling, but also stabilizes the analysis due to the complementary nature of both modalities. For instance, it is well established that MEG is insensitive to quasi-radial orientation components, while EEG is sensitive to radial activity as well (Cohen and Cuffin, 1983). Therefore, the benefits of a combined analysis have been emphasized in order to capture the core characteristics of the source by at least one modality and thereby stabilizing source analysis (Dassios et al., 2007), e.g., in epilepsy research (see Chapter 7). Simulation studies in a realistic head model have confirmed that the MEG is more sensitive to tangentially oriented sources, while the EEG was shown to be more sensitive to radial and deep cortical sources (Piastra et al., 2021). Combined measurements require that the EEG setup is non-magnetic and the subject's head still fits into the MEG dewar with electrodes attached to the head surface (Hari and Puce, 2017). Further technical aspects for combining EEG and MEG data sets are discussed in Section 3.4.

3. Mathematical background to the EEG and MEG forward problems

In many applications, the aim of EEG/MEG measurements is to reconstruct the underlying cerebral sources from the electric potential (EEG) or magnetic field (MEG) measured at the sensors. In order to solve this ill-posed *inverse problem*, accurate solutions of the *forward problem* need to be computed by simulating EEG/MEG signals that result from brain activity. Regarding EEG, the electric potential is computed by solving an elliptic partial differential equation, while an integral is evaluated to calculate the magnetic field in case of MEG (Brette and Destexhe, 2012).

In this chapter, the mathematical background related to the EEG and MEG forward problems is presented. Based on Maxwell's equations of electromagnetism, the Poisson equation for the electric potential is derived and an integral expression to compute the magnetic field based on the law of Biot-Savart is introduced in Section 3.1. In simplified geometrical head models, (quasi-)analytical expressions exist for the EEG and MEG forward solutions, which are outlined in Section 3.2 for concentric spherical head models. As more realistically shaped head models require numerical approaches, Section 3.3 presents the mathematical framework for solving the forward problems using the finite element method (FEM). In Section 3.4, postprocessing steps to prepare the forward solutions for inverse methods are presented, including their evaluations at the sensors and SNR transformations for a combined analysis. Additionally, the concepts of transfer and leadfield matrices are introduced.

In the following, we employ the convention of describing vector fields such as the magnetic field $\mathbf{B} : \mathbb{R}^3 \to \mathbb{R}^3$ with bold letters in order to better distinguish them from scalar fields, e.g., the electric potential $u : \mathbb{R}^3 \to \mathbb{R}$.

3.1. Derivation of the EEG/MEG forward problems

The forward problem in EEG applications refers to the calculation of the electric potential at the electrodes, while the MEG forward problem involves the computation of the magnetic field components at the sensors outside the head, both generated by a given current distribution inside the brain. In the following, mathematical formulations for the EEG and MEG forward problems will be derived based on Maxwell's equations of electromagnetism.

In general, electromagnetic phenomena are governed by Maxwell's macroscopic equations (Maxwell, 1861, 1865). Taking the bioelectrical properties and generators underlying EEG and MEG into account, it has been argued that the contributions of the time derivatives can be neglected and the quasi-static approximation of Maxwell's equations can be presumed (De Munck and Van Dijk, 1991; Hämäläinen et al., 1993; Plonsey and Heppner, 1967), which is defined as follows (De Munck and Van Dijk, 1991; Hämäläinen et al., 1993).

Definition 3.1: ***Quasi-static approximation of Maxwell's equations.*** *For biological tissues, we assume that the magnetic permeability* μ *approximately corresponds to the one in free space* $\mu_0 = 4\pi 10^{-7}\frac{\mathrm{Tm}}{\mathrm{A}}$*, so that the relations between the electric displacement field* $\mathbf{D}$ *and the electric field* $\mathbf{E}$*, as well as the magnetic field* $\mathbf{B}$ *and the magnetizing field* $\mathbf{H}$ *are governed by the constitutive equations*

$$\begin{aligned}\mathbf{D} &= \varepsilon_0 \varepsilon_r \mathbf{E},\\ \mathbf{H} &= \frac{1}{\mu_0}\mathbf{B},\end{aligned}$$

where the electric permittivity of the material is given as the product of the permittivity of free space ε_0 *and the relative permittivity* ε_r*. Then, the quasi-static approximation of Maxwell's equations in* $\mathbb{R}^3$ *can be stated as*

$$\begin{aligned}\nabla \cdot \mathbf{E} &= \frac{\rho}{\varepsilon_0 \varepsilon_r},\\ \nabla \times \mathbf{E} &= 0,\\ \nabla \times \mathbf{B} &= \mu_0\, \mathbf{j}, && (3.1)\\ \nabla \cdot \mathbf{B} &= 0, && (3.2)\end{aligned}$$

where ρ *denotes the electric charge density and* $\mathbf{j}$ *the electric current density.*

The rotation-free electric field can be expressed as the gradient field of a scalar electric potential u as $\mathbf{E} = -\nabla u$. The current density $\mathbf{j}$ can then be stated as the sum of the primary current density $\mathbf{j}^p$ and the secondary current density resulting from return currents $\mathbf{j}^s = \boldsymbol{\sigma}\mathbf{E}$ following Ohm's law, as

$$\mathbf{j} = \mathbf{j}^p - \boldsymbol{\sigma}\nabla u, \qquad (3.3)$$

where $\boldsymbol{\sigma}$ denotes the electrical conductivity. Applying the divergence to both sides of (3.1), and inserting (3.3) yields a Poisson equation for the electric potential, leading to the following definition of the EEG forward problem (Brette and Destexhe, 2012; De Munck and Peters, 1993).

Definition 3.2: ***EEG forward problem.*** *Let $\Omega \subset \mathbb{R}^3$ be the head domain with a sufficiently smooth boundary $\partial\Omega$ and let the conductivity be given by symmetric, positive definite tensors $\boldsymbol{\sigma} : \Omega \to \mathbb{R}^{3x3}$. Then, the EEG forward problem is to find the electric potential $u : \Omega \to \mathbb{R}$ that solves*

$$\begin{aligned} \nabla \cdot (\boldsymbol{\sigma} \nabla u) &= \nabla \cdot \mathbf{j}^p \quad \text{in } \Omega, \\ \boldsymbol{\sigma} \nabla u \cdot \mathbf{n} &= 0 \qquad\quad \text{on } \partial\Omega, \end{aligned} \tag{3.4}$$

where $\mathbf{n}$ denotes the outer surface normal.

In case of isotropic tissue, the conductivity can be written in a simplified way as a scalar field $\sigma : \Omega \to \mathbb{R}^+$. Zero Neumann boundary conditions on the head surface $\partial\Omega$ are assumed, as air has an electric conductivity several orders of magnitude smaller than biological tissue (Seran et al., 2017).

Typically, the primary current is modeled as an equivalent current dipole (Brette and Destexhe, 2012; Hämäläinen et al., 1993) which is defined as follows.

Definition 3.3: ***Current dipole model.*** *For dipole location $\mathbf{x}_0 \in \Omega$ and moment vector $\mathbf{q} \in \mathbb{R}^3$, the current dipole (or mathematical point dipole) is defined as*

$$\mathbf{j}^p(\mathbf{x}) = \mathbf{q}\delta(\mathbf{x} - \mathbf{x}_0), \tag{3.5}$$

where δ is the Dirac delta distribution.

Classical solutions u to the *strong formulation* of the EEG forward problem presented in Def. 3.2, i.e., $u \in C^2(\Omega) \cap C^1(\bar{\Omega})$, only exist for restrictive regularity assumptions on the right-hand side as well as the conductivity, which are typically not met (Braess, 2007). As to the conductivity, it is usually either assigned to each tissue type or each voxel value is inferred from DTI measurements. In both cases, only piecewise constant values can be presumed, i.e., $\boldsymbol{\sigma}_{ij} \in L^\infty(\Omega)$, $1 \leq i, j \leq 3$. Additionally, the evaluation of the singular source term $\nabla \cdot (\mathbf{q}\delta_{\mathbf{x}_0})$, which results from inserting (3.5) into the right-hand side term of (3.4), poses challenges to the applicability of the theoretical FEM framework. In Section 3.3, a weak formulation for the EEG forward problem will be derived and different approaches to deal with the singular source term are addressed.

Regarding MEG, the forward problem refers to the calculation of the magnetic field at the sensor positions outside the head generated by a current distribution inside the brain.

It is closely related to EEG, as the integral expression for the magnetic field which will be derived in the following based on Hansen et al. (2010), Plonsey and Heppner (1967) and Hämäläinen et al. (1993), requires the solution of the EEG forward problem.

As the magnetic field is characterized by zero divergence following Maxwell's equation (3.2), it can be expressed as the curl of the magnetic vector potential $\hat{\mathbf{A}}$, i.e., $\mathbf{B} = \nabla \times \hat{\mathbf{A}}$. Using Coulomb's gauge $\nabla \cdot \hat{\mathbf{A}} = 0$, it follows from (3.1) that

$$\mu_0 \, \mathbf{j} = \nabla \times \mathbf{B} = \nabla \times (\nabla \times \hat{\mathbf{A}}) = \nabla(\nabla \cdot \hat{\mathbf{A}}) - \nabla^2 \hat{\mathbf{A}} = -\nabla^2 \hat{\mathbf{A}}. \tag{3.6}$$

Consequently, $\hat{\mathbf{A}}$ can be written as the solution of the Poisson equation in (3.6):

$$\hat{\mathbf{A}}(\mathbf{x}_s) = \frac{\mu_0}{4\pi} \int\limits_{\Omega} \frac{\mathbf{j}(\mathbf{x})}{\|\mathbf{x}_s - \mathbf{x}\|_2} \, d\mathbf{x}, \tag{3.7}$$

for a measurement position $\mathbf{x}_s$. Using the relation $\mathbf{B} = \nabla \times \hat{\mathbf{A}}$ in combination with (3.7) and the quotient rule for the curl operator results in the law of Biot-Savart, which is stated in the following definition of the MEG forward problem (Cheyne and Papanicolaou, 2017; Hämäläinen et al., 1993).

Definition 3.4: ***MEG forward problem.*** *Let* Ω *denote the head domain,* σ *the conductivity,* $\mathbf{j}$ *a given current distribution in the brain and* u *the electric potential. Then, the MEG forward problem refers to the computation of the magnetic field* $\mathbf{B}$ *outside the head volume conductor for a measurement position* $\mathbf{x}_s \in \mathbb{R}^3 \setminus \Omega$*, which can be calculated using the law of Biot-Savart as*

$$\begin{aligned} \mathbf{B}(\mathbf{x}_s) &= \frac{\mu_0}{4\pi} \int\limits_{\Omega} \mathbf{j}(\mathbf{x}) \times \frac{\mathbf{x}_s - \mathbf{x}}{\|\mathbf{x}_s - \mathbf{x}\|_2^3} \, d\mathbf{x} \\ &= \underbrace{\frac{\mu_0}{4\pi} \int\limits_{\Omega} \mathbf{j}^p(\mathbf{x}) \times \frac{\mathbf{x}_s - \mathbf{x}}{\|\mathbf{x}_s - \mathbf{x}\|_2^3} \, d\mathbf{x}}_{\mathbf{B}^p} \underbrace{- \frac{\mu_0}{4\pi} \int\limits_{\Omega} \boldsymbol{\sigma}(\mathbf{x}) \nabla u(\mathbf{x}) \times \frac{\mathbf{x}_s - \mathbf{x}}{\|\mathbf{x}_s - \mathbf{x}\|_2^3} \, d\mathbf{x}}_{\mathbf{B}^s}, \end{aligned} \tag{3.8}$$

where $\mathbf{B}^p(\mathbf{x}_s)$ *denotes the primary magnetic field and the secondary magnetic field* $\mathbf{B}^s(u, \mathbf{x}_s)$ *depends on the solution of the EEG forward problem.*

While the secondary magnetic field is computed numerically once the EEG forward problem is solved, an analytical expression exists for the primary magnetic field.

Remark 3.1: ***Primary magnetic field.*** *The primary magnetic field* $\mathbf{B}^p$ *can be computed analytically for a dipolar source at location* $\mathbf{x}_0 \in \Omega$ *and moment vector* $\mathbf{q} \in \mathbb{R}^3$ *(Sarvas,* *1987):*

$$\mathbf{B}^p(\mathbf{x}_s) = \frac{\mu_0}{4\pi}\mathbf{q} \times \frac{\mathbf{x}_s - \mathbf{x}_0}{||\mathbf{x}_s - \mathbf{x}_0||_2^3}. \tag{3.9}$$

Note that there are different definitions of the MEG forward problem, an alternative formulation relies on the computation of the magnetic field component in measurement direction via the magnetic flux using Stokes' theorem, which involves the computation of a coil surface integral over the magnetic vector potential $\hat{\mathbf{A}}$ (Vorwerk, 2016).

3.2. (Quasi-)Analytical solutions

In simplified geometric scenarios, (quasi-)analytical expressions for the EEG and MEG forward problems exist. Most relevant for applications in neuroscience are multi-layered spherical head volume conductor models as a rough approximation of the head geometry, which will be considered in the following.

For EEG, De Munck and Peters (1993) derived series expansion formulas to compute the electric potential at the electrode positions on the outer sphere surface. Following De Munck and Peters (1993) and Wolters (2017), the quasi-analytical EEG solution can be computed as follows.

Definition 3.5: ***Quasi-analytical EEG solution in concentric spherical head model.*** *Let the head model consist of N concentric spheres, each layer is assumed to have a constant conductivity $\sigma_i \in \mathbb{R}^+$, $1 \leq i \leq N$. As previously, we consider a dipolar source at location $\mathbf{x}_0$ with moment $\mathbf{q}$, and the electrode position on the outer sphere surface is denoted by $\mathbf{x}_s$. The radial coordinates of the sensor and dipole locations are denoted by r_s and r_0, respectively. Let ω_{0s} further be the angular distance between electrode and source.*

Then, the potential at the electrode can be computed as

$$u(\mathbf{x}_0, \mathbf{x}_s) = \frac{1}{4\pi}\langle \mathbf{q}, S_0 \frac{\mathbf{x}_s}{r_s} + (S_1 - \cos(\omega_{0s})S_0)\frac{\mathbf{x}_0}{r_0}\rangle,$$

with the terms S_0 and S_1 defined as

$$S_0 = \frac{F_0}{r_0}\frac{\Lambda}{R^3} + \frac{1}{r_0}\sum_{n=1}^{\infty}\left[(2n+1)R_n(r_0, r_s) - F_0\Lambda^n\right]P_n'(\cos(\omega_{0s})),$$

$$S_1 = F_1\frac{\Lambda(\cos(\omega_{0s})) - \Lambda^2}{R^3} + \sum_{n=1}^{\infty}\left[(2n+1)R_n'(r_0, r_s) - F_1 n\Lambda^n\right]P_n(\cos(\omega_{0s})).$$

The scalar terms F_0, F_1, Λ and R, which are independent of n, as well as the coefficients R_n and their derivatives can be computed analytically using the geometric characteristics and piecewise homogeneous conductivities (De Munck and Peters, 1993). P_n and P_n' denote the Legendre polynomials and their derivatives (Bronstein et al., 2008).

For the MEG forward solution, an analytical closed-form expression in a multi-layer spherical head volume conductor model with piecewise homogeneous conductivities was formulated by Sarvas (1987).

Definition 3.6: ***Analytical MEG solution in concentric spherical head model.*** *Let the head model consist of N concentric spheres and let the sphere center be the origin of the coordinate system. Then, the $\mathbf{B}$ field at location $\mathbf{x}_s$ outside the volume conductor can be computed as*

$$\begin{aligned}
\mathbf{B}(\mathbf{x}_s) &= \frac{\mu_0}{4\pi F^2}\left(F\mathbf{q}\times\mathbf{x}_0 - [(\mathbf{q}\times\mathbf{x}_0)\cdot\mathbf{x}_s]\nabla F\right), \textit{ with} \\
F &= a\left(xa + x^2 - \mathbf{x}_0\cdot\mathbf{x}_s\right), \\
\nabla F &= \left(x^{-1}a^2 + a^{-1}\mathbf{a}\cdot\mathbf{x}_s + 2a + 2x\right)\mathbf{x}_s - \left(a + 2x + a^{-1}\mathbf{a}\cdot\mathbf{x}_s\right)\mathbf{x}_0, \\
\mathbf{a} &= \mathbf{x}_s - \mathbf{x}_0, \quad a = |\mathbf{a}|, \quad x = |\mathbf{x}_s|.
\end{aligned}$$

Here, the physical constant μ_0 denotes the magnetic permeability of vacuum, see Def. 3.1.

It is worth noting that in this simplified spherical head model, the magnetic field at a sensor position outside the volume conductor does not depend on its conductive properties. Additionally, the magnetic field is not influenced by the radii of spherical layers either, it only depends on the source and measurement locations relative to the sphere center (Cheyne and Papanicolaou, 2017; Sarvas, 1987). Another important implication is that the **B** field vanishes for radial dipole orientations as the cross product between dipole moment and position is zero. In case the brain is modeled as a sphere, this implies that sources located on gyral crowns and sulcal valleys are not visible in the MEG, as the dipole orientation perpendicular to the cortex is radial to the sphere surface in these cases.

3.3. Numerical solutions using the finite element method

For more complex realistically shaped head models, without analytical formulations available, different approaches have been suggested and applied to solve the EEG/MEG forward problems numerically (Pruis et al., 1993). One commonly used approach is the boundary element method (BEM) which computes the surface potentials using triangulated surfaces of head tissue compartments each assigned with a homogeneous isotropic conductivity (Geselowitz, 1967; Gramfort et al., 2011; Stenroos and Sarvas, 2012). Typically, three nested surfaces (inner and outer skull, outer scalp) are used, although theoretically, non-nested surfaces are also possible to incorporate (Kybic et al., 2006). This method is widely used in practice due to its comparatively low computational effort. However, BEM does not allow for anisotropic tissue, and the accurate modeling of complex-shaped layers such as CSF would add a high number of additional degrees of freedom which would significantly increase the computational effort, as BEM involves the inversion of a small but dense system matrix (Hallez et al., 2007; Vorwerk et al., 2012). Other numerical methods adopted to solve the EEG/MEG forward problems include the finite difference method (FDM) (Cuartas Morales et al., 2019; Montes-Restrepo et al., 2014; Vatta et al., 2009) and the finite volume method (FVM) (Cook and Koles, 2006). Both of these methods potentially allow for anisotropy by including a larger computational stencil that takes more neighboring degrees of freedom into account.

In the following, we will focus on the finite element method (FEM), which is able to cope with anisotropic tissue as well as complex geometries and has been widely used in EEG/MEG analysis (Azizollahi et al., 2018; Gençer and Acar, 2004; Piastra et al., 2021; Vorwerk et al., 2014). A weak formulation of the EEG forward problem is introduced in Section 3.3.1, and a discretization of the EEG and MEG forward problems using a conforming FEM approach is presented in Section 3.3.2. Subsequently, different approaches to model the dipolar source are introduced in Section 3.3.3.

3.3.1. Weak formulation

The *strong formulation* of the EEG forward problem presented in (3.4) implies restrictive regularity conditions which are typically not satisfied. In this section, we will therefore derive a *weak formulation* of the above-mentioned problem. The content of this section is mainly based on Braess (2007) and Evans (1998) which contain further details on Sobolev space theory.

We assume that the head domain $\Omega \subset \mathbb{R}^3$ is open with a piecewise smooth boundary. The space $L^2(\Omega)$ refers to measurable functions for which u^2 is Lebesgue-integrable, its scalar product associated with the norm $\|\cdot\|_{L^2}$ is defined as $\langle u, v\rangle_{L^2} = \int_\Omega u\, v\, d\mathbf{x}$. Before introducing Sobolev spaces, we define weak derivatives (Braess, 2007; Ciarlet, 2002).

Definition 3.7: ***Weak derivative.*** *Let* $\boldsymbol{\alpha} = (\alpha_1, \dots, \alpha_d) \in \mathbb{N}^d$ *denote a multi-index with the norm* $|\boldsymbol{\alpha}| := \sum_{i=1}^d \alpha_i$. *Then,* $u \in L^2(\Omega)$ *has a weak derivative* v *defined as*

$$v = \partial^{\boldsymbol{\alpha}} u := \frac{\partial^{|\boldsymbol{\alpha}|} u}{\partial_{x_1}^{\alpha_1} \dots \partial_{x_d}^{\alpha_d}},$$

if $v \in L^2(\Omega)$ *and for all* $\varphi \in C_0^\infty(\Omega)$

$$\langle \varphi, v \rangle_{L^2} = (-1)^{|\boldsymbol{\alpha}|} \langle \partial^{\boldsymbol{\alpha}} \varphi, u \rangle_{L^2}.$$

Definition 3.8: ***Sobolev space.*** *The Sobolev space* $H^k(\Omega)$ *for* $k \in \mathbb{N}_0$ *is defined as*

$$H^k(\Omega) = \left\{ u \in L^2(\Omega) : \partial^{\boldsymbol{\alpha}} u \in L^2(\Omega), |\boldsymbol{\alpha}| \leq k \right\},$$

with the associated norm

$$\|u\|_{H^k} = \sqrt{\langle u, u \rangle_k} = \sqrt{\sum_{|\boldsymbol{\alpha}| \leq k} \|\partial^{\boldsymbol{\alpha}} u\|_{L^2}^2}.$$

In combination with the norm $\|\cdot\|_{H^k}$, the space $H^k(\Omega)$ is a Hilbert space Braess (2007). In particular, $H^1(\Omega)$ denotes the space of scalar functions in $L^2(\Omega)$ with weak derivatives also in $L^2(\Omega)$. We introduce the following subspaces which will be used to admit a unique solution of the weak formulation despite pure homogeneous Neumann boundary conditions.

Definition 3.9: ***Sobolev space with zero mean.*** *The Sobolev space with zero mean* $H_*^k(\Omega)$ *for* $k \in \mathbb{N}_0$ *is defined as*

$$H_*^k(\Omega) = \left\{ u \in H^k(\Omega) : \int_\Omega u \, d\mathbf{x} = 0 \right\}.$$

In order to derive the weak formulation of the EEG forward problem, we start with Poisson's equation (3.4) with the source term $f := \nabla \cdot \mathbf{j}^p$. Assuming a sufficiently regular right-hand side function $f \in L^2(\Omega)$, we multiply with a test function $v \in V$ which will be defined later. Integrating over the domain Ω and applying integration by parts yields

$$\int_\Omega \boldsymbol{\sigma} \nabla u \cdot \nabla v \, d\mathbf{x} = -\int_\Omega f v \, d\mathbf{x},$$

as the boundary integral vanishes due to the zero Neumann boundary conditions. This leads to the following definition of the weak formulation of the EEG forward problem.

Definition 3.10: ***Weak EEG forward problem formulation.*** *In its weak formulation, the EEG forward problem is to find $u \in V$, such that*

$$a(u,v) = l(v) \quad \forall v \in V, \tag{3.10}$$

where the bilinear form $a(u,v)$ and the linear form $l(v)$ are defined as

$$a(u,v) = \int_\Omega \boldsymbol{\sigma} \nabla u \cdot \nabla v \, d\mathbf{x} \tag{3.11}$$

$$l(v) = -\int_\Omega f v \, d\mathbf{x}. \tag{3.12}$$

An important finding to prove existence and uniqueness of solutions of partial differential equations is given by the Lax-Milgram theorem (Evans, 1998).

Theorem 3.1: ***Lax-Milgram.*** *Let X denote a Hilbert space with norm $\|.\|$ and $a : X \times X \to \mathbb{R}$ be a bilinear form which is*

$$\begin{array}{ll} (i)\ \textit{continuous}: & \exists c_1 \in \mathbb{R},\ c_1 > 0 : |a(u,v)| \leq c_1 \|u\| \|v\|, \textit{ and} \\ (ii)\ \textit{coercive}: & \exists c_2 \in \mathbb{R},\ c_2 > 0 : \ a(u,u) \geq c_2 \|u\|^2 \end{array}$$

for all $u, v \in X$. Then, for a bounded linear functional $l : X \to \mathbb{R}$, there exists a unique element $u \in X$ such that for all $v \in X$

$$a(u,v) = l(v).$$

Note that for the bilinear form defined in (3.11), $a(1,v) = 0$ for any $v \in H^1(\Omega)$. Therefore, a solution $u \in H^1(\Omega)$ is not unique, as any constant can be added. However, for a sufficiently regular right-hand side, assuming that l is an element of the dual space $(H^1_*(\Omega))'$, existence and uniqueness of a solution of the weak formulation can be shown for the subspace $H^1_*(\Omega)$ defined in Def. 3.9 (Wolters et al., 2007c), as shown in the following.

Theorem 3.2: ***Existence and uniqueness of weak solution.*** *Let $l \in (H^1_*(\Omega))'$ and the conductivity tensors $\boldsymbol{\sigma} : \Omega \to \mathbb{R}^{3\times 3}$ be piecewise constant and symmetric positive definite. Then, there exists a unique solution u of the weak formulation in Def. 3.10 in the space $V := H^1_*(\Omega)$.*

Proof: It is shown that the prerequisites of the Lax-Milgram theorem are met for the bilinear form defined in (3.11). First, the continuity requirement can be shown for any $u, v \in H^1(\Omega)$. As the conductivity is piecewise constant, the domain Ω can be divided into pairwise disjoint subdomains $\Omega = \bigcup_k \bar{\Omega}_k$ with constant conductivity tensors $\boldsymbol{\sigma}(\mathbf{x}) = \boldsymbol{\sigma}_k$ for $\mathbf{x} \in \Omega_k$. Due to the symmetry and positive definiteness of $\boldsymbol{\sigma}_k$, there exists an orthogonal matrix $\mathbf{S}_k$ such that $\boldsymbol{\Lambda}_k = \mathbf{S}_k^T \boldsymbol{\sigma}_k \mathbf{S}_k$, where $\boldsymbol{\Lambda}_k$ is a diagonal matrix with real positive eigenvalues $(\lambda_k)_i$ of $\boldsymbol{\sigma}_k$, $1 \leq i \leq 3$. Therefore, each subintegral over Ω_k can be transformed so that $\boldsymbol{\sigma}_k$ is diagonalized by applying the rotation $\mathbf{T}_k : \Omega_k \to \Omega_k^{'}$, $\mathbf{x} \mapsto \boldsymbol{\xi}$, with $\mathbf{T}_k(\mathbf{x}) = \mathbf{S}_k^T \mathbf{x}$, and vice versa $\mathbf{T}_k^{-1}(\mathbf{x}) = \mathbf{S}_k \mathbf{x}$, with $|\det(\nabla \mathbf{T}_k)| = 1$ due to the orthogonality of $\mathbf{S}_k$. This yields

$$\begin{aligned}
|a(u,v)| &= \left| \int_\Omega \boldsymbol{\sigma} \nabla u \cdot \nabla v \, d\mathbf{x} \right| \\
&= \left| \sum_k \int_{\Omega_k^{'}} \boldsymbol{\Lambda}_k \nabla' u \cdot \nabla' v \, d\boldsymbol{\xi}_k \right| \\
&\overset{(*)}{\leq} \sum_k \int_{\Omega_k^{'}} |\boldsymbol{\Lambda}_k \nabla' u| \, |\nabla' v| \, d\boldsymbol{\xi}_k \\
&\leq \sigma_{\max} \sum_k \int_{\Omega_k} |\nabla u| \, |\nabla v| \, d\mathbf{x},
\end{aligned}$$

using the Cauchy-Schwarz inequality in $(*)$. Here, $\sigma_{\max} := \max_{k,i} (\lambda_k)_i$ denotes the largest eigenvalue of all conductivity tensors in Ω. Summation over the subdomains again yields

$$\begin{aligned}
\sigma_{\max} \int_\Omega |\nabla u| \, |\nabla v| \, d\mathbf{x} &\overset{(**)}{\leq} \sigma_{\max} \|\nabla u\|_{L^2} \|\nabla v\|_{L^2} \\
&\leq c_1 \|u\|_{H^1} \|v\|_{H^1},
\end{aligned}$$

with $c_1 = \sigma_{\max}$, applying the Hölder inequality in $(**)$.

Second, it can be shown that the bilinear form is coercive for any $u \in V$. Similar to the proof of continuity, the integral is subdivided into domains on which the conductivity is constant and rotated to the coordinate system in which this tensor is diagonal

$$\begin{aligned}
a(u,u) &= \int_\Omega \boldsymbol{\sigma} \nabla u \cdot \nabla u \, d\mathbf{x} \\
&= \sum_k \int_{\Omega_k^{'}} \boldsymbol{\Lambda}_k \nabla' u \cdot \nabla' u \, d\boldsymbol{\xi}_k \\
&\geq \sigma_{\min} \int_\Omega |\nabla u|^2 \, d\mathbf{x}
\end{aligned}$$

where $\sigma_{\min} = \min_{k,i}(\lambda_k)_i$ denotes the smallest eigenvalue of all conductivity tensors in Ω. It follows that

$$\begin{aligned}\sigma_{\min}\int_\Omega |\nabla u|^2\,d\mathbf{x} &= \sigma_{\min}\|\nabla u\|_{L^2}^2\\ &= \frac{\sigma_{\min}}{2}\left(\|\nabla u\|_{L^2}^2+\|\nabla u\|_{L^2}^2\right)\\ &\overset{(***)}{\geq} \frac{\sigma_{\min}}{2}\|\nabla u\|_{L^2}^2+\frac{\sigma_{\min}}{2\tilde{c}^2}\|u\|_{L^2}^2\\ &\geq c_2\|u\|_{H^1}^2,\end{aligned}$$

where $c_2 = \frac{\sigma_{\min}}{2}\min\{1,\frac{1}{\tilde{c}^2}\}$. For $(***)$, a variant of the Friedrich-Poincaré inequality is used, stating that for any $u \in H^1(\Omega)$, there exists a constant $\tilde{c} = \tilde{c}(\Omega)$, such that $\|u\|_{L^2} \leq \tilde{c}\left(|\bar{u}| + \|\nabla u\|_{L^2}\right)$, with $\bar{u} = \frac{1}{|\Omega|}\int_\Omega u\,d\mathbf{x}$ (Braess (2007), p. 32). Here, the condition $u \in V$ is used, as in our case $\bar{u} = 0$. Following Theorem 3.1, the variational problem (3.10) is well-posed and admits a unique solution $u \in H^1_*(\Omega)$. ☐

Remark 3.2: ***Compatibility condition.*** *In the proof of Theorem 3.2, it is shown that there exists a unique* $u \in H^1_*(\Omega)$ *that solves the variational problem for all* $v \in H^1_*(\Omega)$*. This can be generalized to all* $\tilde{v} \in H^1(\Omega)$*, using the relation* $\tilde{v} = v + 1\cdot c$*, for* $c \in \mathbb{R}$, $v \in H^1_*(\Omega)$ *(Wolters et al., 2007c). As* $a(u,1) = 0$ *for any* $u \in H^1(\Omega)$*, it is required that* $l(1) = 0$ *as well for their equality, which is referred to as the compatibility condition.*

In order to apply Theorem 3.2, $l(v)$ needs to be sufficiently regular. In particular, it is required that $f \in L^2(\Omega)$, which is not fulfilled for the mathematical point dipole. For the Dirac delta distribution, which is used in the definition of the mathematical point dipole (Def. 3.3), the following statement about its regularity can be made (Taylor (2011), p.319).

Remark 3.3: ***Sobolev space of Dirac delta distribution.*** *The* δ*-distribution centered at a point* $\mathbf{x}_0 \in \mathbb{R}^3$ *and its partial derivatives are in the following fractional Sobolev spaces*

$$\begin{aligned}\delta &\in H^{-3/2-\varepsilon}(\mathbb{R}^3),\\ D^{\boldsymbol{\alpha}}\delta &\in H^{-3/2-|\boldsymbol{\alpha}|-\varepsilon}(\mathbb{R}^3),\end{aligned}$$

for $\varepsilon > 0$.

Different approaches to address the singularity of the source term are discussed in Section 3.3.3, after the FEM discretization is introduced.

3.3.2. FEM discretization

In this section, the computation of the numerical solution of the weak formulation of the EEG forward problem will be presented. The notations and definitions are mainly based on Braess (2007) and Ciarlet (2002).

Instead of searching for a solution in the infinite-dimensional function space in which the EEG forward problem is posed, a finite-dimensional subspace is constructed in which the problem is discretized. In this thesis we focus on conforming discretizations, i.e., we consider a finite-dimensional subspace V_h of V. Besides this standard Continuous Galerkin (CG-)FEM, there are also non-conforming variants worth mentioning which have been used to solve the EEG/MEG forward problems, including the Discontinuous Galerkin (DG) and the Unfitted Discontinuous Galerkin (UDG) finite element methods. Due to a larger number of degrees of freedom, DG-FEM is computationally more expensive, but can result in higher accuracies in low-resolution scenarios in which a thin skull layer may produce physically inaccurate discretizations (Engwer et al., 2017; Piastra et al., 2018). UDG-FEM additionally relies on an implicit description of the tissue layers via level-sets and does not require a geometry-adapted volumetric mesh (Nüßing et al., 2016).

In order to discretize the weak formulation of the EEG problem (3.10), we assume that the domain Ω has a polygonal boundary and can be divided into regular polyhedra. Furthermore, we make the following assumptions on the spatial discretization (Braess, 2007).

Definition 3.11: ***Admissible tesselation.*** *A tesselation $\mathscr{T}_h = \{T_1, \dots, T_m\}$ of Ω is called admissible, if the following conditions are met:*

(i) $\bigcup_{i=1}^{m} T_i = \bar{\Omega}$,

(ii) if $T_i \cap T_j$ for $i \neq j$ consists of exactly one point, it is a shared node of both elements,

(iii) if $T_i \cap T_j$ for $i \neq j$ consists of more than one point, it is a shared edge (2D) or face (3D) of both elements.

This definition implies, for instance, that the tesselation does not contain any hanging nodes. Based on a suitable spatial decomposition, finite elements can be formally defined (Braess, 2007; Ciarlet, 2002; Ohlberger, 2012).

Definition 3.12: ***Finite Element.*** *A finite element is defined as the triple (T, Π, Σ) with the following properties:*

(i) $T \subset \bar{\Omega}$ is a polyhedron,

(ii) Π *is a k-dimensional space spanned by real-valued functions referred to as shape functions defined over the set T,*

(iii) Σ *consists of k linearly independent linear forms over* Π *which form a basis of the dual space* Π' *and are called degrees of freedom.*

A particular form of finite element is the Lagrange or nodal finite element.

Definition 3.13: ***Lagrange finite element.*** *Using the notations defined above, a finite element* (T, Π, Σ) *is called a Lagrange finite element, if all degrees of freedom are of the form* $p \mapsto p(a_i)$ *for* $p \in \Pi$*, where* $a_i \in T$ *are called Lagrange nodes.*

In practice, it suffices to define a finite element for a reference geometry and use coordinate transformations in order to generalize this concept to any element in the tesselation. For details on the implementation of FEM, see, e.g., Sander (2020) and Ohlberger (2012). The definition of finite elements only includes local function spaces defined on an element $T \in \mathscr{T}_h$. In order to construct a subspace of $H^1(\Omega)$, we consider the following space and construct a global nodal basis.

Definition 3.14: ***Finite element space.*** *For the space of polynomials* P^k *of degree* $k \in \mathbb{N}$*, the space of continuous and piecewise polynomial functions is defined as*

$$V_h^k := \left\{ v_h \in C^0(\bar{\Omega}) : v_h|_T \in P^k \quad \forall T \in \mathscr{T}_h(\Omega) \right\}.$$

According to this definition, the finite element space is conforming as $V_h^k(\Omega)$ is a subset of $H^1(\Omega)$ (Braess (2007), p.59). We will only consider first-order finite element spaces $(k = 1)$ and choose piecewise linear functions in $P^1 = \mathbb{P}^1$ for triangular/tetrahedral meshes and piecewise bi-/trilinear functions in $P^1 = \mathbb{Q}^1$ for quadrilateral/hexahedral meshes. If no ambiguities arise, the superscript k will be omitted and the notation $V_h := V_h^1$ is used. For investigations of higher order FEM to solve the EEG forward problem see, e.g., Grüne (2014). For a canonical basis of V_h we consider the global set of all element-based Lagrange nodes and identify mutual nodes of adjacent elements on the interfaces, for the choice of finite element space this corresponds to the vertices of the tesselation.

Remark 3.4: ***Nodal basis.*** *Each element* $u_h \in V_h$ *can be expressed as*

$$u_h(\mathbf{x}) = \sum_{i=1}^{n} u_i \varphi_i(\mathbf{x}). \tag{3.13}$$

Here, $u_i = u_h(\mathbf{x}_i)$ *denotes the function value at the Lagrange nodes that are associated with the vertices of the tesselation* $\mathscr{N} = \{\mathbf{x}_1, \ldots, \mathbf{x}_n\}$*, and the nodal basis functions* $\varphi_i \in V_h$ *for*

$1 \leq i \leq n$ are defined as

$$\varphi_i(\mathbf{x}_j) = \delta_{ij} \quad \forall \mathbf{x}_j \in \mathcal{N},$$

where δ denotes the Kronecker delta.

This leads to the following definition of the discretized formulation of the EEG forward problem.

Definition 3.15: ***Discrete EEG forward problem formulation.*** *The discrete FEM formulation of (3.10) is to find $u_h \in V_h$ such that*

$$a(u_h, v_h) = l(v_h) \quad \forall v_h \in V_h, \tag{3.14}$$

with $a(\cdot,\cdot)$ and $l(\cdot)$ defined in (3.11) and (3.12), respectively. This can be formulated algebraically as

$$\mathbf{A}\mathbf{u} = \mathbf{b}, \tag{3.15}$$

with the coefficient vector $\mathbf{u} = (u_1, \ldots, u_n)^T$, the stiffness matrix $\mathbf{A} \in \mathbb{R}^{n \times n}$ and the right-hand side or load vector $\mathbf{b} \in \mathbb{R}^n$ with entries defined as

$$A_{ij} = a(\varphi_i, \varphi_j) = \int_\Omega \boldsymbol{\sigma} \nabla \varphi_i \cdot \nabla \varphi_j \, d\mathbf{x}, \tag{3.16}$$

$$b_i = l(\varphi_i) = -\int_\Omega f \varphi_i \, d\mathbf{x}. \tag{3.17}$$

By construction, the basis functions $(\varphi_i)_{i=1}^n$ only have a small support, i.e., the adjacent elements sharing the node associated with it. This choice of basis therefore results in a sparse stiffness matrix. The number of entries in the right-hand side vector **b** depends on the source modeling approach and will be discussed in the following section.

3.3.3. Source modeling approaches

The irregularity of the mathematical point dipole poses problems to the applicability of the theoretical FEM framework, as indicated in Section 3.3.1. Different source modeling approaches have emerged that determine how the right-hand side term of the EEG forward problem $f = \nabla \cdot \mathbf{j}^p$, with the mathematical point dipole at location $\mathbf{x}_0$ and moment $\mathbf{q}$ given by $\mathbf{j}^p(\mathbf{x}) = \mathbf{q}\delta(\mathbf{x} - \mathbf{x}_0)$ (Def. 3.3), is treated.

In this section, three different approaches are described which will be applied in this thesis. The partial integration and the St. Venant source model are both *direct* approaches, as they approximate the dipolar source term by a monopole distribution in the vicinity of the dipole location, resulting in a sparse right-hand side vector. The subtraction source model follows an *indirect* approach by splitting the electric potential into two parts and thereby effectively dissolving the singularity.

Other source models not discussed in this thesis include, e.g., the Whitney or H(div) approach, which relies on the discretization of the primary current density $\mathbf{j}^p$ using a vector-valued function space such that $\nabla \cdot \mathbf{j}^p \in L^2$ (Pursiainen et al., 2011, 2016; Vorwerk, 2016).

Partial integration approach

The general idea of the partial integration approach is to shift the derivative of the delta distribution to the test functions (Bauer et al., 2015; Lew et al., 2009b). The right-hand side integral over $\langle \nabla \cdot \mathbf{j}^p, \varphi_i \rangle$ in the FEM discretization (3.17) is reformulated by applying integration by parts using the limit formulation of the mathematical point dipole (Bauer et al., 2015). The resulting right-hand side vector in (3.15) then has entries of the form

$$b_i^{\mathrm{PI}} = \begin{cases} \langle \mathbf{q}, \nabla \varphi_i(\mathbf{x}_0) \rangle & \text{if } \mathbf{x}_0 \in \operatorname{supp}(\varphi_i), \\ 0 & \text{else,} \end{cases}$$

where $\mathbf{x}_0$ denotes the dipole location and $\mathbf{q}$ its moment as in Def. 3.3. Note that this formulation implies that the derivatives of the test functions φ_i are defined at the dipole position. This is not necessarily the case for Lagrangian shape functions at the interfaces of elements. We therefore assume that the dipole location does not exactly lie on the edge of an element. Due to the small support of the nodal Lagrangian shape functions, the partial integration approach results in a right-hand side vector which only has as many non-zero entries as the element containing the dipole has vertices, i.e., 4 (tetrahedra) or 8 (hexahedra).

St. Venant approach

The St. Venant source model relies on the principle of St. Venant originally formulated in the context of elasticity theory (De Saint-Venant, 1853). Applied to bioelectromagnetism, it states that a point dipole can be replaced by a distribution of monopoles without significant impact on the potential observed from a distance, e.g., at surface electrodes. Following this principle, there are several different possibilities how to choose the source distribution of this *blurred dipole*, leading to different variants of the St. Venant approach. The underlying ideas and mathematical description of the classical St. Venant source model are, for instance, provided in Buchner et al. (1997), Wolters et al. (2007b), Medani et al. (2015), Vorwerk (2016) and Vorwerk et al. (2019b). In CG-FEM, the monopoles are typically located on the FE nodes, more precisely we use those nodes contained in the subset $\mathscr{M} \subset \mathscr{N}$ which share a common edge (2D) or face (3D) with the vertex closest to the source location. The entries of the right-hand side vector in (3.15) are then of the form

$$b_i^{\mathrm{VEN}} = \begin{cases} q_i & \text{if } \mathbf{x}_i \in \mathscr{M}, \\ 0 & \text{else.} \end{cases}$$

The monopole loads q_i are chosen as the minimum of a Tikhonov-Phillips regularization problem in which the difference between the moments of the blurred and the original dipole is minimized in combination with a regularization of the monopole distribution (Vorwerk et al., 2019b; Wolters et al., 2007b). Similar to the partial integration approach, this vector is still sparse but has more non-zero entries that correspond to the number of neighboring vertices around the node closest to the source location, e.g., 27 in a regular hexahedral mesh. For a detailed mathematical derivation we refer to Wolters et al. (2007b) and Vorwerk et al. (2019b).

Subtraction source model

The subtraction source model adopts a different approach and handles the singular source indirectly (Awada et al., 1997; Bertrand et al., 1991). In Wolters et al. (2007c), the *projected subtraction approach* for the EEG forward problem and its theoretical foundation was presented, which was further improved by the *full subtraction approach* introduced by Drechsler et al. (2009). Here, we will review the most important theoretical findings.

In general, the subtraction approach relies on the assumption that there exists a small area Ω^∞ around the source location $\mathbf{x}_0$ where the conductivity has a constant value $\boldsymbol{\sigma}^\infty$. In finite element meshes with element-wise constant conductivity values this assumption is automatically fulfilled by an area at least containing the element with the source. The gray matter compartment in which the source is located is usually modeled as isotropic (Shimony et al., 1999), but the derivation of the subtraction approach also holds for locally constant anisotropic conductivity around the source (Drechsler et al., 2009; Wolters et al., 2007c).

Definition 3.16: ***Infinity and correction potential.*** *Let the source location* $\mathbf{x}_0 \in \Omega^\infty \subset \Omega$ *with constant conductivity* $\boldsymbol{\sigma}(\mathbf{x}) = \boldsymbol{\sigma}^\infty$ *for* $\mathbf{x} \in \Omega^\infty$. *The potential and the conductivity can* *then be split into two contributions, a singularity contribution and a correction part*

$$u(\mathbf{x}) = u^{\infty}(\mathbf{x}) + u^{\mathrm{c}}(\mathbf{x}), \tag{3.18}$$

$$\boldsymbol{\sigma}(\mathbf{x}) = \boldsymbol{\sigma}^{\infty} + \boldsymbol{\sigma}^{\mathrm{c}}(\mathbf{x}). \tag{3.19}$$

The singularity contribution u^{∞} *is the solution of Poisson's equation in an unbounded domain with conductivity* $\boldsymbol{\sigma}^{\infty}$

$$\nabla \cdot \boldsymbol{\sigma}^{\infty} \nabla u^{\infty} = \nabla \cdot \mathbf{j}^{p} \quad \text{in } \mathbb{R}^3. \tag{3.20}$$

There exist analytical expressions for u^{∞} as well as ∇u^{∞} which contain a singularity at the dipole location $\mathbf{x}_0$, see, e.g., Drechsler et al. (2009). Inserting the above decompositions (3.18) and (3.19) into the EEG forward problem (3.4) and using (3.20) yields a Poisson equation for the correction potential.

Definition 3.17: ***Forward problem for the correction potential.*** *The forward problem for the correction potential in the subtraction approach is to find* $u^{\mathrm{c}} : \Omega \to \mathbb{R}$ *that solves*

$$-\nabla \cdot (\boldsymbol{\sigma} \nabla u^{\mathrm{c}}) = \nabla \cdot (\boldsymbol{\sigma}^{\mathrm{c}} \nabla u^{\infty}) \quad \text{in } \Omega,$$
$$\boldsymbol{\sigma} \nabla u^{\mathrm{c}} \cdot \mathbf{n} = -\boldsymbol{\sigma} \nabla u^{\infty} \cdot \mathbf{n} \quad \text{on } \partial\Omega.$$

As $\boldsymbol{\sigma}^{\mathrm{c}}(\mathbf{x}) = 0$ for all $\mathbf{x} \in \Omega^{\infty}$ by definition, the singularity of ∇u^{∞} on the right-hand side is effectively dissolved by this approach. Similarly to the derivation of the weak formulation described in Section 3.3.1 we integrate over the domain Ω, multiply with a test function $v \in H^1(\Omega)$ and apply integration by parts. This results in the following weak formulation of the forward problem for the correction potential.

Definition 3.18: ***Weak formulation for the correction potential.*** *The weak formulation of the subtraction approach can then be formulated as finding* $u^{\mathrm{c}} \in H^1_*(\Omega)$ *such that*

$$a(u^{\mathrm{c}}, v) = l^{\mathrm{c}}(v) \quad \forall v \in H^1(\Omega), \tag{3.21}$$

with the bilinear form $a(\cdot,\cdot)$ *as defined in (3.11) and the linear form* $l^{\mathrm{c}}(\cdot)$ *defined as*

$$l^{\mathrm{c}}(v) = -\int_{\Omega} \boldsymbol{\sigma}^{\mathrm{c}} \nabla u^{\infty} \cdot \nabla v \, d\mathbf{x} - \int_{\partial\Omega} \boldsymbol{\sigma}^{\infty} \nabla u^{\infty} \cdot v \mathbf{n} \, d\mathbf{x} \tag{3.22}$$

Remark 3.5: ***Existence and uniqueness.*** *In Wolters et al. (2007c), it is shown that* l^{c} *is well-defined and bounded, in particular* $l^{\mathrm{c}} \in (H^1_*(\Omega))'$, *and that the compatibility condition (see Remark 3.2) is fulfilled. In combination with Theorem 3.2 which shows the coercivity* *and continuity of the bilinear form, it follows from the Lax-Milgram theorem that there exists a unique* $u^{\mathrm{c}} \in H^1_*(\Omega)$ *solving the variational problem (3.21) for all* $v \in H^1(\Omega)$.

For a detailed convergence analysis providing error estimates for the finite element solution u_h^{c}, we refer to Wolters et al. (2007c). It is worth noting that for the subtraction approach, numerical errors increase for sources that come closer to the next conductivity jump (Wolters et al., 2007c).

Analogously to (3.15), the FEM discretization of the subtraction approach using nodal basis functions can be expressed in the algebraic form

$$\mathbf{A}\mathbf{u}^{\mathrm{c}} = \mathbf{b}^{\mathrm{c}}, \tag{3.23}$$

with right-hand side vector entries $b_i^{\mathrm{c}} = l^{\mathrm{c}}(\varphi_i)$ as defined in (3.22) and the vector $\mathbf{u}^{\mathrm{c}}$ with the evaluations of the correction potential at the degrees of freedom. Once the correction potential u^{c} is computed numerically, the complete potential u can be derived via (3.18) by adding the singularity contribution u^{∞}. The subtraction approach results in a dense right-hand side vector $\mathbf{b}^{\mathrm{c}}$ in the FEM discretization, as the support of the singularity potential u^{∞} covers the entire domain Ω. As a result, the subtraction approach is computationally more expensive than the direct approaches, as the assembly of the right-hand side as well as the multiplication of the transfer matrix with this vector (see Section 3.4) is more demanding. In Nüßing (2018), a more efficient alternative to the classical subtraction approach, the *localized subtraction approach*, was introduced for DG-FEM and adapted using the CG-FEM framework in Lange (2021). It restricts the support of the singularity potential to a patch around the source location which is significantly smaller than Ω, but large enough to achieve a comparable accuracy.

3.4. Efficient solution postprocessing and leadfield computation

In this section, we bridge the gap between the theoretical formulation of the forward problems and the actual application to experimental data. In a first step, the EEG/MEG forward solutions are evaluated at the electrodes (EEG) or coils (MEG) and the underlying assumptions on sensor modeling are explained. Second, we introduce the concept of transfer matrices which are an efficient way to compute the forward solutions at the sensors for many dipoles. Subsequently, we present further postprocessing steps of the discrete solutions and introduce the concept of leadfield matrices.

Evaluations at sensors

In EEG/MEG source analysis applications, forward solutions are required to be compared to the experimentally measured signals. In Section 3.3.2, a FEM framework was derived that approximates the EEG forward solution using the discrete representation u_h for the electric potential. In order to allow a direct comparison to realistic data, the simulated EEG signals need to be evaluated at each electrode. Regarding MEG, the integral for the magnetic field needs to be evaluated at the sensors, using the discretized EEG forward solution. For this step, the sensor characteristics need to be modeled adequately.

Several assumptions are made with respect to the sensor layout for EEG and MEG in this thesis. Regarding EEG, the point electrode model (PEM) is adopted. In this most frequently used approach, each electrode is represented by a single point, i.e., the centroid of the electrode, and the electrode signal is computed by evaluating the electric potential at this location, in our application on the scalp surface (Hallez et al., 2007; Vorwerk et al., 2014). Alternatively, the electrodes' shapes and impedances can be taken into account using the complete electrode model (CEM) (Pursiainen et al., 2012; Vermaas et al., 2020). For MEG, each separate coil measures the magnetic flux over the surface area of the coil and these coil signals are then combined into the channel signal, typically expressed as the flux density in units of tesla (Cheyne and Papanicolaou, 2017). From a practical point of view, this implies that the MEG forward solution is first computed for all coils and then mapped to the channels in order to be comparable with the measured data. One underlying assumption we use in this work is that the **B** field in measurement direction does not vary significantly over the coil surface. As a result, we assume that the coil signal can be approximated by a point evaluation of the magnetic field at the coil center in the corresponding measurement orientation perpendicular to the coil surface. Higher-order integration of the magnetic flux density, especially for sensors above the source, may further improve the accuracy of the MEG forward solutions but is neglected here due to the limited improvement and increased computational burden (Dachwitz, 2019).

In the following, the evaluations of the numerically computed components of the EEG/MEG forward solutions at the physical measurement units are described. For EEG, this refers to the evaluation of the electric potential at the electrodes, while for MEG this entails the evaluation of the secondary magnetic flux density measured by a single coil. The MEG channel (e.g., gradiometer) signals are then composed of linear combinations of coil signals, which is a further postprocessing step described later in this section. Here, a general expression for the sensor evaluations is presented, which is then discretized in the following.

Definition 3.19: ***Sensor evaluations.*** *Let* $N \in \{N_{\text{elec}}, N_{\text{coil}}\}$ *denote the number of electrodes or magnetometer coils, respectively. Each sensor* i*,* $1 \leq i \leq N$*, is defined by its center* $\mathbf{c}_i \in \mathbb{R}^3$ *and, in case of MEG, its measurement orientation* $\mathbf{o}_i \in \mathbb{R}^3$*. Then, the signal evaluation at the respective sensor can be expressed as a linear functional* $s_{\cdot,i} \in H^{-1}(\Omega)$*, with*

$$\begin{aligned} s_{\text{EEG},i}(u) &:= u(\mathbf{c}_i) && \text{for } 1 \leq i \leq N_{\text{elec}}, \\ s_{\text{MEG},i}(u) &:= \mathbf{o}_i \cdot \mathbf{B}^s(u, \mathbf{c}_i) && \text{for } 1 \leq i \leq N_{\text{coil}} \end{aligned}$$

for each modality, where u *and* $\mathbf{B}^s$ *are defined in Def. 3.10 and Def. 3.4, respectively.*

These functionals for the signal evaluations at the electrodes (EEG) or coils (MEG) can be approximated using the FEM discretizations derived in Section 3.3.2.

Definition 3.20: ***Discretized sensor evaluations.*** *Using the notations of Def. 3.19, the discretized formulation of the sensor evaluations is given by*

$$\begin{aligned} s_{\text{EEG},i}(u_h) &= u_h(\mathbf{c}_i) && \text{for } 1 \leq i \leq N_{\text{elec}}, \\ s_{\text{MEG},i}(u_h) &= \mathbf{o}_i \cdot \mathbf{B}^s(u_h, \mathbf{c}_i) && \text{for } 1 \leq i \leq N_{\text{coil}}, \end{aligned}$$

with u_h *defined in (3.13). Algebraically, this evaluation at the sensors is equivalent to*

$$\mathbf{s}_i \cdot \mathbf{u}, \qquad \text{for } 1 \leq i \leq N,$$

where $\mathbf{u} \in \mathbb{R}^n$ *is the discrete FEM solution vector defined in (3.15) and* $\mathbf{s}_i \in \mathbb{R}^n$ *consists of the sensor functional evaluations for the nodal basis functions* $(\varphi_j)_{j=1}^n$ *with entries of the form*

$$(\mathbf{s}_i)_j = s_{\cdot,i}(\varphi_j) \qquad \text{for } 1 \leq i \leq N,\ 1 \leq j \leq n.$$

Taking all sensors into account, this results in a linear system of the form

$$\tilde{\mathbf{u}} = \mathbf{S}\mathbf{u},$$

for the scalar sensor evaluations $\tilde{\mathbf{u}} \in \mathbb{R}^N$*, with* $\mathbf{S} = (\mathbf{s}_1, \ldots, \mathbf{s}_N)^T \in \mathbb{R}^{N \times n}$*.*

Transfer matrices

In principle, the EEG forward solution can be computed by solving the linear system (3.15) resulting from the FEM discretization for the solution vector $\mathbf{u}$. As described in the previous section, this solution vector can be subsequently used to evaluate the signal at the electrodes (EEG) or coils (MEG) for further postprocessing. Using this *direct approach*, a linear system needs to be solved for every source. In many source analysis applications, however, this can be computationally expensive due to a large number of possible sources, typically in the range of several thousands (Michel and Brunet, 2019). The number of sensors, on the other hand, is typically much smaller than the number of potential sources, e.g., in the range of a few hundred (Gross, 2019; Hari and Puce, 2017). In cases where the considered sources largely outnumber the electrodes (EEG) or coils (MEG), the *transfer matrix approach* has been proposed as a more efficient method to compute EEG and MEG forward solutions (Wolters et al., 2004).

Definition 3.21: ***Transfer matrix.*** *Let* $\mathbf{S} \in \mathbb{R}^{N \times n}$ *be the EEG or MEG sensor evaluation matrix as defined in Def. 3.20 with* $N \in \{N_{\text{elec}}, N_{\text{coil}}\}$, *and let* $\mathbf{A} \in \mathbb{R}^{n \times n}$ *denote the stiffness matrix from the FEM discretization of the EEG forward problem defined in (3.16). Then, the transfer matrix* $\mathbf{T} \in \mathbb{R}^{N \times n}$ *is defined as*

$$\mathbf{T} = \mathbf{S}\mathbf{A}^{-1}$$

for each modality.

By definition, the EEG and MEG transfer matrices are independent of the source modeling approach and, once computed, can be multiplied to different right-hand sides. Thereby, transfer matrices allow for a more efficient the computation of the forward solutions.

Remark 3.6. *Using the transfer matrix* $\mathbf{T}$ *for EEG or MEG, the potential at the electrodes (EEG) or the secondary magnetic field component at the coils (MEG) from a source with a right-hand side vector* $\mathbf{b}$ *can be computed by a matrix-vector multiplication using (3.15) as*

$$\mathbf{T}\mathbf{b} = \mathbf{S}\mathbf{A}^{-1}\mathbf{b} = \mathbf{S}\mathbf{u} = \tilde{\mathbf{u}}.$$

Using the transfer matrix approach thereby avoids solving a linear system for every source, its computation instead only requires to solve a linear system for each sensor.

Remark 3.7. *The transfer matrix can be computed by solving* $\mathbf{A}\mathbf{T}^T = \mathbf{S}^T$ *for each column of* $\mathbf{S}^T$, *using the symmetry of the stiffness matrix* $\mathbf{A}$. *Therefore, a linear system needs to be solved for each sensor, i.e.,* N *times.*

Note that for the subtraction source model, the transfer matrix only computes the magnetic field associated with the correction potential (Piastra, 2019).

Further solution postprocessing

In order to be comparable to the experimentally measured data, further postprocessing is usually necessary, depending on the modality and the transformations applied to the realistic data. In this section, we focus on three postprocessing steps used in this thesis that map the previously computed signal at the coils or electrodes $\tilde{\mathbf{u}}$ to a postprocessed vector $\mathbf{p}(\tilde{\mathbf{u}}) \in \mathbb{R}^N$ with $N \in \{N_{\text{elec}}, N_{\text{chan}}\}$, that has the same dimensions as the measured data. For MEG, this entails the mapping from coil-based evaluations to channel (e.g., gradiometer) signals and the addition of the analytically computed primary magnetic field component.

First, a typical postprocessing step for simulated EEG data is to re-reference the signal in accordance with the measured data. In this thesis, we will use average-referenced measured and simulated EEG signals.

Definition 3.22: ***Average-referencing of EEG signals.*** *The EEG signals at the electrodes can be re-referenced with respect to the average signal* $u_{\text{ref}} = \frac{1}{N_{\text{elec}}} \sum_i \tilde{u}_i$ *using the transformation* $\mathbf{p} : \mathbb{R}^{N_{\text{elec}}} \to \mathbb{R}^{N_{\text{elec}}}$, *whose components are defined as*

$$p_i(\tilde{\mathbf{u}}) = \tilde{u}_i - u_{\text{ref}}, \quad \text{for } 1 \leq i \leq N_{\text{elec}}. \tag{3.24}$$

In general, other references are also possible, e.g., specific electrode signals $u_{\text{ref}} = \tilde{u}_i$ for $1 \leq i \leq N_{\text{elec}}$, or combinations of several signals (Hari and Puce, 2017).

The second postprocessing step described here applies to numerically computed MEG forward solutions. Previously, the computation of the numerical component of the magnetic field, i.e., the secondary **B** field, evaluated in the measurement direction of a single coil, was described. In order to compute the signals at the channel level, in our case gradiometers, the coil signals are combined using the weights defined by the respective MEG system. For instance, an axial gradiometer consists of two oppositely wound coils which measure the **B** field in opposite directions at a small distance apart. The channel output is then composed of the sum of both coil signals, possibly in addition to reference channel contributions.

Definition 3.23: ***MEG channel evaluations.*** *Let the matrix* $\mathbf{G} \in \mathbb{R}^{N_{\text{chan}} \times N_{\text{coil}}}$ *denote the mapping from* N_{coil} *coil signals to the* N_{chan} *channel signals as defined by the respective MEG system. Then, the MEG signal at the channels can be computed using the transformation* $\mathbf{p} : \mathbb{R}^{N_{\text{coil}}} \to \mathbb{R}^{N_{\text{chan}}}$ *which is defined as*

$$\mathbf{p}(\tilde{\mathbf{u}}) = \mathbf{G}(\mathbf{b}^p + \tilde{\mathbf{u}}), \tag{3.25}$$

where $\tilde{\mathbf{u}} \in \mathbb{R}^{N_{\text{coil}}}$ *denotes the secondary magnetic field components measured by single coils and* $\mathbf{b}^p \in \mathbb{R}^{N_{\text{coil}}}$ *contains the analytical primary magnetic field components which can* *be computed using the analytical formula defined in (3.9). Its elements are of the form* $b_i^p = \mathbf{o}_i \cdot \mathbf{B}^p(\mathbf{c}_i)$*, where* $\mathbf{c}_i$ *and* $\mathbf{o}_i$ *refer to the coil centers and measurement orientations, respectively, for sensor* $1 \leq i \leq N_{\text{coil}}$.

Note that the conventions regarding the assembly and processing of the gradiometer transformation matrix $\mathbf{G}$ may vary in different software toolboxes, even for the same raw data. This may include, for instance, the ordering of reference coils or the convention of reporting the sign of the coil orientation in combination with the sign of the respective entries in $\mathbf{G}$.

The third postprocessing transformation is a frequently used approach to combine EEG and MEG data. In general, combining EEG and MEG can prevail over single modality evaluations, see, for instance, Chapter 7 regarding epilepsy research. However, the combined recording and evaluation of both data sets poses several challenges. In addition to practical obstacles related to the availability of both modalities, such as high acquisition and maintenance costs of classical MEG systems, several other issues need to be addressed for their combined analysis. One important aspect is that in order to be comparable with each other, the measurements need to be transformed to a common space. One frequently used approach to transform EEG and MEG measurements into a unitless measure, is by performing an SNR transformation. The general idea is to normalize each sensor signal based on the noise strength estimated from an ideally signal-free time window (e.g., the prestimulus interval). Following the SNR definition of Fuchs et al. (1998), this transformation is defined as follows.

Definition 3.24: ***Signal-to-noise ratio (SNR) transformation.*** *Let* $N \in \{N_{\text{elec}}, N_{\text{chan}}\}$ *denote the number of EEG or MEG channels, and let* $m_{ij} = m_i(t_j) \in \mathbb{R}$ *refer to the measured signal at time point* t_j*,* $1 \leq j \leq k$*, within a signal-free time interval at sensor i,* $1 \leq i \leq N$*. Then, the noise amplitude of this sensor is defined as*

$$n_i = \sqrt{\frac{1}{k-1} \sum_{j=1}^{k} (m_{ij} - \bar{m}_i)^2}, \quad \textit{with } \bar{m}_i = \sum_{j=1}^{k} \frac{m_{ij}}{k}. \tag{3.26}$$

Any sensor signal vector $\tilde{\mathbf{u}} \in \mathbb{R}^N$ *can then be transformed to its SNR by the transformation* $\mathbf{p} : \mathbb{R}^N \rightarrow \mathbb{R}^N$*, whose components are defined as*

$$p_i(\tilde{\mathbf{u}}) = \frac{\tilde{u}_i}{n_i}, \quad \text{for } 1 \leq i \leq N. \tag{3.27}$$

Applying this transformation for the measured and simulated EEG and MEG signals at the sensors yields unitless measures for both modalities which can be concatenated for a combined analysis. Naturally, SNR transformations can also be applied to single modality data to reduce noise by attaching more importance to those channels which are comparatively less influenced by noise as estimated from the prestimulus interval. When using this transformation for a combined analysis, an important issue is the generation of a suitable head volume conductor model, as especially the EEG is influenced by head geometries and conductivities. This is also described in more detail in Chapter 1 and addressed in this thesis.

Leadfield matrices

For simplicity, we have assumed a single dipolar source so far, which leads to a specific right-hand side vector. Usually, source reconstruction algorithms rely on precomputed forward solutions for a given set of possible sources. Each dipolar source is defined by its location and moment vector, typically with unit strength. As source orientations, either all Cartesian directions are considered or constraints are imposed, e.g., by assuming outward-pointing normals to the cortical surface (Brette and Destexhe, 2012; Hämäläinen et al., 1993). As a frequently used concept in the field of EEG/MEG source analysis, we therefore introduce the notation of leadfield matrices which are concatenations of solution vectors for a given set of sources.

Definition 3.25: ***Leadfield matrix.*** *Let* $n_x \in \mathbb{N}$ *be the number of possible dipolar sources, each source* $\mathbf{x}_j = (\mathbf{x}_{0j}, \mathbf{q}_j) \in \mathbb{R}^6$ *for* $1 \leq j \leq n_x$ *defined by its position* $\mathbf{x}_{0j}$ *and moment* $\mathbf{q}_j$*, respectively. Let further* $N \in \{N_{\text{elec}}, N_{\text{chan}}\}$ *denote the number of EEG or MEG channels and* $\mathbf{p}(\tilde{\mathbf{u}})$ *the postprocessed forward solution vector at the channels. Then, the leadfield matrix* $\mathbf{L} \in \mathbb{R}^{N \times n_x}$ *consists of the forward solutions computed at all channels and for all considered sources, i.e., each element* L_{ij} *indicates the signal* $p_i(\tilde{\mathbf{u}})$ *at channel* i *for a given dipolar source* $\mathbf{x}_j$*.*

The solution vectors themselves can either be computed using the direct or the transfer matrix approach, although for a large number of sources the latter is more efficient, as discussed previously.

4. A novel pipeline for calibrated head volume conductor models

In this chapter, a novel procedure for calibrating head models with respect to skull conductivity is presented. The mathematical description of the algorithm as well as investigations in spherical head models are published in Schrader et al. (2020).

This chapter is organized in the following way. First, we introduce the underlying inverse problem and motivate our calibration pipeline by highlighting its novelty in comparison to existing calibration approaches in Section 4.1. In Section 4.2, the mathematical description of the algorithm is presented and each step is described in detail. Finally, two variations of this algorithm are introduced in Section 4.3 which will later be applied and discussed.

4.1. Motivation and problem description

In the previous chapter, we introduced the mathematical background to the EEG and MEG forward problems, which can be stated as follows: Given a source distribution and a head volume conductor model, i.e., a geometrical representation of the head tissues and their conductivities, find the potential or the magnetic field measured by EEG or MEG, respectively. Forward solutions for different sources are required in order to solve the inverse source reconstruction problem, which is typically the main interest of EEG and MEG analysis. This inverse problem can be stated as: Given a head volume conductor model and measured EEG and MEG data, find the underlying source characteristics. The source reconstruction problem is ill-posed, as different source distributions can lead to the same measured data and high levels of noise can distort the measurements and lead to unstable solutions (Hari and Puce, 2017). Both of the above-mentioned problems assume that the conductivity profile of the head volume conductor is known. Typically, literature conductivity values are assigned to the head tissues in volume conductor models even though reported values may vary largely, see Section 2.2 for a detailed overview. Another important inverse problem is therefore related to the conductivity estimation: Given a geometric model of the head and source characteristics underlying EEG/MEG measurements, reconstruct the tissue conductivities. Individually estimating conductivities increases the time and effort of constructing a feasible head volume conductor model, but has been suggested to improve the accuracy in EEG and combined EEG/MEG source analysis scenarios, for instance, in the context of presurgical epilepsy diagnosis (Aydin et al., 2017, 2014). Special attention has been paid to individually estimate skull conductivity, which has been emphasized as the most influential parameter (Saturnino et al., 2019; Schmidt et al., 2015; Vorwerk et al., 2019a). Papageorgakis (2017) proved that there exists a unique solution of the EEG conductivity estimation problem of finding the skull conductivity σ_{skull}, given a three-compartment spherical head model with predefined $\sigma_{\text{scalp}} = \sigma_{\text{brain}}$, and a known source as well as boundary EEG data. A closely related approach to solve the conductivity estimation problem is based on the modality of EIT, a technique where a small current is passed through the head using pairs of electrodes on the scalp (Abascal et al., 2008; Fernández-Corazza et al., 2018; Hallez et al., 2007; Oostendorp et al., 2000). Based on the measured potential and the known current source and sink, the (skull) conductivity of the volume conductor can be estimated.

Under realistic conditions, both the conductivity profile and the source characteristics are usually unknown. Therefore, we will use a combined procedure to reconstruct the source characteristics and the skull conductivity as the most influential conductivity parameter. The calibration procedure presented here is based on both EEG and MEG modalities and exploits their respective strengths. There have been efforts to estimate skull conductivity in combination with the underlying source from single-modality EEG (Akalin Acar et al., 2016; Lew et al., 2009a). One of the challenges of this approach is the strong observed correlation between skull conductivity and source depth in source analysis (Vorwerk et al., 2019a), which could counterbalance each other in a combined EEG-based reconstruction of the skull conductivity and the dipole characteristics. Thus, it has been suggested that the additional use of MEG stabilizes the skull conductivity estimation due to its complementarity to EEG and its lower sensitivity to skull and skin conductivity (Antonakakis et al., 2020; Baysal and Haueisen, 2004; Fuchs et al., 1998; Huang et al., 2007; Wolters et al., 2010).

With regard to the source reconstruction, *a priori* knowledge of the well-studied early components of somatosensory evoked potential (SEP) and field (SEF) data is exploited. More precisely, the underlying source of the P20/N20 peak is used in the reconstruction, which refers to the component of averaged EEG/MEG data approximately 20 ms after the somatosensory stimulus is applied. There is strong evidence suggesting that the generator of the P20/N20 response is a mainly focal, single dipolar source with predominantly tangential orientation which is located in the contralateral Brodmann area 3b in the postcentral gyrus within the primary somatosensory cortex (Allison et al., 1991; Antonakakis et al., 2019; Götz et al., 2014; Nakamura et al., 1998). Due to these characteristics and *a* *priori* knowledge, the P20/N20 topographies of somatosensory data have often been used for calibration purposes (Antonakakis et al., 2020, 2019; Aydin et al., 2014; Fuchs et al., 1998; Huang et al., 2007; Vallaghé and Clerc, 2009). Based on these preliminaries, the combined reconstruction problem for the dipole characteristics and the skull conductivity can be defined as follows.

Definition 4.1: ***Dipole and skull conductivity reconstruction problem.*** *Let the SEP and SEF data of the P20/N20 component (*$\mathbf{m}_{\mathrm{EEG}}$ *and* $\mathbf{m}_{\mathrm{MEG}}$*), a geometrical head model* Ω *including a given skull (compacta) compartment* $\Omega_{\mathrm{skull}} \subset \Omega$ *with tissue conductivities* $\boldsymbol{\sigma}(\mathbf{x})$ *for* $\mathbf{x} \in \Omega \backslash \Omega_{\mathrm{skull}}$ *be given. Then, the dipole and best skull conductivity approximation problem is to find the homogenized isotropic bulk skull conductivity* $\sigma_{\mathrm{skull}} \in \mathbb{R}^+$ *as well as the underlying dipole characteristics, i.e., the dipole location* $\mathbf{x}_0 \in \mathbb{R}^3$*, its unit length orientation* $\mathbf{o} \in \mathbb{R}^3$ *and magnitude* $m \in \mathbb{R}$*.*

By exploiting the complementarities of EEG and MEG, the calibration procedure presented here builds upon already existing approaches such as Aydin et al. (2014) and Antonakakis et al. (2020, 2019). In these methods, a predefined discrete set of skull conductivity values is compared, thereby limiting the accuracy of the calibration result as the optimum may lie in between sampled values. In Aydin et al. (2014), for instance, 11 discrete values irregularly distributed within the interval [0.0016, 0.033] S/m were used based on literature values. As an extension of this method, Antonakakis et al. (2020, 2019) added the value of 0.0008 S/m (Altakroury, 2017) to extend the possible range, and two further values manually chosen in the vicinity of the suspected optimum.

Furthermore, the above-mentioned studies use a time-consuming manual calibration procedure involving different toolboxes. In particular, SimBio[1] is used to compute EEG and MEG leadfields for the entire source grid. These are imported to the commercial Curry[2] toolbox which is used for the inverse methods in combination with tailored MATLAB (The MathWorks Inc., Natick, Massachusetts) scripts. This amount of manual work poses challenges to the usability in clinical applications and large group studies.

In this work, a complete mathematical description of the calibration algorithm and different variants is provided in order to increase its usability. Additionally, we use an optimization method which iteratively updates the skull conductivity parameter in order to find the best fitting value. While in Aydin et al. (2014) and Antonakakis et al. (2020, 2019), their calibration algorithm was applied to one, five and 20 realistic cases without an assessment of its reliability in a controlled scenario, we will use a multi-layer sphere model with (quasi-)

---

[1] https://www.mrt.uni-jena.de/simbio/index.php/Main_Page

[2] https://compumedicsneuroscan.com/products/by-name/curry/

analytical EEG/MEG solutions, in order to systematically investigate the accuracy of our algorithm without the impact of approximation errors to the realistic scenario as well as numerical errors, see Chapter 5. We thereby propose an automated and accurate calibration procedure based on MATLAB which can be integrated into existing EEG/MEG analysis pipelines. Once the skull conductivity is individually fitted, the calibrated head model can be further used to evaluate EEG or combined EEG/MEG data sets, for instance, in presurgical epilepsy diagnosis (Aydin et al., 2017) or to individually optimize sensor configurations in brain stimulation (Huang et al., 2017; Sadleir et al., 2012; Saturnino et al., 2019; Schmidt et al., 2015).

4.2. A novel calibration algorithm

The procedure for calibrating head models with respect to skull conductivity presented is based on the reconstruction of the underlying source of the SEP/SEF P20/N20 component. The calibration algorithm exploits the different sensitivity profiles of both EEG and MEG modalities and uses the strengths of each modality. In spherical head models, where (quasi-)analytical solutions exist, the MEG signal is independent of the conductivity profile of the volume conductor (Sarvas, 1987). In the realistic case, the MEG forward solution was shown to be insensitive to conductivity changes in the skull and scalp compartments which are not in the immediate vicinity of the source (Haueisen et al., 1997; Lew et al., 2013). The EEG forward solution, on the other hand, largely depends on volume conduction effects and has been shown to be most sensitive to skull conductivity due to its high resistivity in comparison to the other head tissues (Vorwerk et al., 2019a). In addition, skull conductivity and reconstructed source depth are strongly correlated when performing source analysis using EEG alone (Akalin Acar and Makeig, 2013; Antonakakis et al., 2019; Chen et al., 2010; Vorwerk et al., 2019a). Regarding source orientation, the analytical MEG forward solution is zero for radial sources in sphere model scenarios (Sarvas, 1987), while the numerical MEG forward solution in realistic head models is insensitive to quasi-radial orientation components (Antonakakis et al., 2019; Fuchs et al., 1998; Piastra et al., 2021).

The steps for calibrating head models with respect to skull conductivity are summarized in Algorithm 1. In the following, we explain the required input, the first step consisting of an MEG single dipole deviation scan, the second step that reconstructs the dipole and minimizes the residual variance to the measured data, as well as the output of the algorithm in detail.

First, the input for the algorithm is described. As mentioned above, the algorithm requires

```
Algorithm 1: Calibration procedure

Input: $\mathbf{m}_{\mathrm{EEG}}, \mathbf{m}_{\mathrm{MEG}}, l_{\mathrm{EEG}}, l_{\mathrm{MEG}}, \sigma_{\min}, \sigma_{\max}, \varepsilon$
    1. Perform an MEG single dipole deviation scan to find the optimal dipole position:
        a) $\mathbf{x}_{\mathrm{MEG}} = \underset{\mathbf{x} \in S}{\operatorname{argmin}} \| l_{\mathrm{MEG}}(\mathbf{x})\ [l_{\mathrm{MEG}}(\mathbf{x})]^{+}\ \mathbf{m}_{\mathrm{MEG}} - \mathbf{m}_{\mathrm{MEG}} \|_2^2$
        b) $\mathbf{L}_{\mathrm{MEG},x_{\mathrm{MEG}}} = l_{\mathrm{MEG}}(\mathbf{x}_{\mathrm{MEG}})$
    2. Find $\sigma_{\mathrm{skull,est}} = \operatorname{argmin}_{\sigma_{\mathrm{skull}} \in (\sigma_{\min}, \sigma_{\max})} r(\sigma_{\mathrm{skull}})$ using Brent's method, which
       proposes $\sigma_{\mathrm{skull}}^{i}$ iteratively ($i = 0, 1, \ldots$), with the residual variance defined as
           $r(\sigma_{\mathrm{skull}}^{i}) := \frac{\| \mathbf{L}_{\mathrm{EEG},x_{\mathrm{MEG}},\sigma_{\mathrm{skull}}^{i}} \mathbf{q}_{\mathrm{est}} - \mathbf{m}_{\mathrm{EEG}} \|_2^2}{\| \mathbf{m}_{\mathrm{EEG}} \|_2^2},$
       where $\mathbf{L}_{\mathrm{EEG},x_{\mathrm{MEG}},\sigma_{\mathrm{skull}}^{i}}$ and the dipole moment $\mathbf{q}_{\mathrm{est}}$ are computed as follows:
        a) $\mathbf{L}_{\mathrm{EEG},x_{\mathrm{MEG}},\sigma_{\mathrm{skull}}^{i}} = l_{\mathrm{EEG}}(\mathbf{x}_{\mathrm{MEG}}, \sigma_{\mathrm{skull}}^{i})$
        b) $\mathbf{q}_{\mathrm{EEG},x_{\mathrm{MEG}}} = [\mathbf{L}_{\mathrm{EEG},x_{\mathrm{MEG}},\sigma_{\mathrm{skull}}^{i}}]^{+}\ \mathbf{m}_{\mathrm{EEG}}$
        c) $\mathbf{o}_{\mathrm{est}} = \frac{\mathbf{q}_{\mathrm{EEG},x_{\mathrm{MEG}}}}{\| \mathbf{q}_{\mathrm{EEG},x_{\mathrm{MEG}}} \|_2}$
        d) $m_{\mathrm{est}} = [\mathbf{L}_{\mathrm{MEG},x_{\mathrm{MEG}}}\ \mathbf{o}_{\mathrm{est}}]^{+} \cdot \mathbf{m}_{\mathrm{MEG}}$
        e) $\mathbf{q}_{\mathrm{est}} = \mathbf{o}_{\mathrm{est}} m_{\mathrm{est}}$
       Terminate iteration, when $|\sigma_{\mathrm{skull}}^{i+1} - \sigma_{\mathrm{skull}}^{i}| < \varepsilon$.
Output: $\mathbf{x}_{\mathrm{MEG}}, \mathbf{o}_{\mathrm{est}}, m_{\mathrm{est}}, r(\sigma_{\mathrm{skull,est}}), \sigma_{\mathrm{skull,est}}$
```

reference (measured) EEG and MEG data $\mathbf{m}_{\mathrm{EEG}} \in \mathbb{R}^{N_{\mathrm{EEG}}}$, $\mathbf{m}_{\mathrm{MEG}} \in \mathbb{R}^{N_{\mathrm{MEG}}}$, where N_{EEG} denotes the number of electrodes and N_{MEG} refers to the number of MEG channels, e.g., gradiometers. In practice, these are the measured topographies of the P20/N20 component at the sensors. Additionally, functions $l_{\mathrm{EEG}} : \mathbb{R}^3 \times \mathbb{R}^+ \to \mathbb{R}^{N_{\mathrm{EEG}} \times 3}, (\mathbf{x}, \sigma_{\mathrm{skull}}) \mapsto \mathbf{L}_{\mathrm{EEG},x,\sigma_{\mathrm{skull}}}$ and $l_{\mathrm{MEG}} : \mathbb{R}^3 \to \mathbb{R}^{N_{\mathrm{MEG}} \times 3}, \mathbf{x} \mapsto \mathbf{L}_{\mathrm{MEG},x}$ are required as input. They compute the EEG and MEG leadfields $\mathbf{L}_{\mathrm{EEG},x,\sigma_{\mathrm{skull}}}$ and $\mathbf{L}_{\mathrm{MEG},x}$, respectively, i.e., the simulated sensor signals for a dipolar source at location $\mathbf{x}$ with unit-strength moments oriented in the three Cartesian directions. The forward calculations are influenced by the head volume conductor model and sensor characteristics. The MEG leadfield has a reduced rank, i.e., $\operatorname{rank}(\mathbf{L}_{\mathrm{MEG},x}) = 2$ in the spherical case, as the MEG is not affected by radial sources in this analytical case (Sarvas, 1987; Wolters et al., 1999). Note that we omit σ_{skull} as a variable in the computation of the MEG leadfield. This can be justified by the fact that in the spherical case, the MEG forward solution is independent of the conductivity profile. For the realistic volume conductor model, as the MEG is insensitive to skull conductivity changes (Haueisen et al., 1997; Lew et al., 2013), we suggest to use a standard skull conductivity for the leadfield computation in order to minimize the computational cost. In Aydin et al. (2014), MEG single dipole deviation scans (SDDSs) were performed with varying skull conductivities for one patient. According to these results, no localization difference (using a 2 mm source grid resolution) was found in the investigated interval of [0.0016, 0.033] S/m for a six-compartment realistic head model. In a three-compartment model, no localization differences were observed for skull conductivities in the range [0.0016, 0.007] S/m that contained the estimated optimal value of 0.0024 S/m. In case a spherical head model is used, (quasi-)analytical forward solutions exist, while they need to be computed numerically for realistically shaped head models. Additionally, a range $(\sigma_{\min}, \sigma_{\max}) \subset \mathbb{R}^+$ for the skull conductivity parameter estimation and a convergence tolerance $\varepsilon \in \mathbb{R}^+$ are needed.

In the following, Step 1 in Algorithm 1 is described in detail, which determines the source location. MEG, which is insensitive to skull conductivity, has the capability to localize the underlying P20/N20 source in the primary somatosensory cortex with high accuracy, even in the case that skull conductivity is not accurately chosen (Aydin et al., 2014; Fuchs et al., 1998; Nakamura et al., 1998). Therefore, similar to Antonakakis et al. (2020), Wolters et al. (2010) and Aydin et al. (2014), an SDDS using the SEF data is performed to find the optimal source location $\mathbf{x}_{\text{MEG}}$ within the source space, a set of possible sources within the gray matter or homogenized brain compartment. General mathematical background and definitions related to equivalent current dipole scans can be found in A.1. The best fitting position $\mathbf{x}_{\text{MEG}}$ is computed in Step 1a) as the source location within the source grid S, that in combination with the best fitting moment vector $\hat{\mathbf{q}}_{\text{MEG}}(\mathbf{x})$ produces a leadfield with the lowest error when compared to the measured reference data $\mathbf{m}_{\text{MEG}}$, i.e.,

$$\mathbf{x}_{\text{MEG}} = \operatorname*{argmin}_{\mathbf{x} \in S} \| l_{\text{MEG}}(\mathbf{x}) \hat{\mathbf{q}}_{\text{MEG}}(\mathbf{x}) - \mathbf{m}_{\text{MEG}} \|_2^2. \tag{4.1}$$

Here, the best fitting moment $\hat{\mathbf{q}}_{\text{MEG}}(\mathbf{x})$ (with respect to $\mathbf{m}_{\text{MEG}}$) for each source location $\mathbf{x}$ is the moment vector for which $\| l_{\text{MEG}}(\mathbf{x}) \mathbf{q}_{\text{MEG}}(\mathbf{x}) - \mathbf{m}_{\text{MEG}} \|_2$ is minimal. The solution with the minimal Euclidean norm to this linear least-squares problem can be computed as follows (James, 1978; Planitz, 1979)

$$\hat{\mathbf{q}}_{\text{MEG}}(\mathbf{x}) = [l_{\text{MEG}}(\mathbf{x})]^+ \, \mathbf{m}_{\text{MEG}} \quad \text{for } \mathbf{x} \in S. \tag{4.2}$$

Here, the notation $[\cdot]^+$ denotes the Moore-Penrose pseudo-inverse of a matrix (Golub and Kahan, 1965), see also A.1 for more details. Any real matrix, in our case $\mathbf{L} \in \mathbb{R}^{N\times 3}$ with $N \in \{N_{\text{EEG}}, N_{\text{MEG}}\}$, can be factorized by its singular value decomposition (SVD) as $\mathbf{L} = \mathbf{U\Sigma V}^T$ with the orthogonal matrices $\mathbf{U} \in \mathbb{R}^{N\times N}$ and $\mathbf{V} \in \mathbb{R}^{3\times 3}$, as well as the rectangular diagonal matrix $\mathbf{\Sigma} \in \mathbb{R}^{N\times 3}$ containing its non-negative *singular values*. The pseudo-inverse $[\mathbf{L}]^+ \in \mathbb{R}^{3\times N}$ of $\mathbf{L}$ can then be computed as $[\mathbf{L}]^+ = \mathbf{V\Sigma}^+\mathbf{U}^T$, where $\mathbf{\Sigma}^+$ is obtained from $\mathbf{\Sigma}$ by replacing its non-zero diagonal entries by their reciprocals and transposing the matrix. Note that due to the reduced rank of the MEG leadfield for a spherical head volume conductor there are only two non-zero singular values in this case. Insertion of the expression for $\hat{\mathbf{q}}_{\text{MEG}}(\mathbf{x})$ in (4.2) into (4.1) then results in the formula presented in Step 1 of Algorithm 1. For a realistic head model, the computation of the MEG forward solution $l_{\text{MEG}}(\mathbf{x})$ for each node in the source space is more efficient using the transfer matrix approach (Wolters et al., 2004), see also Section 3.4. Nevertheless, this first step is computationally expensive, as there are typically several hundred MEG sensors Gross (2019). In Step 1b), the MEG leadfield of the source location $\mathbf{L}_{\text{MEG},x_{\text{MEG}}} \in \mathbb{R}^{N_{\text{MEG}}\times 3}$ is stored and will be used in the second step to fit the magnitude of the source.

In Step 2 of the algorithm, the aim is to fix the moment of the dipole with location $\mathbf{x}_{\text{MEG}}$ determined in Step 1 in a way that exploits the strengths of both EEG and MEG and results in a forward solution with minimal residual variance to the measured EEG data $\mathbf{m}_{\text{EEG}}$. The residual variance indicates the degree to which both solutions differ and is defined in A.4. Brent's method (Brent, 1973), a derivative-free minimization method which iteratively proposes skull conductivity values σ^i_{skull} $(i = 0, 1, \dots)$ within the predefined range, is used for this purpose. In the following, the substeps that are performed in each iteration for a given conductivity value σ^i_{skull} are explained in detail, followed by more details on the minimization method. First, in Step 2a), the EEG leadfield $\mathbf{L}_{\text{EEG},x_{\text{MEG}},\sigma^i_{\text{skull}}} \in \mathbb{R}^{N_{\text{EEG}}\times 3}$ is computed for the source location $\mathbf{x}_{\text{MEG}}$ and the three orthonormal Cartesian vectors, for the given skull conductivity value. In the numerical (realistic) case, the linear system resulting from the FEM discretization can be solved directly for the three right-hand sides and the transfer matrix approach is not advantageous in this case. Nevertheless, the assembly of the stiffness matrix and the solution of the linear systems is still dominating the computational effort within this second step. In the following Step 2b), the best fitting moment $\mathbf{q}_{\text{EEG},x_{\text{MEG}}} \in \mathbb{R}^3$ with respect to the EEG reference data is determined using a least-squares fit, similar to Step 1, using the pseudo-inverse of the leadfield matrix. This moment vector is divided by its norm to determine the unit strength orientation in Step 2c). Since EEG is sensitive to both radial and tangential orientation components, this orientation $\mathbf{o}_{\text{est}} \in \mathbb{R}^3$ is chosen as the optimal orientation. Subsequently, in step 2d), the magnitude of the source is determined.

As the source strength is influenced by skull conductivity in an EEG-based reconstruction (Vorwerk et al., 2019a), the source amplitude $m_{\text{est}} \in \mathbb{R}$ for this fixed source orientation is determined from the MEG reference data $\mathbf{m}_{\text{MEG}}$ again by a least-squares fit. This is because the tangential component of this source orientation must match the measured MEG, which in turn is insensitive to skull conductivity. The optimal moment vector $\mathbf{q}_{\text{est}} \in \mathbb{R}^3$ is then composed of the orientation $\mathbf{o}_{\text{est}}$ determined by EEG and the magnitude m_{est} determined using MEG, see Step 2e). Finally, once these components are computed for a given skull conductivity σ^i_{skull}, the residual variance is computed between the reference EEG signal and the forward EEG solution for the current skull conductivity and the reconstructed dipole with source location $\mathbf{x}_{\text{MEG}}$ and moment $\mathbf{q}_{\text{est}}$. The aim is to find the skull conductivity which minimizes this term, i.e., which leads to an EEG leadfield for the fitted dipole which best explains the measured P20/N20 SEP data.

Brent's method is used for this minimization process which has the advantage that it does not require the computation of the function's derivative (Brent, 1973). In our application, the derivative cannot be computed directly and would need to be approximated numerically, which would require additional function evaluations. For more details on the optimization method, see A.2. In general, the algorithm assumes a function $f : I \to \mathbb{R}$ for $I \subset \mathbb{R}$ that is unimodal (see Def. A.5) on a given search interval $[a,b] \subset I$. For a continuous function, this means that it reaches its minimum exactly once in $[a,b]$ (Brent, 1973). If f is not unimodal on the search interval, Brent's method may result in a local instead of the global minimum. For the spherical case, we will observe convergence to the optimum in a controlled setting in Chapter 5. Regarding realistic scenarios, similar algorithms resulted in calibration curves of unimodal shapes as presented in Aydin et al. (2014) and Antonakakis et al. (2020).

Brent's method combines the benefits of both Golden-section search and successive parabolic interpolation which are briefly described in the following, mainly based on the notations and findings presented in Brent (1973) and Press et al. (2007), see also A.2 for more details. First, the method of Golden-section search is presented (Brent, 1973; Kiefer, 1953). In general, unlike finding a root of a function which is bracketed by two function evaluations with opposite sign, a minimum requires three evaluations such that for $a < x_1 < b$ it holds that $f(x_1) < min(f(a), f(b))$. Using Golden-section search, this initial point would be chosen such that the proportion of the larger to the smaller subinterval is equal to the *golden ratio* $\Phi := \frac{1+\sqrt{5}}{2} \approx 1.618$. In each iteration, the function is evaluated at an additional point chosen in the larger subinterval such that the interval that brackets the minimum successively shrinks, i.e., the new interval is $1/\Phi \approx 0.618$ times the width of the former one. Therefore, Golden-section search linearly converges (Brent, 1973). This method thereby resembles the bisection method applied for finding a root which reduces each interval by a factor of 0.5 in each iteration. However, as minimization requires three function evaluations to bracket a minimum, bisection applied in this context would lead to irregular reductions of the previous interval which makes this method harder to predict with a possibly worse reduction of the interval.

Second, Brent's method involves inverse parabolic interpolation which assumes the function can be approximated by a parabola close to its minimum (Brent, 1973; Jarratt, 1967). It is thereby the analogue to the secant method for finding a root which assumes a linear approximation in its vicinity. In each iteration, the function is additionally evaluated at the minimum of a parabola that is fitted through the three points of a given bracketing interval, see Def. A.8. Out of these four points, the one with the lowest function evaluation and its two neighbors constitute the next bracketing interval. This method fails if the three points are collinear and convergence to the minimum is not guaranteed. However, if the function is sufficiently regular, convergence is superlinear with an order larger than approximately 1.325 (Brent, 1973).

The motivation of Brent's method is to benefit from the convergence properties of inverse parabolic fitting if the function allows, but rely on Golden-section search otherwise to ensure reliability. A detailed algorithmic description of Brent's method can be found in Brent (1973) and Press et al. (2007). In every iteration, it updates six not necessarily distinct points. Initially, the first step is a Golden-section iteration that finds a third point in a given interval. Subsequently, inverse parabolic interpolation is attempted, which is accepted if the constructed minimum lies inside the current bracketing interval and if it entails a movement from the current optimal value that is less than half of the movement of the second last step (Press et al., 2007). Otherwise, the iteration step is performed using Golden-section search. This cycle is repeated until the tolerance criterion is reached, i.e., the suggested value in the next iteration does not vary significantly any more based on the provided tolerance ε.

As output, the algorithm returns the optimal skull conductivity value $\sigma_{\text{skull,est}}$ which results in a residual variance of $r(\sigma_{\text{skull,est}})$, as well as the estimated dipole characteristics $\mathbf{x}_{\text{MEG}}$, $\mathbf{o}_{\text{est}}$ and m_{est}.

4.3. Variations of the calibration algorithm

The steps of Algorithm 1 are chosen to best exploit the respective advantages of EEG and MEG modalities. Two variations of the calibration algorithm are presented here which are applied and discussed in the following chapters. The first variant determines the (quasi-) tangential orientation vector using MEG data and only relies on EEG for the (quasi-)radial contribution. In the second one, the residual variance with respect to combined EEG/MEG data is used.

Fitting the (quasi-)tangential orientation using MEG

The motivation to use EEG in order to determine the source orientation is based on the observation that MEG is less sensitive (or unaffected in case of a spherical head model) to (quasi-)radial orientation components (Antonakakis et al., 2019; Fuchs et al., 1998; Piastra et al., 2021). Instead of fitting the orientation with respect to EEG, it is also possible to fit this vector in two separate steps, using MEG to fit the (quasi-)tangential component and EEG only for the (quasi-)radial component. For this purpose, the dipole moment $\mathbf{q}_{\text{est}} \in \mathbb{R}^3$ can be split into two components

$$\begin{aligned} \mathbf{q}_{\text{est}} &= \mathbf{q}_{\text{rad}} + \mathbf{q}_{\text{tan}} \\ &= m_{\text{rad}}\mathbf{o}_{\text{rad}} + \mathbf{q}_{\text{tan}}. \end{aligned} \tag{4.3}$$

with the unit vector in (quasi-)radial direction $\mathbf{o}_{\text{rad}}$ and the corresponding strength m_{rad}.

In spherical head models, the distinction between radial and tangential orientation components is clear as they are defined as orthogonal and parallel with respect to the tangent plane through the surface point closest to the dipole. By contrast, in realistic models, there are two different approaches to define the quasi-radial and quasi-tangential components of a dipolar source. One possible option is to use geometric properties such as the local curvature of a segmented tissue surface in the closest point, typically the inner skull boundary (Haueisen et al., 2012; Piastra et al., 2021). Another approach which is adopted here is to define the quasi-radial orientation as the source orientation with the weakest contribution to the MEG leadfield defined by its singular value decomposition (Ahlfors et al., 2010; Huang et al., 2007; Piastra et al., 2021). The modifications in comparison to Algorithm 1 are summarized in Variant 1. In comparison to Algorithm 1, only the computation of $\mathbf{q}_{\text{est}}$ is modified. Step 1 as well as Step 2a) and the minimization procedure remain identical and are not repeated here.

In Step 2b) of this variant, the (quasi-)tangential component of the moment is fitted using the MEG reference data, which is accomplished using a truncated singular value decomposition (TSVD) of the leadfield matrix, see also A.1 for more details. For a given SVD $\mathbf{L} = \mathbf{U}\mathbf{\Sigma}\mathbf{V}^T$ we assume that the diagonal entries in $\mathbf{\Sigma}$ are sorted in descending order. In the spherical case, the lowest singular value Σ_3 is 0 as MEG is unaffected by radial sources. In the realistic case, the smallest singular value is expected to be close to zero such that the MEG leadfield can be well represented by a matrix of rank 2 as $\mathbf{L}_{12} = \mathbf{U}_{12}\mathbf{\Sigma}_{12}\mathbf{V}_{12}^T$, where

Variant 1: Modifications for fitting the (quasi-)tangential orientation using MEG

2. **b)** $\mathbf{q}_{\text{tan}} = \mathbf{V}_{12}\;[\mathbf{\Sigma}_{12}]^{+}\;\mathbf{U}_{12}^{T}\;\mathbf{m}_{\text{MEG}}$,

where $\mathbf{U}_{12} \in \mathbb{R}^{N_{\text{MEG}}\times 2}$, $\mathbf{\Sigma}_{12} \in \mathbb{R}^{2\times 2}$ and $\mathbf{V}_{12} \in \mathbb{R}^{3\times 2}$ result from a TSVD and are associated with the two largest singular values:

$$\mathbf{L}_{\text{MEG},x_{\text{MEG}}} = \mathbf{U\Sigma V}^{T} = (\mathbf{U}_{12}\mathbf{U}_{3})\begin{pmatrix}\mathbf{\Sigma}_{12} & \mathbf{0}\\ \mathbf{0} & \Sigma_{3}\end{pmatrix}(\mathbf{V}_{12}\mathbf{V}_{3})^{T}$$

c) $\mathbf{o}_{\text{rad}} = \mathbf{V}_{3}$

d) $m_{\text{rad}} = [\mathbf{L}_{\text{EEG},x_{\text{MEG}},\sigma^{i}_{\text{skull}}}\mathbf{o}_{\text{rad}}]^{+}\cdot\left(\mathbf{m}_{\text{EEG}} - \mathbf{L}_{\text{EEG},x_{\text{MEG}},\sigma^{i}_{\text{skull}}}\mathbf{q}_{\text{tan}}\right)$

e) $\mathbf{q}_{\text{est}} = m_{\text{rad}}\mathbf{o}_{\text{rad}} + \mathbf{q}_{\text{tan}}$

f) $m_{\text{est}} = \|\mathbf{q}_{\text{est}}\|_{2}$

g) $\mathbf{o}_{\text{est}} = \dfrac{\mathbf{q}_{\text{est}}}{m_{\text{est}}}$

$\mathbf{U}_{12} \in \mathbb{R}^{N_{\text{MEG}}\times 2}$ and $\mathbf{V}_{12} \in \mathbb{R}^{3\times 2}$ and the diagonal matrix $\mathbf{\Sigma}_{12} \in \mathbb{R}^{2\times 2}$. These are obtained from the full-rank SVD by discarding the zero rows as well as the row and column containing the smallest singular value Σ_{33} in $\mathbf{\Sigma}$, and those rows/columns in $\mathbf{U}$ and $\mathbf{V}$ that are multiplied with these. The component of the dipole moment in (quasi-)tangential orientation is then computed by multiplying the pseudo-inverse of the low-rank approximation of the MEG leadfield with the reference data $\mathbf{m}_{\text{MEG}}$. As the columns in $\mathbf{V}$ contain the principal dipole orientations associated with the singular values, the unit (quasi-)radial orientation vector $\mathbf{o}_{\text{rad}}$ is given as the third column in $\mathbf{V}$ as described in Step 2c). In the following step, the strength in (quasi-)radial orientation is fitted using EEG by finding the magnitude $m_{\text{rad}} \in \mathbb{R}$ that minimizes

$$\begin{aligned}&\left\|\mathbf{L}_{\text{EEG},x_{\text{MEG}},\sigma^{i}_{\text{skull}}}\left(m_{\text{rad}}\mathbf{o}_{\text{rad}} + \mathbf{q}_{\text{tan}}\right) - \mathbf{m}_{\text{EEG}}\right\|_{2}\\ =&\left\|\left(\mathbf{L}_{\text{EEG},x_{\text{MEG}},\sigma^{i}_{\text{skull}}}\mathbf{o}_{\text{rad}}\right)m_{\text{rad}} - \left(\mathbf{m}_{\text{EEG}} - \mathbf{L}_{\text{EEG},x_{\text{MEG}},\sigma^{i}_{\text{skull}}}\mathbf{q}_{\text{tan}}\right)\right\|_{2}\end{aligned}$$

using equation (4.3) and the distributivity of the leadfield matrix multiplication. The solution is again computed using the pseudo-inverse matrix, as summarized in Step 2d). Note that $\mathbf{U}$ and $\mathbf{V}$ in the SVD are not uniquely defined and therefore the magnitude m_{rad} may be negative due to a flipped orientation vector $\mathbf{o}_{\text{rad}}$. As both are multiplied and added to $\mathbf{q}_{\text{tan}}$ in Step 2e) following (4.3), this does not have an effect on the result. The moment vector is then decomposed into its strength and unit-length orientation in Steps 2f) and 2g).

Minimization of residual variance with respect to combined EEG/MEG

In many applications, the calibrated head model is constructed in order to allow combined EEG/MEG analysis. Therefore, a possible modification of Algorithm 1 is to minimize the residual variance to combined EEG/MEG data, i.e., to use the concatenated reference data sets and leadfields. These modifications are summarized in Variant 2.

Variant 2: Modifications for computing the residual variance with respect to combined EEG/MEG

2. Find $\sigma_{\text{skull,est}} = \operatorname{argmin}_{\sigma_{\text{skull}} \in (\sigma_{\min}, \sigma_{\max})} r(\sigma_{\text{skull}})$ using Brent's method, which proposes σ^i_{skull} iteratively ($i = 0, 1, \ldots$), with the residual variance defined as

$$r(\sigma^i_{\text{skull}}) := \frac{\|\mathbf{L}_{\text{EMEG},x_{\text{MEG}},\sigma^i_{\text{skull}}} \mathbf{q}_{\text{est}} - \mathbf{m}_{\text{EMEG}}\|_2^2}{\|\mathbf{m}_{\text{EMEG}}\|_2^2},$$

where

$$\mathbf{m}_{\text{EMEG}} := \begin{pmatrix} \mathbf{m}_{\text{EEG}} \\ \mathbf{m}_{\text{MEG}} \end{pmatrix}, \qquad \mathbf{L}_{\text{EMEG},x_{\text{MEG}},\sigma^i_{\text{skull}}} := \begin{pmatrix} \mathbf{L}_{\text{EEG},x_{\text{MEG}},\sigma^i_{\text{skull}}} \\ \mathbf{L}_{\text{MEG},x_{\text{MEG}}} \end{pmatrix}.$$

In comparison to Algorithm 1, only the computation of the residual variance differs taking both EEG and MEG into account, while the other steps are identical. As reference data, $\mathbf{m}_{\text{EMEG}} \in \mathbb{R}^{N_{\text{EEG}}+N_{\text{MEG}}}$ is used, while the concatenated leadfield is used for the forward solutions, i.e., $\mathbf{L}_{\text{EMEG},x_{\text{MEG}},\sigma^i_{\text{skull}}} \in \mathbb{R}^{(N_{\text{EEG}}+N_{\text{MEG}})\times 3}$.

In order to combine EEG and MEG data and leadfields, both need to be transformed to a unit-free space. The choice of this transformation defines how different channels and modalities are weighted and thereby influences the result. A commonly used approach is the SNR transformation described in Section 3.4 which will be used within this thesis.

In both spherical and realistic volume conductor models, the optimal moment $\mathbf{q}_{\text{est}}$ depends on the skull conductivity parameter. In the spherical case, in which the MEG is unaffected by radial dipole orientation components, this modified algorithm only alters the result if the least-squares fit for the orientation using EEG yields a different tangential orientation component. In the realistic case, both orientation components influence the MEG, although quasi-radial components have a smaller effect. Skull conductivity has a negligible influence on the MEG forward solution (Haueisen et al., 1997; Lew et al., 2013), which is therefore only computed once in Step 1 due to performance reasons.

5. Validation and evaluation in spherical head models

In this chapter, the novel calibration algorithm is evaluated in a controlled spherical head model scenario in which (quasi-)analytical solutions exist for the EEG/MEG forward problems. In a preparatory study presented in Section 5.1, the influence of tissue conductivities on the EEG forward solution in the spherical model is analyzed. In Section 5.2, the calibration method is tested in this well-controlled setup using realistic noise levels as well as dipoles at different eccentricities with strengths and orientations related to somatosensory experiments.

5.1. Influence of conductivities on EEG pole distance and error measures

In this section, the impact of varying conductivities on the EEG forward solution is investigated in more detail using a four-layer spherical head model. On the one hand, the effect of different tissue conductivities on the location of the topography peaks (pole distance) resulting from a dipolar source is analyzed. On the other hand, the influence on different error measures related to topography and magnitude is examined.

5.1.1. Materials and Methods

In the following, the characteristics of the head model and the investigated measures are explained. First, the spherical head volume conductor model and the considered conductivity ranges are described. Second, details on the test dipoles and the computation of the EEG forward solution are provided. Third, a definition of the pole distance as well as the other error measures is presented.

Spherical head volume conductor model

For this study, a four-layer spherical head model with radii and standard conductivities defined in Table A.1 was used. Each tissue conductivity was varied within the ranges summarized in Table 5.1. These intervals are almost identical to the ones considered in the sensitivity study in Vorwerk et al. (2019a). The lower bound for the skull conductivity range, however, was extended based on Altakroury (2017) and McCann et al. (2019). Additionally, the CSF range here is based on the weighted mean of 1.71 S/m ± 0.30 S/m as reported in McCann et al. (2019), as this review takes into account more studies than Baumann et al. (1997), which is the sole reference in Vorwerk et al. (2019a). In a corrected version (McCann et al., 2021), an exclusion of several studies yielded a slightly higher weighted mean of 1.74 S/m ± 0.17 S/m, due to the reduced standard deviation this new range is covered in the interval indicated in Table 5.1. For the homogenized brain compartment used here, the range for the gray matter compartment considered in Vorwerk et al. (2019a) was adopted, as both tissues are typically assigned the same conductivity of 0.33 S/m (Gonçalves et al., 2003b; Vorwerk et al., 2014).

Table 5.1.: Conductivity ranges for the four-compartment spherical head model with radii and standard conductivity values as defined in A.3.

Tissue	**Minimum (S/m)**	**Maximum (S/m)**	**References**
Scalp	0.28	0.87	(Vorwerk et al., 2019a)
Skull	0.0008	0.033	(Altakroury, 2017; McCann et al., 2019; Vorwerk et al., 2019a)
CSF	1.41	2.01	(McCann et al., 2019)
Brain	0.22	0.67	(Vorwerk et al., 2019a)

Computation of the EEG forward solution

As test dipoles, three tangentially oriented dipoles with unit strength at eccentricities 0.2, 0.821 and 0.982 were considered, a subset of the eccentricities considered in the study presented in Section 5.2. In general, eccentricity indicates the ratio between the distance of the source location to the sphere center and the inner sphere radius and is defined in A.3. The eccentricity of the middle dipole corresponds to a typical distance to the inner skull of the P20/N20 source, and the other values represent more extreme scenarios in order to provide a better overview of the behavior for dipoles at different eccentricities, see also Section 5.2.1.

The dipoles and the center of the sphere are collinear, their moment vectors define a plane that passes through the center point of the sphere. Due to the symmetric properties of the spherical volume conductor model, the maximal and minimal surface potentials resulting from the dipoles lie on this circle, i.e., their *orthodrome*. The spherical head model with the test dipoles is depicted in Figure 5.1a).

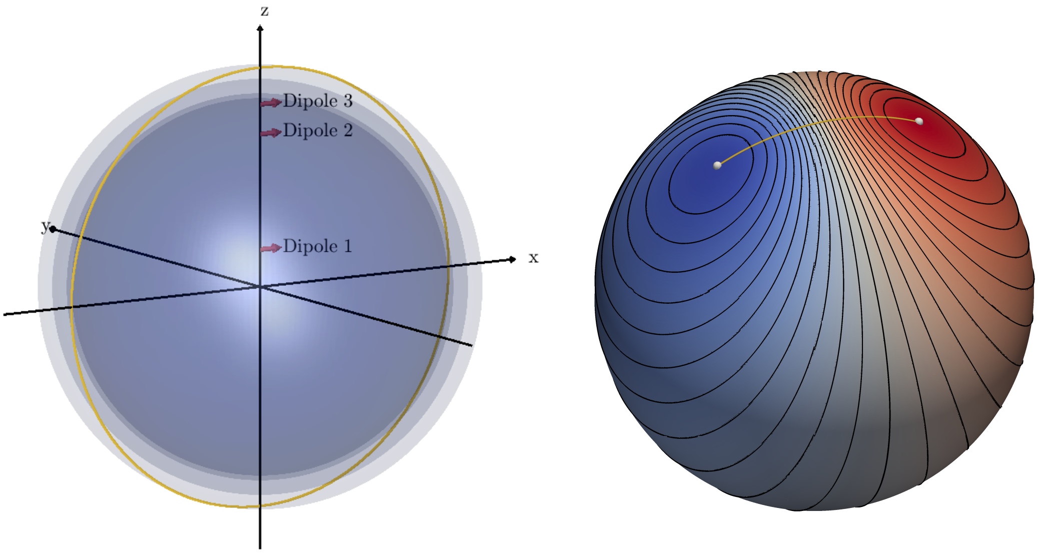

a) b)

Figure 5.1.: Head model and pole distance measure: a) Tangential test dipoles in spherical four-layer head model. The surface of the plane defined by the dipole locations and orientations is shown in yellow. b) Exemplary potential distribution on the spherical surface. The pole distance, i.e., the shortest curve on the spherical surface connecting the maximal and minimal potential, is shown in yellow.

The (quasi-)analytical EEG solutions were computed following the series expansion formulas in De Munck and Peters (1993) for the test dipoles in the four-layer sphere model. Each tissue conductivity was varied separately within the ranges described in Table 5.1, uniformly sampled at 1000 points. Additionally, scalp and skull conductivity were varied simultaneously, each parameter sampled at 100 points within the indicated ranges. For the topography peak distance, the (quasi-)analytical EEG solution was computed for 10 000 positions on the orthodrome, while 31 589 points on the entire surface were used for the computation of the error measures related to the complete surface potential, as described in the following section.

Computation of pole distance and error measures

The pole distance indicates the length of the shortest curve connecting the potential peak and trough on the surface and is depicted in Figure 5.1b). Let a and b denote the surface points with the highest and lowest potential with spherical coordinates (r, θ_a, ϕ_a) and (r, θ_b, ϕ_b), respectively, where r denotes the radius, θ_i the azimuthal and ϕ_i the elevation angles for $i \in \{a, b\}$. The pole distance d, i.e., the orthodromic distance between these points, is then defined as (Bronstein et al., 2008)

$$d = r \cdot \arccos\left[\cos(\phi_a) \cdot \cos(\phi_b) \cdot \cos(\theta_a - \theta_b) + \sin(\phi_a) \cdot \sin(\phi_b)\right]. \tag{5.1}$$

Note that due to the outer radius of $r = 92$ mm (see Table A.1) the maximal pole distance resulting from a radial dipole is half the circumference, i.e., approximately 289 mm.

In addition to the pole distance, three different error measures were computed between the forward solution for a specific set of conductivities and the forward solution for the standard conductivities which was used as a reference solution. These errors include the relative difference measure (RDM) which indicates deviations in topography, while the magnitude error (MAG) is reflecting differences in magnitude. Additionally, the residual variance (RV) was computed, which is a more general measure indicating the degree to which the data sets vary. Detailed definitions of these error measures can be found in A.4.

5.1.2. Results

In the following, the results of this simulation study are presented. First, the effect of varying conductivity values on the EEG pole distance is explained. Second, the results regarding the influence of conductivity variations on the error measures RDM, MAG and RV are outlined.

Topography peak distance

The effects of varying conductivities in the four-layer spherical head model on the pole distance of the quasi-analytical EEG topography as defined in (5.1) are summarized in Figure 5.2.

In Figure 5.2a), each conductivity is varied separately, while standard values are used for the other tissues. For the standard values (marked as circles for each conductivity), the pole distance is approximately 238 mm (dipole 1), 95 mm (dipole 2) and 55 mm (dipole 3).

Overall, skull conductivity has the largest effect on pole distance. The higher the skull conductivity values within the considered range, the lower the pole distance. Scalp conductivity has the second largest impact, while the relationship between conductivity and pole

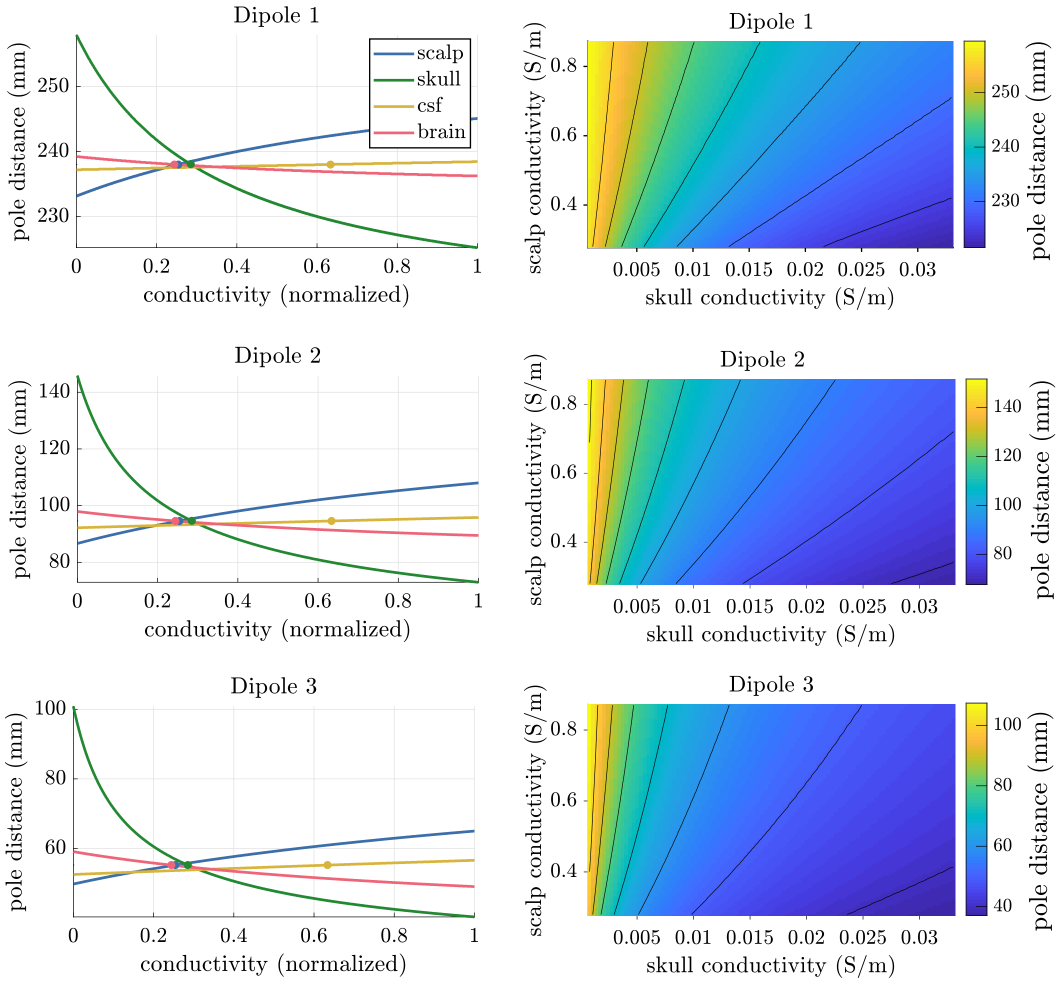

a) b)

Figure 5.2.: EEG topography pole distance for varying tissue conductivities in spherical model and three dipoles with eccentricity 0.2 (top), 0.821 (middle) and 0.982 (bottom): a) Pole distance when varying each tissue conductivity *separately* within the predefined range, reported conductivity values are normalized with respect to each conductivity range, the standard value for each tissue is marked as a circle. b) Pole distance when varying scalp and skull conductivities *simultaneously* within the predefined range. Isolines are indicated in black.

distance is reversed. Brain and CSF compartments have a comparatively smaller influence on the pole distance and show a negative and positive correlation between conductivity and pole distance, respectively. The eccentricities of the test dipoles mainly affect the absolute distance as deeper sources lead to a larger pole distance, note the different value ranges in Figure 5.2a). The relative effects between the different tissue conductivities are similar between different eccentricities. For the middle dipole which has the most relevant eccentricity when considering sources resembling the generator of the P20/N20 response, the pole distances observed lie within the ranges [72.96 mm, 145.86 mm] (skull), [86.66 mm, 107.99 mm] (scalp), [89.49 mm, 97.93 mm] (brain) and [92.21 mm, 95.85 mm] (CSF) when varying the respective conductivity.

In Figure 5.2b), scalp and skull conductivities are varied simultaneously in the predefined ranges. The isolines have an almost linear slope with slightly higher curvature for the more eccentric dipoles. Additionally, they have a higher gradient for more eccentric dipoles and for lower skull conductivity values, i.e., for the same increase in skull conductivity, a larger increase in scalp conductivity is needed to counterbalance the effect on pole distance.

Effect on error measures

In the following, the effects of varying conductivities on different error measures are presented. The errors between the EEG solution computed with varying conductivities inside the defined ranges and the solution with the standard conductivities are summarized in Figure 5.3.

For the topographic error measured by the RDM in Figure 5.3a), skull conductivity has the largest effect, followed by scalp conductivity, with only small effects of brain and CSF conductivity variations. For the most relevant eccentricity when considering the P20/N20 source (dipole 2), the minimal conductivities considered lead to RDM errors of 11.08% (skull), 2.93% (scalp), 0.81% (brain) and 0.57% (CSF). Conductivities at the upper bound of the considered intervals lead to RDM errors of 8.4% (skull), 4.04% (scalp), 1.23% (brain) and 0.3% (CSF). The absolute errors increase for more eccentric sources (note the different error ranges), while the relative influences in comparison to the other tissue types remain almost unchanged.

Considering the magnitude error depicted in Figure 5.3b), the largest effect can be observed for skull conductivity as well. For larger skull conductivities, the magnitude of the EEG forward solution becomes higher compared to the reference solution and the MAG error is in the positive range, while it is negative for smaller values. Brain followed by scalp conductivity variations have the second and third highest effects, with only small effects of CSF conductivity variations. For all three tissue types, the relationship between conductivity and MAG error is reversed compared to the effect of varying skull conductivity. For the middle dipole, the MAG errors are -78.47% (skull), 29.58% (brain), 19.22% (scalp) and 4.96% (CSF) for the minimal conductivities and 37.29% (skull), -41.29% (brain),

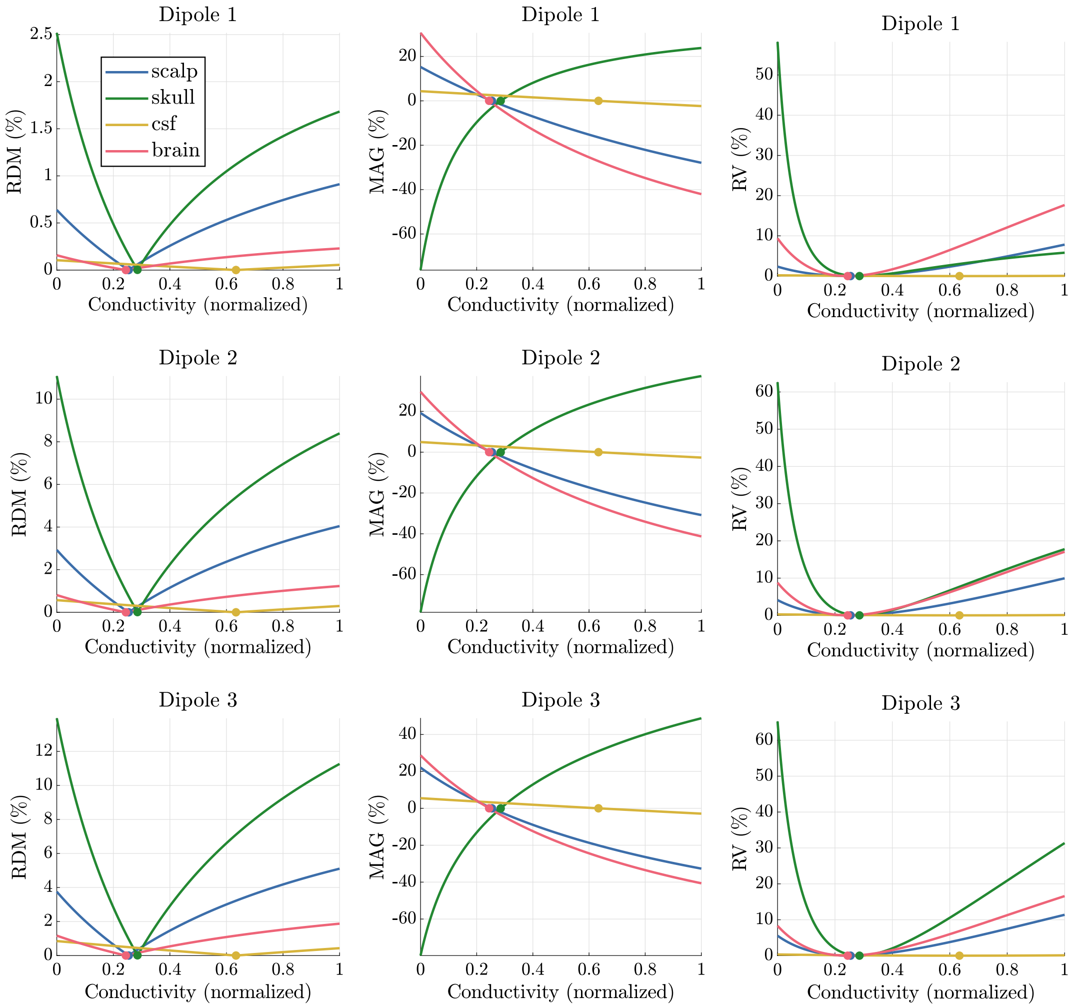

a) b) c)

Figure 5.3.: Error measures computed between the EEG forward solution using separately varying tissue conductivities compared to the solution using standard values for three dipoles with eccentricity 0.2 (top), 0.821 (middle) and 0.982 (bottom): a) RDM, b) MAG and c) RV percentage errors as defined in A.4. Reported conductivity values are normalized with respect to each conductivity range, the standard value for each tissue is marked as a circle.

−30.82% (scalp) and −2.65% (CSF) for the highest considered conductivity values.

The errors related to the RV measure are summarized in Figure 5.3c). This error measure also identifies skull conductivity as the most influential parameter, especially for conductivity values smaller than the standard value, but also for higher values for more eccentric sources. This is followed by brain (especially for lower eccentricities) and scalp conductivity, while the influence of CSF conductivity variations is negligible. For the middle dipole, the RV is at 62.63% (skull), 8.78% (brain), 4.1% (scalp) and 0.26% (CSF) for the lower bound of the conductivity ranges and 17.77% (skull), 17.08% (brain), 9.95% (scalp) and 0.07% (CSF) for the upper conductivity ranges.

5.1.3. Discussion

Overall, the results emphasize the importance of skull (and scalp) conductivity on EEG forward modeling. Varying skull conductivity within the predefined range based on reported literature values caused the largest differences in pole distance as well as the largest spans for RDM, MAG and RV errors. While scalp conductivity was observed as the second most important parameter with regard to pole distance and RDM, brain conductivity had the second largest effect on MAG and RV. Variations in CSF conductivity within the considered interval had the lowest effect on both pole distance and error measures.

These results are predominantly in accordance with other findings presented in literature. The importance of skull conductivity and scalp conductivity on EEG and TES has been emphasized by different sensitivity studies (Saturnino et al., 2019; Schmidt et al., 2015; Vallaghé and Clerc, 2009; Vorwerk et al., 2019a). A low skull conductivity compared to the other tissues results in a smeared EEG topography (Nunez and Srinivasan, 2006), and consequently to a larger distance between EEG topography poles resulting from a dipolar source. Individual differences in pole distance have also been investigated by Antonakakis et al. (2020) using simulated EEG topographies from a dipolar source reconstructed from the somatosensory evoked P20/N20 responses in realistic six-compartment head models, reporting mean distances in 20 participants of approximately 121 mm ± 32 mm.

Our results also fit well to the reported effect of skull conductivity on source depth. According to simulation studies in spheres and realistic models, deeper source reconstructions are obtained if a higher skull conductivity is assumed for the inverse method compared to the reference forward solution (Chen et al., 2010; Vorwerk et al., 2019a). Even though pole distance is only one characteristic of the surface topography which can be used for inverse analysis, our results show that a smaller pole distance is observed for both higher skull conductivity values and more eccentric sources, therefore the same pole distance can be obtained by changing either the eccentricity of the source or the skull conductivity.

Additionally, Vorwerk et al. (2019a) report a reverse effect of skull and scalp conductivity on source depth. We found a reverse effect of both parameters on pole distance, indicating that different combinations of both parameters can counterbalance the effect and result in the same value, as visualized by the isolines in Figure 5.2b).

Regarding the relatively high influence of brain conductivity variations on the error measures, especially on MAG and RV (see Figure 5.3), it has to be taken into account that the volume of the brain compartment is largely overestimated in the spherical head model. Using a realistic segmentation, CSF would fill the subarachnoid space and ventricles of the brain. Additionally, white and gray matter have different conductive properties and are not distinguished here. While the conductivity of 0.33 S/m is often used as a standard value for gray matter (Vorwerk et al., 2019a), homogenized white matter is often assigned a conductivity value of 0.14 S/m or anisotropic conductivities are considered based on DTI-MRI measurements, see Section 2.2.

The low uncertainty in CSF conductivity played a negligible role which is in accordance with the results presented in Vorwerk et al. (2019a), even though a larger range was considered here. However, the importance of modeling the CSF compartment has been emphasized in the context of EEG and MEG analysis (Rice et al., 2013; Vorwerk et al., 2014; Wolters et al., 2006).

5.2. Application of calibration algorithm

In this section, the algorithm for calibrating head models with respect to skull conductivity, which was presented in Section 4.2, is validated and evaluated in a well-controlled setup. The methodology and most of the results presented in this chapter are published in Schrader et al. (2020).

For this simulation study, a four-layer spherical head model was used. With (quasi-) analytical EEG and MEG forward solutions available, errors could be systematically quantified without any interplay with numerical errors that are unavoidable in realistic head modeling setups. We investigated the effects of different realistic noise levels as well as dipole sources with strengths and orientations related to somatosensory experiments. Although the focus lies on dipole characteristics corresponding to the generator of the P20/N20 component of somatosensory evoked responses, dipoles at different eccentricities and orientations were used in order to investigate the possibility of calibrating by means of other sources. In general, reported individual values for other tissue conductivities also vary (McCann et al., 2019), see also Section 2.2. Since scalp conductivity has been shown to be the second most important conductivity in EEG analysis (Vallaghé and Clerc, 2009; Vorwerk et al., 2019a), the effects of wrong assumptions about this parameter on the calibration result and subsequent EEG source analysis were investigated as well. In addition to these scenarios, the two variations of the calibration algorithm presented in Section 4.3 were applied and compared to the standard algorithm. In all of these test scenarios, the (quasi-)analytical solutions were used for the forward calculations in order to focus on the impact of varying specific parameters in the setup. Subsequently, the calibration algorithm was applied using FEM approaches to numerically solve the EEG/MEG forward problems. In one test scenario, different source modeling approaches as presented in Section 3.3 were compared. In a second case, the calibration results are compared for different tetrahedral and hexahedral meshes that were used for the FEM computations.

5.2.1. Materials and Methods

In the following, the setup of the test scenario and the analysis pipeline are presented based on Schrader et al. (2020). First, the characteristics of the spherical head volume conductor and the sensor arrangement are described, followed by a description of the test dipoles and the source space which is used for the single dipole deviation scans. Subsequently, the noise levels used to simulate more realistic reference data are explained. Finally, a complete overview of the analysis pipeline is presented and the investigated error measures are defined.

Spherical head model and sensors

For the construction of the spherical model and the sensor layout, one of the five combined EEG/MEG recordings from Chapter 6 was used, see Section 6.1.1 for more details on ethical clearance and data acquisition. A standard concentric four-layer sphere model (scalp, skull, CSF, brain) was fitted to the registered 73 electrode positions. The resulting radii and reference conductivities are summarized in Table A.1. For the MEG sensor positions and orientations, the realistic sensor setup of this measurement was used consisting of 271 first-order axial gradiometers and 13 reference coils. The spherical head model and the EEG/MEG sensors are visualized in Figure 5.4a).

For the test scenarios using FEM approaches to solve the forward problems numerically, different meshes were used for the spatial discretization of the head model. The number of nodes and elements of the tetrahedral and hexahedral meshes are summarized in Table 5.2. Geometry-adapted hexahedral meshes were created with the FieldTrip toolbox (Oostenveld et al., 2011) using a node-shift parameter of 0.3 in order to reduce stair-case effects (Camacho et al., 1997; Wolters et al., 2007a). These meshes, i.e., $\text{hex}_{390\text{k}}$ and $\text{hex}_{3041\text{k}}$, correspond to an edge length of 2 mm and 1 mm, respectively. The tetrahedral meshes were created using the Gmsh toolbox (Geuzaine and Remacle, 2009), the edge length was adjusted so that

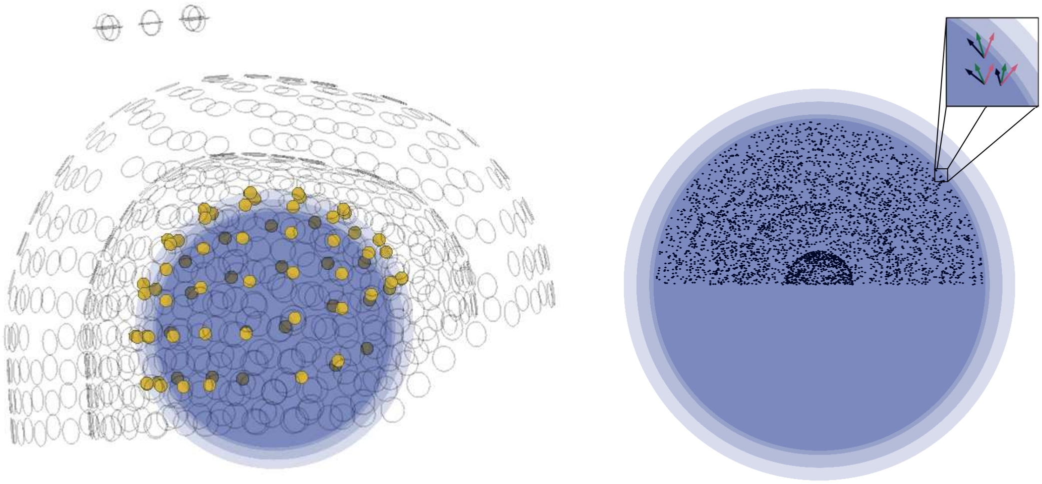

a) b)

Figure 5.4.: Four-layer spherical volume conductor model with a) realistic electrodes (yellow) and axial gradiometer coils (gray) and b) 500 test dipoles at 8 eccentricities within the upper hemisphere oriented tangentially (black arrows) or elevated by 25° (green) or 65° (red) towards the radial direction. Modified from Schrader et al. (2020).

Table 5.2.: Characteristics of the two tetrahedral ($\text{tet}_{52\text{k}}$, $\text{tet}_{389\text{k}}$) and the two hexahedral ($\text{hex}_{390\text{k}}$, $\text{hex}_{3041\text{k}}$) meshes for the FEM computations. The hexahedral meshes were created with a node-shift parameter of 0.3 and correspond to a resolution of 2 mm and 1 mm, respectively.

Mesh	$\text{tet}_{52\text{k}}$	$\text{tet}_{389\text{k}}$	$\text{hex}_{390\text{k}}$	$\text{hex}_{3041\text{k}}$
Nodes	52 469	388 886	389 848	3 041 456
Elements	290 659	2 287 096	370 869	2 966 035

the resolution close to the thin tissue layers is finer. The number of nodes was chosen to approximately match the number of nodes of hexahedral meshes with a given edge length. The mesh $\text{tet}_{389\text{k}}$ has approximately as many nodes as the 2 mm resolution hexahedral mesh $\text{hex}_{390\text{k}}$ and the number of nodes in $\text{tet}_{52\text{k}}$ approximately corresponds to a 4 mm hexahedral mesh which is not used here due to its inadequacy to model the fine 2 mm CSF layer. Details of the meshes are presented in Figure 5.5.

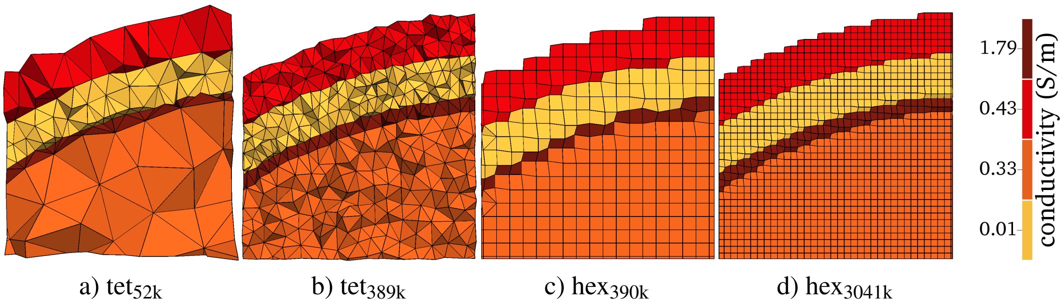

a) $\mathrm{tet}_{52\mathrm{k}}$ b) $\mathrm{tet}_{389\mathrm{k}}$ c) $\mathrm{hex}_{390\mathrm{k}}$ d) $\mathrm{hex}_{3041\mathrm{k}}$

Figure 5.5.: Clipped sections of the meshes used for the FEM computations to solve the EEG/MEG forward problems numerically. For the tetrahedral grids a) $\mathrm{tet}_{52\mathrm{k}}$ and b) $\mathrm{tet}_{389\mathrm{k}}$ the resolution is finer close to the thin tissue layers. The geometry-adapted hexahedral meshes c) $\mathrm{hex}_{390\mathrm{k}}$ and d) $\mathrm{hex}_{3041\mathrm{k}}$ were created with a node-shift parameter of 0.3 and have a resolution of 2 mm and 1 mm, respectively.

Test dipoles and source grid

The properties of the test dipoles used in the simulations, i.e., their locations, unit orientations and strengths, were chosen based on source reconstructions of evoked responses. SEP and SEF data sets were measured in five healthy participants using combined EEG/MEG and three different types of somatosensory stimulation. First, the median nerve at the wrist was electrically stimulated invoking a small movement of the thumb, this stimulation type is referred to as electric-wrist (EW) stimulation in the following. Additionally, a stimulation of the distal phalanx of the right index finger was applied using either a pneumato-tactile (PT) stimulus that involved an air-driven membrane or a Braille-tactile (BT) stimulator using a device with movable plastic pins. For details on the data acquisition and experimental paradigms for the somatosensory experiments, see Section 6.1.1. In Antonakakis et al. (2019), the P20/N20 response in these data sets, i.e., the peak of the EEG/MEG signals approximately 20 ms after stimulus onset, was then reconstructed in a six-compartment realistic head model. The average strengths of this reconstructed source of the SEP/SEF responses were 25.1 μAmm ± 6.5 μAmm, (EW), 9.7 μAmm ± 6.0 μAmm (BT) and 4.7 μAmm ± 2.2 μAmm (PT) for the three types of stimulation, respectively (Antonakakis et al., 2019). In a follow-up study involving 20 participants, mean P20/N20 source depths of 15.5 mm ± 4.5 mm were observed, which were measured as the minimal distance to the inner skull surface (Antonakakis et al., 2020). Regarding the orientation, these reconstructed sources tended to be tangentially oriented with a mean elevation angle towards the radial direction of 25.5° ± 18.6°, the largest outlier was observed with an angle of 65°.

Based on these observations from realistic experimental setups, the test dipole characteristics were defined. As source locations, 500 points at eight different eccentricities ranging from 0.2 to 0.982 relative to the inner (brain) sphere surface were randomly positioned in the upper half of the spherical model (Marsaglia, 1972). The investigated eccentricities contain the value of 0.821 which translates to a distance of approximately 15.5 mm to the inner skull surface which corresponds to the reconstructed P20/N20 source depth observed in Antonakakis et al. (2020). Other eccentricities were investigated to account for individual variations and to analyze the accuracy of the algorithm under more varying conditions. This might especially be relevant if other sources than the generator of the somatosensory evoked P20/N20 peak are considered for the calibration procedure which might be closer to the region of interest in EEG/MEG source analysis or the target in optimized TES. For each dipole location, a random tangentially oriented unit vector was created and elevated by 25° and 65° to simulate the average and the extreme experimentally observed P20/N20 source orientations (Antonakakis et al., 2020). The test dipole locations and orientations are visualized in Figure 5.4b). In one study presented in the following, the dipole strengths corresponding to the three different stimulation types (EW, PT, BT) were used and compared to each other. In all other test scenarios, the dipole strength related to EW stimulation was used.

In addition to the test dipoles, a regular source grid was created within the upper hemisphere of the brain compartment for the MEG single dipole deviation scans. In order to avoid an *inverse crime* which usually leads to overly optimistic source reconstruction results (Kaipio and Somersalo, 2005), the test dipole locations were not part of the source space. Moreover, the source space nodes did not correlate with the FEM mesh nodes. A resolution of 2 mm was used in most test cases with mean distances between each test dipole and its closest source space node of 0.97 mm ± 0.28 mm. When comparing numerical source modeling approaches, a resolution of 4 mm was used for the source space in combination with a subset of 100 dipoles per eccentricity due to the high computational cost of calculating the MEG leadfield using the subtraction approach. In this setup, the mean distance between each test dipole and its closest source grid node is 1.9 mm ± 0.57 mm.

Realistic noise levels

For each test dipole, the (quasi-)analytical solutions were computed using the closed formula by Sarvas (1987) for MEG and the series expansion formulas based on De Munck and Peters (1993) for EEG, see Section 3.2. To create more realistic conditions, noise was added to these solutions in most scenarios, either in the form of uncorrelated Gaussian noise or using actual EEG/MEG baseline signals. In order to determine realistic noise strengths for this purpose, the average standard deviation per channel of the baseline signals within the interval $[-100\ \text{ms}, -5\ \text{ms}]$ before stimulus onset was computed for the EW data set in Antonakakis et al. (2019), which was approximately 0.13 μV for electrodes and 3.2 fT for gradiometers. In some test scenarios, white Gaussian noise with this average strength was generated and added to the reference data. In other cases, EEG and MEG signals at random prestimulus time points of the EW measurement of one test subject were scaled to correspond to the mean standard deviation of all five subjects and added to the reference data. Since the noise was added at the sensor level, a better SNR is achieved for more superficial sources than for deep sources with identical strength, as it is the case in realistic applications.

When combining EEG/MEG data for the computation of the residual variance as done in Variant 2 of the calibration algorithm, both data sets needed to be transformed to a unit-free space. For this purpose, the reference data which was distorted using scaled prestimulus noise and the forward solutions at each channel were divided by the noise estimation obtained from the prestimulus interval of an EW stimulation dataset scaled to the mean of five participants.

Overview of analysis pipeline

The calibration procedure was tested in this controlled scenario using the spherical head model and test dipoles described in the previous sections. An overview of the analysis pipeline is provided in Figure 5.6. As input, reference solutions $\mathbf{m}_{\text{EEG}}$ and $\mathbf{m}_{\text{MEG}}$ were computed using the (quasi-)analytical EEG/MEG forward solutions. For these calculations, the standard conductivities defined in Table A.1 were used, only in one test scenario $\sigma_{\text{scalp,ref}}$ was varied by ±25% and ±50% when investigating the effect of erroneous assumptions on other conductivities. In most test scenarios, noise with realistic strength was added, as described in more detail in the previous section.

Using this reference data, the calibration was performed using Algorithm 1 or one of its two variations. The possible parameter range for σ_{skull} was defined by its lower and upper bounds $\sigma_{\min} = 0.0008$ S/m and $\sigma_{\max} = 0.033$ S/m, respectively. The convergence tolerance was set to $\varepsilon = 10^{-5}$ S/m. For the leadfield functions l_{EEG} and l_{MEG}, the (quasi-) analytical EEG and MEG solutions were used in most cases with the skull conductivity of the respective optimization step for the EEG solution. For the numerical approaches, CG-FEM solutions were computed for the tetrahedral or hexahedral meshes. Three different source models were compared, i.e., the partial integration, the St. Venant and the subtraction approach, as described in Section 3.3. Regarding the St. Venant source model, a reference length of $a_{\mathrm{ref}} = 20$ mm, a relaxation factor of $\lambda = 10^{-6}$, a maximal moment order of $n_0 = 2$ and a weighting exponent of $s = 1$ using the notations of Wolters et al. (2007a) were used, which have been often used as standard values (Nüßing, 2018; Vorwerk, 2016; Wolters et al., 2007a). In addition, monopoles were only placed on vertices belonging to elements of the dipole compartment, in our case the homogenized brain compartment, in order to fulfill the *St. Venant condition* for an improved accuracy for sources close to conductivity jumps (Medani et al., 2015). In Nüßing (2018), a generalization of the standard formulation of the St. Venant method was provided and different variations to choose the distribution of sources were presented and compared. A modification we adopted in the computations in this thesis is to use mixed moments as opposed to considering only diagonal moments (Nüßing, 2018). For the subtraction approach, a second order integration scheme was used for the computation of the volume and the surface integrals (Drechsler et al., 2009).

As output, the calibration algorithm then returned the estimated dipole location $\mathbf{x}_{\mathrm{MEG}}$, its unit orientation $\mathbf{o}_{\mathrm{est}}$ and magnitude m_{est} as well as the estimated skull conductivity $\sigma_{\mathrm{skull,est}}$ which were then compared to the reference values using the error measures described in the following.

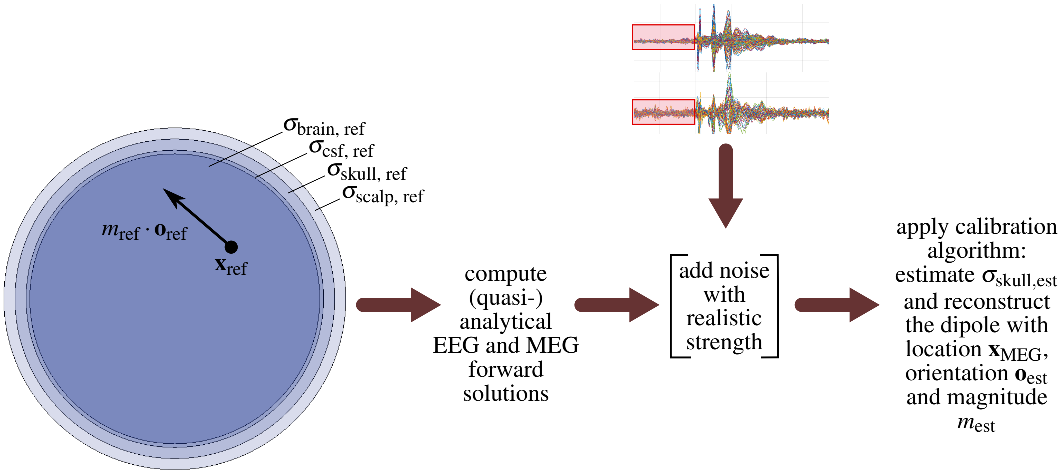

Figure 5.6.: Analysis pipeline: (Quasi-)analytical EEG and MEG solutions are computed for test dipoles with realistic characteristics in the spherical head model with standard reference conductivities. Noise with realistic strength is added in most test scenarios. Then, Algorithm 1 is applied which reconstructs the dipolar source while fitting the skull conductivity parameter as a further degree of freedom. Modified from Schrader et al. (2020).

Error measures

The accuracy of the calibration results was evaluated by different error measures. First, the relative error between estimated and reference skull conductivity (%) is given as

$$e_{\text{skull}} = 100 \cdot \frac{\sigma_{\text{skull,est}} - \sigma_{\text{skull,ref}}}{\sigma_{\text{skull,ref}}}. \tag{5.2}$$

As the range for possible skull conductivity values was set to (0.0008, 0.033) S/m, values for e_{skull} lie within the interval $(-92\%, 230\%)$. In order to quantify the errors related to the dipole reconstruction, the localization error e_{loc} (mm), the orientation error e_{ori} (degrees) and the magnitude error e_{mag} (%) compared to the reference dipole are defined as

$$e_{\text{loc}} = ||\mathbf{x}_{\text{MEG}} - \mathbf{x}_{\text{ref}}||_2, \tag{5.3}$$

$$e_{\text{ori}} = \cos^{-1}\left(\mathbf{o}_{\text{est}} \cdot \mathbf{o}_{\text{ref}}\right), \tag{5.4}$$

$$e_{\text{mag}} = 100 \cdot \frac{m_{\text{est}} - m_{\text{ref}}}{m_{\text{ref}}}. \tag{5.5}$$

In rare cases with extremely low SNR, Algorithm 1 may result in a negative fitted magnitude parameter m_{est}. For the error measures, we use the convention that $m_{\text{est}} \in \mathbb{R}^+$, which is achieved by flipping the orientation $\mathbf{o}_{\text{est}}$ in these cases. In one test scenario, the depth error e_{depth} (mm) is additionally indicated which is defined as

$$e_{\text{depth}} = ||\mathbf{x}_{\text{MEG}} - \mathbf{c}||_2 - ||\mathbf{x}_{\text{ref}} - \mathbf{c}||_2, \tag{5.6}$$

where $\mathbf{c} \in \mathbb{R}^3$ denotes the center of the sphere.

5.2.2. Results

In the following, the results of the analysis pipeline are presented. In a preliminary investigation, the implementation of the algorithm was verified under ideal conditions. In the following, three scenarios are presented based on Schrader et al. (2020). First, the dipole strengths corresponding to three somatosensory experiments were compared using two different realistic noise scenarios. Second, the role of different dipole orientations and third, the influence of scalp conductivity uncertainty was investigated. In addition to these scenarios, the two variants of the algorithm were applied and compared to the results of the standard algorithm. After these investigations using exclusively (quasi-)analytical EEG/MEG forward solutions in order to quantify the errors in a controlled setting, the impact of numerical errors was analyzed. For this purpose, FEM forward solutions were computed using different source models and meshes.

Verification in an ideal scenario

In this preliminary investigation, the implementation of the algorithm is verified in a controlled scenario under best possible conditions. In order to be able to reconstruct the dipoles exactly, the dipole locations were added to the source grid, i.e., an *inverse crime* was allowed (Kaipio and Somersalo, 2005). In addition, no noise was added to the (quasi-)analytical reference solutions in this scenario. The results show that the dipole characteristics and the skull conductivity can be reliably reconstructed up to the given tolerance. On average, 9.17 function evaluations were required in the minimization process, including 2.17 (plus 1 initial) Golden-section search and 6 inverse parabolic interpolation steps. Figure 5.7 shows exemplary calibration curves with the residual variance evaluations in Step 2 of Algorithm 1 for five tangential dipoles at different eccentricities. For comparison, Figure 5.7a) shows the goal function evaluations for the entire interval $[\sigma_{\text{min}}, \sigma_{\text{max}}]$ uniformly sampled every 10^{-4} S/m. All curves have a global minimum at the reference skull conductivity of 0.01 S/m and reach their highest values at the lower interval boundary. Additionally, the calibration curves tend to be steeper for more eccentric sources, especially for higher skull

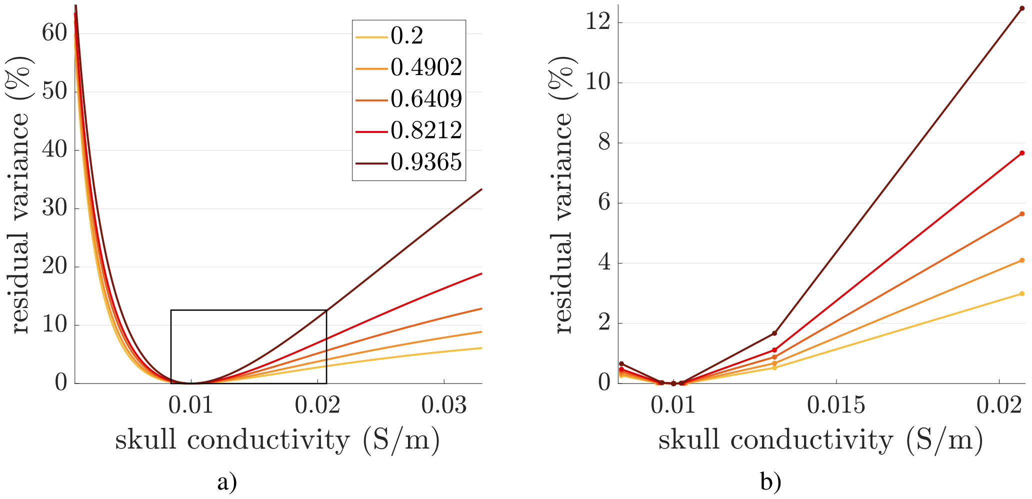

a)

b)

Figure 5.7.: Exemplary calibration curves for five tangential dipoles at different eccentricities ranging from 0.2 to 0.9365. The residual variance as defined in Step 2 of Algorithm 1 is evaluated for a) the entire interval $[\sigma_{\text{min}}, \sigma_{\text{max}}]$ uniformly sampled every 10^{-4} S/m and b) using the iteration values for the skull conductivity in the minimization process when applying Algorithm 1. This value range is indicated as a black rectangle in subfigure a).

conductivities. This is in accordance with the results presented in the previous section, in particular Figure 5.3c) showing the RV for varying conductivities. Figure 5.7b) only shows the function evaluations when applying the minimization in Algorithm 1. According to Brent's method, the goal function is never evaluated at the interval boundaries and instead only a small sample of function evaluations is used within the interval.

These findings indicate that the calibration algorithm can accurately reconstruct the reference skull conductivity with a small number of iterations in an ideal (inverse crime) setting. In the following, the calibration procedure will be tested under more realistic scenarios in order to quantify the effects of different factors on the reconstruction errors.

Different dipole strengths of somatosensory experiments

In this scenario, the test dipole strengths m_{ref} were varied to correspond to magnitudes experimentally observed in somatosensory experiments using three stimulation types, these results are based on (Schrader et al., 2020). Tangential test dipoles were used with magnitudes corresponding to EW, BT and PT stimulation in somatosensory experiments. Two different noise scenarios were investigated, based on realistic baseline strength as described in more detail in Section 5.2.1.

First, white Gaussian noise was added to the (quasi-)analytical EEG and MEG reference solutions. The resulting errors for the reconstructed dipole (e_{loc}, e_{ori} and e_{mag}) and the skull conductivity error e_{skull} as defined in (5.2) – (5.5) are shown in Figure 5.8. Overall, all error measures decrease for higher dipole strengths. The errors in localization (Figure 5.8a)) and magnitude (Figure 5.8c)) which are determined using MEG, are at a low level and nearly constant for rather eccentric sources. This includes the most relevant eccentricity of 0.821, which approximately corresponds to the P20/N20 source depth. At this eccentricity, the localization errors are 1.1 mm ± 0.4 mm (EW), 1.2 mm ± 0.5 mm (BT) and 1.7 mm ± 0.8 mm (PT) and the magnitude errors 0.1% ± 2.6% (EW), 0.02% ± 3.1% (BT) and 0.3% ± 4.4% (PT). For deeper sources, the errors strongly increase. The dipole orientation errors (Figure 5.8b)) are mainly influenced by the noise level related to the stimulation types, at an eccentricity of 0.821, they are 1.1° ± 0.6° (EW), 2.7° ± 1.5° (BT) and 5.5° ± 3.1° (PT), respectively. The calibration procedure results in errors for the estimated skull conductivity (Figure 5.8d)) of 0.06% ± 5.4% (EW), 1.0% ± 10.5% (BT) and 3.3% ± 20.8% (PT) at an eccentricity of 0.821. Additionally, the mean over all sensors of the absolute SNR is indicated for all conditions in Figure 5.8e). It increases with eccentricity and source strength, i.e., electric wrist stimulation leads to the best SNR. Additionally, it is higher for MEG than for EEG, with mean values of 12.8 (EW), 5.0 (BT) and 2.6 (PT)

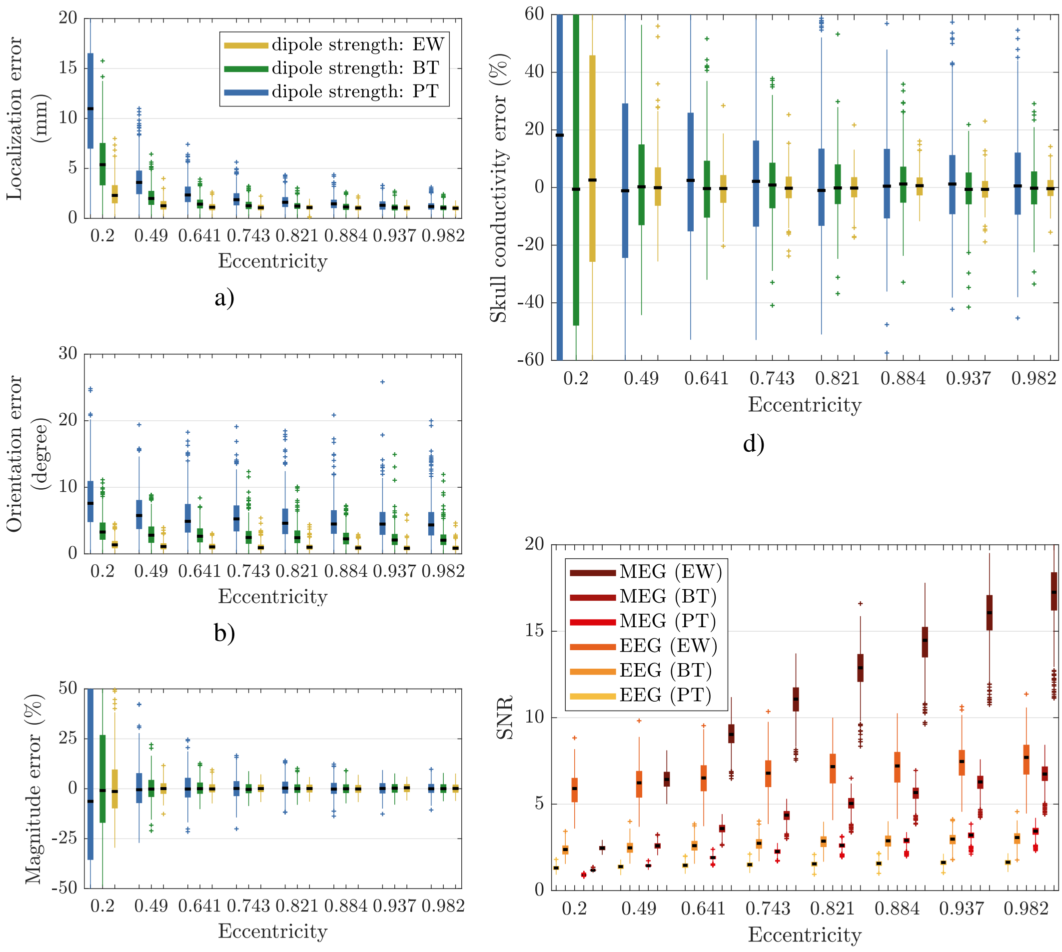

a) b) c) d) e)

Figure 5.8.: Calibration results for tangential sources with magnitudes corresponding to strengths observed in electric wrist (EW), Braille-tactile (BT) or pneumato-tactile (PT) somatosensory experiments, while white Gaussian noise with a realistic strength was added to the (quasi-)analytical reference solutions. Source reconstruction errors with regard to a) localization, b) orientation and c) magnitude, d) skull conductivity errors and e) mean absolute SNRs are shown for test dipoles at different eccentricities plotted on a logarithmic scale. Boxplots show the 25th and 75th percentiles and the median. Modified from Schrader et al. (2020).

for MEG and 7.0 (EW), 2.8 (BT) and 1.5 (PT) for EEG at the most relevant eccentricity of 0.821. Note that for the deepest sources under consideration with an eccentricity 0.2, the MEG least-squares fit in step 2d) to determine the best fitting magnitude in the calibration Algorithm 1 resulted in a negative value for 23 (PT) dipoles. As a result, the orientation

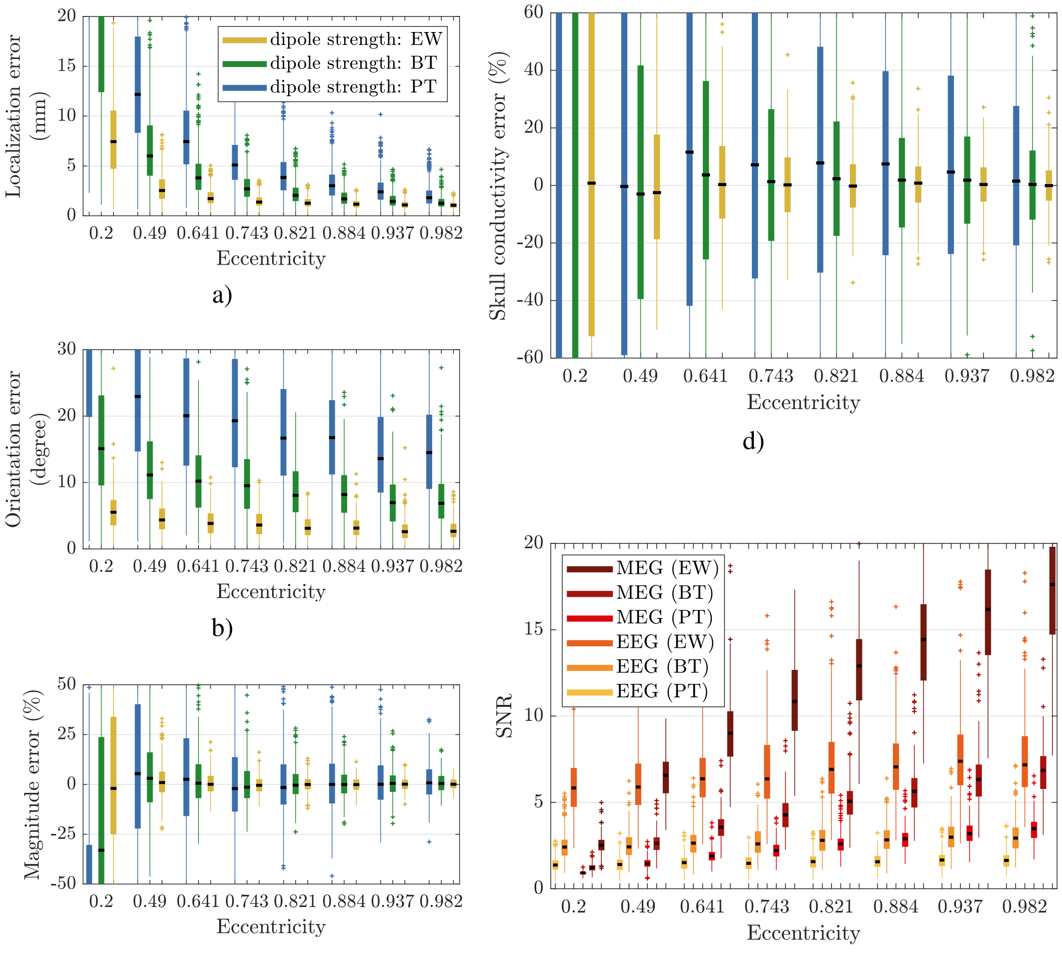

a)

b)

c)

d)

e)

Figure 5.9.: Calibration results for tangential sources with magnitudes corresponding to strengths observed in electric wrist (EW), Braille-tactile (BT) or pneumato-tactile (PT) somatosensory experiments, while baseline noise was added to the (quasi-)analytical reference solutions. Source reconstruction errors with regard to a) localization, b) orientation and c) magnitude, d) skull conductivity errors and e) mean absolute SNRs are shown for test dipoles at different eccentricities plotted on a logarithmic scale. Boxplots show the 25th and 75th percentiles and the median. Modified from Schrader et al. (2020).

which is fitted using the EEG data in step 2c) was flipped, resulting in orientation errors of almost 180° (not in the displayed range).

In a second scenario, noise from the prestimulus interval was added to the (quasi-) analytical solutions, as described in Section 5.2.1. The resulting errors for the reconstructed dipole (e_{loc}, e_{ori} and e_{mag}), the skull conductivity errors e_{skull} and the resulting absolute

SNRs for each condition are shown in Figure 5.9. Compared to the previous investigation using Gaussian noise, the errors show a similar trend, but are at an overall higher level. All error measures tend to increase for lower dipole strengths and deeper sources, as the SNR decreases. For the most relevant eccentricity of 0.821, the mean localization errors are 1.3 mm ± 0.5 mm (EW), 2.3 mm ± 1.2 mm (BT) and 4.3 mm ± 2.7 mm (PT), as shown in Figure 5.9a). The orientation errors (Figure 5.9b)) at this eccentricity are 3.3° ± 1.7° (EW), 8.6° ± 4.4° (BT) and 18.0° ± 9.6° (PT). The magnitude errors ((Figure 5.9c)) are at -0.01% ± 3.9% (EW), 0.2% ± 8.2% (BT) and 1.4% ± 18.7% (PT), respectively. The calibration procedure results in errors for the estimated skull conductivity (Figure 5.9d)) of 0.5% ± 10.9% (EW), 3.5% ± 28.0% (BT) and 16.1% ± 60.0% (PT) at an eccentricity of 0.821. The mean absolute SNRs over all channels for each condition are depicted in Figure 5.9e). The SNR increases with eccentricity and source strength and is higher for MEG than for EEG, mean values are at 12.9 (EW), 5.0 (BT) and 2.6 (PT) for MEG and 7.2 (EW), 2.9 (BT) and 1.6 (PT) for EEG. As previously, the calibration resulted in a negative magnitude and orientation errors of nearly 180° for 8 (EW), 85 (BT) and 143 (PT) dipoles at eccentricity 0.2 and 16 (PT) dipoles at eccentricity 0.49.

As we observe overall skull conductivity errors of 0.06% ± 5.4% using Gaussian noise in combination with electric wrist stimulation at our eccentricity of interest at 0.821, which are in a similarly low range when compared to using prestimulus noise, we will proceed in the following with only Gaussian noise scenarios. In the discussion, we will address the question of how to further optimize our stimulation protocols to minimize spatial correlations in overlayed noise and to achieve the best SNR.

Different source orientations

In the following investigation based on Schrader et al. (2020), the dipole orientations were varied to investigate the accuracy of the calibration in case of radial orientation components. For that purpose, each dipole was either tangentially oriented or rotated by 25° or 65° towards the radial direction, see Section 5.2.1. In this test scenario, white Gaussian noise with realistic strength was used to distort the reference solutions and the dipole strengths corresponded to EW stimulation which resulted in the highest SNR in the previous study. Therefore, the results for tangential dipoles here correspond to the results in the previous section using Gaussian noise and EW stimulation.

The resulting errors for the reconstructed dipole (e_{loc}, e_{ori} and e_{mag}), the skull conductivity errors e_{skull} and the resulting mean absolute SNRs for each condition are shown in Figure 5.10. For the most relevant eccentricity of 0.821 when considering the P20/N20 source, the

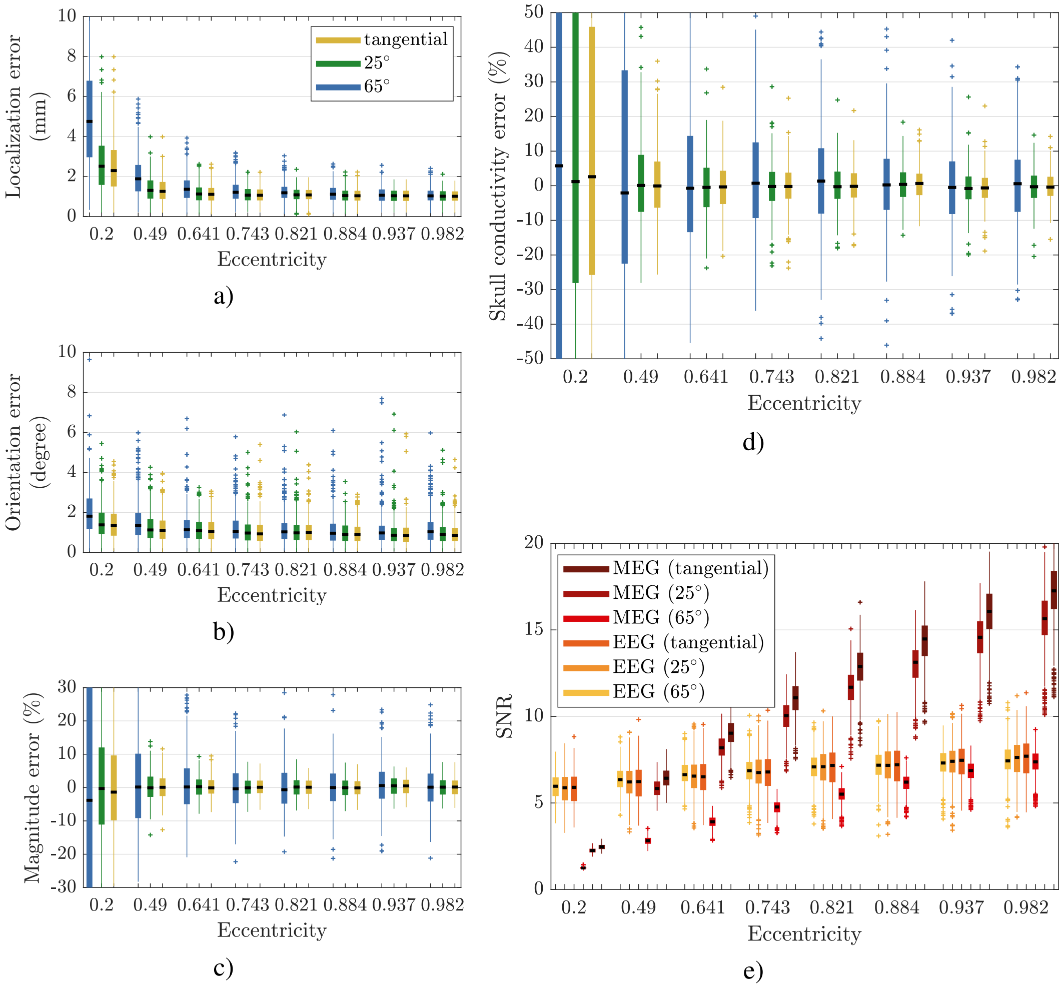

a)

b)

c)

d)

e)

Figure 5.10.: Calibration results for sources with different orientations (tangential or rotated by 25° or 65°), while white Gaussian noise with realistic strength was added to the (quasi-)analytical reference solutions. Source reconstruction errors with regard to a) localization, b) orientation and c) magnitude, d) skull conductivity errors and e) mean absolute SNRs are shown for test dipoles at different eccentricities plotted on a logarithmic scale. Boxplots show the 25th and 75th percentiles and the median. Modified from Schrader et al. (2020).

mean localization errors are 1.1 mm ± 0.4 mm (tangential; 25°) and 1.2 mm ± 0.5 mm (65°), as shown in Figure 5.10a). The orientation errors (Figure 5.10b)) at this eccentricity lie at 1.1° ± 0.6° (tangential), 1.1° ± 0.7° (25°) and 1.2° ± 0.8° (65°). The magnitude errors (Figure 5.10c)) are at 0.1% ± 2.6% (tangential), 0.1% ± 2.9% (25°) and −0.1% ± 6.7% (65°), respectively. The calibration procedure results in errors for the estimated skull conductivity (Figure 5.10d)) of 0.06% ± 5.4% (tangential), 0.1% ± 6.0% (25°) and

1.7% ± 14.2% (65°) at an eccentricity of 0.821. The absolute SNR values for MEG are higher for more tangentially oriented sources with mean ratios of 12.8 (tangential), 11.6 (25°) and 5.5 (65°), see Figure 5.10e). Regarding EEG, the reported SNR values are largely independent of source orientations with mean values of 7.0 (tangential; 25°) and 7.1 (65°) at 0.821. For 32 (65°) dipoles at eccentricity 0.2, the calibration procedure resulted in a negative magnitude, thus flipping the orientation obtained from EEG.

Erroneous scalp conductivity assumptions

In the previous investigations, literature values were adopted for brain, CSF and scalp tissue conductivities. Inconveniently, these values are also subject to a relatively high uncertainty

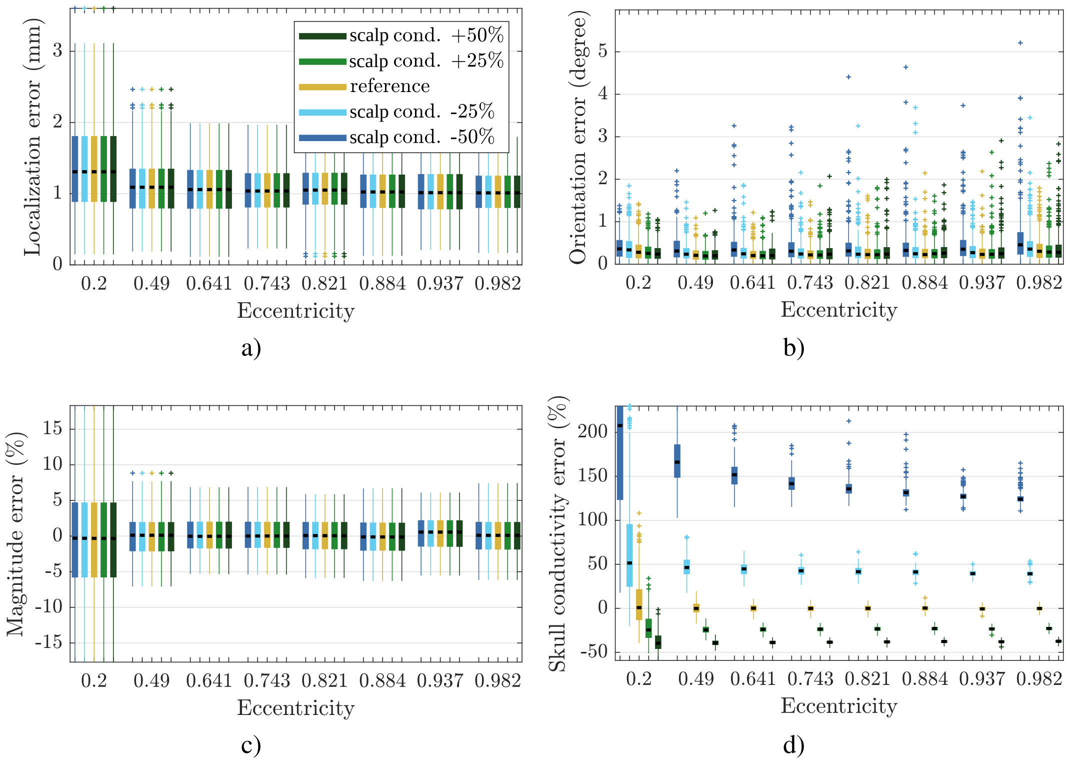

a) b)

c) d)

Figure 5.11.: Calibration results for tangential sources using varying reference scalp conductivities of ±25 and ±50%, compared to the standard value 0.43 S/m (yellow). No noise was added to the reference solutions. Source reconstruction errors with regard to a) localization, b) orientation and c) magnitude and d) skull conductivity errors are shown for test dipoles at different eccentricities plotted on a logarithmic scale. Boxplots show the 25^{th} and 75^{th} percentiles and the median. Modified from Schrader et al. (2020).

and reported values vary (McCann et al., 2019). Due to the importance of scalp conductivity which has been emphasized as the second most important conductivity (Vallaghé and Clerc, 2009; Vorwerk et al., 2019a), we investigated the effect of wrong assumptions about this value on the proposed calibration algorithm, the results presented here are based on Schrader et al. (2020). In the following, the results are presented for applying the calibration algorithm with varying reference scalp conductivities. Afterwards, the impact of different scalp conductivities in combination with standard and fitted skull conductivity parameters on EEG source reconstructions is investigated.

For the purpose of testing the algorithm taking scalp conductivity uncertainty into account, the reference scalp conductivity $\sigma_{\text{scalp, ref}}$, which is unknown in reality, was varied by 25% and 50%, while the standard value of 0.43 S/m was used for the leadfield calculations in the calibration procedure. No noise was added to the reference solutions in order to focus on the effect of scalp conductivity uncertainty in this scenario. The resulting errors for the reconstructed dipole (e_{loc}, e_{ori} and e_{mag}) and the skull conductivity errors e_{skull} are reported in Figure 5.11. The dipole reconstruction errors are at a very low level for all eccentricities. The mean localization errors (Figure 5.11a)) are below 1.4 mm with a standard deviation smaller than 0.6 mm, and are independent of the conductivity profile. The average orientation errors (Figure 5.11b)) are smaller than 0.6° with a standard deviation below 0.6°. The magnitude errors (Figure 5.11c)) have a mean value of maximally 0.3%, with a standard deviation smaller than 7.4%. At an eccentricity of 0.821, the calibration procedure results in overall skull conductivity estimation errors (Figure 5.11d)) of 136.4% ± 8.6% (41.9% ± 5.0%) in case the real scalp conductivity is 50% (25%) lower compared to the standard value, and −38.1% ± 2.2% (−23.4% ± 2.8%) in case it is 50% (25%) higher. For test dipoles at neighboring eccentricities, the errors are in a similar range.

Our main aim of calibrating head models is to improve EEG or combined EEG/MEG source analysis and optimize TES montages. In other words, we are not interested in the actual physical resistivity of the skull, but rather fit this important parameter in our procedure to best explain realistic data in combination with the other properties of the head volume conductor model. We thereby exploit *a priori* information available in data sets of well-studied somatosensory evoked responses. As a result, the individually fitted skull conductivity is expected to lead to better source analysis results in combination with the head volume conductor model when compared to the standard value, irrespective of whether it in fact accurately reports skull conductivity. In order to investigate this aspect, which in practical applications may even be more important, we performed an EEG single dipole deviation scan taking the uncertainty of scalp conductivity into account and compared the fitted to the standard skull conductivity. For the computation of reference solutions $\mathbf{m}_{\text{EEG}}$,

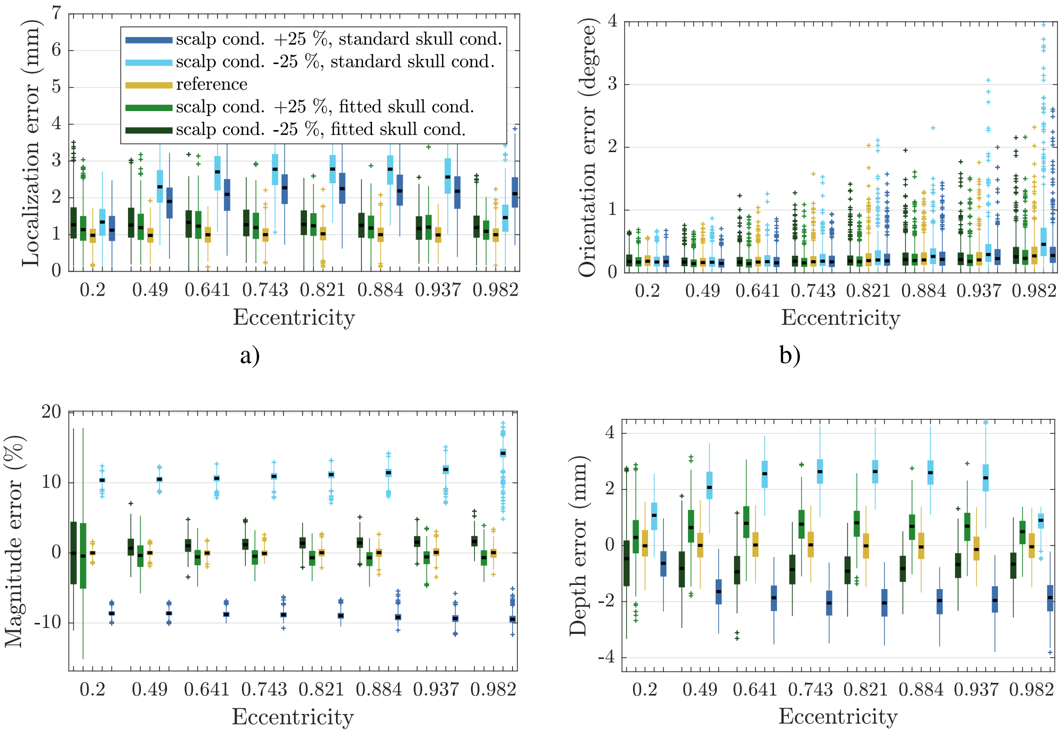

a) b)

c) d)

Figure 5.12.: EEG single dipole deviation scan results for tangential sources using reference scalp conductivities deviating −25% (0.32 S/m) or +25% (0.54 S/m). For the forward solutions, the standard scalp conductivity 0.43 S/m was used and either the standard (blue) or fitted (green) skull conductivities (see Figure 5.11). Source reconstruction errors with regard to a) localization, b) orientation, c) magnitude and d) depth are shown for test dipoles at different eccentricities plotted on a logarithmic scale. Boxplots show the 25th and 75th percentiles and the median. Modified from Schrader et al. (2020).

a scalp conductivity $\sigma_{\text{scalp,ref}}$ was used which was either 25% higher (0.54 S/m) or lower (0.32 S/m) compared to the standard value of 0.43 S/m. This standard value was used for the leadfield computations within the calibration algorithm, thus, the real value was either under- (+25%) or overestimated (−25%). Additionally, either the standard or the fitted skull conductivities (see Figure 5.11) were used in the calibration procedure. In Figure 5.12, the errors of the EEG single dipole deviation scan are shown when using different scalp and skull conductivities. For a better comparison, the results are also shown for using the correct values (yellow). The results show that when using the standard scalp conductivities (over- or underestimating the reference value by 25%), the localization errors (Figure

5.12a)) are higher for the standard skull conductivity with mean values of 2.8 mm for over- (light blue) and 2.2 mm for underestimating (dark blue) scalp conductivity for dipoles with an eccentricity of 0.821. These errors mainly correlate with depth differences, as shown in Figure 5.12d). While orientation errors are overall at a very low range (Figure 5.12b)), the errors in magnitude (Figure 5.12c)) at this eccentricity are on average 11.1% (−8.9%) for over- (underestimating) scalp conductivity. In case the fitted skull conductivities are used, these errors can be reduced, leading to mean localization errors of maximally 1.3 at the most relevant eccentricity for over- (dark green) and underestimating (light green) scalp conductivity. Note that on average, the test dipoles are 0.97 mm away from the closest source space node, see Section 5.2.1.

In order to illustrate the influence of scalp/skull conductivity changes on the EEG forward solution, Figure 5.13 shows the quasi-analytical EEG solution sampled at the sphere surface for a tangential dipole at eccentricity 0.821. The topographies are shown for a scalp conductivity increased by 50% (left), the standard values (middle) and standard scalp conductivity with the fitted skull conductivity (right). The isolines on the topographies indicate that the EEG solution using fitted skull conductivity in combination with the standard scalp conductivity (right) closely resembles the one using the reference conductivity (left) when compared to using standard values for both (middle).

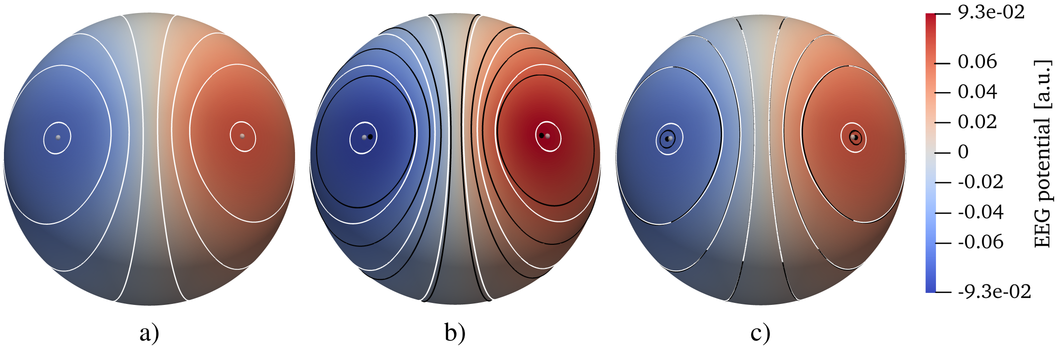

Figure 5.13.: EEG topography for tangential dipole at eccentricity 0.821 with a) scalp conductivity increased by 50% compared to the standard value, standard skull conductivity, b) standard scalp and skull conductivities, c) standard scalp conductivity, fitted skull conductivity. The white isolines of a) are also indicated as a reference for b) and c) in addition to their black isolines, all isolines indicate the same set of values. Minimum and maximum values are marked by small spheres.

Variations of the algorithm

In the following investigation, the results of Algorithm 1 are compared to the results of its two modifications presented in Section 4.3.

In a first comparison, Variant 1 is applied which determines the tangential orientation component using MEG and only uses EEG for the radial component. For a set of test dipoles which are either tangentially oriented or radially rotated by 65°, the results of this comparison to the standard version of the algorithm are presented in Figure 5.14.

The same Gaussian noise vectors were added to the reference solution in both conditions, therefore the localization errors presented in Figure 5.14a) are identical between both al-

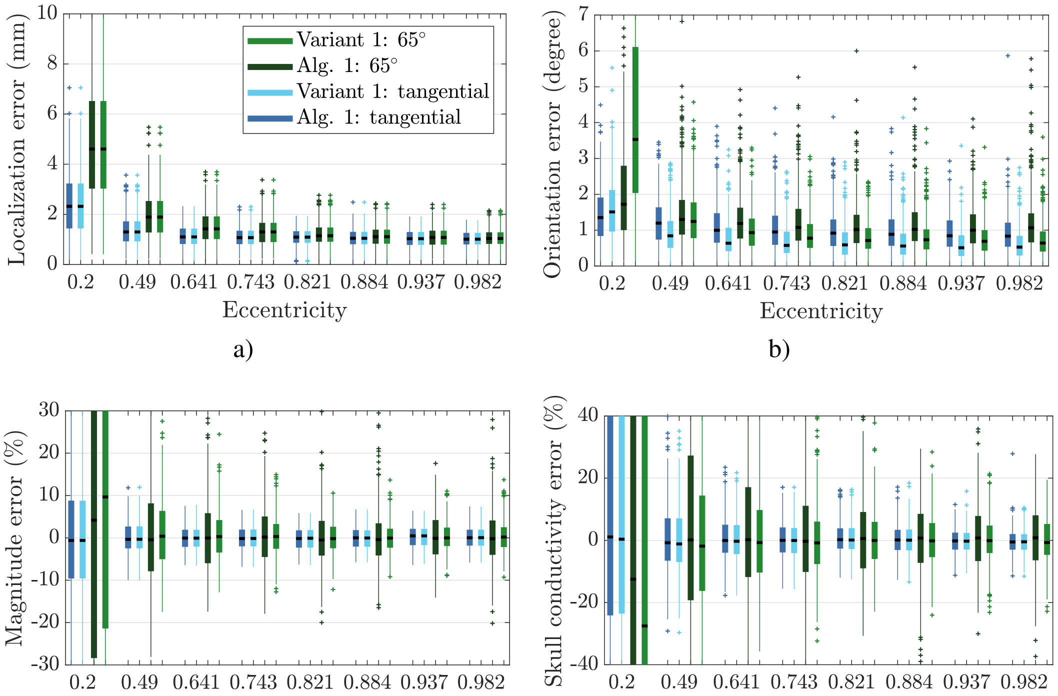

a) b)

c) d)

Figure 5.14.: Calibration results comparing Algorithm 1 with its Variant 1 in which the tangential orientation component is determined using MEG. Sources with a strength corresponding to EW stimulation are either tangentially oriented or rotated by 65° and Gaussian noise with realistic strength was added to the reference solutions. Source reconstruction errors with regard to a) localization, b) orientation and c) magnitude and d) skull conductivity errors are shown for test dipoles at different eccentricities plotted on a logarithmic scale. Boxplots show the 25th and 75th percentiles and the median.

gorithms and correspond to the results presented for different dipole orientations in Figure 5.10. Regarding the orientation errors, it can be observed that for the lowest eccentricity, Variant 1 results in higher errors than Algorithm 1. However, Algorithm 1 results in orientation errors of almost 180° for 27 source at this eccentricity for the more radial dipoles due to a negative fitted magnitude, while this effect cannot be observed for Variant 1. As dipole eccentricities increase, this trend reverses and for the most relevant eccentricity of 0.821, the orientation errors are 0.99° ± 0.58° (0.68° ± 0.47°) for Algorithm 1 (Variant 1) for tangential sources and 1.12° ± 0.68° (0.8° ± 0.45°) using Algorithm 1 (Variant 1) for sources with an elevation angle of 65°. For tangential sources, almost no difference in magnitude errors as well as skull conductivity errors can be observed between algorithms and the results are comparable to the ones presented in Figure 5.10. For the more radial dipoles (65°), however, magnitude errors shown in Figure 5.14c) are at 0.03% ± 6.52% (0.02% ± 3.82%) for Algorithm 1 (Variant 1) at an eccentricity of 0.821. Overall, the calibration procedure results in errors of 1.23% ± 14% (0.36% ± 8.96%) using Algorithm 1 (Variant 1) for the estimated skull conductivity at this eccentricity for dipoles with an elevation angle of 65° as presented in Figure 5.14d).

In a second comparison, Variant 2 was applied which minimizes the RV to the combined EEG/MEG reference data instead of only taking the EEG signal into account for the computation of the goal function. For a set of test dipoles which are either tangentially oriented or radially rotated by 65°, the calibration results using Variant 2 are presented in Figure 5.15. In order to allow this combined analysis of both modalities, the data sets were transformed to a comparable value range by means of an SNR transformation using the signal noise in the prestimulus interval as described in more detail in Section 5.2.1. Overall, the dipole reconstruction and skull conductivity estimation errors are in a comparable range for both Algorithm 1 and Variant 2. As the same noise vectors were added for both calibration algorithms, no difference in localization errors can be observed. For an eccentricity of 0.821, orientation errors only slightly differ, with errors of 2.92° ± 1.51° (2.9° ± 1.55°) for tangential and 3.36° ± 1.89° (3.13° ± 1.79°) for the more radial dipoles for Algorithm 1 (Variant 2). Magnitude errors are at -0.09% ± 3.54% (-0.07% ± 3.55%) for tangential and 0.86% ± 14.66% (0.94% ± 14.32%) for rotated dipoles using Algorithm 1 (Variant 2). The skull conductivity estimation errors are at 0.63% ± 10.14% (2.7% ± 20.06%) for tangential and 5.65% ± 32.05% (5.56% ± 36.13%) for dipoles elevated by 65° for Algorithm 1 (Variant 2). A negative magnitude, thus a flipped orientation, results for one dipole (tangential) and 130 dipoles (65°) at an eccentricity of 0.2 and for 2 dipoles (65°) at an eccentricity of 0.49, for both versions of the calibration algorithm.

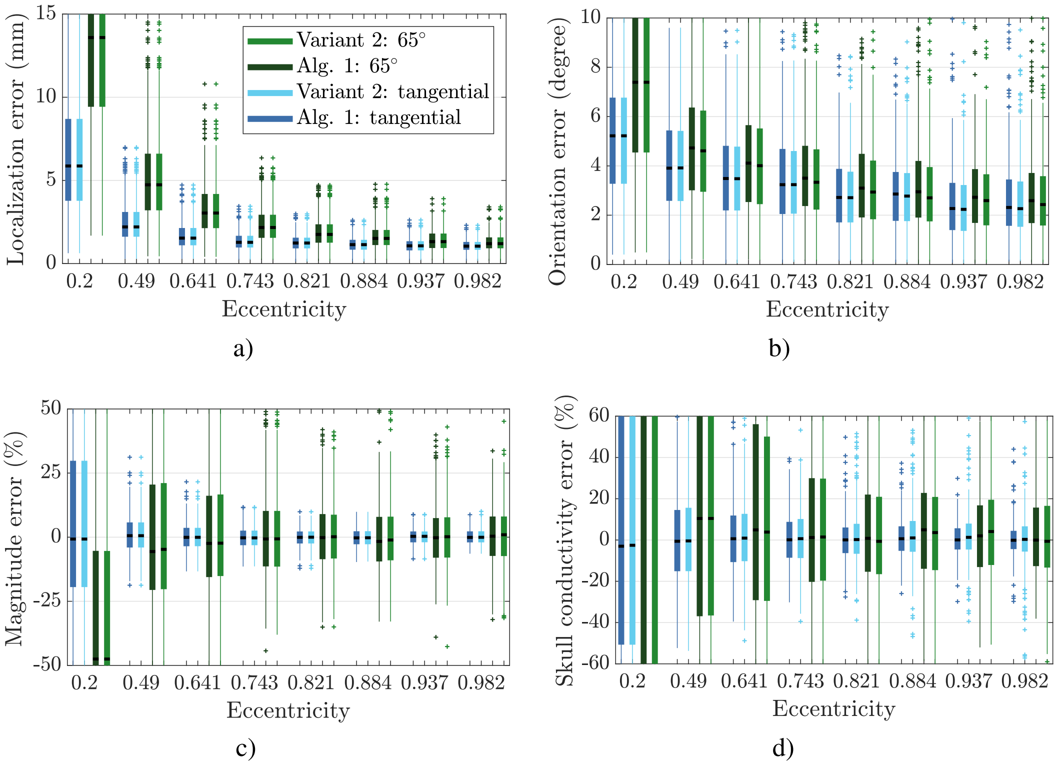

a) b) c) d)

Figure 5.15.: Calibration results comparing Algorithm 1 with its Variant 2 which minimizes the RV to the combined EEG/MEG reference data. Sources with a strength corresponding to EW stimulation are either tangentially oriented or rotated by 65° and prestimulus noise was added to the reference solutions. Data sets were scaled using noise estimations from realistic prestimulus intervals to combine both modalities. Source reconstruction errors with regard to a) localization, b) orientation and c) magnitude and d) skull conductivity errors are shown for test dipoles at different eccentricities plotted on a logarithmic scale. Boxplots show the 25th and 75th percentiles and the median.

Numerical forward solutions

Previously, the (quasi-)analytical EEG and MEG forward solutions were used in the calibration procedure. In this scenario, numerical CG-FEM forward solutions were used for the leadfield computation in the calibration algorithm.

In a first analysis, different source models, i.e., the partial integration, the St. Venant and the subtraction approach are used within the same tetrahedral mesh ($\text{tet}_{52\text{k}}$) for a subset of 100 dipoles at each eccentricity. A source grid with a resolution of 4 mm was used, resulting in a mean distance of 1.9 mm between each dipole and the closest source space node. The results of this comparison are shown in Figure 5.16. Overall, localization and magnitude errors are at a similarly low range for all source models with small differences only for the most extreme eccentricities. The partial integration approach tends to result in higher errors, especially regarding the orientation and skull estimation errors. The errors using the subtraction and the St. Venant approach are in a comparable range for most eccentricities, except that the subtraction approach performed best for the deepest sources, while the opposite holds for the most eccentric sources investigated. At the most relevant eccentricity of 0.821 regarding the P20/N20 source depth, localization errors are at 1.99 mm ± 0.74

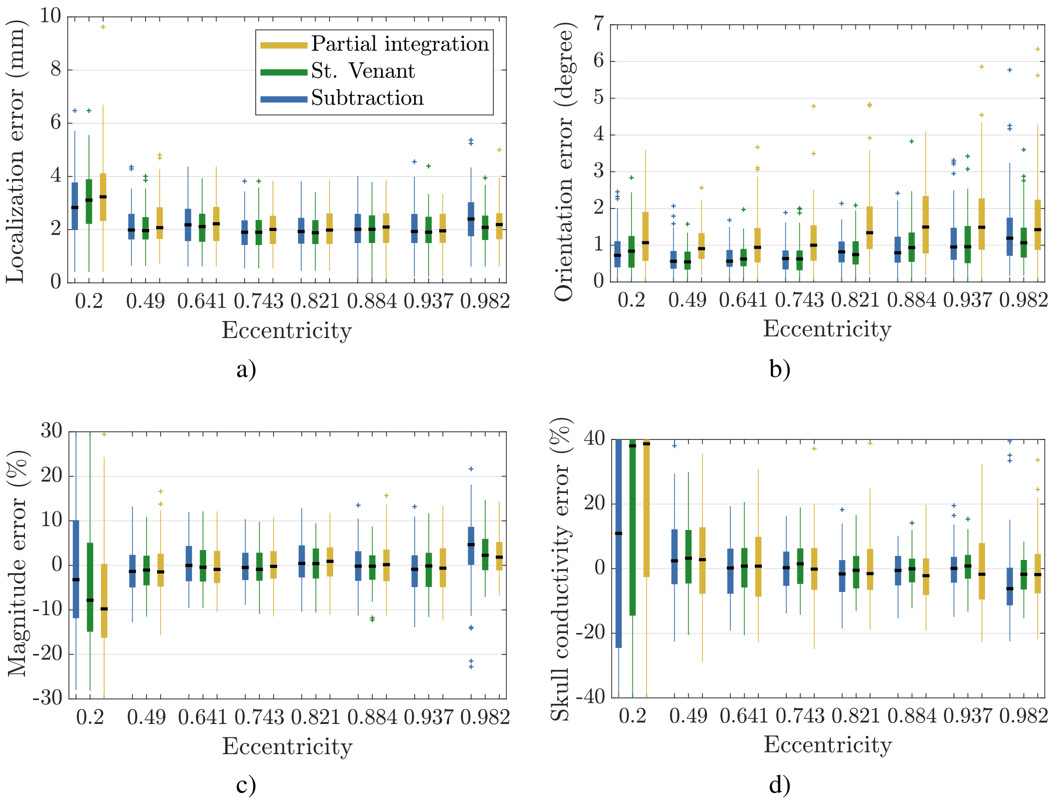

a) b) c) d)

Figure 5.16.: Calibration results for different numerical source models: Partial integration, St. Venant and subtraction approach. The tetrahedral mesh tet$_{52\text{k}}$ was used for the CG-FEM forward computations. The source grid for the single dipole deviation scan had a resolution of 4 mm. Sources with a strength corresponding to EW stimulation were tangentially oriented, no noise was added to the reference solutions. Source reconstruction errors with regard to a) localization, b) orientation and c) magnitude and d) skull conductivity errors are shown for 100 test dipoles at different eccentricities plotted on a logarithmic scale. Boxplots show the 25th and 75th percentiles and the median.

mm (subtraction), 1.91 mm ± 0.65 mm (St. Venant) and 2.06 mm ± 0.78 mm (partial integration). Orientation errors of 0.81° ± 0.43° (subtraction), 0.81° ± 0.46° (St. Venant) and 1.53° ± 0.9° (partial integration) and magnitude errors of 0.71% ± 5.01% (subtraction), 0.36% ± 4.62% (St. Venant) and 0.87% ± 4.98% (partial integration) can be observed at this eccentricity. The overall reconstructed skull conductivity errors are at $-1.8\% \pm 7.19\%$ (subtraction), $-0.79\% \pm 6.7\%$ (St. Venant) and $-0.23\% \pm 9.6\%$ (partial integration).

In a second comparison, different tetrahedral and hexahedral meshes with varying degrees of freedom were used for the FEM forward computations. The St. Venant source model was

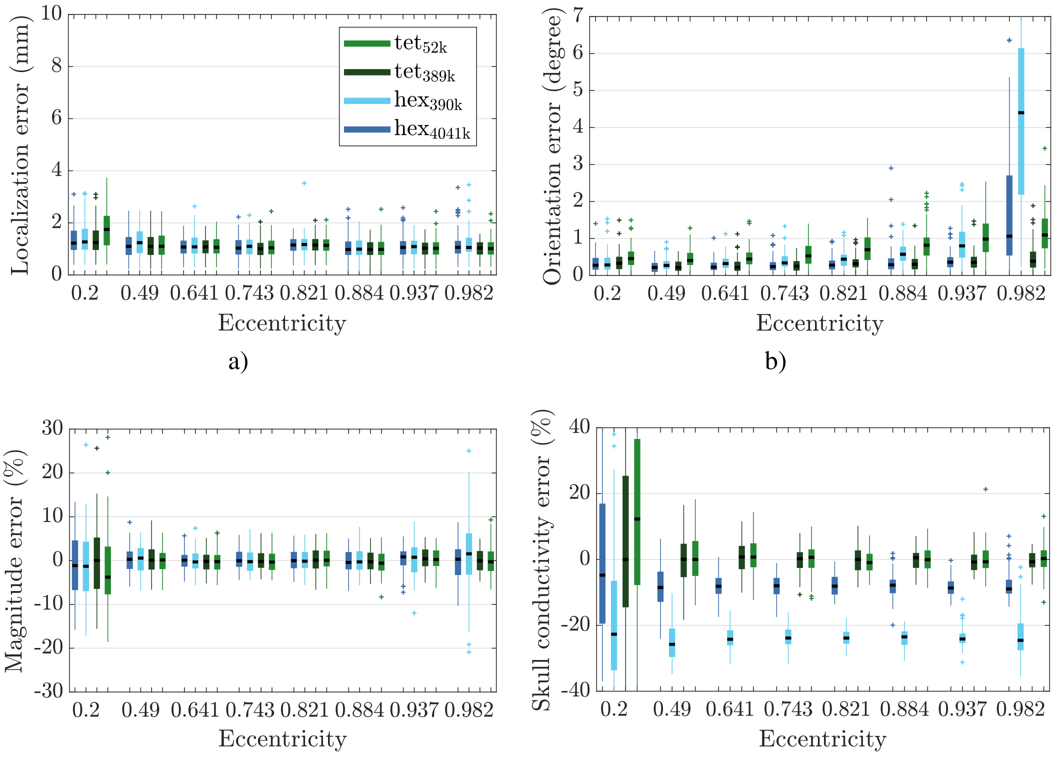

a)

b)

c)

d)

Figure 5.17.: Calibration results using different FEM meshes (tet$_{52k}$, tet$_{389k}$, hex$_{390k}$, hex$_{3041k}$) for the numerical computation of the EEG/MEG forward solutions in combination with the St. Venant source model. Sources with a strength corresponding to EW stimulation were tangentially oriented, no noise was added to the reference solutions. Source reconstruction errors with regard to a) localization, b) orientation and c) magnitude and d) skull conductivity errors are shown for 100 test dipoles at different eccentricities plotted on a logarithmic scale. Boxplots show the 25th and 75th percentiles and the median.

employed to discretize the source term and for the MEG single dipole deviation scan, a regular source grid with a 2 mm resolution was used, as described in more details in Section 5.2.1. The results of the calibration are shown in Figure 5.17.

Overall, localization and magnitude errors are at a similarly low range for all meshes with minor differences especially for the deepest and most eccentric sources. Orientation errors increase for more eccentric sources and tend to be higher for coarser meshes and hexahedral meshes when comparing the number of degrees of freedom. At an eccentricity of 0.821, orientation errors are at 0.3° ± 0.17° ($\text{hex}_{3041\text{k}}$), 0.44° ± 0.24° ($\text{hex}_{390\text{k}}$), 0.34° ± 0.19° ($\text{tet}_{389\text{k}}$) and 0.73° ± 0.38° ($\text{tet}_{52\text{k}}$). The skull conductivity errors are centered around zero for the tetrahedral meshes, while a negative shift can be observed at all eccentricities for the hexahedral meshes, especially for the coarser mesh $\text{hex}_{390\text{k}}$. These errors are at $-7.89\% \pm 3.37\%$ ($\text{hex}_{3041\text{k}}$), $-23.82\% \pm 2.61\%$ ($\text{hex}_{390\text{k}}$), $-0.06\% \pm 3.62\%$ ($\text{tet}_{389\text{k}}$) and $-0.66\% \pm 3.62\%$ ($\text{tet}_{52\text{k}}$) at the most relevant eccentricity.

5.2.3. Discussion

The aim of this study was to apply the calibration algorithm presented in Chapter 4 in a simplified spherical head volume conductor model where (quasi-)analytical solutions for the EEG and MEG forward problems exist. In this well-controlled setup, the algorithm can be tested without interference from numerical errors which are inevitable when using realistic head models. The accuracy of the calibration algorithm was tested under different conditions that simulate realistic scenarios.

In a preparatory study, example calibration curves of the goal function in Step 1 of Algorithm 1 indicated unimodal calibration curves that have a higher gradient for more superficial sources. In order to converge to the correct skull conductivity value with an accuracy defined by the given tolerance of $\varepsilon = 10^{-5}$ S/m, the algorithm required only approximately 9 iterations.

In the following, three test cases were presented based on Schrader et al. (2020). In a first scenario, source strengths related to three types of somatosensory experiments were compared. Noise with realistic strength was added to the reference solutions, either in the form of white Gaussian noise or prestimulus signals. The results presented in Figures 5.8 and 5.9 in Section 5.2.2 indicate that overall, the skull conductivity and dipole characteristics can be reliably reconstructed for sources resembling the generator of the somatosensory P20/N20 response. Based on dipole strengths reconstructed in Antonakakis et al. (2019), the best results were achieved when using the stimulation type related to the highest SNR (EW), followed by BT stimulation. When using dipole strengths related to EW stimulation, as well as tangential sources at an eccentricity of 0.821 which approximately corresponds to the P20/N20 source depth, the resulting mean estimated skull conductivity errors were at 0.06% ± 5.4% (EW) when white Gaussian noise was used. When using prestimulus noise, these observed errors were slightly higher at 0.5% ± 10.9%, even though the same mean standard deviation per channel was used. Possible reasons might be related to the filter settings or could result from the high stimulation rate that could lead to a correlation of the prestimulus signals at the sensor level as the previous trial could still be processed in the somatosensory network even after the next trial already started. The time-locked averaged data could therefore contain weak signals in the time period before the trigger that originate from later components of the somatosensory response of the previous trial. Further somatosensory experiments may be required in order to optimize these experimental parameters. The best tradeoff between a high stimulation rate that increases the number of trials and results in a clear P20/N20 topography with a high SNR, and a prestimulus interval with minimal correlated noise from the previous trial has to be found.

In a second scenario presented in Figure 5.10 in Section 5.2.2, the source orientation was varied to examine the effect of radial components of different strengths. White Gaussian noise with a realistic strength was added to the reference solutions. As the MEG is unaffected by radial components in the spherical test case, an increased radial orientation component is equivalent to reducing the strength of the dipole for this modality, as only the tangential component influences the forward solution. Similar to the previous scenario, the localization and magnitude errors, which are related to the MEG signal, were nearly constant for more eccentric sources and increase for deeper sources, as well as for more radial dipoles. This is due to the sensor level noise, as especially deeper sources which produce a smaller surface signal, are harder to detect. In addition, the 2 mm resolution of the source space created a lower bound for the localization errors, as the mean distance to the closest source space node was 0.97 mm to avoid an inverse crime (Kaipio and Somersalo, 2005). The results show that tangential sources led to the lowest errors, although sources radially rotated by 25° only produced slightly higher errors for the skull conductivity and dipole characteristics.

In a third investigation, the influence of wrongly assigned scalp conductivity was analyzed without adding artificial noise, the results were summarized in Figures 5.11 and 5.12. The low dipole reconstruction errors are mainly due to the source space resolution and increasing numerical errors for the computation of the pseudo-inverse of the MEG leadfield matrix for deeper sources. There are no localization error differences between conditions, as the MEG is unaffected by the conductive profile in the multi-layer sphere model. In contrast to the dipole reconstruction errors, high skull conductivity errors can be observed.

However, when performing an EEG single dipole deviation scan while the reference scalp conductivity is either under- or overestimated, the results show that the dipole localization errors are largely diminished when using the fitted skull conductivity instead of the standard value. Thereby, the fitted skull conductivity largely counterbalances the effect of the wrong assumption on scalp conductivity. The opposite effect of scalp and skull conductivity on source localization, especially on source depth, has also been emphasized in Vorwerk et al. (2019a). This scenario illustrates that only one free parameter, namely the most influential skull conductivity parameter, is fitted in our calibration procedure. However, the other conductivity values also indirectly affect the procedure. Skull conductivity is not physically measured, but this parameter is fitted in a way that in combination with the other assumed conductivities the data is best explained.

Following these investigations, the calibration was performed using the two variants of the algorithm and the results were compared to the output of the standard algorithm. Using Variant 1, which fits the tangential orientation component using MEG reference data, led to similar results for tangential sources and slightly smaller errors for more radial test dipoles. Note that noise with realistic strength was added in this scenario, which resulted in a better SNR for MEG than for EEG for most eccentricities, as shown, e.g., in Figure 5.8. Therefore, the SNR of both modalities could potentially be used as an indicator of which modality is more reliable with regard to fitting the tangential orientation component. When Variant 2 was used for the calibration procedure, which minimizes the RV with respect to the combined EEG/MEG reference data, almost no differences in the dipole reconstruction and skull conductivity estimation errors could be observed. Notably, the calibration curves tended to be more flat when using this variant, indicating that the goal function evaluations showed fewer variations for MEG.

In the subsequent investigation, numerical forward solutions were used in the calibration procedure instead of the (quasi-)analytical expressions. In one comparison, different source modeling approaches, i.e., the partial integration, the St. Venant and the subtraction model, were used to discretize the source and assemble the right-hand side vector in the FEM computations. Regarding the accuracy of the calibration algorithm, the partial integration approach resulted in slightly higher errors, while the St. Venant and the subtraction approach yielded similar errors for dipole eccentricities of interest. An important additional factor are computation times, which were approximately 80 times higher for the subtraction approach for the entire calibration process compared to the other two methods. The most expensive component was the computation of the MEG leadfield for the source grid nodes which needs to be computed for the MEG single dipole deviation scans and is unrelated to the number of test dipoles. As a result, the St. Venant approach seems to offer the best compromise between accuracy and feasibility, which is in accordance with other investigations (Lew et al., 2009b; Vorwerk et al., 2014; Wolters et al., 2007b). This source model was therefore also used in the following chapter for the calibration of realistic head models. The localized variation of the subtraction approach could significantly reduce the computational burden of this source model and potentially offer a feasible alternative to the St. Venant approach (Lange, 2021; Nüßing, 2018). In a second comparison, different tetrahedral and hexahedral meshes were used for the FEM forward solutions. In general, the results indicate that the tetrahedral meshes were able to accurately reconstruct the dipole characteristics and the skull conductivity. Only small differences in skull conductivity errors between the coarser and the finer tetrahedral meshes could be observed, indicating that both grids can accurately model the spherical surfaces. Skull conductivity was systematically underestimated using hexahedral meshes, especially for the coarser mesh hex_{390}. In addition to the difficulty of modeling the curvature of a spherical model using hexahedrons even with a node-shift of vertices on the boundaries, this is probably due to the difficulty of representing the 2 mm thin CSF layer by hexahedrons with an edge length of 2 mm. In total, 10 128 nodes of the mesh hex_{390} mesh belonged to both elements labeled as skull as well as brain. In CG-FEM, the Lagrangian shape functions span all neighboring elements and thereby allow the current to flow through a single vertex. These physically unreasonable *leakage effects* in EEG through these points have been investigated mainly in the context of skull leakages and could be prevented using DG-FEM (Engwer et al., 2017; Vorwerk, 2016). In the finer mesh hex_{4041}, this effect of an underestimated skull conductivity is largely alleviated. Additionally, these results resemble the skull conductivity estimation results using wrong assumptions of scalp conductivity, therefore it might be interesting to investigate if the calibrated skull conductivities result in lower source reconstruction errors when compared to standard values as well.

This study was intended to apply the presented calibration algorithm in a controlled spherical head volume conductor model and quantify the errors for different realistic source and noise scenarios. In the following chapter, the algorithm will be applied to experimentally measured SEP/SEF data sets and realistic head volume conductor models.

6. Application in realistic head models

In this chapter, the algorithm is applied to calibrate realistic head volume conductor models using experimentally measured P20/N20 topographies of SEP/SEF data sets. The aim is to bring the calibration pipeline closer to realistic applications and investigate the impact of specific processing steps and parameter choices in this setting.

Compared to the previous investigations in controlled spherical head volume conductor models, several changes apply. One important aspect is the utilization of experimentally measured SEP/SEF data sets. These signals need to be preprocessed to reduce artifacts and yield clear P20/N20 topographies with a high SNR. Additionally, the sensors of the SEP/SEF data acquisition need to be registered to the discretized head model.

Another major difference is the application to individually segmented, realistically shaped head volume conductor models. They distinguish up to six different tissue types, including skull spongiosa for an accurate modeling of the inhomogeneous skull tissue, and account for white matter anisotropy. These complex head models have been suggested in order to accurately model the head characteristics for an improved accuracy in source analysis (McCann and Beltrachini, 2021; Ollikainen et al., 1999; Ramon et al., 2004; Vorwerk et al., 2014). Using realistically shaped head models as opposed to spherical models has two major implications. First, there are no (quasi-)analytical EEG and MEG solutions available for realistically shaped volume conductor models and therefore, the forward solutions need to be computed numerically. Various methods have been proposed to accurately solve the EEG and MEG forward problems and model the source term (Azizollahi et al., 2018; Beltrachini, 2019; Cuartas Morales et al., 2019; Montes-Restrepo et al., 2014; Piastra et al., 2018), see Chapter 3 for an overview of the FEM discretization and different source modeling approaches that are used in this work. Second, an important difference compared to spherical models is that the MEG solution is not independent of the head tissue conductivities in realistically shaped head models. However, their influence on MEG forward solutions is mainly restricted to the conductivity profile in the vicinity of the source (Haueisen et al., 1997). Skull (and scalp) conductivities, however, which are the most influential parameters for the EEG forward solutions (Vorwerk et al., 2019a), only have a small impact on the MEG solution in a realistic head model (Brette and Destexhe, 2012;

Haueisen et al., 1997; Lew et al., 2013). However, it has been suggested to model skull defects such as post-surgical burr holes for an improved MEG forward and inverse analysis (Lau et al., 2016).

For layered spherical models of the head, the importance of skull conductivity on EEG forward solutions was emphasized in Section 5.1. Regarding realistic head models, this effect is visualized in Figure 6.1 using an exemplary data set. Simulated EEG and MEG topographies for an approximately tangentially oriented dipole in a six-compartment realistic head model are shown for different skull conductivities. The MEG topographies (top) are nearly identical when using skull conductivities of 0.02 S/m as shown in Figure 6.1a), and 0.002 S/m, see Figure 6.1b). The EEG (bottom) topographies for the same volume conductor models, however, are largely influenced by different skull conductivities. The scalp potential is overall higher and the peak and trough are closer to each other when using a skull conductivity of 0.02 S/m, see Figure 6.1c), compared to the EEG signal when using a skull conductivity of 0.002 S/m as shown in Figure 6.1d). This insensitivity of MEG to skull conductivity justifies the use of a single dipole deviation scan with standard conductivities to determine the P20/N20 source location as opposed to repeating this computationally expensive step for every iterative skull conductivity value in the calibration procedure.

This chapter is organized as follows. First, the methodology is described in Section 6.1. This includes information about data acquisition and processing as well as details on the calibration procedure. In Section 6.2, the results of the calibration procedure using realistic data sets are presented. Various scenarios, such as different forward modeling approaches and reference data choices, are investigated and compared. Third, these findings are discussed in Section 6.3.

6.1. Materials and Methods

In this section, the real data sets and analysis steps which were performed to apply the calibration procedure are presented. In Section 6.1.1, details on the experimental setup and measurements are presented. Subsequently, Section 6.1.2 contains information about the preprocessing steps for the SEP/SEF data, the characteristics of the realistic head volume conductor models and provides further details on the calibration steps.

6.1.1. Data acquisition

This analysis is based on simultaneous EEG/MEG data as well as MRI measurements that were recorded of five (including three male) right-handed healthy participants aged $32.4 \pm$

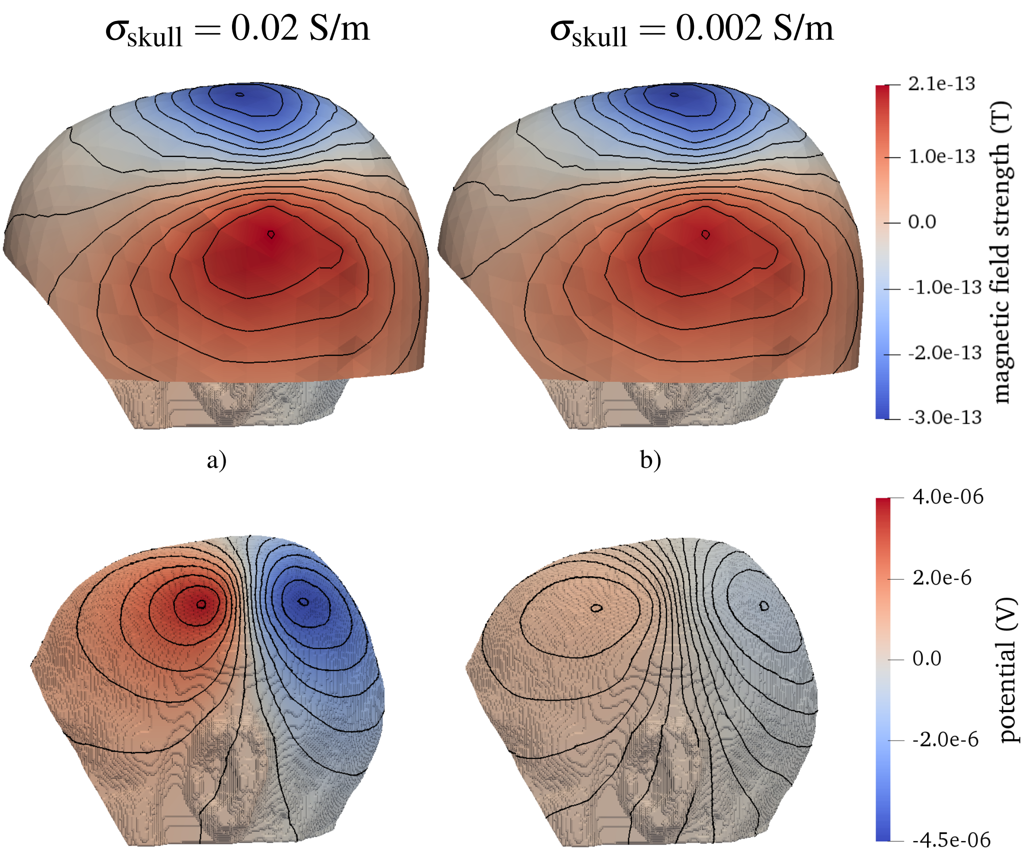

a) b)

c) d)

Figure 6.1.: Simulated MEG (top) and EEG (bottom) topographies for skull conductivities of 0.02 S/m (left) and 0.002 S/m (right) resulting from an approximately tangentially oriented source with 20 nAm strength in a six-compartment realistic isotropic head volume conductor model, using standard conductivities for the other tissues. The MEG topographies were interpolated from 777 quasi-radially measuring magnetometer signals, the electric potential was computed on a node-shifted hexahedral mesh with 1 mm edge length. FEM forward solutions were computed with the DUNEuro toolbox using the St. Venant source model. Subfigures c) and d) are published in a similar form in Gross et al. (2021).

9.5 years. All volunteers had given written informed consent prior to the experiment and the measurements had been approved by the ethics committee of the University of Erlangen, Faculty of Medicine on 10.05.2011 (Ref. No. 4453).

Somatosensory evoked responses were recorded using simultaneous EEG/MEG. The EEG signals were measured using a 10–10 system (EASYCAP GmbH, Herrsching, Germany) and the electrode positions on the head were digitized using a Polhemus device (FASTRAK, Polhemus Incorporated, Colchester, Vermont, USA). MEG was recorded using a whole-head system with 275 axial gradiometers and 29 reference coils (CTF, VSM MedTech Ltd., Vancouver, Canada).

Three types of somatosensory experiments were conducted using different stimuli. First, the median nerve was electrically stimulated at the right wrist using a square pulse stimulator (Astro-Med, Inc., Grass Instrument Division, West Warwick, USA), referred to as electric-wrist (EW) stimulation. This type of stimulus activates a mixture of afferent and efferent fibers and is often used due to its high SNR (Buchner et al., 1994; Nevalainen et al., 2014; Okada et al., 1996; Theuvenet et al., 2005). Experimentally, this stimulation was performed with monophasic square-wave electrical pulses with 5 ms duration. The strength of the stimuli was manually adjusted to have the minimal amplitude still evoking a movement of the thumb.

In the other two somatosensory experiments tactile stimuli were applied to the distal phalanx of the right index finger using two different devices. In general, these more natural stimuli primarily activate slowly responding mechanoreceptors in the skin and lead to lower signal strengths and longer latencies when compared to EW stimulation (Mertens and Lütkenhöner, 2000; Nevalainen et al., 2014; Rossini et al., 1996). One tactile stimulus was a balloon membrane (Custom production: *Elektro- und Feinmechanische Werkstätten der Medizinischen Fakultät*, University of Münster, Münster, Germany), which was fixed to the index finger using a plastic clip and expanded using air blasts (Mertens and Lütkenhöner, 2000; Rossini et al., 1996). This stimulation type is abbreviated as pneumato-tactile (PT) stimulation. The other tactile stimulus was a Braille stimulator (metec AG, Stuttgart, Germany), of which four of the eight small plastic pins were elevated and pressed against the index finger (Onishi et al., 2010; Schubert et al., 2008). This stimulus type is referred to as Braille-tactile (BT) stimulation. In both of these two tactile experimental setups, pink noise was presented to the participants in order to avoid time-correlated artifacts in the auditory cortices due to the operating sounds of the stimulation devices.

The stimulus onset asynchrony (SOA) was randomly varied between 400–500 ms (EW; PT) and 600–700 ms (BT) which resulted in circa 1200 trials (EW; PT) and 880 trials (BT) during an approximately 9 min. long measurement interval for every condition. The signals were sampled at 1200 Hz and an online low-pass filter of 300 Hz was used.

In addition to these functional data sets, imaging data was recorded using a MAGNETOM Prisma 3 T device (Release D13, Siemens Medical Solutions, Erlangen, Germany). T1- and T2-weighted MRI as well as DTI-MRI for the estimation of white matter tissue anisotropy information were recorded. For details on the respective measurement sequences, see Antonakakis et al. (2019). During both functional and imaging data acquisition, markers were positioned on three head landmarks, i.e., left and right preauricular points and nasion, for registration purposes. Additionally, both measurement sessions were performed in supine position to reduce head movements. A consistent positioning of the head is also important to avoid possible brain shifts between supine and prone position, which can lead to large thickness differences of the CSF compartment as well as large resulting differences in EEG topography (Rice et al., 2013).

6.1.2. Analysis pipeline

In the following, the analysis steps for calibrating realistic head volume conductors using SEP/SEF data are described in more detail. This includes information about the preprocessing of the functional data sets, the realistic head volume conductor models and the application of the calibration algorithm.

Preprocessing of SEP/SEF data

The raw data were cut into epochs of $[-100$ ms, 200 ms$]$ around the trigger time point ($t = 0$ ms) identifying the stimulus onset. Additionally, the signals were filtered around the frequency spectrum of interest using a bandpass filter of 20–250 Hz (Buchner et al., 1994). A notch filter of 50 Hz and harmonics was used to eliminate power line noise. A semi-automatic artifact rejection was applied in order to clean the data. On average, 0.1 (MEG) and 3.7 (EEG) channels as well as 5.1 trials were rejected within each experimental condition. Afterwards, the averages of the signals over all trials were computed for each sensor in order to remove uncorrelated noise and see the event-related responses. The EEG data were re-referenced using the mean signal at the electrodes at each time point as a reference. For the computation of the SNR, prestimulus intervals of $[-100$ ms, -5 ms$]$ for EW and PT and $[-100$ ms, -15 ms$]$ for BT stimulation were used for the noise estimation. The time period directly before the stimulus onset was avoided due to potential interference of the stimulation artifact. As a measure of signal amplitude, the global mean field power (GMFP), i.e., the standard deviation of the sensor signals, was computed for each sampled time point (Esser et al., 2006; Lehmann and Skrandies, 1980). For the determination of the P20/N20 peak time point, $t = t_p$, the maximum of the GMFP of the SNR-transformed combined EEG/MEG data was determined for this component. The exact peak time point depends on many factors, ranging from subject-specific characteristics such as age or arm length to data processing parameters such as different filtering settings (Nevalainen et al., 2014; Stöhr et al., 2005). Different considerations need to be taken into account when choosing the time sample(s) of the reference data. On the one hand, the signal has the best SNR at the peak of the P20/N20 component, where the amplitude is the highest. On the other hand, it is important to define the best moment that captures the underlying source which is assumed to be of single dipolar nature (Allison et al., 1991; Nakamura et al., 1998). The signal should not contain weak contributions from earlier activated regions, e.g., contributions from thalamic activity (Götz et al., 2014; Rezaei et al., 2020; Stöhr et al., 2005). Similarly, the activation should not have propagated yet to cortical areas involved in the later somatosensory responses, in particular, Brodmann area 1 at the top of the postcentral gyrus, which is linked to the somatosensory activity following the P20/N20 component (Allison et al., 1991; Peterson et al., 1995; Stöhr et al., 2005). Therefore, different time points and time intervals were used for the computation of the reference data. Besides the peak time point $t = t_p$, its preceding time point $t = t_{p-1}$, and averages over two or three sampled time points including the peak time point were used. Note that due to the sampling rate of 1200 Hz, the span between two successive recorded time points is $\triangle t \approx 0.83$ ms. All preprocessing steps were carried out in FieldTrip (Oostenveld et al., 2011), see also Chapter 8 for more details on software-related aspects.

Head volume conductor models

From MRI data, individually segmented realistic six-compartment volume conductor models with white matter anisotropy tensors were constructed. The tissue types of scalp, skull compacta, skull spongiosa, CSF, gray matter and white matter were distinguished. This segmentation and meshing process was not performed as part of this work, the head models in combination with the registered sensor positions, the anisotropic tensors and the source space grid within the gray matter compartment was obtained from Antonakakis et al. (2019), which contains further details on their construction. Geometry-adapted hexahedral FEM meshes were used with a resolution of 1 mm and a node-shift parameter of 0.3 in order to reduce staircase effects (Camacho et al., 1997; Wolters et al., 2007a). On average, they consisted of 3 487 282 nodes and 3 396 950 elements (Antonakakis et al., 2019). The source grids with a resolution of 2 mm contained on average 16 757 possible dipole locations in the gray matter.

The following standard conductivity values were used for the MEG forward solutions in the single dipole deviation scan and for the tissues other than skull (compacta) for the EEG forward solutions within the optimization process. For the six-compartment models, values of 0.0042 (skull compacta) and 0.01512 S/m (skull spongiosa) were used for the skull compartment (Antonakakis et al., 2019; Aydin et al., 2014; Buchner et al., 1997; Fuchs et al., 1998), which corresponds to a ratio of 3.6 (Akhtari et al., 2002). For the other tissue types, standard values of 0.43 (scalp), 1.79 S/m (CSF) and 0.33 S/m (gray matter) were used (Aydin et al., 2014; Baumann et al., 1997; Vorwerk et al., 2014). Regarding white matter conductivity, either an isotropic standard value of 0.14 S/m was used (Antonakakis et al., 2019; Ramon et al., 2004; Vorwerk et al., 2014), or anisotropic voxel-based values inferred from DTI measurements were used which were scaled to match the isotropic values using the effective medium approach (Rullmann et al., 2009; Tuch et al., 2001). For the three-compartment models used in one of the comparisons, in addition to the scalp tissue, skull spongiosa and compacta were homogenized to a single skull compartment with a standard conductivity of 0.01 S/m and the inner tissues were simplified to a homogenized brain compartment with standard conductivity of 0.33 S/m (Aydin et al., 2014; Vorwerk et al., 2014).

Calibration procedure

After these preprocessing steps, the realistic head models were calibrated using the procedure and the same range for possible skull conductivity values as described in Chapter 4. In the six-compartment models, the skull compacta conductivity was fitted, while the ratio to skull spongiosa conductivity remained unchanged. As reference data $\mathbf{m}_{\text{MEG}}$ and $\mathbf{m}_{\text{EEG}}$, the measured MEG and EEG P20/N20 peak signals were used, which were preprocessed as described in the beginning of this section to clean the data of artifacts and produce the best possible SNR. In most scenarios, the EW stimulation data sets were used due to their high SNR. In Antonakakis et al. (2019), EW stimulation data sets were used to calibrate head models, which were then used for source analysis using the BT and PT data sets. In one comparison study in this work, BT and PT data sets were used directly for the calibration procedure. For the leadfield computations l_{MEG} and l_{EEG}, a CG-FEM discretization as described in Chapter 3 was used. As source modeling approaches, the St. Venant source model was typically chosen based on the comparison of accuracy and computational cost using spherical models (Chapter 5), except for one comparison in which the partial integration approach was also applied. Due to the high computational costs of the subtraction approach and because the results were not substantially improved, this source model was not taken into account here.

As already discussed in detail in Chapter 4, MEG is insensitive to skull conductivity in the realistic case, therefore Step 1 in Algorithm 1 was only computed once for the standard conductivities and not within the loop in Step 2 in order to minimize computational costs. For the computation of the MEG leadfield for the entire source grid nodes in all

Cartesian directions, the more efficient transfer matrix approach (see Section 3.4) was used (Wolters et al., 2004). Once the source location was fixed in Step 1 of Algorithm 1, the EEG leadfield was only computed for this specific location. Therefore, the potential could be computed faster by directly solving the linear system of the FEM discretization instead of using the transfer matrix approach. For the parameters regarding the source models and the calibration algorithm, the same values were chosen as in the numerical study in Chapter 5.

All computations were performed in MATLAB (The MathWorks Inc., Natick, Massachusetts, USA), using the FieldTrip toolbox for the realistic data processing and the MATLAB interface of DUNEuro for the EEG and MEG forward computations, see Chapter 8 for more details.

6.2. Results

In the following, the results of the calibration procedure using realistic head volume conductor models and SEP/SEF data sets are summarized and the effects of several parameters on the calibration are investigated. In Section 6.2.1, the choice of reference data for the calibration procedure is investigated, including the impact of SNR transformations. Next, Section 6.2.2 presents the calibration results in case different somatosensory experiments are used for the acquisition of P20/N20 data sets. Section 6.2.3 then summarizes the calibration results for different head volume conductor models and in Section 6.2.4 different source modeling approaches are used. Finally, the two variants of the algorithm as presented in Chapter 4 are compared in Section 6.2.5.

6.2.1. Choice of reference data

An important aspect of the calibration pipeline is the preprocessing of the functional SEP/SEF data, e.g., the choice of filtering, the channel selection and the trial rejection due to artifacts. This section focuses on two particular aspects of data processing and their effects on the calibration result. First, the influence of applying SNR transformations for the EEG and MEG data is investigated. Second, the choice of the time point or interval, which is chosen as the optimal representation of the activity underlying the P20/N20 component, is analyzed.

Influence of SNR transformation

In general, SNR transformations emphasize the relative importance of signals measured by those sensors which are least affected by noise and are commonly used to combine modalities, see Section 3.4. For an exemplary data set, the effect on an SNR transformation is visualized in Figure 6.2. At the top, Figure 6.2a) shows the GMFP of single modality EEG and MEG for the time window [−20 ms, 70 ms]. This includes the stimulation onset which is followed by a stimulation artifact and the early somatosensory evoked responses. In Figure 6.2b), the GMFP computed for the SNR-transformed data of both modalities is shown. Additionally, the GMFP of the combined data is depicted which is used for the determination of the peak time point of the P20/N20 response.

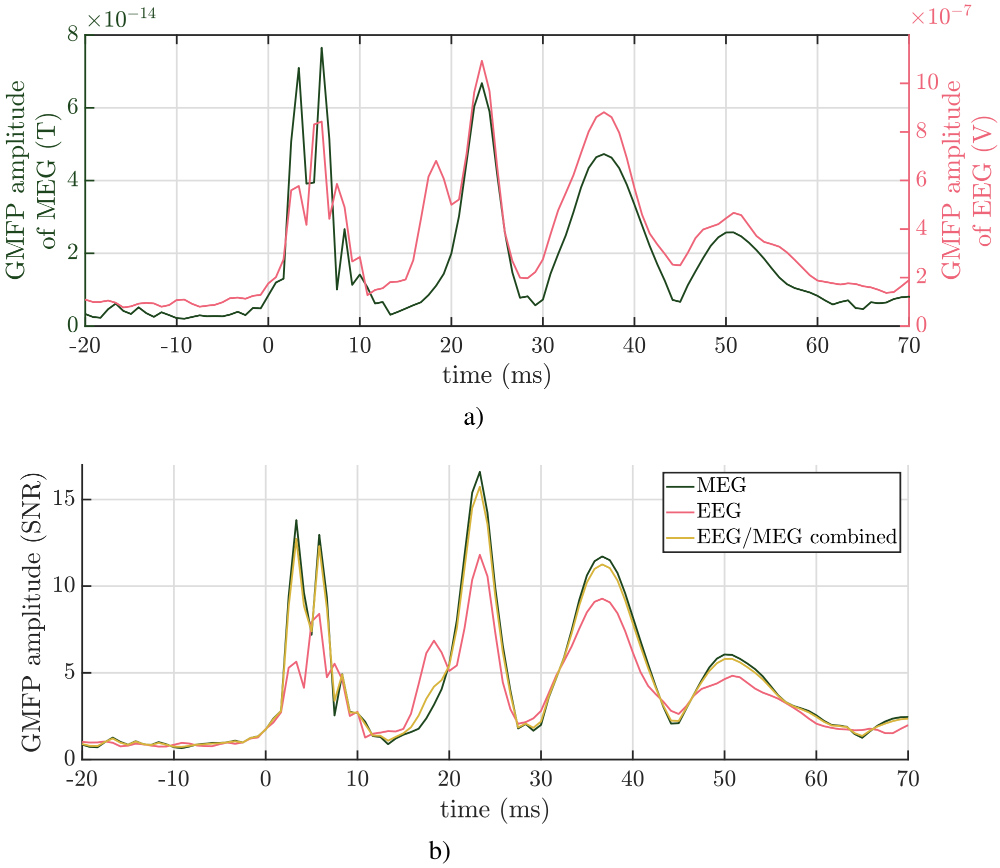

a)

b)

Figure 6.2.: Global mean field power (GMFP) of a) preprocessed averaged EEG and MEG data without SNR transformation and b) SNR-transformed EEG, MEG and combined data for an exemplary data set shown for the time window [−20 ms, 70 ms] around the stimulus onset ($t = 0$ ms).

Except for using Variant 2 which requires the combination of EEG and MEG data, an SNR transformation is not necessary for the calibration pipeline, as every individual step of Algorithm 1 is performed using single modality data. In order to investigate the effect of SNR transformations, the calibration pipeline was applied to five realistic data sets with EW stimulation using reference data and leadfields that were either transformed using the noise estimation of the prestimulus interval as described in Section 6.1.2 or the original data associated with physical units were used. The resulting calibration curves and the estimated skull conductivity values are shown in Figure 6.3. Using SNR-transformed data yielded fitted skull conductivity values of 3.05 mS/m ± 1.08 mS/m with mean minimal RV values of 5.57% ± 2.2%. Compared to these results, the minimal RV was higher for four of the five subjects in case the data was not SNR-transformed, with mean differences of -0.19 mS/m ± 0.16 mS/m for the fitted skull conductivity and 1.77% ± 2.85% for the RV.

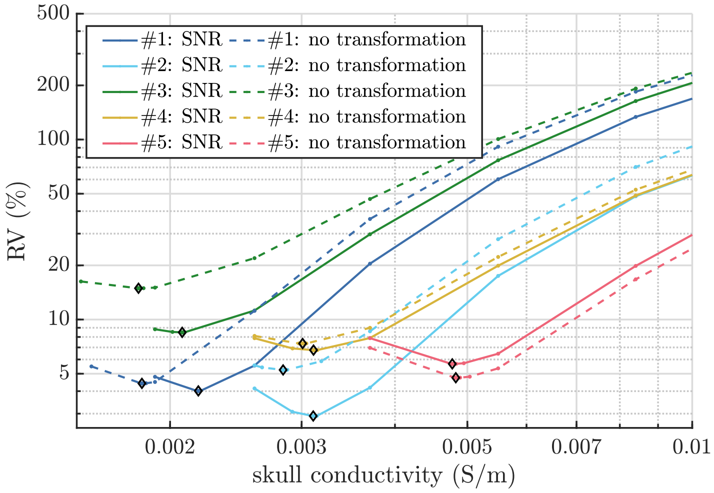

Figure 6.3.: Influence of SNR transformations on calibration results using EW stimulation data sets of five subjects. Reference EEG/MEG data of the P20/N20 peak and leadfields are either transformed to SNR (dashed lines) or not (solid lines). The results are plotted on a logarithmic scale, minimum values are highlighted in black. An anisotropic realistic six-compartment head model was used in combination with the St. Venant source model for the FEM forward computations.

In the remainder of this chapter, SNR transformations will be used for the measured data sets and numerically computed leadfields. The calibration results of the SNR-transformed data sets presented here will be used as a reference to report the effects of differing various parameters in the calibration pipeline.

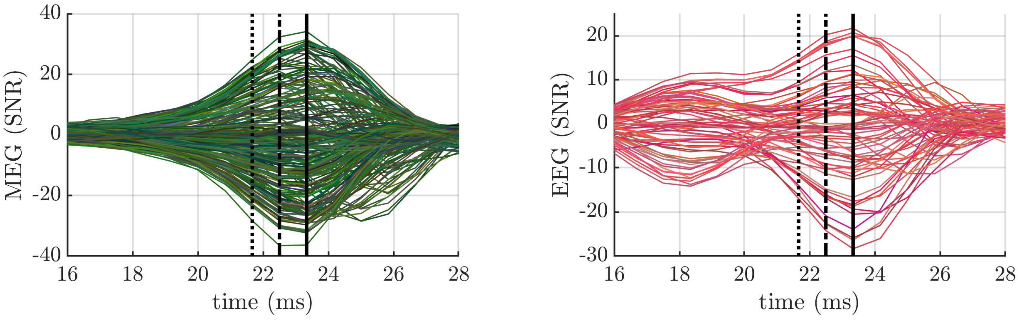

a)

b)

Figure 6.4.: SNR-transformed a) MEG and b) EEG butterfly plots of the P20/N20 component of an exemplary EW stimulation data set. The peak, i.e., $t = t_p$ (solid line) and the two preceding sampled time points $t = t_{p-1}$ (dashed) and $t = t_{p-2}$ (dotted) are marked.

Timing of reference data

In order to investigate the impact of varying latencies and time intervals for the reference data, these parameters were varied in the calibration procedure using the EW stimulation data sets. Initially, the peak time point of the P20/N20 component was determined using the GMFP of combined EEG/MEG for each data set. Figure 6.4 shows this time point for an exemplary data set in combination with the two preceding sampled time points. The topographies for these time points only show minor differences, mainly related to the decreasing magnitude for earlier time points, while the signal distribution seems nearly identical across these three time points and their averages. In order to analyze how the choice of the time point or period considered for the reference data influences the calibration, the pipeline was performed for reference data at the peak time point $t = t_p$, its preceding sampled time point $t = t_{p-1}$, and averaged over the intervals containing two or three time points, i.e., $[t_{p-1}, t_p]$ or $[t_{p-2}, t_p]$, respectively. The results of this comparison are shown in Figure 6.5 for all five subjects. The impact of using different time points or intervals varies across subjects, although for most subjects only a small influence could be observed. Compared to the results using the peak time point, differences in skull conductivity estimation of -0.26 mS/m ± 0.39 mS/m (t_{p-1}), -0.066 mS/m ± 0.32 mS/m ($[t_{p-1}, t_p]$) and -0.22 mS/m ± 0.38 mS/m ($[t_{p-2}, t_p]$) were observed for the three alternatives. Regarding the RV, the differences were -0.012% ± 1.57% (t_{p-1}), -0.4% ± 1.03% ($[t_{p-1}, t_p]$) and 0.026% ± 1.45% ($[t_{p-2}, t_p]$) compared to the results using the peak time point.

In the following investigations presented in this chapter, the peak time point of the

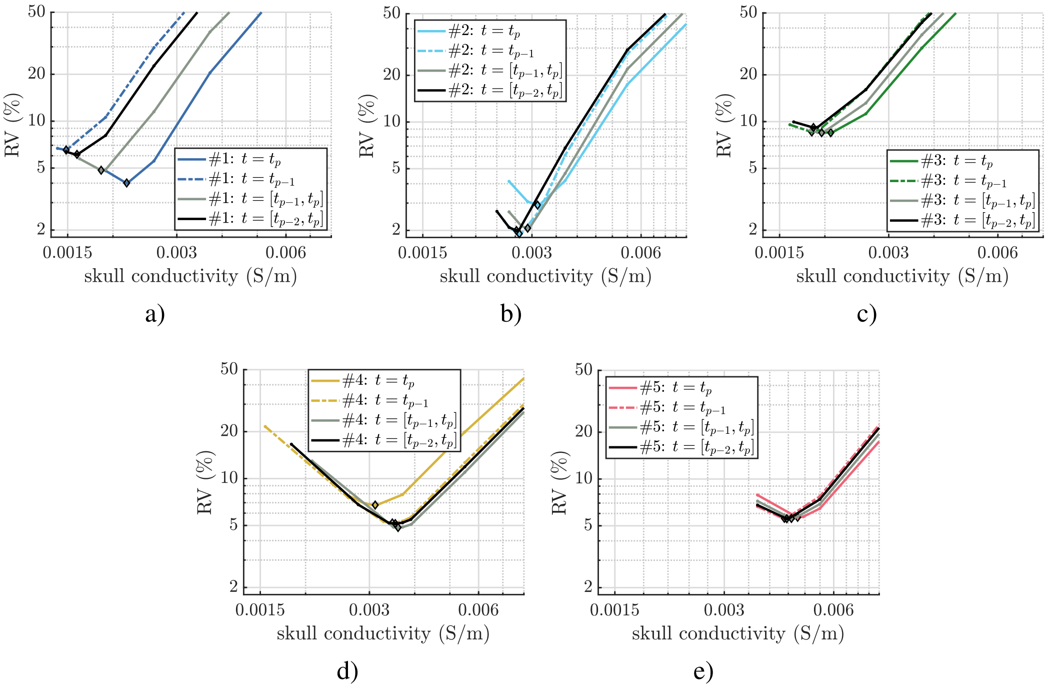

a) b) c)

d) e)

Figure 6.5.: Influence of reference data timing on calibration results using EW stimulation for five subjects plotted on a logarithmic scale. The P20/N20 peak $t = t_p$ (solid, colored), its preceding time sample $t = t_{p-1}$ (dashed; colored) or averages over $[t_{p-1}, t_p]$ (gray) or $[t_{p-2}, t_p]$ (black) were used. Minimum values are highlighted in black. An anisotropic realistic six-compartment head model was used for the FEM forward computations with the St. Venant source model.

P20/N20 component is used for the reference data in the calibration pipeline.

6.2.2. Differences between somatosensory experiments

So far in these investigations, the EW stimulation data sets were used for the calibration procedure. A complete exemplary data set comprising all three stimulation types is shown in Figure 6.6. On the left, butterfly plots of SNR-transformed EEG and MEG data sets for all stimulation types are shown and the peak of the P20/N20 component is marked. Note that the time delays for the P20/N20 peak have technical reasons and do not reflect pathological processing of somatosensory signals in the healthy participants. Instead, they are due to the offset between the trigger onset and the time the device mechanically applies the stimulus (e.g., the air membrane is fully inflated for PT stimulation) and the larger processing times of the tactile stimuli applied at the index finger (Antonakakis et al., 2019; Mertens

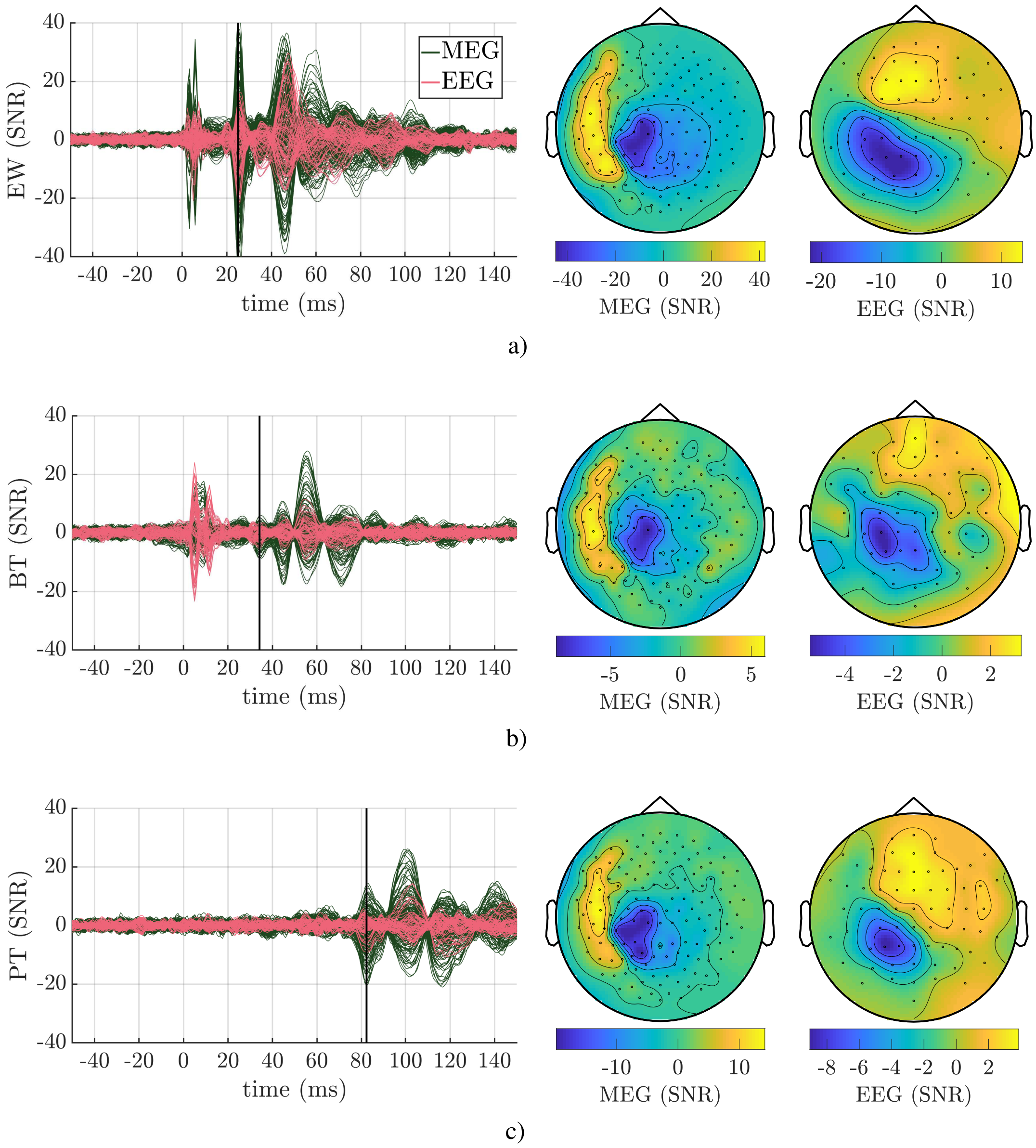

Figure 6.6.: Exemplary SEP/SEF data set of three experimental setups involving a) EW, b) BT and c) PT stimulation. In the butterfly plots (left) of SNR-transformed EEG and MEG data the peak of the P20/N20 component is marked in black. The topography plots for MEG (middle) and EEG (right) are visualized for this time point. Note the varying data range for the topography plots.

and Lütkenhöner, 2000; Nevalainen et al., 2014). For the P20/N20 peak time point, the MEG (middle) and EEG (right) topography plots are shown for all somatosensory experiments. The topographies of the three stimulation types are similar for each subject, while differences can be mainly observed in their magnitudes, with smaller signal strengths for PT and especially BT stimulation.

The calibration results for using the three somatosensory stimulation types are summarized in Figure 6.7. For all subjects, EW stimulation yielded the lowest RV values for the optimal skull conductivity. Compared to EW stimulation data sets, PT stimulation yielded differences in fitted skull conductivity of 1.23 mS/m ± 3.07 mS/m, while BT stimulation resulted in overall larger differences of 3.37 mS/m ± 4.42 mS/m. Regarding the RV, both alternatives led to higher values with differences of 7.4% ± 7.2% for PT and 13.6% ± 4.97% for BT stimulation compared to the results using EW stimulation data sets. For the remaining calibration results presented in this chapter, the EW data sets were used.

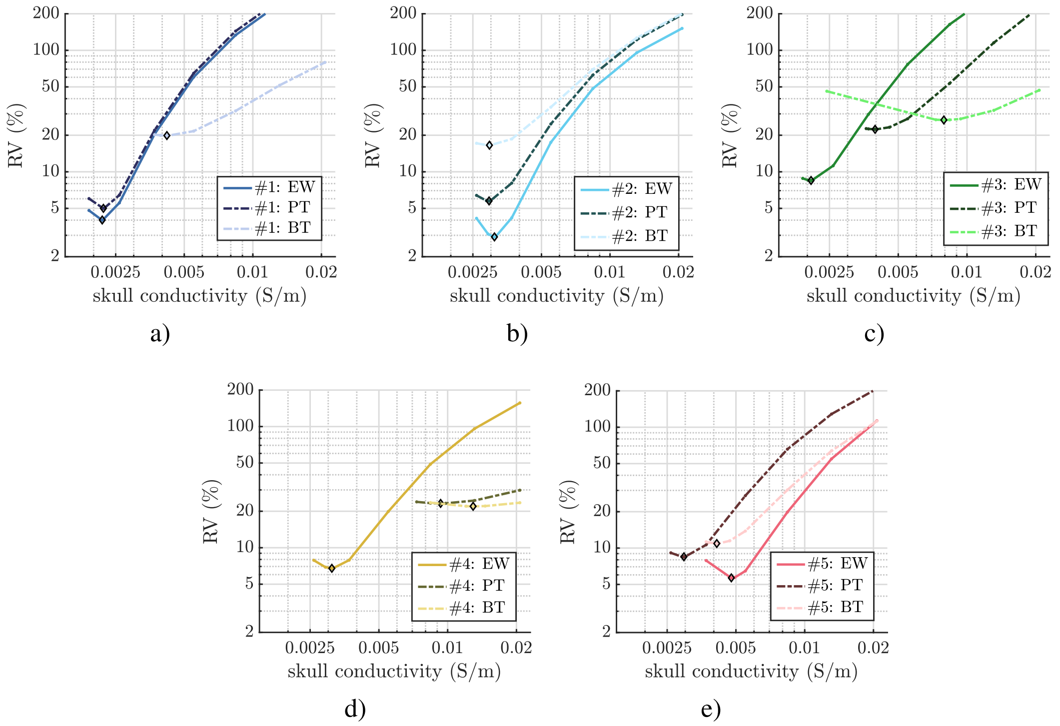

a)

b)

c)

d)

e)

Figure 6.7.: Calibration results using the three different somatosensory stimulation types of EW (solid lines), PT (dark; dashed) and BT (light; dashed) of five subjects plotted on a logarithmic scale. Minimum values are highlighted in black. An anisotropic realistic six-compartment head model was used in combination with the St. Venant source model for the FEM forward computations.

6.2.3. Comparison of head volume conductor models

In this section, the effect of different head volume conductor models on the fitted skull conductivity is investigated. For this purpose, head models with varying degrees of homogenization of tissue compartments were calibrated with respect to skull conductivity. An anisotropic six-compartment head volume conductor, which has been previously used, was compared to a six-compartment model with isotropic white matter conductivity and a simplified three-compartment model consisting of brain, skull and scalp tissue compartments. The calibration results using these different volume conductor models are shown in Figure 6.8 for all five subjects.

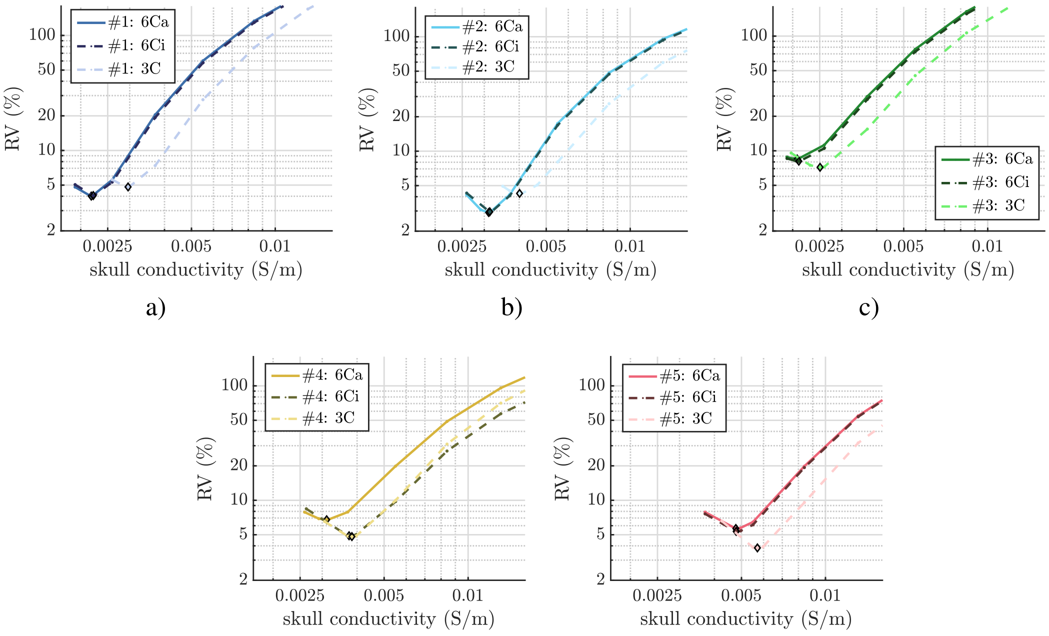

a) b) c)

d) e)

Figure 6.8.: Calibration results using EW stimulation data sets for head volume conductor models with homogenized tissue compartments for five subjects: six-compartment models with anisotropic (solid lines) or isotropic white matter compartment (dark; dashed) and three-compartment models (light; dashed). The results are plotted on a logarithmic scale, the minimum values are highlighted in black. The St. Venant source model was used for the FEM forward computations.

Overall, only small differences can be observed between the calibration results of isotropic and anisotropic six-compartment models, while the fitted skull conductivity of the three-compartment models tended to be slightly higher compared to the most detailed model. Compared to the realistic six-compartment anisotropic (6Ca) head model, the skull conductivity estimations differ by 0.15 mS/m ± 0.27 mS/m for the isotropic six-compartment model (6Ci) and by 0.75 mS/m ± 0.2 mS/m for the three-compartment model (3C). Differences of −0.49% ± 0.79% (6Ci) and −0.58% ± 1.55% (3C) resulted for the minimal RV using the homogenized meshes.

6.2.4. Numerical source models

For the comparison of different source modeling approaches, the calibration pipeline was applied using either the St. Venant source model, as done in the previous investigations, or the partial integration approach for the FEM forward computations.

The results of this comparison are presented in Figure 6.9. Overall, only small differences can be observed when comparing the calibration curves for both conditions of all subjects. When using the partial integration approach, the skull conductivity estimation differed by −0.05 mS/m ± 0.053 mS/m and the minimal RV by −0.21% ± 0.52% compared to using the St. Venant approach.

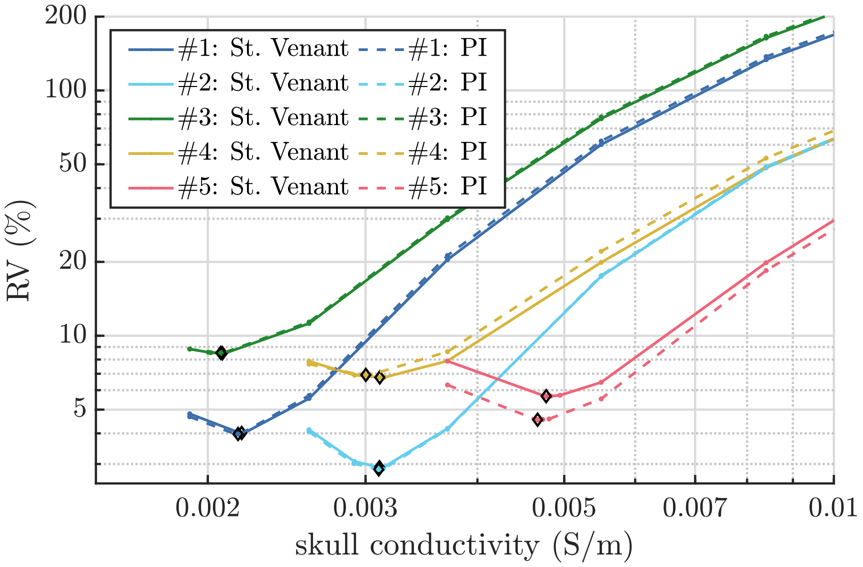

Figure 6.9.: Influence of source modeling approaches on the calibration results using EW stimulation for five subjects, the St. Venant approach (solid lines) is compared to the partial integration (PI) source model (dashed lines). The results are plotted on a logarithmic scale, the minimum values are highlighted in black. An anisotropic realistic six-compartment head model was used for the FEM forward computations.

6.2.5. Variations of the calibration algorithm

In order to compare the variants of the calibration algorithm, the pipeline was applied to the five EW data sets using either the standard Algorithm 1 as done in the previous comparisons, or one of its two alternatives. Variant 1 determines the tangential orientation component using MEG, whereas Variant 2 minimizes the RV with respect to combined EEG/MEG reference data.

The calibration results of this comparison are presented in Figure 6.10. The calibration curves for Variant 1 have a similar shape and minimal values, with mean differences in skull conductivity estimations of -0.11 mS/m $\pm$ 0.12 mS/m compared to applying Algorithm 1. Overall, calibration curves are flatter when using Variant 2, especially notable for Subject 2 shown in Figure 6.10b). Skull conductivity estimations differ by -0.11 mS/m $\pm$ 0.4

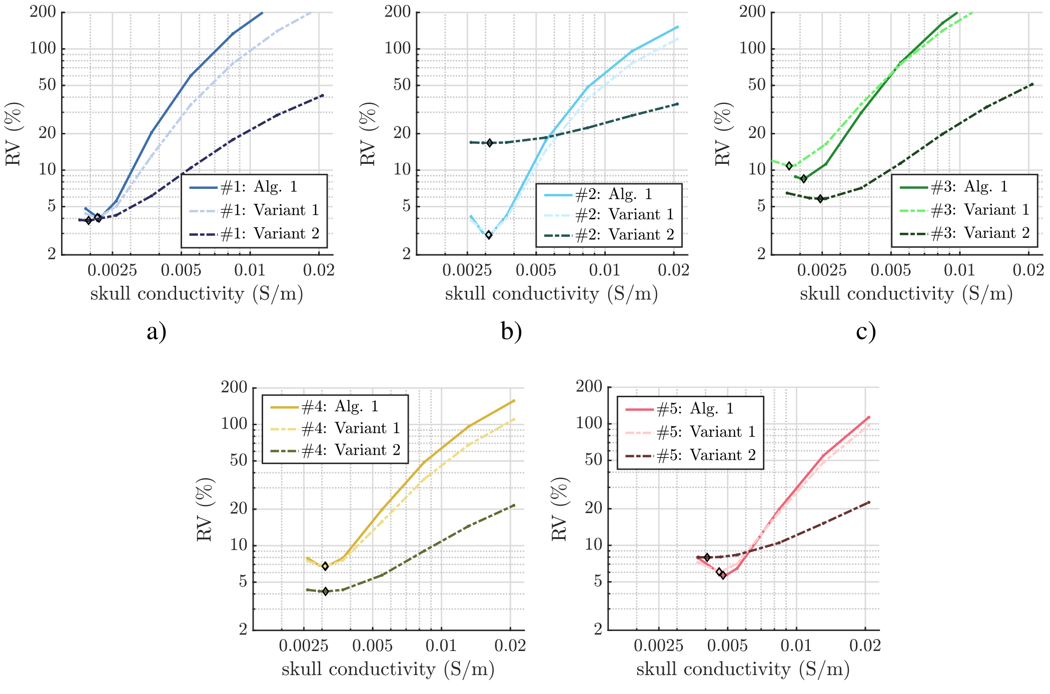

a)

b)

c)

d)

e)

Figure 6.10.: Calibration results for EW stimulation data sets using either Algorithm 1 (solid lines), Variant 1 (light; dashed) or Variant 2 (dark; dashed) for five subjects. The results are plotted on a logarithmic scale, minimum values are highlighted in black. An anisotropic realistic six-compartment head model was used in combination with the St. Venant source model for the FEM forward computations.

mS/m when using Variant 2 compared to Algorithm 1. Regarding the resulting minimal RV, differences of 0.57% ± 1.01% (Variant 1) and 2.14% ± 6.86% (Variant 2) could be observed.

6.3. Discussion

In this chapter, the calibration algorithm was applied to realistic head volume conductor models using experimentally measured SEP/SEF data sets. In contrast to the scenarios in controlled spherical head models with simulated reference data, the actual generator of the P20/N20 activity and the conductivity profile of the volume conductor models are unknown. Consequently, only relative differences of the calibration results between conditions can be indicated.

In a first investigation, the effects of different processing steps of the reference data were analyzed. When SNR-transformed EEG and MEG data were used for the calibration, mean skull compacta conductivity values of 3.05 mS/m ± 1.08 mS/m were fitted. Compared to the calibration results without SNR transformations, only small changes in optimized skull conductivity could be observed. However, smaller RV values resulted from the minimization, indicating that the EEG reference data could be better explained by the fitted dipole. When different time samples and intervals of the P20/N20 component were used for the EEG and MEG reference data, the results regarding the skull conductivity estimation and the minimal resulting RV varied across subjects, while for most of them only minor differences could be observed. Overall, minimal RV differences of less than 0.4% on average could be observed between the results using the time sample before the P20/N20 peak and averages over two and three time samples compared to the results using the peak of the component.

In a second comparison, the calibration results were compared using P20/N20 topographies of three different somatosensory experiments. As a result, both alternatives to EW stimulation resulted in large differences in skull conductivity and higher RV values. The results of the calibration when PT stimulation was used were closer to the results of EW stimulation with mean differences of 1.23 mS/m, while BT stimulation data resulted in mean differences of 3.37 mS/m. On average, differences between minimal RV values were as high as 7.4% (PT) and 13.6% (BT) compared to EW stimulation, indicating that EW stimulation is better suited for the calibration pipeline due to its high SNR. However, while on average 1200 trials were measured for EW and PT stimulation, only 880 trials were recorded using the BT experimental setup due to the larger SOA. It can be assumed that larger measurement times involving more stimuli would lead to a higher SNR of the P20/N20 component. Additionally, the experimentally used SOA could be further optimized for a better tradeoff between a large number of trials improving the SNR and a noise-free prestimulus interval. While the results with PT stimulation, compared to BT stimulation, were closer to EW stimulation in most cases in this realistic scenario, the opposite was the case in the simulated spherical head model scenarios as presented in Chapter 5. In those investigations, the stimulation types were characterized by different dipole strengths, based on source reconstructions in realistic models that were calibrated using the EW stimulation data sets in Antonakakis et al. (2019). In realistic cases, the SNR of the averaged signal may be used as an indication to determine how well a stimulation data set is suited for calibration purposes.

In the third section, different volume conductor models were calibrated with respect to skull conductivity. Homogenization of the white matter tissue in the six-compartment head models only had minor effects on the calibration results. This is most probably due to the scaling of the anisotropic tensors that resulted in mean eigenvalues matching the isotropic value using the effective medium approach (Rullmann et al., 2009; Tuch et al., 2001), and the rather superficial location of the cortical source underlying the P20/N20 component (Wolters et al., 2006). Regarding the homogenized three-compartment model, skull conductivity estimations differed by on average 0.75 mS/m, thereby emphasizing the role of the volume conductor model for the calibration pipeline. During the calibration, skull conductivity is fitted for a specific volume conductor model and assumptions on other conductivities are taken into account, thereby different volume conductor models can yield different fitted values, even though the actual physical properties of the skull are identical.

In the following two investigations, similar findings were observed as in the controlled spherical scenarios. This includes only minor differences between source modeling approaches (St. Venant and partial integration) which were observed in the calibration pipeline. Additionally, the results obtained using the two variants of the calibration algorithm were similar to the results of the standard algorithm with mean differences of fitted skull conductivities of only -0.11 mS/m for both variants. The second variation that minimizes the RV with respect to combined EEG/MEG data had overall flatter calibration curves and larger variations regarding the minimal RV with mean differences compared to Algorithm 1 of $2.14\% \pm 6.86\%$.

Overall, the results indicate inter-individual differences in fitted skull conductivity values that motivate an individual approach to estimate this important parameter in EEG and combined EEG/MEG source analysis as suggested in this thesis. The fitted skull conductivity values differ from the results presented in Antonakakis et al. (2019), even though the same underlying data sets were used. The reasons for this can probably be attributed to several methodological differences in both studies. One important difference is that in contrast to (Antonakakis et al., 2019), we did not use gray matter anisotropy for the following reasons. On the one hand, only low degrees of radial cortical anisotropy could be observed for gray matter tissue (Heidemann et al., 2010; Shimony et al., 1999; Vorwerk et al., 2014) and on the other hand, partial volume effects due to a limited resolution of the DTI measurements can manipulate the conductivity characteristics of this compartment (Koo et al., 2009; Vorwerk et al., 2014). Further differences include the independent preprocessing pipeline (e.g., filtering parameters, trial and channel rejection due to artifacts) using different toolboxes and varying reference time points for the P20/N20 component. Additionally, while a skull conductivity of 0.0016 S/m was used for the MEG single dipole deviation scans in Antonakakis et al. (2019), standard values of 0.01 S/m (three-compartment models) or 0.0042 S/m (six-compartment models) were used here.

In this investigation, the calibration algorithm was applied to realistic data sets and the effects of different parameters on the calibration were studied. In the future, larger group studies are required to generalize the findings presented here and draw statistically valid conclusions.

7. Application in presurgical epilepsy diagnosis

The aim of individually calibrated head volume conductor models is to improve the accuracy of EEG source reconstructions and allow a combined analysis of EEG/MEG data. Due to their complementarity, is has been suggested that an improved spatial resolution can be achieved when both modalities are combined in comparison to single modality analysis results (Cohen and Cuffin, 1983; Fuchs et al., 1998; Sharon et al., 2007). This chapter focuses on presurgical epilepsy diagnosis as a specific field of application of EEG/MEG source analysis.

Epilepsy is a chronic disease which is characterized by recurring unprovoked seizures caused by abnormal neuronal activity (Ghosh et al., 2021; Josephson et al., 2011). It is estimated that around 50 million people worldwide suffer from epilepsy, rendering it one of the most common neurological disorders (Ghosh et al., 2021; Lüders et al., 2006). Despite improvements over the past decades in anti-epileptic drug (AED) therapy, sustained seizure freedom cannot be achieved for approximately 20–30% of patients (Eadie, 2012; Ghosh et al., 2021). For these drug-resistant or refractory epilepsy cases, surgery is a potential alternative treatment option (Kwan and Brodie, 2000; Mitchell et al., 2012). If applicable, the aim is to surgically remove the *epileptogenic zone*, i.e., the minimal amount of cortical tissue that needs to be removed for the patient to become seizure-free (Lüders et al., 2006). Several diagnostic techniques are typically employed in presurgical diagnostics to help identify this theoretically defined area. One of them is the localization of the *irritative zone*, which is defined as the cortical tissue generating *interictal spikes*, i.e., abnormal discharges between epileptic seizures (Lüders et al., 2006). The relationship between these two regions is complex, but it has been suggested that the irritative zone is usually more widespread than the epileptogenic zone (Hasegawa, 2016; Lüders et al., 2006). Due to their high temporal resolution, the irritative zone can be localized using (non-invasive or invasive) EEG and/or MEG, which can be complemented by EEG-triggered fMRI to estimate the volume of this area (Hasegawa, 2016; Lüders et al., 2006).

The complementary nature of both EEG and MEG modalities has been emphasized in the context of presurgical epilepsy diagnosis by several investigations (Barkley and Baumgartner, 2003; Ebersole and Ebersole, 2010). A study by Knake et al. (2006) found that interictal epileptiform discharges could be detected by both modalities in approximately 58% of 67 patients investigated (3 were excluded due to MEG artifacts), while they were only visible in EEG in 3% and only in MEG in 13% of the patients. Similarly, Iwasaki et al. (2005) found that overall, interictal activity was detectable in approximately 72% of 43 epilepsy patients in both modalities with a median of nearly 26% of total spikes visible in both EEG and MEG modalities. Additionally, interictal spikes were only visible in a single modality in about 2% (EEG) and 19% (MEG) of patients. In a simulation study using a realistically shaped head model and realistic background noise, MEG was more sensitive for sources less than 30° rotated away from the tangential plane, while for sources with more than 45° deviation, EEG was more sensitive (Haueisen et al., 2012). The contribution of MEG to surgery planning and long-term seizure freedom by providing non-redundant information has also been highlighted in a retrospective analysis of 1000 patients in Rampp et al. (2019).

Due to these complementarities, a simultaneous acquisition of both modalities in combination with an individual or combined analysis has been suggested (Barkley and Baumgartner, 2003; Ebersole and Ebersole, 2010; Haueisen et al., 2012). The benefits of combined EEG/MEG analysis have been shown in the context of localizing interictal spikes in order to define the irritative zone, for instance, in cases of weak signal such as the spike onset (Aydin et al., 2017, 2015). When combining modalities, the importance of an accurate head modeling and conductivity estimation has been emphasized for a high accuracy (Aydin et al., 2015; Rampp and Stefan, 2007).

In the following, EEG/MEG recordings of interictal epileptiform activity of an epilepsy patient are analyzed using a calibrated head volume conductor model.

7.1. Materials and Methods

The data set, which was retrospectively investigated, is from a female patient who suffered from pharmaco-resistant epilepsy. With regard to her seizure semiology, she reported a somatosensory aura of the left arm followed by tonic-clonic movements of the left arm and hand. High-resolution MRI measurements indicated an FCD type IIb in the superior parietal lobe. The lesion with an extend of approximately 1.2 cm^3 and the surrounding tissue were surgically removed in 2018. After the resection, the patient was seizure-free for one year, without further follow-up examinations. The patient was between 27 and 34 years old at the time of the measurements, which took place pre- and postoperative. She had given written informed consent before the measurements and all procedures have been approved by the ethics committee of the University of Erlangen, Faculty of Medicine on 10.05.2011 (Ref. No. 4453). This epilepsy case was also analyzed in the context of beamformer approaches for the inverse problem in Neugebauer et al. (2022).

In a first block of combined EEG/MEG data acquisition, SEP/SEF measurements were recorded using EW stimulation of the median nerve on both the right and the left wrist in a random order with a varying SOA of 350–450 ms between the trials. These measurements of approximately 13 min. yielded 973 (972) trials for right (left) wrist stimulation. Additionally, (DTI-)MRI data were acquired for the generation of a realistic head volume conductor model, for details on the experimental setup for the functional SEP/SEF and imaging data acquisition, see Section 6.1.1. For the recording of interictal epileptiform activity, five measurement blocks each with a duration of eight minutes were recorded in supine position and the data was sampled at 2400 Hz and later downsampled to 300 Hz. In these measurements, a board-certified epileptologist marked 248 epileptic spikes.

The analysis pipeline for the SEP/SEF data and the head modeling pipeline for the creation of an individual anisotropic six-compartment head model were identical to the methodology described in Section 6.1.2. Regarding the preprocessing of the interictal spike recordings, the signals were filtered around the frequency spectrum of interest using a band-pass filter of 1–100 Hz (Birot et al., 2014; Rampp et al., 2019; Stefan et al., 2003), in addition to a notch filter of 50 Hz and harmonics to account for power line noise. The data were cut into epochs of $[-500$ ms, 300 ms$]$ around the spike peak ($t = 0$ ms) and averaged. The EEG data were re-referenced using the common average reference (CAR). A semi-automatic artifact and noisy channel rejection was applied, overall 70 EEG electrodes and 271 MEG channels were used for further analysis. For each sensor, an SNR transformation was applied based on the noise strength in the time interval $[-500$ ms, -150 ms$]$ before the spike peak. For the localization of the epileptic spikes, the middle of the rising flank was chosen in order to account for possibly propagated activity at the spike peak (Aydin et al., 2014; Lantz et al., 2003).

The calibration of the six-compartment head model was performed with the SNR-transformed data using the St. Venant source model and the peak of the P20/N20 component, using the same methodology as for the other realistic data sets as described in Section 6.1.2. In the calibrated six-compartment head model, the interictal activity of either single modality EEG, MEG, or combined data was localized using equivalent current dipole scans as described in Def. A.4. For this purpose, a source grid of 2 mm resolution in the gray matter compartment was used.

7.2. Results

For right wrist stimulation, the calibration procedure resulted in a fitted skull conductivity of 0.0047 S/m, while left wrist stimulation resulted in a calibrated value of 0.0036 S/m. However, due to the somatosensory aura and the vicinity of the somatosensory network to the suspected epileptogenic zone in the superior parietal lobe, the following source reconstructions are based on the fitted value for the right wrist stimulation.

For the reconstruction of interictal epileptiform activity, the time point $t = -3.3$ ms before the spike peak was chosen, which is approximately located on the middle of the rising flank. The butterfly plots of the averaged EEG and MEG data and topographies of this time point

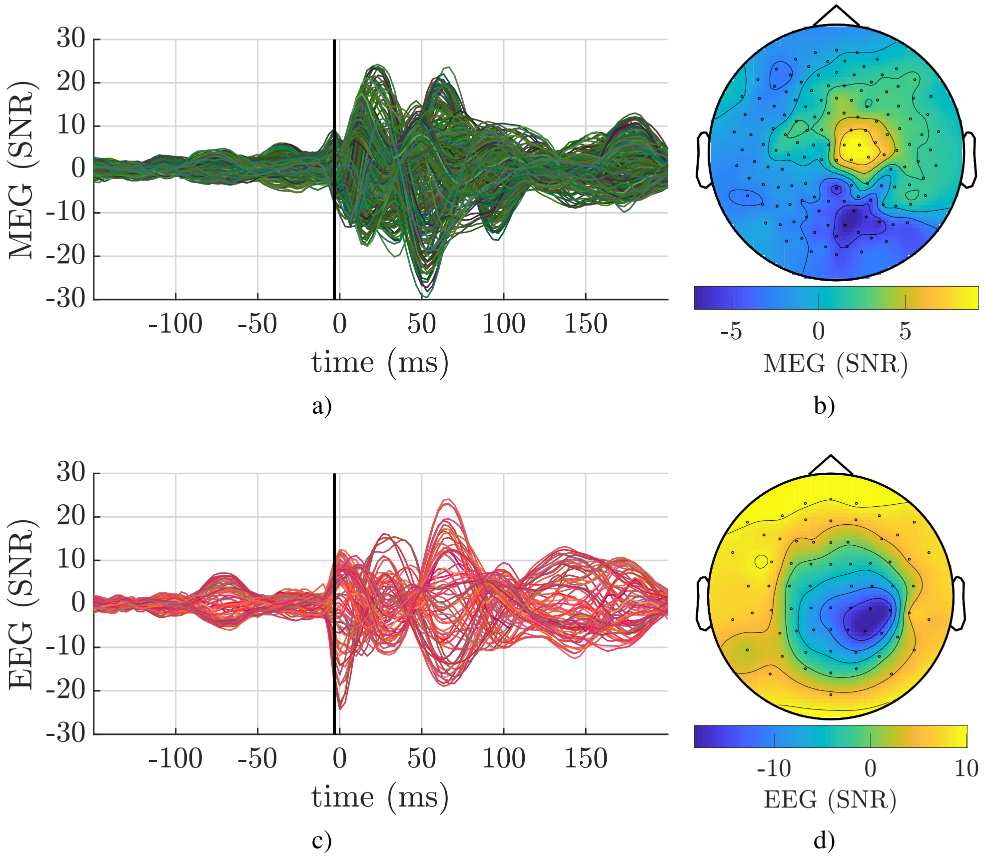

Figure 7.1.: MEG (top) and EEG (bottom) recordings of interictal epileptiform activity. a) Butterfly plots of SNR-transformed signals in the time interval [-150 ms, 200 ms] around the spike peak (0 ms), the time point -3.3 ms is marked in black, and b) topographies of this time point, note the varying signal range for the topography plots.

are shown in Figure 7.1. Both EEG and MEG topographies show peaks over the right parietal lobe. Absolute SNR values of 2.58 ± 1.85 with a maximum strength of 9.35 can be observed for MEG. The absolute SNR values of the EEG channels are overall higher with 6.19 ± 4.04, the maximum strength is measured at electrode P4 with an SNR of -18.36.

Single dipole deviation scans were performed using EEG, MEG, or combined modalities. The resulting source localizations are shown in Figure 7.2. The dipole locations and orientations are superimposed on slices of the post-operative T1-MRI which are chosen to cut through the resected area. The planes used for the visualization are marked by gray lines, the resected area is located around their intersections. The best fitting dipole according to a single modality EEG dipole scan is located inside the resected area with a GOF of approximately 0.97. The MEG data can be best explained by a more medially located dipole outside the resected area with a GOF of 0.9. Regarding combined EEG/MEG analysis, the single dipole deviation scan results in a best fitting dipole location on the medial side of the resected area as well, but closer to the resected area as the single modality MEG result. The maximum GOF of this dipole is 0.89. In all three conditions, the reconstructed dipole orientation is rather radially oriented.

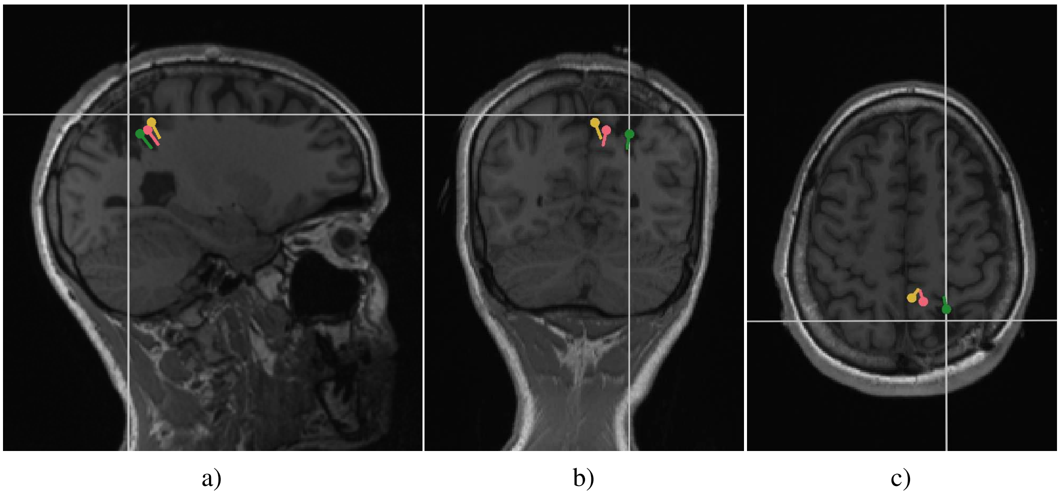

Figure 7.2.: Single dipole deviation scan results for EEG (green), MEG (yellow) or combined EEG/MEG (red) superimposed on the post-surgical T1-MRI (not in radiological convention): a) saggital, b) coronal and c) axial planes through the resected area, the slices used for the visualization are marked by gray lines.

7.3. Discussion

In the investigated epilepsy case, the fitted skull conductivity was close to the standard value of 0.0042 S/m and therefore only minor differences in the source reconstruction are expected. The analysis of the right wrist stimulation was chosen to avoid interplay with the epileptiform activity and due to its high SNR. In other patients, right or left hand stimulation or a combination of both may be used for the calibration, depending on the region of interest and an assumed independence from the epileptogenic network. In general, it has been suggested that equivalent sources of early somatosensory evoked responses are generally stronger in the left hemisphere, i.e., following right arm stimulation (Jung et al., 2003; Rossini et al., 1996). However, the small proportion of left-handed subjects in both studies does not allow any final conclusions with regard to the influence of handedness on this observation. Possibly, the SNR of the P20/N20 peaks of right and left wrist stimulation could be used as an indicator which data set should be used for the calibration.

The positive surgery outcome one year after the resection suggests that the epileptogenic zone was inside the resected area, although further follow-up examinations might be necessary to confirm this result. In this retrospective analysis, we used single dipole deviation scans to localize interictal epileptiform activity recorded by EEG, MEG or combined modalities in a calibrated six-compartment head model. The maximum GOF value and therefore the best fitting dipole was located directly inside the resected volume for EEG. The MEG and combined EEG/MEG dipole scans resulted in more medial source localizations outside the resected area, with the combined dipole scan result closer to the EEG result and the resected area. The topography plots at the time point of the rising flank of the marked interictal spikes indicate a rather radial orientation, which is also observed in the source reconstructions. This is also reflected in the higher SNR of EEG compared to MEG data and could explain the superiority of EEG in this case. However, combined EEG/MEG resulted in a fitted dipole closer to the resected area than single modality MEG.

While only the dipole scan result is shown in Figure 7.2, the distribution of the GOF in the source space shows overall high values inside and close to the resected area with only small variations among the best fitting dipoles. More sophisticated source analysis methods could be applied for more reliable reconstructions, e.g., using beamforming approaches as done in Neugebauer et al. (2022).

8. Software implementation

In this chapter, software-related aspects are addressed in more detail. The organization of the code that implements the calibration procedure and the respective tools that were used are outlined in Section 8.1. In Section 8.2, more details are provided about the software toolbox DUNEuro which was used for the EEG and MEG forward solutions in this thesis.

8.1. Calibration procedure

The code implementing the calibration pipeline for the computations in this thesis was written in MATLAB (The MathWorks Inc., Natick, Massachusetts). Some external tools were used for specific tasks, most importantly DUNEuro (Schrader et al., 2021) for the computation of the EEG/MEG forward solutions and FieldTrip[1] (Oostenveld et al., 2011) for most of the preprocessing steps for the realistic SEP/SEF data sets. Figure 8.1 summarizes the stages of the calibration procedure. In the following, each step is described in more detail.

The input for the calibration is provided as an INI file that defines data paths and parameter settings as key-value pairs. This includes general information (e.g., the output path) and details about the head model (e.g., standard conductivity values), the sensors (e.g., coil positions and orientations), the source modeling approach, the source grid and the optimization procedure (e.g., the interval for the skull conductivity parameter). Additional configurations for using realistic data include information on the SEP/SEF data set, preprocessing parameters (e.g., filter bandwidth) and specifications for the dipole scan (e.g., the timing of the P20/N20 component). For the spherical scenarios, the test dipole characteristics, details about the reference data computation (e.g., noise characteristics) and parallelization settings to compute substeps (e.g., the dipole deviation scan) for several dipoles in parallel are provided.

After the input data is processed, the EEG/MEG reference data is prepared. In case realistic P20/N20 topographies of SEP/SEF data sets are used, the signals are preprocessed using FieldTrip. In a first step, the function `ft_definetrial` is used to specify the data

---

[1] https://www.fieldtriptoolbox.org/

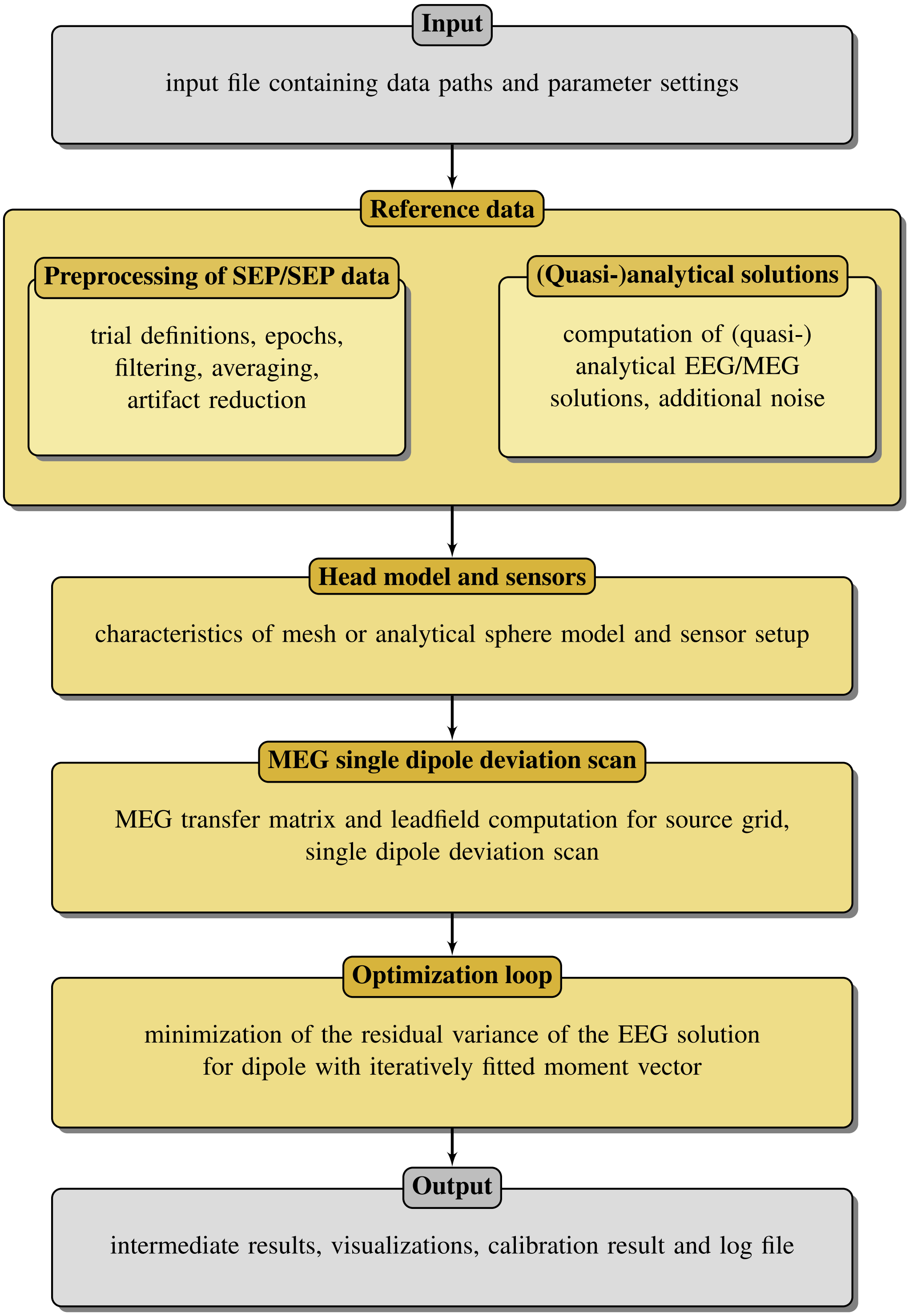

Figure 8.1.: Calibration pipeline: Diagram outlines input, most important subsequent steps and output of the calibration code.

segments of interest. Secondly, a bandwidth filter and a notch filter are applied to remove power line noise using `ft_preprocessing`. The function `ft_rejectvisual` is then used to visually identify and remove bad channels and trials from the data. Afterwards, `ft_timelockanalysis` creates a time-locked average over all trials for each sensor. For the computation of the GMFP, the function `ft_globalmeanfield` was applied. As SNR transformations are currently not supported in FieldTrip, the noise estimation from the prestimulus interval and the transformation of the signals were computed using custom MATLAB functions.

In case (quasi-)analytical reference solutions are used in combination with a spherical head model, the analytical MEG solution is computed using the closed formula by Sarvas (1987). The quasi-analytical EEG forward solutions are obtained using the series expansion formulas following De Munck and Peters (1993) based on the implementations of the SimBio library[2]. In some cases, noise with specified characteristics is computed and added to these forward solutions.

Independently from the functional data, the anatomical data in form of the head model and the registered sensors need to be processed. In principle, FieldTrip offers functionality regarding imaging data segmentation and meshing of head models as well as sensor registration algorithms (Oostenveld et al., 2011; Vorwerk et al., 2018). However, the head models were obtained from Antonakakis et al. (2019) and the sensors were already registered using Curry[3]. Therefore, the head model and sensor characteristics were transformed to the standard formats used in FieldTrip. During this step the different conventions of MEG sensor formats in Curry and FieldTrip are taken into account. The coil positions and measurement orientations obtained from Curry are not directly compatible with the gradiometer transformation matrix extracted from the functional data via FieldTrip, as the ordering of (reference) coils differs, and the measurement direction of the outer coil layer for the axial gradiometers is flipped.

Once these components are prepared, the MEG single dipole deviation scan of Step 1 of Algorithm 1 is performed. For this purpose, the MEG leadfield for the indicated source grid is computed using the transfer matrix approach. The computation of the transfer matrix can be done in separate blocks if specified in the input file to reduce memory requirements. This step is done using the MATLAB interface of the DUNEuro toolbox which was integrated in FieldTrip, as presented in more detail in the following section. For the solution of the linear system, an algebraic multigrid (AMG) preconditioned conjugate gradient (CG) solver is used following Lew et al. (2009b) and Wolters et al. (2002). The Intel© Threading Building

---

[2] https://www.mrt.uni-jena.de/simbio/index.php?title=Main_Page

[3] https://compumedicsneuroscan.com/products/by-name/curry/

Blocks (TBB) library[4] allows multi-threading for the computation of the transfer matrix and its multiplication with the right-hand side vector for the leadfield computation.

In the subsequent step, the residual variance of the EEG solution for the iteratively fitted dipole moment is optimized. The MATLAB routine `fminbnd` is used which implements Brent's method. In each iteration, the direct EEG solution of the dipole location determined in the previous step is computed for the given skull conductivity parameter using the DUNEuro software toolbox. The dipole orientation and magnitude are computed and the residual variance for this iterative step is returned. Once the tolerance criterion is met, the optimization is terminated.

In addition to the calibration results, several intermediate results are produced as output. These include the MEG transfer matrix and leadfield, sensors and head model in FieldTrip format and the dipole scan results. Additionally, several figures are produced in this process. For instance, butterfly plots of the SEP/SEF data with marked time point or interval of interest are plotted, and topography plots visualize the P20/N20 component using the FieldTrip function `ft_topoplotER`. Moreover, the head model with the sensor setup and the final reconstructed dipole as well as the mesh are visualized.

8.2. DUNEuro software toolbox

This section focuses on the DUNEuro toolbox which was used for the FEM computations in this thesis to solve the EEG/MEG forward problems numerically. DUNEuro is a free and open source C++ software tool offering sophisticated modern FEM discretizations for these mathematical problems using a variety of different source models (Schrader et al., 2021). DUNEuro builds upon the *Distributed and Unified Numerics Environment* (DUNE) framework[5], an open source C++ library that provides broad functionality related to the numerical solution of partial differential equations (Bastian et al., 2008a,b; Sander, 2020). The core functions are implemented in the module `duneuro`, while `duneuro-matlab` and `duneuro-py` offer bindings to MATLAB and Python scripting languages, respectively. The software is available under the open-source GPL and is managed in a GitLab repository[6]. In the following, the focus lies on two developments of DUNEuro supported by this thesis.

One major advancement is the increase in accessibility and usability by providing a comprehensive documentation of the features and user interfaces of DUNEuro. Schrader et al. (2021) contains detailed installation instructions and example scripts with in-depth expla-

---

[4] github.com/intel/tbb

[5] http://www.dune-project.org

[6] https://gitlab.dune-project.org/duneuro

nations of the DUNEuro forward computation workflow, parameters and input/output interfaces. For this purpose, example data sets were made available that include discretizations of a spherical four-compartment and two realistic six-compartment head models (Piastra et al., 2020; Schrader et al., 2021), as visualized in Figure 8.2. Using these head models,

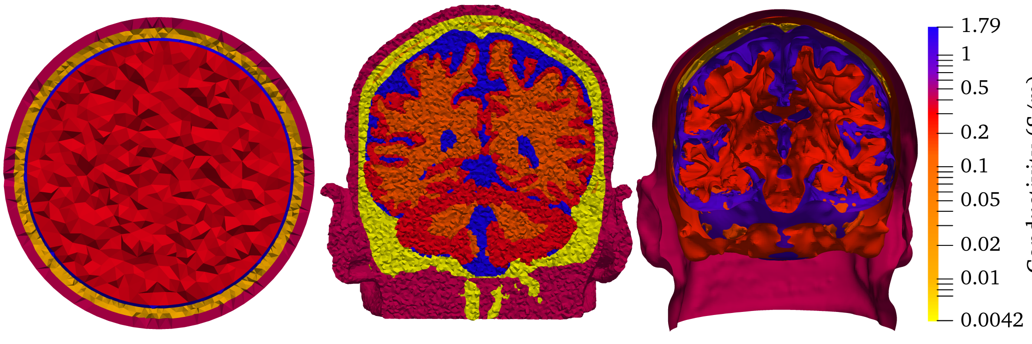

a) b) c)

Figure 8.2.: Example head models include a) a tetrahedral spherical four-compartment model, and two realistic six-compartment models: b) a tetrahedral and c) an unfitted model (cropped) for which the tissue boundaries are given as level sets. The conductivity is shown on a logarithmic scale. For the unfitted model in c), the values on the internal boundaries indicate the mean between the two adjacent tissue conductivities. Modified from Schrader et al. (2021).

example scripts in Python (and MATLAB) for the computation of the EEG forward solution are provided and explained using different settings. For instance, different FEM approaches besides the standard Lagrangian (CG) method are applied, i.e., the DG and UDG-FEM. Moreover, an overview of currently supported source models for the different FEM approaches is provided, some of which are used in the example scripts (i.e., the partial integration, St. Venant, Whitney and subtraction source models). The transfer matrix approach and the direct solution approach are both employed and example solutions are visualized using ParaView (Ahrens et al., 2005). Two exemplary DUNEuro forward computations for the tetrahedral spherical and realistic models are visualized in Figure 8.3a) and b), respectively. Additionally, an example is provided of how the forward solutions of DUNEuro can be embedded in a complete source analysis pipeline. For this application, the source underlying the P20/N20 component of an SEP data set was localized in the primary somatosensory cortex with a single dipole deviation scan using UDG-FEM forward solutions of DUNEuro. The GOF computed in this procedure for the normally constrained source space is visualized in Figure 8.3c). In the context of providing easier access to the DUNEuro toolbox, the management of experimental features was improved by implementing dynamic options

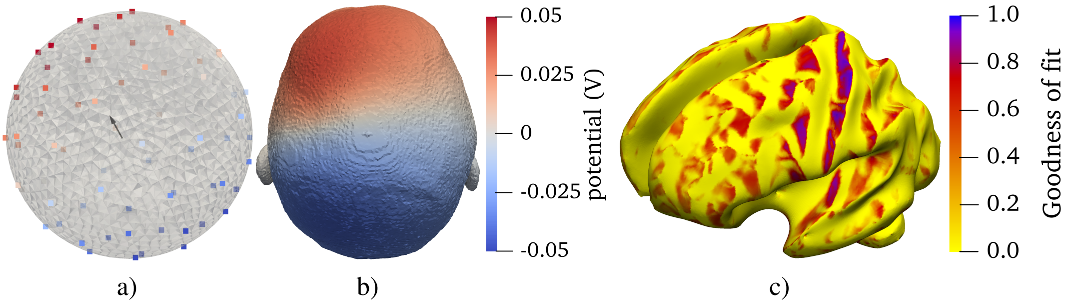

Figure 8.3.: Example EEG forward computations using DUNEuro: EEG forward solutions for an exemplary dipole using a) CG-FEM and the transfer matrix approach in the spherical head model, b) DG-FEM using the direct solution approach in the tetrahedral realistic model. c) Realistic application: UDG-FEM forward solutions for the unfitted model were used for a single dipole deviation scan to localize the P20/N20 component of an SEP data set. GOF is shown on an inflated model of the source space. Modified from Schrader et al. (2021).

and runtime verifications to enable or disable experimental features. This way, the continuous integration of new features is facilitated from the developer perspective, while the user can not unknowingly access features which are not thoroughly tested yet. Additionally, a list of used features (e.g., source models and FEM approaches) is internally maintained and the user is able to print a list of related publications for more details using the function `print_citations`. For further details related to the DUNEuro software toolbox, e.g., about the software structure, dependencies and parameter explanations we refer to Schrader et al. (2021) and the documentation provided in GitLab[7].

The second development related to DUNEuro addressed here is the integration into the high-level toolbox FieldTrip (Oostenveld et al., 2011). In general, FEM approaches for solving the EEG/MEG forward problems can take into account complex realistic geometries and anisotropic tissue conductivities and achieve high numerical accuracies (Lew et al., 2009b; Vorwerk et al., 2012; Wolters et al., 2007c). However, the workload associated with the generation of realistic FEM head models and limited accessibility to FEM software have created practical obstacles to the broad usage of these approaches for neuroscientific applications (Vorwerk et al., 2018). One major advancement in reducing these barriers was the integration of FEM solutions as implemented by the SimBio toolbox into FieldTrip (Vorwerk et al., 2018). More precisely, EEG forward solutions using the St. Venant source model were made accessible by this high-level toolbox. This embedding allows an easy integration

---

[7] https://gitlab.dune-project.org/duneuro/duneuro/-/wikis/

of FEM forward solutions into complete EEG and multimodal analysis pipelines, including head model generation, data preprocessing, source analysis and visualization. In order to profit from this functionality and automatize the calibration pipeline presented here, the FEM approaches to solve the EEG and MEG forward problems using the DUNEuro toolbox were made accessible in a similar way via the FieldTrip toolbox. The main access to the C++ DUNEuro toolbox is provided by the *duneuro-matlab* module that compiles a MATLAB executable (MEX) file and thereby enables the usage of DUNEuro functionality from MATLAB. An overview of the main high-level FieldTrip functions related to the computation of EEG/MEG forward solutions and the respective DUNEuro functions which are called therein is presented in Table 8.1.

Table 8.1.: Main high-level FieldTrip functions related to solving the EEG/MEG forward problems and the corresponding DUNEuro functions called therein

High-level FieldTrip interface	**DUNEuro function calls**
`ft_prepare_headmodel` volume conductor model construction	`duneuro_meeg` driver creation
`ft_prepare_vol_sens` connection of head model and sensors	`set_electrodes` (EEG) `set_coils_and_projections` (MEG) transfer of sensor information `compute_eeg_transfer_matrix` (EEG) `compute_meg_transfer_matrix` (MEG) computation of transfer matrix
`ft_prepare_leadfield` computation of leadfield	`apply_eeg_transfer` (EEG) `apply_meg_transfer` (MEG) leadfield computation with transfer matrix

After the preparation of the anatomical data, the forward computation pipeline typically starts with the high-level FieldTrip function `ft_prepare_headmodel`. This function takes information about the mesh and conductivities as input, typically created using the FieldTrip function `ft_prepare_mesh` and sets up initial steps for the forward computations. If `'duneuro'` is selected in the input configuration as the forward method, the driver as the main interface of the DUNEuro code is created internally. In this step, the mesh information is passed to DUNEuro and the FEM stiffness matrix is assembled. Subsequently, the FieldTrip function `ft_prepare_vol_sens` can be called, which combines the head model created previously and the sensor information, typically obtained from the functional data header. In this step, the sensor information, i.e., the characteristics of the electrodes (EEG) or magnetometers (MEG), are passed to DUNEuro using the functions `set_electrodes` or `set_coil_and_projections`, respectively. Afterwards, the computationally expensive transfer matrix computation is performed using the DUNEuro function calls `compute_eeg_transfer_matrix` (EEG) or `compute_meg_transfer_matrix` (MEG). Once the source grid is prepared, for instance, by using the FieldTrip routine `ft_prepare_sourcemodel`, the leadfield can be computed. This is done by the FieldTrip function `ft_prepare_leadfield`, which internally calls the respective DUNEuro functions `apply_eeg_transfer` in case of EEG or `apply_meg_transfer` for MEG forward computations. Here, the source model needs to be specified for the assembly of the right-hand side vector, which is multiplied to the transfer matrix computed previously. Regarding MEG, two postprocessing steps are performed at this stage. First, the analytical primary magnetic field is computed using an external MATLAB script and added to the numerically computed secondary magnetic field component. Second, the gradiometer transformation matrix is multiplied to the leadfield matrix in order to compute the forward solutions on the channel level. Once the forward EEG/MEG solutions are computed, they can be further used in source analysis applications in combination with the preprocessed functional data.

In general, parameters for the DUNEuro functions can either be directly passed to the high-level functions via configuration structures in accordance with the software design of FieldTrip, or default values are internally set. For instance, the St. Venant model is chosen as the default source modeling approach with standard parameters if not specified otherwise.

Currently, CG-FEM, in combination with the St. Venant, partial integration or subtraction (EEG) source model, is integrated in the FieldTrip-DUNEuro pipeline. However, due to the modular design of the MATLAB-interface of DUNEuro, an inclusion of other FEM or source modeling approaches is easily possible by only changing a few parameter options in the low-level FieldTrip functions in most cases.

For a summary of ongoing projects and future developments regarding the DUNEuro software toolbox, see Section 9.3.

9. Discussion and outlook

In this thesis, we presented a novel algorithm to calibrate FEM head models with respect to skull conductivity using EEG/MEG data of somatosensory experiments. This algorithm was tested in a controlled spherical head model scenario and the impact of varying specific parameters such as noise levels, source orientations or numerical discretizations were investigated. Subsequently, the algorithm was applied to calibrate realistic head models with respect to skull conductivity, providing further insights, e.g., into the effect of SNR transformations or the latency of the reference data. Additionally, an epilepsy data set was analyzed using combined EEG/MEG analysis as an example of a clinical application of the calibration procedure. A summary and interpretation of these results can be found in the discussion sections within Chapters 5–7, respectively. We now discuss three aspects in more detail and give an outlook regarding the development of the calibration algorithm and its software. First, current limitations and possible improvements of the calibration pipeline are presented in Section 9.1. Second, options to exploit the new generation of OPM sensors for a calibration using MEG are discussed in section 9.2. Third, an outlook on software-related aspects such as the integration of DUNEuro into high-level toolboxes is presented in Section 9.3.

9.1. Applications and further development of the calibration algorithm

In this section, several limitations and assumptions of the calibration procedure are discussed and possible improvements are presented.

In general, the calibration algorithm requires both EEG and MEG modalities to be experimentally available which may limit its applicability, as especially conventional MEG systems are expensive in their acquisition and maintenance (Gross, 2019). However, MEG is required for the stabilization of the calibration procedure by fixing the source location, as attempts to calibrate head models using EEG alone (Lew et al., 2009a) have turned out to be too unstable due to the strong correlation between source depth and skull conductivity

(Vorwerk et al., 2019a).

Moreover, an important assumption in our calibration procedure is the concept of a singular point dipole underlying the P20/N20 component of somatosensory evoked responses. Former studies indicate that the assumption of a single dipolar source in Brodmann area 3b is justified (Allison et al., 1991; Antonakakis et al., 2020; Nakamura et al., 1998). However, the contribution from thalamic pathways as well as the degree of simultaneous activity in the primary and secondary somatosensory cortices are not resolved conclusively (Hari and Forss, 1999; Haueisen et al., 2007; Rezaei et al., 2020). Additionally, the limitations of the equivalent current dipole model have been emphasized by experimental evidence suggesting extended cortical generators of sensory-evoked components in the range of up to several cm^2 (Lü and Williamson, 1991; Riera et al., 2012). Therefore, numerical approaches using multipolar source models have been proposed in order to better describe extended sources (Barkhau, 2021; Beltrachini, 2018; Jerbi et al., 2004; Vorwerk et al., 2019b).

For the determination of the source location, an unconstrained MEG single dipole deviation scan is used in the calibration algorithm. Figure 9.1 shows the goodness of fit which is minimized in this step for each source space node located in the gray matter. On the left, in Figure 9.1a), this measure is depicted using the P20/N20 component of an SEF data set. The maximal GOF for the reconstructed dipole (black) is 0.98, with similarly high values in the neighboring areas. For comparison, Figure 9.1b) on the right shows the same measure for EEG, indicating overall higher values and a more extended distribution. As the actual source distribution is unknown in the realistic model, it is hard to determine the localization error in this step. However, more sophisticated source localization approaches could be applied. For instance, regularization could be used to stabilize the MEG source localization (Wolters et al., 1999) or more sophisticated source localization methods such as the multiple signal classification (MUSIC) technique could be applied (Brette and Destexhe, 2012; Mosher et al., 1992; Mosher and Leahy, 1999).

As the GOF is similarly high for dipole locations on adjacent gyral walls, the initial MEG single dipole deviation scan is sensitive to possible error sources, such as the co-registration process between the structural imaging data of the head and functional EEG/MEG data. In the EEG/MEG measurements, the electrode positions as well as the location of three anatomical landmarks are recorded on the head surface, while the characteristics of the MEG sensors are recorded in a coordinate system based on these landmarks. Small head movements in the MEG can not be entirely avoided even though the measurements were already performed in supine position. The functional data was then registered to the head models based on these three landmarks which were marked and recorded as well in the MRI measurements. This co-registration process could be improved in several ways. One

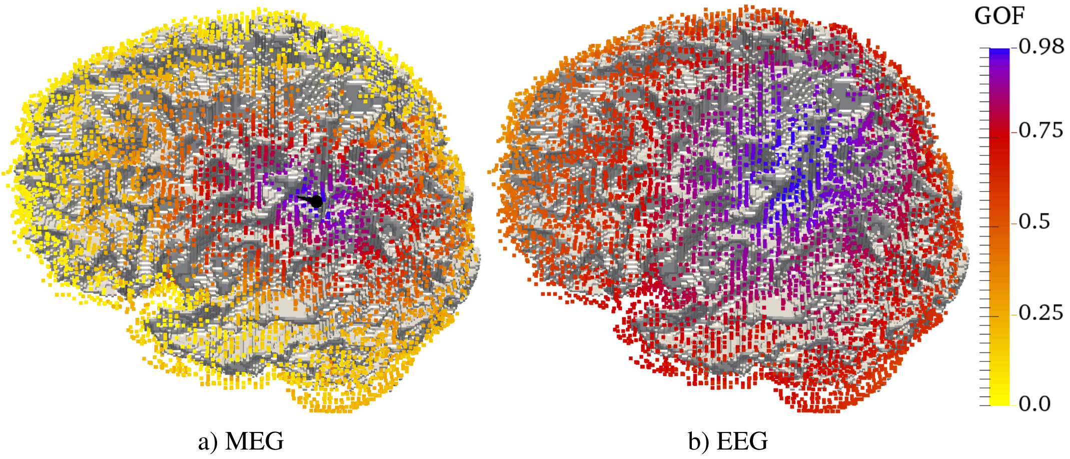

a) MEG b) EEG

Figure 9.1.: Goodness of fit (GOF) as defined in A.4 for each source space node as computed for an a) MEG and b) EEG single dipole deviation scan using the P20/N20 component of an SEF and SEP example data set. Standard conductivities as well as CG-FEM and the St. Venant source model were used for the MEG and EEG leadfield computations. The source grid is visualized on top of the white matter compartment. On the left, the dipole reconstructed in the calibration procedure is depicted in black.

alternative could be to complement the landmark-based registration approach with a more advanced surface-based fitting that uses a large sample of points on the scalp surface and aligns them to the head model surface (Theiß et al., 2016; Whalen et al., 2008). Theiß et al. (2016) compared these registration approaches and found average MEG source localization differences of 8.76 mm with a maximum value of 14.99 mm across 5 subjects. In this study, a realistic single shell model was used for the analysis. It is possible that a source space restricted to the gray matter compartment in a more distinctive model might affect these results. Due to registration errors, the optimal position might lie within a sulcus which is not included in the source grid, which might lead to sources with a similarly high fit on different sides of a gyrus or sulcus. Moreover, the new generation of OPM sensors, which can be placed adjacent to the scalp surface using a helmet, could contribute to reduce the co-registration errors in conventional cryogenic MEG systems due to small head movements in the dewar during the measurement period (Boto et al., 2018, 2017; Tierney et al., 2019). In addition, several other advanced methods have been suggested to reduce co-registration errors, such as fast camera-based measurement techniques for the digitization of sensor positions (Clausner et al., 2017) or 3D-printed subject-specific foam head-casts (Troebinger et al., 2014).

Overall, there are several factors that can influence the accuracy of the calibration result, especially in realistic scenarios, and some of them were investigated in the previous chapters. These influences can range from experimental parameters such as the size of the sensor array, the number of trials or noise levels to individual factors, e.g., source orientation or depth. Therefore, a useful tool to assess the reliability of the result could be to compute a certainty measure or confidence interval for the calibration result based on some of these factors and their influence on the skull conductivity estimation. Additionally, the quality of EEG and MEG measurements could be assessed based on factors such as their respective SNR. This measure could be used to estimate the reliability of both modalities in order to decide, e.g., if the tangential orientation component should be determined using EEG (Algorithm 1) or MEG (Variant 1).

Moreover, other SEP/SEF data (e.g., *tibialis* nerve stimulation or stimuli applied both at the left and right wrist) or auditory evoked responses could be used alternatively or in conjunction for a further stabilization of the proposed calibration approach (Schrader et al., 2020).

From a computational point of view, clinical applications and larger group studies require an efficient application of the algorithm. For the St. Venant and partial integration source models, the computationally expensive part is the assembly of the MEG transfer matrix. Using the multi-threading implemented in DUNEuro for the computation and multiplication with the MEG transfer matrix, the calibration procedure can easily be performed on a standard computer over night for a 1 mm resolution hexahedral mesh as done in Chapter 6. Possibly, modern approaches for the estimation of the conductivity-dependent leadfield matrices using model order reduction or hierarchical tensor formats together with leadfield interpolation might further reduce the computation times of the calibration pipeline (Beltrachini, 2017; Schrader et al., 2020; Werthmann et al., 2020).

Additionally, modern unfitted FEM approaches to solve the EEG/MEG forward problems, e.g., UDG or CutFEM (Nüßing, 2018; Nüßing et al., 2016), might be used for the leadfield computations in the calibration algorithm. These methods have the advantage that they do not require a geometry-conforming triangulation and might therefore reduce the complexity of the head volume conductor model generation. Similarly, new source modeling approaches, such as the localized subtraction approach (Lange, 2021; Nüßing, 2018), might be accurate and efficient alternatives to the source modeling approaches investigated in this thesis.

Future studies may also investigate the effects of applying the calibration algorithm with regard to the computation of optimized TES montages (Guler et al., 2016; Huang et al., 2017).

9.2. MEG sensitivity to head tissue conductivities

In our calibration procedure, we exploit the insensitivity of MEG in combination with the sensitivity of EEG to skull conductivity to fit this important parameter for an improved EEG and combined EEG/MEG analysis. A question we address here is whether the sensitivity of MEG to other head tissue conductivities in realistic head models could be used to estimate these (e.g., gray matter) conductivity parameters.

For a spherical head geometry, the analytical MEG forward solution is independent of tissue resistivities and radial sources do not produce a magnetic field outside the volume conductor (Sarvas, 1987). When comparing point magnetometers that measure the magnetic field components in radial and tangential orientation for tangentially oriented sources, however, two observations can be made (Piastra et al., 2018; Sarvas, 1987). First, for sensors measuring the radial field component, the contribution from the secondary magnetic field $\mathbf{B}^s$ is zero. Second, regarding the tangential field component, contributions from the primary and secondary magnetic fields almost cancel each other out.

For a realistically shaped head model, MEG was shown to be sensitive to tissue conductivities close to the source (Haueisen et al., 1997). This impact only exists through the contribution of the secondary magnetic field $\mathbf{B}^s$ that involves the integration of $\boldsymbol{\sigma}\nabla u$, as the primary magnetic field $\mathbf{B}^p$ does not depend on the conductivity profile. Based on the observation that the contribution of this secondary component is zero for radially measuring magnetometers in a spherical model, a hypothesis would be that this effect is more pronounced for (quasi-)tangentially measuring magnetometers.

Based on these considerations, it would be interesting to investigate if the predominantly tangentially oriented P20/N20 source of somatosensory evoked responses would have an impact on magnetometers measuring in (quasi-)tangential orientation that is large enough for a possible calibration of tissue conductivities close to the source in realistic models. Practically, this could be realized using the new generation of OPM sensors which could be placed directly on the scalp and (simultaneously) measure (quasi-)tangential and (quasi-) radial magnetic field components (Boto et al., 2018; Tierney et al., 2020). A sensitivity analysis similar to Vorwerk et al. (2019a) could provide further insights into the effects of varying tissue conductivities on the MEG forward solution, more precisely, on the magnetic field components evaluated close to the scalp in (quasi-)tangential and (quasi-)radial direction.

9.3. DUNEuro: Current projects and objectives

In this thesis, the DUNEuro toolbox was used to compute FEM solutions of the EEG/MEG forward problems. As an open-source software toolbox with bindings to MATLAB and Python, DUNEuro provides modern FEM discretizations and a variety of source modeling approaches. An overview of currently implemented features as well as installation instructions, documented test data and scripts are provided in Schrader et al. (2021), see also Section 8.2 for more details. In the following, we will address several ongoing projects and goals with regard to the development of this toolbox.

One important aspect with respect to the long-term maintainability and reliability of the code is related to a modern development workflow that includes a reliable testing infrastructure. The DUNEuro modules are hosted in a central GitLab repository[1] that offers a broad range of project management tools, including version control, code review and issue tracking. Besides the modules `duneuro`, `duneuro-py` and `duneuro-matlab`, this includes `duneuro-tests` which already provides system tests comparing the transfer matrix approach with the direct approach and EEG forward solutions with a reference solution for different mesh geometries, FEM and source modeling approaches. As DUNEuro is embedded in the DUNE framework, large parts of the code base on which DUNEuro relies, e.g., related to solvers or function spaces, are already part of an automated testing pipeline. However, further efforts are necessary to implement a complete continuous integration and delivery pipeline for DUNEuro. This could also include the provision of precompiled binaries for MATLAB and Python for different platforms which would also facilitate the integration into external toolboxes. Currently, the software is developed and used on Linux operating systems. As this limits its accessibility for many users, a more flexible usability from other operating systems is aspired. Technical problems, mainly associated with the Windows integration, have been partly solved in a manual compilation pipeline and are planned to be automated in the future.

Several FEM and source modeling approaches are already supported by DUNEuro, and users can easily switch between different methods by modifying parameters in the input configurations (Schrader et al., 2021). There are ongoing efforts to integrate further features, some of which already have a prototype implementation but need further testing and documentation. For instance, the mathematical formulations for electric and magnetic brain stimulation are closely related to the EEG and MEG forward problems based on Helmholtz reciprocity (Nolte, 2003; Vallaghé et al., 2008; Wagner et al., 2016). A first prototype implementation of transcranial electric stimulation is already integrated but requires further

---

[1] https://gitlab.dune-project.org/duneuro

testing. Moreover, additional FEM variants, e.g., CutFEM (Erdbrügger, 2021; Nüßing, 2018) or MixedFEM (Stubbemann, 2021; Vorwerk, 2016), and source models such as variants of the St. Venant approach (Barkhau, 2021; Nüßing, 2018) have been developed but are not fully supported yet.

In order to make the sophisticated numerical approaches in DUNEuro available for a broad range of applications, an integration into high-level toolboxes with a large number of users in the neuroscientific community is currently pursued. Popular non-commercial and multi-platform software tools which offer a complete analysis pipeline including EEG/MEG data preprocessing, source analysis and visualization are the MATLAB-based toolboxes BrainStorm (Tadel et al., 2011) and FieldTrip (Oostenveld et al., 2011) and the Python-based MNE-Python (Gramfort et al., 2013). While BrainStorm offers a graphical user interface, FieldTrip and MNE-Python functions can be called from scripts provided by the user. An integration into these tools will increase the usability of DUNEuro, allow an embedding in already existing analysis pipelines and facilitate comparisons to other methods, such as BEM approaches. In Section 8.2, details on the integration of EEG and MEG forward solutions using FEM approaches implemented in DUNEuro into the FieldTrip toolbox are provided. Additionally, parts of the functionality that DUNEuro offers have already been integrated in Brainstorm (Medani et al., 2021). In the future, this integration could be further improved and automated, e.g., by providing precompiled MATLAB bindings.

In addition to these ongoing efforts, a more detailed documentation would further facilitate the usability of the toolbox. Therefore, a declared aim is to extend the documentation of parameters and test scripts and include additional tutorials that cover further aspects and new features.

10. Summary

The conductive profile of the head volume conductor model, in particular skull conductivity, has a large impact on EEG-based source reconstructions (Montes-Restrepo et al., 2014; Vorwerk et al., 2019a) and on TES (Saturnino et al., 2019; Schmidt et al., 2015). Conductivities are most commonly assigned to homogenized tissue compartments based on literature values, although reported measured data is often inconsistent (McCann et al., 2019). This approach disregards variations in conductivity across and within subjects, e.g., based on age or pathology, which have been indicated for several tissue compartments including skull conductivity (Antonakakis et al., 2020; Hoekema et al., 2003; McCann et al., 2019; Wendel et al., 2010).

In this thesis, we presented a novel approach to calibrate head volume conductor models with respect to skull conductivity, whose importance in comparison to other head tissue conductivities has been emphasized in EEG and TES sensitivity analyses (Saturnino et al., 2019; Schmidt et al., 2015; Vallaghé and Clerc, 2009; Vorwerk et al., 2019a).

The calibration procedure utilizes the complementary properties of the non-invasive modalities of EEG and MEG, for which ethical approval is commonly obtained without difficulties. It thereby relies on measurements performed under *in vivo* conditions and in the relevant frequency range, as resistivity measurements of head tissues vary for different frequencies (Akhtari et al., 2002; Stinstra and Peters, 1998; Tang et al., 2009). The calibration procedure requires a short block of SEP/SEF data acquisition which can then be used to simultaneously reconstruct the generator of the early P20/N20 component and to fit the skull conductivity parameter that best explains the data in combination with the volume conductor model. Within the calibration algorithm, Brent's method (Brent, 1973) is used to find the best fitting skull conductivity in a continuous parameter space, which results in more accurate results using a comparable number of iterations compared to similar discrete manual approaches (Antonakakis et al., 2020, 2019; Aydin et al., 2014). By providing a comprehensive mathematical description and by using an optimization method to iteratively update the skull conductivity parameter, an automated calibration procedure is suggested that can be easily integrated into existing analysis pipelines. For the numerical computation of EEG/MEG forward solutions, the DUNEuro toolbox is used that offers a variety of source model discretizations for FEM approaches.

The accuracy of the calibration procedure was evaluated in spherical head volume conductor models, for which (quasi-)analytical solutions of the EEG and MEG forward problems exist, using realistic noise levels and test dipole characteristics. Subsequently, realistic head models of healthy participants were calibrated using different settings and somatosensory experiments. The results indicate that for sources resembling the neuronal generator of the early somatosensory evoked P20/N20 component, calibrated skull conductivity can be estimated under realistic noise conditions. Additionally, source reconstruction errors resulting from incorrectly assigned scalp conductivity values could be mitigated when using the fitted value as opposed to the standard skull conductivity. Regarding different somatosensory experiments, electric stimulation of the median nerve at the wrist resulted in the best SNR and therefore the most accurate results among the investigated experimental designs.

The individualized head models that are created by applying the calibration procedure can be used for EEG or combined EEG/MEG source analysis, e.g., for the localization of interictal activity in presurgical epilepsy diagnosis (Aydin et al., 2017), or for optimized individual multi-channel TES setups (Guler et al., 2016; Huang et al., 2017; Wagner et al., 2016). Thus, a feasible automatic calibration pipeline is presented in this thesis which is a promising new method to replace commonly used standard models by individually calibrated volume conductor models that could lead to more reliable EEG or combined EEG/MEG source analysis results and improved targeting in individually optimized TES in the future.

A. Appendix

A.1. Background to single dipole deviation scans

In the following, general background to solving the inverse EEG/MEG problem using a single dipole deviation scan (SDDS) is provided. We start by introducing (truncated) singular value decompositions based on (Golub and Kahan, 1965).

Definition A.1: ***Singular value decomposition (SVD).*** *For any matrix* $\mathbf{A} \in \mathbb{R}^{m \times n}$ *there exists a decomposition of the form*

$$\mathbf{A} = \mathbf{U}\mathbf{\Sigma}\mathbf{V}^T,$$

with orthogonal matrices $\mathbf{U} \in \mathbb{R}^{m \times m}$ *and* $\mathbf{V} \in \mathbb{R}^{n \times n}$*, and a rectangular diagonal matrix* $\mathbf{\Sigma} \in \mathbb{R}^{m \times n}$ *that contains its non-negative singular values.*

A matrix can be approximated by a matrix of lower rank using a truncated SVD, as described in the following (Golub and Kahan, 1965).

Definition A.2: ***Truncated singular value decomposition (TSVD).*** *A matrix* $\mathbf{A} \in \mathbb{R}^{m \times n}$ *of rank* $r \in \mathbb{N}$*,* $r \leq \min\{m, n\}$ *can be approximated using a truncated singular value decomposition by a matrix* $\hat{\mathbf{A}} \in \mathbb{R}^{m \times n}$ *with rank* $p \in \mathbb{N}$*,* $p < r$ *defined as*

$$\hat{\mathbf{A}} = \mathbf{U}\hat{\mathbf{\Sigma}}\mathbf{V}^T,$$

with $\mathbf{U}$ *and* $\mathbf{V}$ *as defined in Def. A.1, and with* $\hat{\mathbf{\Sigma}}$ *obtained from* $\mathbf{\Sigma}$ *in Def. A.1 by replacing all except the* p *highest singular values by 0.*

For practical reasons related to the computation and storage, a (T)SVD can be expressed in a more compact form in case $m \neq n$ or not all singular values are non-zero.

Remark A.1: ***Compact representation.*** *A (T)SVD related to the p-rank approximation of a matrix* $\mathbf{A} \in \mathbb{R}^{m \times n}$ *with* $p \leq rank(A)$ *can be expressed in a more compact form* $\hat{\mathbf{A}} = \tilde{\mathbf{U}}\tilde{\mathbf{\Sigma}}\tilde{\mathbf{V}}^T$*, where* $\tilde{\mathbf{U}} \in \mathbb{R}^{m \times p}$*,* $\tilde{\mathbf{V}} \in \mathbb{R}^{n \times p}$ *and* $\tilde{\mathbf{\Sigma}} \in \mathbb{R}^{p \times p}$ *are obtained from the corresponding matrices in Def. A.1 or Def. A.2 with removed columns and rows which are multiplied with 0.*

In the following, a generalization of the concept of inverse matrices for non-square or singular matrices is introduced. The following definition of the Moore-Penrose or pseudo-inverse of a matrix is based on Planitz (1979).

Definition A.3: ***Moore-Penrose inverse.*** *The Moore-Penrose inverse* $[\mathbf{A}]^+ \in \mathbb{R}^{n\times m}$ *of a matrix* $\mathbf{A} \in \mathbb{R}^{m\times n}$ *satisfies the following criteria*

$$\begin{array}{llll} i) & \mathbf{A}[\mathbf{A}]^+\mathbf{A} = \mathbf{A} & iii) & (\mathbf{A}[\mathbf{A}]^+)^T = \mathbf{A}[\mathbf{A}]^+ \\ ii) & [\mathbf{A}]^+\mathbf{A}[\mathbf{A}]^+ = [\mathbf{A}]^+ & iv) & ([\mathbf{A}]^+\mathbf{A})^T = [\mathbf{A}]^+\mathbf{A}. \end{array}$$

A generalized inverse that satisfies the conditions above exists for any matrix and is unique (James, 1978). The Moore-Penrose inverse can be computed using the SVD of a matrix, as defined in Def. A.1 (Golub and Kahan, 1965).

Remark A.2: ***Computation of the Moore-Penrose inverse.*** *The pseudo-inverse of a matrix* $\mathbf{A} \in \mathbb{R}^{m\times n}$ *with SVD* $\mathbf{A} = \mathbf{U}\mathbf{\Sigma}\mathbf{V}^T$ *(see Def. A.1) can be computed by*

$$[\mathbf{A}]^+ = \mathbf{V}[\mathbf{\Sigma}]^+\mathbf{U}^T,$$

where $[\mathbf{\Sigma}]^+$ *is obtained from* $\mathbf{\Sigma}$ *by replacing the non-zero singular values by their reciprocals.*

The main value of the pseudo-inverse is related to solving linear least-squares problems, as summarized in the following finding from Planitz (1979) which also contains the respective proof.

Corollary A.1. *For* $\mathbf{A} \in \mathbb{R}^{m\times n}$ *and* $\mathbf{b} \in \mathbb{R}^m$*, the unique vector* $\mathbf{x} \in \mathbb{R}^n$ *with the smallest Euclidean norm that minimizes* $||\mathbf{A}\mathbf{x} - \mathbf{b}||_2$ *is given by* $\mathbf{x} = [\mathbf{A}]^+\mathbf{b}$.

In the following, the concept of a single dipole deviation scan is introduced, which is a simple inverse method assuming that measured activity originates from one dipolar source (Brette and Destexhe, 2012; Fuchs et al., 2000; Hämäläinen et al., 1993; Sarvas, 1987).

Definition A.4: ***Singe dipole deviation scan (SDDS).*** *Let* $\mathbf{m} \in \mathbb{R}^N$ *denote a given measurement at* $N \in \mathbb{N}$ *sensors,* $S = \{\mathbf{x}_1, \ldots, \mathbf{x}_n\}$*,* $n \in \mathbb{N}$ *a set of possible source locations and* $\mathbf{L}(\mathbf{x}) \in \mathbb{R}^{N\times 3}$ *the leadfield for a dipole at position* $\mathbf{x} \in S$ *in all Cartesian directions. Then, the dipole which best explains the data is located at* $\hat{\mathbf{x}} \in S$ *with*

$$\hat{\mathbf{x}} = \operatorname*{argmin}_{\mathbf{x}\in S} ||\mathbf{L}(\mathbf{x})\hat{\mathbf{q}}(\mathbf{x}) - \mathbf{m}||_2^2, \quad \textit{where } \hat{\mathbf{q}}(\mathbf{x}) = \operatorname*{argmin}_{\mathbf{q}\in\mathbb{R}^3} ||\mathbf{L}(\mathbf{x})\mathbf{q} - \mathbf{m}||_2 \textit{ for any } \mathbf{x} \in S,$$

with the optimal moment vector $\hat{\mathbf{q}}(\mathbf{x}) \in \mathbb{R}^3$.

Remark A.3. *Following Corollary A.1, the solution with minimal Euclidean norm of the least-squares problem of finding the best fitting moment* $\hat{\mathbf{q}}$ *can be computed using the pseudo-inverse of the leadfield matrix as* $\hat{\mathbf{q}}(\mathbf{x}) = [\mathbf{L}(\mathbf{x})]^{+}\mathbf{m}$.

Thereby, an SDDS scans a grid of possible dipole locations and finds the location, which in combination with the optimal dipole moment, best explains the measured data, i.e., the goodness of fit measure defined in Section A.4 is maximized.

A.2. Background to the optimization method

In this section, basic concepts and findings related to the optimization method for the calibration procedure are presented. As an important preliminary, we first introduce the concept of unimodality following Brent (1973).

Definition A.5: ***Unimodal function.*** *A function* $f : \Omega \to \mathbb{R}$, $\Omega \subset \mathbb{R}$ *is called unimodal on the interval* $[a,b] \subset \Omega$, *if there exists a unique inside value* $\mu \in [a,b]$ *such that f is strictly monotonic decreasing and strictly monotonic increasing either on the intervals* $[a,\mu]$ *and* $(\mu,b]$, *respectively, or on* $[a,\mu)$ *and* $[\mu,b]$.

This definition does not require the function to be continuous, but if it is, the following statement can be made (Brent, 1973).

Corollary A.2. *If a function* $f : \Omega \to \mathbb{R}$ *is unimodal and continuous on* $[a,b] \subset \Omega \subset \mathbb{R}$, *then f reaches its minimum exactly once on [a,b], at the point* μ *of Def. A.5.*

Due to rounding in floating point arithmetic computations, it is important to note that the computed approximation of a unimodal function f is not unimodal, as it is constant for small intervals of points with the same floating point approximation. In Brent (1973), the theory related to unimodality is therefore generalized to δ-unimodality, considering only function evaluations at points whose distance is at least δ.

In the following, we introduce two minimization methods for unimodal functions, *Golden-section search* and *inverse parabolic interpolation*. We start by describing how a function minimum can be bracketed. While the root of a function exists in an interval defined by two points whose function evaluations have different signs, the existence of a minimum requires to know function evaluations at three points as described in the following definition based on Press et al. (2007).

Definition A.6: ***Bracketing of minimum.*** *The minimum of a function $f : \Omega \to \mathbb{R}$ is bracketed by a triplet of points $\{a, x_1, b\} \subset \Omega$ with $a < x_1 < b$, if $f(x_1) < \min\{f(a), f(b)\}$.*

A simple method for finding the minimum of a unimodal function is the Golden-section search, which is described in the following based on Press et al. (2007) and Brent (1973). It can be understood as the equivalent of the bisection method for finding the root of a function, as it consists of successively narrowing the search interval by a constant factor.

Definition A.7: ***Golden-section search.*** *Given an initial bracketing of the minimum of a unimodal function by the triplet $\{a, x_1, b\}$, let s denote the larger subinterval, i.e., $[a, x_1]$ or $[x_1, b]$. The next point is then constructed from the middle point x_1 by moving a distance $\frac{1}{\phi^2}|s|$ into s. Hereby, $\phi := \frac{1+\sqrt{5}}{2}$ denotes the golden ratio. A new bracketing interval is then constructed based on the minimal function evaluation of all previously considered points and its neighbors, and this iteration is repeated until a tolerance criterion is met.*

Remark A.4. *By consistently applying Golden-section search iterations, the ratio between the larger and smaller subinterval within the bracketing interval is equal to ϕ. Additionally, the iteratively constructed new interval is $1/\phi$ times the size of the previous one, thereby assuring linear convergence (Press et al., 2007).*

In the following, inverse parabolic interpolation is described as an additional minimization method for unimodal functions following Press et al. (2007) and Brent (1973), which can be understood as the counterpart of inverse linear interpolation for root-finding problems.

Definition A.8: ***Inverse parabolic interpolation.*** *Given an initial bracketing of the minimum of a unimodal function f by the triplet $\{a, x_1, b\}$, a parabola is fitted through these points and the abscissa of the minimum is computed as*

$$x_2 = b - \frac{1}{2} \frac{(b-a)^2(f(b)-f(x_1)) - (b-x_1)^2(f(b)-f(a))}{(b-a)(f(b)-f(x_1)) - (b-x_1)(f(b)-f(a))}. \tag{A.1}$$

A new bracketing interval is then constructed based on the point with minimal function evaluation of all previously considered points and its neighbors, and this iteration is repeated until a tolerance criterion is met.

Remark A.5. *The term in (A.1) is not defined if the three points through which the parabola is fitted are collinear, as the denominator is zero in that case. In general, convergence of successive parabolic interpolation is not guaranteed. However, if the function is sufficiently regular, convergence is superlinear with an order of approximately 1.325 (Brent, 1973).*

Based on these two minimization techniques, Brent's method is described in the following. The motivation of Brent's method is to benefit from the convergence properties of inverse parabolic fitting if the function allows, but rely on Golden-section search otherwise to ensure reliability. One of its main advantages is that it does not require the computation of derivatives. We provide a short description in the following, a detailed algorithmic description of Brent's method can be found in Brent (1973) and Press et al. (2007).

Definition A.9: ***Brent's method.*** *Given a function* $f : \Omega \to \mathbb{R}$, $\Omega \subset \mathbb{R}$ *which is unimodal on an interval* $[a,b] \subset \Omega$, *an initial inside point is determined using a Golden-section iteration (Def. A.7). Subsequently, inverse parabolic interpolation (Def. A.8) is attempted. The function is evaluated at the minimum of the parabola if this point lies inside the current bracketing interval and if it entails a movement from the current point with the lowest function evaluation that is less than half of the movement of the second last step. Otherwise, the function is evaluated at the point proposed by Golden-section search. In every iteration, the method updates six not necessarily distinct points: the interval boundaries that contain the minimum, values with the least and second least function evaluations, the former value of the latter and the last evaluated point. This cycle is repeated until the tolerance criterion is reached, i.e., the suggested value in the next iteration does not vary significantly any more with respect to a predefined tolerance.*

A.3. Spherical head models

The spherical head model used for validation purposes consists of four concentric spheres which correspond to the tissue types of brain, CSF, skull and scalp. A least-squares fit was used to fit a standard sphere model to the electrode positions of a subject who participated in a somatosensory experiment, keeping the ratios between the respective radii unchanged. The analytical characteristics, i.e., the standard conductivity values and the radii of both the standard and the fitted sphere model are summarized in Table A.1.

In many test scenarios, dipoles at different eccentricities relative to the inner sphere surface representing the brain tissue boundary are considered. For a given inner radius $r_1 \in \mathbb{R}$ and sphere center $\mathbf{c} \in \mathbb{R}^3$ this measure is defined as

$$\mathrm{ECC}(\mathbf{x}) := \frac{\|\mathbf{x} - \mathbf{c}\|_2}{r_1},$$

for any dipole position $\mathbf{x} \in \mathbb{R}^3$.

Table A.1.: Analytical properties of four-layer spherical head model (Baumann et al., 1997; Dannhauer et al., 2011; Haueisen et al., 1997; Ramon et al., 2004).

Tissue	**Standard model: radii (mm)**	**Fitted model: radii (mm)**	**Conductivity (S/m)**
Scalp	92	89.1	0.43
Skull	86	83.3	0.01
CSF	80	77.5	1.79
Brain	78	75.6	0.33

A.4. Common error measures

In the following, different error measures that are used within this thesis are defined. The relative difference measure (RDM) and the magnitude error (MAG) are indicators to compare two discrete EEG/MEG solutions $\mathbf{u}_{\text{num}}$, $\mathbf{u}_{\text{ref}} \in \mathbb{R}^N$, where N denotes the number of sensors (Brette and Destexhe, 2012; Meijs et al., 1989). A solution of interest $\mathbf{u}_{\text{num}}$ is compared to a reference solution $\mathbf{u}_{\text{ref}}$, e.g., the (quasi-)analytical expressions in spherical models or experimentally measured data. Both errors are often used in combination, as the RDM measures the error related to the topography, while the MAG errors are related to the magnitude of the solution. The RDM (%) and MAG (%) errors are given as

$$\begin{aligned} \text{RDM}(\mathbf{u}_{\text{num}}, \mathbf{u}_{\text{ref}}) &:= 50 \cdot \left\| \frac{\mathbf{u}_{\text{num}}}{||\mathbf{u}_{\text{num}}||_2} - \frac{\mathbf{u}_{\text{ref}}}{||\mathbf{u}_{\text{ref}}||_2} \right\|_2 \%, \\ \text{MAG}(\mathbf{u}_{\text{num}}, \mathbf{u}_{\text{ref}}) &:= 100 \cdot \left(\frac{||\mathbf{u}_{\text{num}}||_2}{||\mathbf{u}_{\text{ref}}||_2} - 1 \right) \%. \end{aligned}$$

The RDM has a lower bound and optimum ($\mathbf{u}_{\text{num}} = \mathbf{u}_{\text{ref}}$) of 0% and an upper bound of 100%, while the MAG error has an optimum of 0%, with a lower bound of -100% and no upper limit.

In addition to these error measures, the residual variance (RV) or goodness of fit (GOF) measures are frequently used, e.g., in the context of single dipole deviation scans (Brette and Destexhe, 2012; Hämäläinen et al., 1993). The relative residual variance indicates the degree to which the computed solution differs from the reference solution and is defined as

$$\text{RV}(\mathbf{u}_{\text{num}}, \mathbf{u}_{\text{ref}}) := \frac{||\mathbf{u}_{\text{num}} - \mathbf{u}_{\text{ref}}||_2^2}{||\mathbf{u}_{\text{ref}}||_2^2}$$

with a minimal and optimal value of 0 indicating that both solutions are identical. Often, the residual variance is indicated in percentage as $\mathrm{RV} = 100 \cdot \mathrm{RV}\ \%$. The goodness of fit (GOF) is closely related to the RV and is computed as

$$\mathrm{GOF}(\mathbf{u}_{\mathrm{num}}, \mathbf{u}_{\mathrm{ref}}) := 1 - \mathrm{RV}(\mathbf{u}_{\mathrm{num}}, \mathbf{u}_{\mathrm{ref}}).$$

It indicates the degree to which the reference data can be explained and is often indicated in percentage as $\mathrm{GOF} = 100 \cdot \mathrm{GOF}\ \%$, similar to the RV.

A.5. Software tools

Numerous open-source tools were essential for the completion of this work, the most important ones are listed here in alphabetical order:

DUNE: functionality related to solving partial differential equations using FEM approaches, e.g., grid managers, linear solvers (Bastian et al., 2008a,b; Sander, 2020), see `https://www.dune-project.org`

DUNEuro: EEG and MEG forward solutions using FEM approaches and the subtraction, partial integration and St. Venant source models (Schrader et al., 2021), see `http://duneuro.org`

FieldTrip: EEG and MEG data preprocessing and analysis, e.g., filtering, artifact rejection, trial selection, averaging, GMFP computation, visualization of 2D topographies and generation of hexahedral spherical meshes (Oostenveld et al., 2011), see `https://www.fieldtriptoolbox.org/`

Gmsh: creation of tetrahedral spherical meshes (Geuzaine and Remacle, 2009), see `https://gmsh.info`

Inkscape: drawing of schematics and figures, see `https://inkscape.org/`

LaTeX: typesetting this thesis, see `https://www.latex-project.org`

ParaView: visualization of meshes and related data, e.g., tissue conductivities or surface potentials (Ahrens et al., 2005), see `https://www.paraview.org`

simbiosphere: computation of quasi-analytical EEG forward solutions in concentric sphere models based on implementations of the SimBio library (`https://www.mrt.uni-jena.de/simbio/index.php?title=Main_Page`), see `https://gitlab.dune-project.org/duneuro/simbiosphere`

List of Symbols

$\mathbf{A}$	Stiffness matrix
$\hat{\mathbf{A}}$	Magnetic vector potential
$\mathbf{B}$	Magnetic field
$\mathbf{B}^p$	Primary magnetic field
$\mathbf{B}^s$	Secondary magnetic field
$\mathbf{D}$	Electric displacement field
δ	Dirac delta distribution
$\mathbf{E}$	Electric field
ε_0	Permittivity of free space
ε_r	Relative permittivity
$\mathbf{H}$	Magnetizing field
$H^k(\Omega)$	Sobolev space of $L^2(\Omega)$ functions with derivatives up to order $k \in \mathbb{N}$ in $L^2(\Omega)$
$H^k_*(\Omega)$	Sobolev space of functions in $H^k(\Omega)$ with zero mean
$\mathbf{j}$	Current density
$\mathbf{j}^p$	Primary current density
$\mathbf{j}^s$	Secondary current density
$\mathbf{L}$	Leadfield matrix
μ_0	Permeability of free space
μ_r	Relative permeability
$\mathbf{q}$	Dipole moment
ρ	Electric charge density
$\boldsymbol{\sigma}, \sigma$	Electrical conductivity
$\mathbf{T}$	Transfer matrix
u	Electrical potential
$[\cdot]^+$	Moore-Penrose pseudo-inverse of a matrix

Acronyms

BT	Braille-tactile stimulation
CAR	Common average reference
CG	Continuous Galerkin
CSF	Cerebrospinal fluid
DAC	Directly applied current
DG	Discontinuous Galerkin
DTI	Diffusion tensor imaging
EEG	Electroencephalography
EIT	Electrical impedance tomography
EW	Electric-wrist stimulation
FCD	Focal cortical dysplasia
FEM	Finite element method
fMRI	Functional magnetic resonance imaging
GMFP	Global mean field power
GOF	Goodness of fit
MAG	Magnitude error
MEG	Magnetoencephalography
MRI	Magnetic resonance imaging
OPM	Optically pumped magnetometer
PT	Pneumato-tactile stimulation
RDM	Relative difference measure
RV	Residual variance
SDDS	Single dipole deviation scan
SEF	Somatosensory evoked field
SEP	Somatosensory evoked potential
SNR	Signal-to-noise ratio

SOA	Stimulus onset asynchrony
SQUID	Superconducting quantum interference device
SVD	Singular value decomposition
TES	Transcranial electric stimulation
TSVD	Truncated singular value decomposition
UDG	Unfitted discontinuous Galerkin

Bibliography

Abascal, J.-F. P. J., Arridge, S. R., Atkinson, D., Horesh, R., Fabrizi, L., De Lucia, M., Horesh, L., Bayford, R. H., and Holder, D. S. (2008). Use of anisotropic modelling in electrical impedance tomography; Description of method and preliminary assessment of utility in imaging brain function in the adult human head. *NeuroImage*, 43(2):258–268. doi:10.1016/j.neuroimage.2008.07.023.

Ahlfors, S. P., Han, J., Belliveau, J. W., and Hämäläinen, M. S. (2010). Sensitivity of MEG and EEG to source orientation. *Brain Topography*, 23(3):227–232. doi:10.1007/s10548-010-0154-x.

Ahrens, J., Geveci, B., and Law, C. (2005). ParaView: An end-user tool for large data visualization. In Hansen, C. D. and Johnson, C. R. (Editors), *The Visualization Handbook*, pages 717–731. Burlington: Butterworth-Heinemann. ISBN 9780123875822.

Akalin Acar, Z., Acar, C. E., and Makeig, S. (2016). Simultaneous head tissue conductivity and EEG source location estimation. *NeuroImage*, 124:168–180. doi:10.1016/j.neuroimage.2015.08.032.

Akalin Acar, Z. and Makeig, S. (2013). Effects of forward model errors on EEG source localization. *Brain Topography*, 26(3):378–396. doi:10.1007/s10548-012-0274-6.

Akhtari, M., Bryant, H. C., Mamelak, A. N., Flynn, E. R., Heller, L., Shih, J. J., Mandelkern, M., Matlachov, A., Ranken, D. M., Best, E. D., DiMauro, M. A., Lee, R. R., and Sutherling, W. W. (2002). Conductivities of three-layer human skull. *Brain Topography*, 14(3):151–167. doi:10.1023/A:1007882102297.

Allison, T., McCarthy, G., Wood, C. C., and Jones, S. J. (1991). Potentials evoked in human and monkey cerebral cortex by stimulation of the median nerve. A review of scalp and intracranial recordings. *Brain*, 114(6):2465–2503. doi:10.1093/brain/114.6.2465.

Altakroury, H. F. (2017). *In-vivo human head conductivity estimation by SEEG and EEG recorded in simultaneous with intracerebral electrical stimulation*. Ph.D. thesis, Université de Lorraine. Available from: https://tel.archives-ouvertes.fr/tel-01709247.

Antonakakis, M., Schrader, S., Aydin, Ü., Khan, A., Gross, J., Zervakis, M., Rampp, S., and Wolters, C. H. (2020). Inter-subject variability of skull conductivity and thickness in calibrated realistic head models. *NeuroImage*, 223:117353. doi:10.1016/j.neuroimage.2020.117353.

Antonakakis, M., Schrader, S., Wollbrink, A., Oostenveld, R., Rampp, S., Haueisen, J., and Wolters, C. H. (2019). The effect of stimulation type, head modeling, and combined EEG and MEG on the source reconstruction of the somatosensory P20/N20 component. *Human Brain Mapping*, 40(17):5011–5028. doi:10.1002/hbm.24754.

Awada, K., Jackson, D., Williams, J., Wilton, D., Baumann, S., and Papanicolaou, A. (1997). Computational aspects of finite element modeling in EEG source localization. *IEEE Transactions on Biomedical Engineering*, 44(8):736–752. doi:10.1109/10.605431.

Aydin, Ü., Rampp, S., Wollbrink, A., Kugel, H., Cho, J.-H., Knösche, T. R., Grova, C., Wellmer, J., and Wolters, C. H. (2017). Zoomed MRI guided by combined EEG/MEG source analysis: A multimodal approach for optimizing presurgical epilepsy work-up and its application in a multi-focal epilepsy patient case study. *Brain Topography*, 30(4):417–433. doi:10.1007/s10548-017-0568-9.

Aydin, U., Vorwerk, J., Dümpelmann, M., Küpper, P., Kugel, H., Heers, M., Wellmer, J., Kellinghaus, C., Haueisen, J., Rampp, S., Stefan, H., and Wolters, C. H. (2015). Combined EEG/MEG can outperform single modality EEG or MEG source reconstruction in presurgical epilepsy diagnosis. *PLOS ONE*, 10(3):1–29. doi:10.1371/journal.pone.0118753.

Aydin, Ü., Vorwerk, J., Küpper, P., Heers, M., Kugel, H., Galka, A., Hamid, L., Wellmer, J., Kellinghaus, C., Rampp, S., and Wolters, C. H. (2014). Combining EEG and MEG for the reconstruction of epileptic activity using a calibrated realistic volume conductor model. *PLOS ONE*, 9(3):e93154. doi:10.1371/journal.pone.0093154.

Azizollahi, H., Aarabi, A., and Wallois, F. (2016). Effects of uncertainty in head tissue conductivity and complexity on EEG forward modeling in neonates. *Human Brain Mapping*, 37(10):3604–3622. doi:10.1002/hbm.23263.

Azizollahi, H., Darbas, M., Diallo, M. M., El Badia, A., and Lohrengel, S. (2018). EEG in neonates: Forward modeling and sensitivity analysis with respect to variations of the conductivity. *Mathematical Biosciences & Engineering*, 15(4):905–932. doi:10.3934/mbe.2018041.

Baillet, S. (2017). Magnetoencephalography for brain electrophysiology and imaging. *Nature Neuroscience*, 20:327–339. doi:10.1038/nn.4504.

Barkhau, C. (2021). *Evaluation of the Multipolar Venant Source Modeling Approach in EEG Source Analysis*. Master's thesis, Westfälische Wilhelms-Universität Münster.

Barkley, G. L. and Baumgartner, C. (2003). MEG and EEG in epilepsy. *Journal of Clinical Neurophysiology*, 20(3):163–178. doi:10.1097/00004691-200305000-00002.

Bastian, P., Blatt, M., Dedner, A., Engwer, C., Klöfkorn, R., Kornhuber, R., Ohlberger, M., and Sander, O. (2008a). A generic grid interface for parallel and adaptive scientific computing. Part II: Implementation and tests in DUNE. *Computing*, 82(2):121–138. doi:10.1007/s00607-008-0004-9.

Bastian, P., Blatt, M., Dedner, A., Engwer, C., Klöfkorn, R., Ohlberger, M., and Sander, O. (2008b). A generic grid interface for parallel and adaptive scientific computing. Part I: Abstract framework. *Computing*, 82(2):103–119. doi:10.1007/s00607-008-0003-x.

Bauer, M., Pursiainen, S., Vorwerk, J., Köstler, H., and Wolters, C. H. (2015). Comparison study for Whitney (Raviart-Thomas)-type source models in finite-element-method-based EEG forward modeling. *IEEE Transactions on Biomedical Engineering*, 62(11):2648–2656. doi:10.1109/TBME.2015.2439282.

Baumann, S. B., Wozny, D. R., Kelly, S. K., and Meno, F. M. (1997). The electrical conductivity of human cerebrospinal fluid at body temperature. *IEEE Transactions on Biomedical Engineering*, 44(3):220–223. doi:10.1109/10.554770.

Baysal, U. and Haueisen, J. (2004). Use of a priori information in estimating tissue resistivities – application to human data in vivo. *Physiological Measurement*, 25(3):737–748. doi:10.1088/0967-3334/25/3/013.

Beltrachini, L. (2017). A reduced order modelling approach for fast generation of lead field matrices. In *BACI 2017 – 2nd International Conference on basic and clinical multimodal imaging, Bern (Switzerland), abstract 157*.

Beltrachini, L. (2018). A finite element solution of the forward problem in EEG for multipolar sources. *IEEE Transactions on Neural Systems and Rehabilitation Engineering*, 27(3):368–377. doi:10.1109/TNSRE.2018.2886638.

Beltrachini, L. (2019). The analytical subtraction approach for solving the forward problem in EEG. *Journal of Neural Engineering*, 16(5):056029. doi:10.1088/1741-2552/ab2694.

Berger, H. (1929). Über das Elektrenkephalogramm des Menschen. *Archiv für Psychiatrie und Nervenkrankheiten*, 87(5):527–570. doi:10.1007/BF01797193.

Bertrand, O., Thévenet, M., and Perrin, F. (1991). *3D finite element method in brain electrical activity studies*. Report of the department of technical physics. Biomagnetic localization and 3D modelling, pp.154-171, Helsinki University of Technology.

Bikson, M., Grossman, P., Thomas, C., Zannou, A. L., Jiang, J., Adnan, T., Mourdoukoutas, A. P., Kronberg, G., Truong, D., Boggio, P., Brunoni, A. R., Charvet, L., Fregni, F., Fritsch, B., Gillick, B., Hamilton, R. H., Hampstead, B. M., Jankord, R., Kirton, H., Adamand Knotkova, Liebetanz, D., Liu, A., Loo, C., Nitsche, M. A., Reis, J., Richardson, J. D., Rotenberg, A., Turkeltaub, P. E., and Woods, A. J. (2016). Safety of transcranial direct current stimulation: Evidence based update 2016. *Brain Stimulation*, 9(5):641–661. doi:10.1016/j.brs.2016.06.004.

Birot, G., Spinelli, L., Vulliémoz, S., Mégevand, P., Brunet, D., Seeck, M., and Michel, C. M. (2014). Head model and electrical source imaging: A study of 38 epileptic patients. *NeuroImage: Clinical*, 5:77–83. doi:10.1016/j.nicl.2014.06.005.

Blausen Medical (2014). Medical gallery of Blausen Medical 2014 (Blausen.com staff). *Wikijournal of Medicine*, 1(2). doi:10.15347/wjm/2014.010.

Borna, A., Carter, T. R., Colombo, A. P., Jau, Y.-Y., McKay, J., Weisend, M., Taulu, S., Stephen, J. M., and Schwindt, P. D. D. (2020). Non-invasive functional-brain-imaging with an OPM-based magnetoencephalography system. *PLOS ONE*, 15(1):1–24. doi: 10.1371/journal.pone.0227684.

Boto, E., Holmes, N., Leggett, J., Roberts, G., Shah, V., Meyer, S. S., Muñoz, L. D., Mullinger, K. J., Tierney, T. M., Bestmann, S., Barnes, G. R., Bowtell, R., and Brookes, M. J. (2018). Moving magnetoencephalography towards real-world applications with a wearable system. *Nature*, 555:657–661. doi:10.1038/nature26147.

Boto, E., Meyer, S. S., Shah, V., Alem, O., Knappe, S., Kruger, P., Fromhold, T. M., Lim, M., Glover, P. M., Morris, P. G., Bowtell, R., Barnes, G. R., and Brookes, M. J. (2017). A new generation of magnetoencephalography: Room temperature measurements using optically-pumped magnetometers. *NeuroImage*, 149:404–414. doi: 10.1016/j.neuroimage.2017.01.034.

Braess, D. (2007). *Finite Elemente: Theorie, schnelle Löser und Anwendungen in der*

Elastizitätstheorie (4. Aufl.). Springer-Lehrbuch. Springer Berlin Heidelberg. ISBN 9783540724490.

Brent, R. P. (1973). *Algorithms for Minimization without Derivatives*. Englewood Cliffs, New Jersey: Prentice-Hall Inc. ISBN 0130223352.

Brette, R. and Destexhe, A. (Editors) (2012). *Handbook of neural activity measurement*. Cambridge: Cambridge University Press. ISBN 9780511979958.

Bronstein, I. N., Semendjajew, K. A., Musiol, G., and Mühlig, H. (2008). *Taschenbuch der Mathematik*. Classics in Applied Mathematics. Frankfurt a. M.: Wissenschaftlicher Verlag Harri Deutsch GmbH. ISBN 9783817120079.

Buchner, H., Fuchs, M., Wischmann, H. A., Dössel, O., Ludwig, I., Knepper, A., and Berg, P. (1994). Source analysis of median nerve and finger stimulated somatosensory evoked potentials: Multichannel simultaneous recording of electric and magnetic fields combined with 3D-MR tomography. *Brain Topography*, 6(4):299–310. doi:10.1007/BF01211175.

Buchner, H., Knoll, G., Fuchs, M., Rienäcker, A., Beckmann, R., Wagner, M., Silny, J., and Pesch, J. (1997). Inverse localization of electric dipole current sources in finite element models of the human head. *Electroencephalography and Clinical Neurophysiology*, 102(4):267–78. doi:10.1016/s0013-4694(96)95698-9.

Camacho, D. L., Hopper, R. H., Lin, G. M., and Myers, B. S. (1997). An improved method for finite element mesh generation of geometrically complex structures with application to the skullbase. *Journal of Biomechanics*, 30(10):1067–1070. doi:10.1016/S0021-9290(97)00073-0.

Chella, F., Marzetti, L., Stenroos, M., Parkkonen, L., Ilmoniemi, R. J., Romani, G. L., and Pizzella, V. (2019). The impact of improved MEG-MRI co-registration on MEG connectivity analysis. *NeuroImage*, 197:354–367. doi:10.1016/j.neuroimage.2019.04.061.

Chen, F., Hallez, H., and Staelens, S. (2010). Influence of skull conductivity perturbations on EEG dipole source analysis. *Medical Physics*, 37(8):4475–84. doi:10.1118/1.3466831.

Cheyne, D. O. and Papanicolaou, A. C. (2017). Magnetoencephalography and magnetic source imaging. In Papanicolaou, A. C. (Editor), *The Oxford Handbook of Functional*

Brain Imaging in Neuropsychology and Cognitive Neurosciences, Oxford library of psychology. New York: Oxford University Press. ISBN 9780199764228.

Cho, J.-H., Vorwerk, J., Wolters, C. H., and Knösche, T. R. (2015). Influence of the head model on EEG and MEG source connectivity analyses. *NeuroImage*, 110:60–77. doi: 10.1016/j.neuroimage.2015.01.043.

Ciarlet, P. (2002). *The Finite Element Method for Elliptic Problems*. Classics in Applied Mathematics. Philadelphia: Society for Industrial and Applied Mathematics. ISBN 9780898715149.

Clausner, T., Dalal, S. S., and Crespo-García, M. (2017). Photogrammetry-based head digitization for rapid and accurate localization of EEG electrodes and MEG fiducial markers using a single digital SLR camera. *Frontiers in Neuroscience*, 11:264. doi: 10.3389/fnins.2017.00264.

Cohen, D. (1972). Magnetoencephalography: Detection of the brain's electrical activity with a superconducting magnetometer. *Science*, 175(4022):664–666. doi:10.1126/science.175.4022.664.

Cohen, D. and Cuffin, B. N. (1983). Demonstration of useful differences between magnetoencephalogram and electroencephalogram. *Electroencephalography and Clinical Neurophysiology*, 56(1):38–51. doi:10.1016/0013-4694(83)90005-6.

Collins, D. L., Zijdenbos, A. P., Kollokian, V., Sled, J. G., Kabani, N. J., Holmes, C. J., and Evans, A. C. (1998). Design and construction of a realistic digital brain phantom. *IEEE Transactions on Medical Imaging*, 17(3):463–468. doi:10.1109/42.712135.

Cook, M. J. D. and Koles, Z. J. (2006). A high-resolution anisotropic finite-volume head model for EEG source analysis. In *2006 International Conference of the IEEE Engineering in Medicine and Biology Society*, pages 4536–4539. doi:10.1109/IEMBS.2006.260314.

Cuartas Morales, E., Acosta-Medina, C. D., Castellanos-Domínguez, G., and Mantini, D. (2019). A finite-difference solution for the EEG forward problem in inhomogeneous anisotropic media. *Brain Topography*, 32(2):229–239. doi:10.1007/s10548-018-0683-2.

Céspedes-Villar, Y., Martinez-Vargas, J. D., and Castellanos-Dominguez, G. (2020). Influence of patient-specific head modeling on EEG source imaging. *Computational and Mathematical Methods in Medicine*, 2020:5076865. doi:10.1155/2020/5076865.

Dachwitz, A. (2019). *Accurate Methods to Compute the MEG Forward Problem*. Master's thesis, Westfälische Wilhelms-Universität Münster.

Dannhauer, M., Lanfer, B., Wolters, C. H., and Knösche, T. R. (2011). Modeling of the human skull in EEG source analysis. *Human Brain Mapping*, 32(9):1383–1399. doi: 10.1002/hbm.21114.

Dassios, G., Fokas, A. S., and Hadjiloizi, D. (2007). On the complementarity of electroencephalography and magnetoencephalography. *Inverse Problems*, 23(6):2541–2549. doi:10.1088/0266-5611/23/6/016.

De Munck, J. C. (1988). The potential distribution in a layered anisotropic spheroidal volume conductor. *Journal of Applied Physics*, 64(2):464–470. doi:10.1063/1.341983.

De Munck, J. C. and Peters, M. J. (1993). A fast method to compute the potential in the multisphere model (EEG application). *IEEE Transactions on Biomedical Engineering*, 40(11):1166–1174. doi:10.1109/10.245635.

De Munck, J. C. and Van Dijk, B. W. (1991). Symmetry considerations in the quasi-static approximation of volume conductor theory. *Physics in Medicine & Biology*, 36(4):521–529. doi:10.1088/0031-9155/36/4/009.

De Saint-Venant, A. J. C. B. (1853). *Memoire sur la torsion des prismes: avec des considérations sur leur fléxion ainsi que sur l'équilibre intérieur des solides élastiques en général, et des formules pratiques pour le calcul de leur résistance à divers efforts s'exerçant simultanément*. S.l.

De Vos, M., Kroesen, M., Emkes, R., and Debener, S. (2014). P300 speller BCI with a mobile EEG system: Comparison to a traditional amplifier. *Journal of Neural Engineering*, 11(3):036008. doi:10.1088/1741-2560/11/3/036008.

Drechsler, F., Wolters, C. H., Dierkes, T., Si, H., and Grasedyck, L. (2009). A full subtraction approach for finite element method based source analysis using constrained Delaunay tetrahedralisation. *NeuroImage*, 46(4):1055–1065. doi:10.1016/j.neuroimage.2009.02.024.

Eadie, M. J. (2012). Shortcomings in the current treatment of epilepsy. *Expert Review of Neurotherapeutics*, 12(12):1419–1427. doi:10.1586/ern.12.129.

Ebersole, J. S. and Ebersole, S. M. (2010). Combining MEG and EEG source modeling in epilepsy evaluations. *Journal of Clinical Neurophysiology*, 27(6):360–371. doi:10.1097/WNP.0b013e318201ffc4.

Egner, T. and Sterman, M. B. (2006). Neurofeedback treatment of epilepsy: From basic rationale to practical application. *Expert Review of Neurotherapeutics*, 6(2):247–257. doi:10.1586/14737175.6.2.247.

Engwer, C., Vorwerk, J., Ludewig, J., and Wolters, C. H. (2017). A discontinuous Galerkin method to solve the EEG forward problem using the subtraction approach. *SIAM Journal on Scientific Computing*, 39(1):B138–B164. doi:10.1137/15M1048392.

Enriquez-Geppert, S., Huster, R. J., and Herrmann, C. S. (2017). EEG-neurofeedback as a tool to modulate cognition and behavior: A review tutorial. *Frontiers in Human Neuroscience*, 11:51. doi:10.3389/fnhum.2017.00051.

Erdbrügger, T.-R. (2021). *CutFEM forward modeling for geometries with touching surfaces in bioelectromagnetism.* Master's thesis, Westfälische Wilhelms-Universität Münster.

Esser, S. K., Huber, R., Massimini, M., Peterson, M. J., Ferrarelli, F., and Tononi, G. (2006). A direct demonstration of cortical LTP in humans: A combined TMS/EEG study. *Brain Research Bulletin*, 69(1):86–94. doi:10.1016/j.brainresbull.2005.11.003.

Evans, L. (1998). *Partial Differential Equations.* Graduate studies in mathematics. American Mathematical Society. ISBN 9780821807729.

Fernández-Corazza, M., Turovets, S., Luu, P., Price, N., Muravchik, C. H., and Tucker, D. (2018). Skull modeling effects in conductivity estimates using parametric electrical impedance tomography. *IEEE Transactions on Biomedical Engineering*, 65(8):1785–1797. doi:10.1109/TBME.2017.2777143.

Fiederer, L. D. J., Vorwerk, J., Lucka, F., Dannhauer, M., Yang, S., Dümpelmann, M., Schulze-Bonhage, A., Aertsen, A., Speck, O., Wolters, C. H., and Ball, T. (2016). The role of blood vessels in high-resolution volume conductor head modeling of EEG. *NeuroImage*, 128:193–208. doi:10.1016/j.neuroimage.2015.12.041.

Fillmore, P. T., Phillips-Meek, M. C., and Richards, J. E. (2015). Age-specific MRI brain and head templates for healthy adults from 20 through 89 years of age. *Frontiers in Aging Neuroscience*, 7:44. doi:10.3389/fnagi.2015.00044.

Fuchs, M., Kastner, J., Wagner, M., Hawes, S., and Ebersole, J. S. (2002). A standardized boundary element method volume conductor model. *Clinical Neurophysiology*, 113(5):702–712. doi:10.1016/S1388-2457(02)00030-5.

Fuchs, M., Wagner, M., and Kastner, J. (2007). Development of volume conductor and source models to localize epileptic foci. *Journal of Clinical Neurophysiology*, 24(2):101–119. doi:10.1097/WNP.0b013e318038fb3e.

Fuchs, M., Wagner, M., Köhler, T., and Wischmann, H. A. (1999). Linear and nonlinear current density reconstructions. *Journal of Clinical Neurophysiology*, 16(23):267–95. doi:10.1097/00004691-199905000-00006.

Fuchs, M., Wagner, M., Wischmann, H.-A., Köhler, T., Theißen, A., Drenckhahn, R., and Buchner, H. (1998). Improving source reconstructions by combining bioelectric and biomagnetic data. *Electroencephalography and Clinical Neurophysiology*, 107(2):93–111. doi:10.1016/S0013-4694(98)00046-7.

Fuchs, M., Wischmann, H.-A., Wagner, M., Drenckhahn, R., and Köhler, T. (2000). Source reconstructions by spatial deviation scans. In Aine, C. J., Stroink, G., Wood, C. C., Okada, Y., and Swithenby, S. J. (Editors), *Biomag 96*, pages 213–216. New York: Springer. doi:10.1007/978-1-4612-1260-7_51.

Geddes, L. A. and Baker, L. E. (1967). The specific resistance of biological material – a compendium of data for the biomedical engineer and physiologist. *Medical and Biological Engineering*, 5(3):271–93. doi:10.1007/BF02474537.

Gençer, N. G. and Acar, C. E. (2004). Sensitivity of EEG and MEG measurements to tissue conductivity. *Physics in Medicine & Biology*, 49(5):701–717. doi:10.1088/0031-9155/49/5/004.

Geselowitz, D. B. (1967). On bioelectric potentials in an inhomogeneous volume conductor. *Biophysical Journal*, 7(1):1–11. doi:10.1016/S0006-3495(67)86571-8.

Geuzaine, C. and Remacle, J.-F. (2009). Gmsh: A 3-D finite element mesh generator with built-in pre- and post-processing facilities. *International Journal for Numerical Methods in Engineering*, 79(11):1309–1331. doi:10.1002/nme.2579.

Ghosh, S., Sinha, J. K., Khan, T., Devaraju, K. S., Singh, P., Vaibhav, K., and Gaur, P. (2021). Pharmacological and therapeutic approaches in the treatment of epilepsy. *Biomedicines*, 9(5):470. doi:10.3390/biomedicines9050470.

Golub, G. and Kahan, W. (1965). Calculating the singular values and pseudo-inverse of a matrix. *Journal of the Society for Industrial and Applied Mathematics: Series B Numerical Analysis*, 2(2):205–224. doi:10.1137/0702016.

Gonçalves, S. I., De Munck, J. C., Verbunt, J. P. A., Bijma, F., Heethaar, R. M., and Lopes da Silva, F. (2003a). In vivo measurement of the brain and skull resistivities using an EIT-based method and realistic models for the head. *IEEE Transactions on Biomedical Engineering*, 50(6):754–767. doi:10.1109/TBME.2003.812164.

Gonçalves, S. I., De Munck, J. C., Verbunt, J. P. A., Heethaar, R. M., and da Silva, F. H. L. (2003b). In vivo measurement of the brain and skull resistivities using an EIT-based method and the combined analysis of SEF/SEP data. *IEEE Transactions on Biomedical Engineering*, 50(9):1124–1127. doi:10.1109/TBME.2003.816072.

Götz, T., Huonker, R., Witte, O. W., and Haueisen, J. (2014). Thalamocortical impulse propagation and information transfer in EEG and MEG. *Journal of Clinical Neurophysiology*, 31(3):253–260. doi:10.1097/WNP.0000000000000048.

Gramfort, A., Luessi, M., Larson, E., Engemann, D. A., Strohmeier, D., Brodbeck, C., Goj, R., Jas, M., Brooks, T., Parkkonen, L., and Hämäläinen, M. S. (2013). MEG and EEG data analysis with MNE-Python. *Frontiers in Neuroscience*, 7:267. doi:10.3389/fnins.2013.00267.

Gramfort, A., Papadopoulo, T., Olivi, E., and Clerc, M. (2011). Forward field computation with OpenMEEG. *Computational Intelligence and Neuroscience*, 923703. doi:10.1155/2011/923703.

Gross, J. (2019). Magnetoencephalography in cognitive neuroscience: A primer. *Neuron*, 104(2):189–204. doi:10.1016/j.neuron.2019.07.001.

Gross, J., Junghöfer, M., and Wolters, C. H. (2021). Bioelectromagnetism in human brain research: New applications, new questions. *The Neuroscientist*. doi:10.1177/10738584211054742.

Grüne, F. (2014). *Validierung von FEM-Ansätzen höherer Ordnung für das EEG-Vorwärtsproblem*. Master's thesis, Westfälische Wilhelms-Universität Münster.

Guler, S., Dannhauer, M., Erem, B., MacLeod, R., Tucker, D., Turovets, S., Luu, P., Erdogmus, D., and Brooks, D. H. (2016). Optimization of focality and direction in dense electrode array transcranial direct current stimulation (tDCS). *Journal of Neural Engineering*, 13(3):036020. doi:10.1088/1741-2560/13/3/036020.

Gutierrez, D., Nehorai, A., and Muravchik, C. H. (2004). Estimating brain conductivities and dipole source signals with EEG arrays. *IEEE Transactions on Biomedical Engineering*, 51(12):2113–2122. doi:10.1109/TBME.2004.836507.

Güllmar, D., Haueisen, J., and Reichenbach, J. R. (2010). Influence of anisotropic electrical conductivity in white matter tissue on the EEG/MEG forward and inverse solution. A high-resolution whole head simulation study. *NeuroImage*, 51(1):145–163. doi:10.1016/j.neuroimage.2010.02.014.

Hallez, H., Van Hese, P., Vanrumste, B., Boon, P., D'Asseler, Y., Lemahieu, I., and Van de Walle, R. (2005). Dipole localization errors due to not incorporating compartments with anisotropic conductivities: Simulation study in a spherical head model. *International Journal of Biolelectromagnetism*, 7:134–137.

Hallez, H., Vanrumste, B., Grech, R., Muscat, J., De Clercq, W., Vergult, A., D'Asseler, Y., Camilleri, K. P., Fabri, S. G., Van Huffel, S., and Lemahieu, I. L. (2007). Review on solving the forward problem in EEG source analysis. *Journal of NeuroEngineering and Rehabilitation*, 4:46–46. doi:10.1186/1743-0003-4-46.

Hämäläinen, M., Hari, R., Ilmoniemi, R. J., Knuutila, J., and Lounasmaa, O. V. (1993). Magnetoencephalography – theory, instrumentation, and applications to noninvasive studies of the working human brain. *Reviews of Modern Physics*, 65(2):413–497. doi:10.1103/RevModPhys.65.413.

Hämäläinen, M. S. and Sarvas, J. (1987). Feasibility of the homogeneous head model in the interpretation of neuromagnetic fields. *Physics in Medicine & Biology*, 32(1):91–97. doi:10.1088/0031-9155/32/1/014.

Hansen, P. C., Kringelbach, M. L., and Salmelin, R. (Editors) (2010). *MEG: An Introduction to Methods*. Oxford University Press, New York. ISBN 0195307232.

Hari, R., Baillet, S., Barnes, G., Burgess, R., Forss, N., Gross, J., Hämäläinen, M., Jensen, O., Kakigi, R., Mauguière, F., Nakasato, N., Puce, A., Romani, G.-L., Schnitzler, A., and Taulu, S. (2018). IFCN-endorsed practical guidelines for clinical magnetoencephalography (MEG). *Clinical Neurophysiology*, 129. doi:10.1016/j.clinph.2018.03.042.

Hari, R. and Forss, N. (1999). Magnetoencephalography in the study of human somatosensory cortical processing. *Philosophical Transactions of the Royal Society of London. Series B: Biological Sciences*, 354(1387):1145–1154. doi:10.1098/rstb.1999.0470.

Hari, R. and Puce, A. (2017). *MEG-EEG Primer*. New York: Oxford University Press. ISBN 9780190497774.

Hasegawa, D. (2016). Diagnostic techniques to detect the epileptogenic zone: Pathophysiological and presurgical analysis of epilepsy in dogs and cats. *The Veterinary Journal*, 215:64–75. doi:10.1016/j.tvjl.2016.03.005.

Haueisen, J., Funke, M., Güllmar, D., and Eichardt, R. (2012). Tangential and radial epileptic spike activity: Different sensitivity in EEG and MEG. *Journal of Clinical Neurophysiology*, 29(4):327–332. doi:10.1097/WNP.0b013e3182624491.

Haueisen, J., Leistritz, L., Süsse, T., Curio, G., and Witte, H. (2007). Identifying mutual information transfer in the brain with differential-algebraic modeling: Evidence for fast oscillatory coupling between cortical somatosensory areas 3b and 1. *NeuroImage*, 37(1):130–136. doi:10.1016/j.neuroimage.2007.04.036.

Haueisen, J., Ramon, C., Eiselt, M., Brauer, H., and Nowak, H. (1997). Influence of tissue resistivities on neuromagnetic fields and electric potentials studied with a finite element model of the head. *IEEE Transactions on Biomedical Engineering*, 44(8):727–735. doi:10.1109/10.605429.

Heidemann, R. M., Porter, D. A., Anwander, A., Feiweier, T., Heberlein, K., Knösche, T. R., and Turner, R. (2010). Diffusion imaging in humans at 7T using readout-segmented EPI and GRAPPA. *Magnetic Resonance in Medicine*, 64(1):9–14. doi:10.1002/mrm.22480.

Hinrichs, H., Scholz, M., Baum, A. K., Kam, J. W. Y., Knight, R. T., and Heinze, H.-J. (2020). Comparison between a wireless dry electrode EEG system with a conventional wired wet electrode EEG system for clinical applications. *Scientific Reports*, 10:5218. doi:10.1038/s41598-020-62154-0.

Hoekema, R., Wieneke, G. H., Leijten, F. S. S., Van Veelen, C. W. M., Van Rijen, P. C., Huiskamp, G. J. M., Ansems, J., and Van Huffelen, A. C. (2003). Measurement of the conductivity of skull, temporarily removed during epilepsy surgery. *Brain Topography*, 16(1):29–38. doi:10.1023/A:1025606415858.

Htet, A. T., Saturnino, G. B., Burnham, E. H., Noetscher, G. M., Nummenmaa, A., and Makarov, S. N. (2019). Comparative performance of the finite element method and the boundary element fast multipole method for problems mimicking transcranial magnetic stimulation (TMS). *Journal of Neural Engineering*, 16(2):024001. doi:10.1088/1741-2552/aafbb9.

Huang, M.-X., Song, T., Hagler Jr., D. J., Podgorny, I., Jousmaki, V., Cui, L., Gaa, K., Harrington, D. L., Dale, A. M., Lee, R. R., Elman, J., and Halgren, E. (2007). A novel integrated MEG and EEG analysis method for dipolar sources. *NeuroImage*, 37(3):731–48. doi:10.1016/j.neuroimage.2007.06.002.

Huang, Y., Liu, A. A., Lafon, B., Friedman, D., Dayan, M., Wang, X., Bikson, M., Doyle, W. K., Devinsky, O., and Parra, L. C. (2017). Measurements and models of electric fields in the in vivo human brain during transcranial electric stimulation. *eLife*, 6:e18834. doi:10.7554/eLife.18834.

Iwasaki, M., Pestana, E., Burgess, R. C., Lüders, H. O., Shamoto, H., and Nakasato, N. (2005). Detection of epileptiform activity by human interpreters: Blinded comparison between electroencephalography and magnetoencephalography. *Epilepsia*, 46(1):59–68. doi:10.1111/j.0013-9580.2005.21104.x.

James, M. (1978). The generalised inverse. *The Mathematical Gazette*, 62(420):109–114. doi:10.2307/3617665.

Jarratt, P. (1967). An iterative method for locating turning points. *The Computer Journal*, 10(1):82–84. doi:10.1093/comjnl/10.1.82.

Jerbi, K., Baillet, S., Mosher, J., Nolte, G., Garnero, L., and Leahy, R. (2004). Localization of realistic cortical activity in MEG using current multipoles. *NeuroImage*, 22(2):779–793. doi:10.1016/j.neuroimage.2004.02.010.

Josephson, S., Freeman, W., and Likosky, D. (Editors) (2011). *Neurohospitalist Medicine*. Cambridge: Cambridge University Press. ISBN 9780511736193.

Jung, P., Baumgärtner, U., Bauermann, T., Magerl, W., Gawehn, J., Stoeter, P., and Treede, R.-D. (2003). Asymmetry in the human primary somatosensory cortex and handedness. *NeuroImage*, 19(3):913–923. doi:10.1016/S1053-8119(03)00164-2.

Kaipio, J. P. and Somersalo, E. (2005). *Statistical and Computational Inverse Problems*. New York: Springer. doi:10.1007/b138659.

Katoch, N., Choi, B. K., Sajib, S. Z. K., Lee, E., Kim, H. J., Kwon, O. I., and Woo, E. J. (2019). Conductivity tensor imaging of in vivo human brain and experimental validation using giant vesicle suspension. *IEEE Transactions on Medical Imaging*, 38(7):1569–1577. doi:10.1109/TMI.2018.2884440.

Kiefer, J. (1953). Sequential minimax search for a maximum. *Proceedings of the American Mathematical Society*, 4(3):502–506. doi:10.2307/2032161.

Knake, S., Halgren, E., Shiraishi, H., Hara, K., Hamer, H. M., Grant, P. E., Carr, V. A., Foxe, D., Camposano, S., Busa, E., Witzel, T., Hämäläinen, M. S., Ahlfors, S. P., Bromfield, E. B., Black, P. M., Bourgeois, B. F., Cole, A. J., Cosgrove, G. R., Dworetzky, B. A., Madsen, J. R., Larsson, P. G., Schomer, D. L., Thiele, E. A., Dale, A. M., Rosen, B. R., and Stufflebeam, S. M. (2006). The value of multichannel MEG and EEG in the presurgical evaluation of 70 epilepsy patients. *Epilepsy Research*, 69(1):80–86. doi:10.1016/j.eplepsyres.2006.01.001.

Koo, B.-B., Hua, N., Choi, C.-H., Ronen, I., Lee, J.-M., and Kim, D.-S. (2009). A framework to analyze partial volume effect on gray matter mean diffusivity measurements. *NeuroImage*, 44(1):136–144. doi:10.1016/j.neuroimage.2008.07.064.

Körber, R., Storm, J.-H., Seton, H., Mäkelä, J., Paetau, R., Parkkonen, L., Pfeiffer, C., Riaz, B., Schneiderman, J., Dong, H., min Hwang, S., You, L., Inglis, B., Clarke, J., Espy, M., Ilmoniemi, R., Magnelind, P., Matlashov, A., Nieminen, J., Volegov, P., Zevenhoven, K., Höfner, N., Burghoff, M., Enpuku, K., Yang, S., Chieh, J.-J., Jukka, K., Laine, P., and Nenonen, J. (2016). SQUIDs in biomagnetism: A roadmap towards improved healthcare. *Superconductor Science & Technology*, 29(11):2–31. doi:10.1088/0953-2048/29/11/113001.

Kwan, P. and Brodie, M. J. (2000). Early identification of refractory epilepsy. *New England Journal of Medicine*, 342(5):314–319. doi:10.1056/NEJM200002033420503.

Kybic, J., Clerc, M., Abboud, T., Faugeras, O., Keriven, R., and Papadopoulo, T. (2005). A common formalism for the integral formulations of the forward EEG problem. *IEEE Transactions on Medical Imaging*, 24(1):12–28. doi:10.1109/TMI.2004.837363.

Kybic, J., Clerc, M., Faugeras, O., Keriven, R., and Papadopoulo, T. (2006). Generalized head models for MEG/EEG: Boundary element method beyond nested volumes. *Physics in Medicine & Biology*, 51(5):1333–1346. doi:10.1088/0031-9155/51/5/021.

Labyt, E., Corsi, M.-C., Fourcault, W., Palacios Laloy, A., Bertrand, F., Lenouvel, F., Cauffet, G., Le Prado, M., Berger, F., and Morales, S. (2019). Magnetoencephalography with optically pumped ^{4}He magnetometers at ambient temperature. *IEEE Transactions on Medical Imaging*, 38(1):90–98. doi:10.1109/TMI.2018.2856367.

Lai, Y., Van Drongelen, W., Ding, L., Hecox, K. E., Towle, V. L., Frim, D. M., and He, B. (2005). Estimation of in vivo human brain-to-skull conductivity ratio from simultaneous extra- and intra-cranial electrical potential recordings. *Clinical Neurophysiology*, 116(2):456–465. doi:10.1016/j.clinph.2004.08.017.

Lalancette, M., Quraan, M., and Cheyne, D. (2011). Evaluation of multiple-sphere head models for MEG source localization. *Physics in Medicine & Biology*, 56(17):5621–5635. doi:10.1088/0031-9155/56/17/010.

Lange, P. (2021). *The Localized Subtraction Source Model.* Master's thesis, Westfälische Wilhelms-Universität Münster.

Lantz, G., Spinelli, L., Seeck, M., De Peralta Menendez, R. G., Sottas, C. C., and Michel, C. M. (2003). Propagation of interictal epileptiform activity can lead to erroneous source localizations: A 128-channel EEG mapping study. *Journal of Clinical Neurophysiology*, 20(5):311–319. doi:10.1097/00004691-200309000-00003.

Lau, S., Güllmar, D., Flemming, L., Grayden, D. B., Cook, M. J., Wolters, C. H., and Haueisen, J. (2016). Skull defects in finite element head models for source reconstruction from magnetoencephalography signals. *Frontiers in Neuroscience*, 10:141. doi:10.3389/fnins.2016.00141.

Law, S. K. (1993). Thickness and resistivity variations over the upper surface of the human skull. *Brain Topography*, 6(2):99–109. doi:10.1007/BF01191074.

Lehmann, D. and Skrandies, W. (1980). Reference-free identification of components of checkerboard-evoked multichannel potential fields. *Electroencephalography and Clinical Neurophysiology*, 48(6):609–621. doi:10.1016/0013-4694(80)90419-8.

Lew, S., Sliva, D. D., Choe, M.-s., Grant, P. E., Okada, Y., Wolters, C. H., and Hämäläinen, M. S. (2013). Effects of sutures and fontanels on MEG and EEG source analysis in a realistic infant head model. *NeuroImage*, 76:282–293. doi:10.1016/j.neuroimage.2013.03.017.

Lew, S., Wolters, C. H., Anwander, A., Makeig, S., and MacLeod, R. (2009a). Improved EEG source analysis using low-resolution conductivity estimation in a four-compartment finite element head model. *Human Brain Mapping*, 30(9):2862–78. doi:10.1002/hbm.20714.

Lew, S., Wolters, C. H., Dierkes, T., Röer, C., and MacLeod, R. S. (2009b). Accuracy and run-time comparison for different potential approaches and iterative solvers in finite element method based EEG source analysis. *Applied Numerical Mathematics*, 59(8):1970–1988. doi:10.1016/j.apnum.2009.02.006.

Li, X., Yu, K., and He, B. (2016). Magnetoacoustic tomography with magnetic induction (MAT-MI) for imaging electrical conductivity of biological tissue: A tutorial review. *Physics in Medicine & Biology*, 61(18):R249–R270. doi:10.1088/0031-9155/61/18/r249.

Lin, F.-H., Witzel, T., Ahlfors, S. P., Stufflebeam, S. M., Belliveau, J. W., and Hämäläinen, M. S. (2006). Assessing and improving the spatial accuracy in MEG source localization by depth-weighted minimum-norm estimates. *NeuroImage*, 31(1):160–171. doi:10.1016/j.neuroimage.2005.11.054.

Lopes da Silva, F. and Rotterdam, A. (1982). Biophysical aspects of EEG and MEG generation. In Niedermeyer, E. and Lopes da Silva, F. (Editors), *Electroencephalography: Basic Principles, Clinical Applications and Related Fields*, pages 15–26. Baltimore MD: Lippincott Williams & Wilkins.

Lopez-Gordo, M. A., Sanchez-Morillo, D., and Valle, F. P. (2014). Dry EEG electrodes. *Sensors*, 14(7):12847–12870. doi:10.3390/s140712847.

Lü, Z. and Williamson, S. (1991). Spatial extent of coherent sensory-evoked cortical activity. *Experimental Brain Research*, 84:411–416. doi:10.1007/BF00231463.

Lüders, H., Najm, I., Nair, D., Widdess-Walsh, P., and Bingman, W. (2006). The epileptogenic zone: General principles. *Epileptic Disorders*, 8 Suppl 2:S1–9.

Marsaglia, G. (1972). Choosing a point from the surface of a sphere. *The Annals of Mathematical Statistics*, 43(2):645–646. doi:10.1214/aoms/1177692644.

Maxwell, J. C. (1861). On physical lines of force. In Niven, W. D. (Editor), *The Scientific Papers of James Clerk Maxwell*, Cambridge Library Collection - Physical Sciences, pages 451–513. Cambridge: Cambridge University Press. doi:10.1017/CBO9780511698095.026.

Maxwell, J. C. (1865). VIII. A dynamical theory of the electromagnetic field. *Philosophical Transactions of the Royal Society of London*, 155:459–512. doi:10.1098/rstl.1865.0008.

Mazziotta, J., Toga, A., Evans, A., Fox, P., Lancaster, J., Zilles, K., Woods, R., Paus, T., Simpson, G., Pike, B., Holmes, C., Collins, L., Thompson, P., MacDonald, D., Iacoboni, M., Schormann, T., Amunts, K., Palomero-Gallagher, N., Geyer, S., Parsons, L., Narr, K., Kabani, N., Goualher, G. L., Boomsma, D., Cannon, T., Kawashima, R., and Mazoyer, B. (2001). A probabilistic atlas and reference system for the human brain: International Consortium for Brain Mapping (ICBM). *Philosophical Transactions of the Royal Society of London. Series B: Biological Sciences*, 356(1412):1293–1322. doi:10.1098/rstb.2001.0915.

McCann, H., Pisano, G., and Beltrachini, L. (2019). Variation in reported human head tissue electrical conductivity values. *Brain Topography*, 32:825–858. doi:10.1007/s10548-019-00710-2.

McCann, H., Pisano, G., and Beltrachini, L. (2021). Correction to: Variation in reported human head tissue electrical conductivity values. *Brain Topography*, 34:110–115. doi:10.1007/s10548-020-00807-z.

McCann, H. M. and Beltrachini, L. (2021). Impact of skull sutures, spongiform bone distribution, and aging skull conductivities on the EEG forward and inverse problems. *Journal of Neural Engineering*. doi:10.1088/1741-2552/ac43f7.

Medani, T., Garcia-Prieto, J., Tadel, F., Schrader, S., Antonakakis, M., Joshi, A., Engwer, C., Wolters, C. H., Mosher, J. C., and Leahy, R. M. (2021). Realistic head modeling of electromagnetic brain activity: An integrated Brainstorm-DUNEuro pipeline from MRI data to the FEM solutions. In Bosmans, H., Zhao, W., and Yu, L. (Editors), *SPIE Medical Imaging 2021: Physics of Medical Imaging*, volume 11595, pages 1369–1376. doi:10.1117/12.2580935.

Medani, T., Lautru, D., Schwartz, D., Ren, Z., and Sou, G. (2015). FEM method for the EEG forward problem and improvement based on modification of the Saint Venant's method. *Progress in Electromagnetics Research*, 153:11–22. doi:10.2528/PIER15050102.

Meijs, J. W. H., Weier, O. W., Peters, M. J., and Van Oosterom, A. (1989). On the numerical accuracy of the boundary element method (EEG application). *IEEE Transactions on Biomedical Engineering*, 36(10):1038–1049. doi:10.1109/10.40805.

Mertens, M. and Lütkenhöner, B. (2000). Efficient neuromagnetic determination of landmarks in the somatosensory cortex. *Clinical Neurophysiology*, 111(8):1478–1487. doi:10.1016/S1388-2457(00)00349-7.

Michel, C. M. and Brunet, D. (2019). EEG source imaging: A practical review of the analysis steps. *Frontiers in Neurology*, 10:325. doi:10.3389/fneur.2019.00325.

Mitchell, J. W., Seri, S., and Cavanna, A. E. (2012). Pharmacotherapeutic and non-pharmacological options for refractory and difficult-to-treat seizures. *Journal of Central Nervous System Disease*, 4:JCNSD.S8315. doi:10.4137/JCNSD.S8315.

Monastra, V. J., Monastra, D. M., and George, S. (2002). The effects of stimulant therapy, EEG biofeedback, and parenting style on the primary symptoms of attention-deficit/hyperactivity disorder. *Applied Psychophysiology and Biofeedback*, 27:231–249. doi:10.1023/A:1021018700609.

Montes-Restrepo, V., Van Mierlo, P., Strobbe, G., Staelens, S., Vandenberghe, S., and Hallez, H. (2014). Influence of skull modeling approaches on EEG source localization. *Brain Topography*, 27(1):95–111. doi:10.1007/s10548-013-0313-y.

Mosher, J., Lewis, P., and Leahy, R. (1992). Multiple dipole modeling and localization from spatio-temporal MEG data. *IEEE Transactions on Biomedical Engineering*, 39:541–57. doi:10.1109/10.141192.

Mosher, J. C. and Leahy, R. M. (1999). Source localization using recursively applied and projected (RAP) MUSIC. *IEEE Transactions on Signal Processing*, 47(2):332–340. doi:10.1109/78.740118.

Murakami, S. and Okada, Y. (2006). Contributions of principal neocortical neurons to magnetoencephalography and electroencephalography signals. *The Journal of Physiology*, 575(3):925–936. doi:10.1113/jphysiol.2006.105379.

Nakamura, A., Yamada, T., Goto, A., Kato, T., Ito, K., Abe, Y., Kachi, T., and Kakigi, R. (1998). Somatosensory homunculus as drawn by MEG. *NeuroImage*, 7(4):377–386. doi:10.1006/nimg.1998.0332.

Neugebauer, F., Antonakakis, M., Unnwongse, K., Parpaley, Y., Wellmer, J., Rampp, S., and Wolters, C. H. (2022). Validating EEG, MEG and combined MEG and EEG beamforming for an estimation of the epileptogenic zone in focal cortical dysplasia. *Brain Sciences*, 12(1):114. doi:10.3390/brainsci12010114.

Nevalainen, P., Lauronen, L., and Pihko, E. (2014). Development of human somatosensory cortical functions – What have we learned from magnetoencephalography: A review. *Frontiers in Human Neuroscience*, 8:158. doi:10.3389/fnhum.2014.00158.

Nicholson, P. W. (1965). Specific impedance of cerebral white matter". *Experimental Neurology*, 13(4):386–401. doi:10.1016/0014-4886(65)90126-3.

Nissinen, A., Kaipio, J. P., Vauhkonen, M., and Kolehmainen, V. (2015). Contrast enhancement in EIT imaging of the brain. *Physiological Measurement*, 37(1):1–24. doi: 10.1088/0967-3334/37/1/1.

Nolte, G. (2003). The magnetic lead field theorem in the quasi-static approximation and its use for magnetoencephalography forward calculation in realistic volume conductors. *Physics in Medicine & Biology*, 48(22):3637–3652. doi:10.1088/0031-9155/48/22/002.

Nunez, P. L. and Srinivasan, R. (2006). *Electric Fields of the Brain – The neurophysics of EEG*. New York: Oxfort University Press, 2 edition. doi:10.1093/acprof: oso/9780195050387.001.0001.

Nüßing, A. (2018). *Fitted and Unfitted Finite Element Methods for Solving the EEG Forward Problem*. Ph.D. thesis, Westfälische Wilhelms-Universität Münster. Available from: http://nbn-resolving.de/urn:nbn:de:hbz:6-67139436770.

Nüßing, A., Wolters, C. H., Brinck, H., and Engwer, C. (2016). The unfitted discontinuous Galerkin method for solving the EEG forward problem. *IEEE Transactions on Biomedical Engineering*, 63(12):2564–2575. doi:10.1109/TBME.2016.2590740.

Ohlberger, M. (2012). Numerik Partieller Differentialgleichungen I. Script from lectures given at the faculty of Mathematics/Computer Science at the University of Münster, Germany.

Öisjöen, F., Schneiderman, J. F., Figueras, G. A., Chukharkin, M. L., Kalabukhov, A., Hedström, A., Elam, M., and Winkler, D. (2012). High-Tc superconducting quantum interference device recordings of spontaneous brain activity: Towards high-Tc magnetoencephalography. *Applied Physics Letters*, 100(13):132601. doi:10.1063/1.3698152.

Okada, J., Shichijo, F., Matsumoto, K., and Kinouchi, Y. (1996). Variation of frontal P20 potential due to rotation of the N20-P20 dipole moment of SEPs. *Brain Topography*, 8:223–228. doi:10.1007/BF01184773.

Ollikainen, J. O., Vauhkonen, M., Karjalainen, P. A., and Kaipio, J. P. (1999). Effects of local skull inhomogeneities on EEG source estimation. *Medical Engineering & Physics*, 21(3):143–154. doi:10.1016/S1350-4533(99)00038-7.

Onishi, H., Oyama, M., Soma, T., Kubo, M., Kirimoto, H., Murakami, H., and Kameyama, S. (2010). Neuromagnetic activation of primary and secondary somatosensory cortex following tactile-on and tactile-off stimulation. *Clinical Neurophysiology*, 121(4):588–593. doi:10.1016/j.clinph.2009.12.022.

Oostendorp, T. F., Delbeke, J., and Stegeman, D. F. (2000). The conductivity of the human skull: Results of in vivo and in vitro measurements. *IEEE Transactions on Biomedical Engineering*, 47(11):1487–1492. doi:10.1109/TBME.2000.880100.

Oostenveld, R., Fries, P., Maris, E., and Schoffelen, J.-M. (2011). FieldTrip: open source software for advanced analysis of MEG, EEG, and invasive electrophysiological data. *Computational Intelligence and Neuroscience*, 2011:1. doi:10.1155/2011/156869.

Oostenveld, R. and Praamstra, P. (2001). The five percent electrode system for high-resolution EEG and ERP measurements. *Clinical Neurophysiology*, 112(4):713–719. doi:10.1016/S1388-2457(00)00527-7.

Papadopoulo, T., Vallaghé, S., and Clerc, M. (2008). The adjoint method for general EEG and MEG sensor-based lead field equations. *Biomag 2010*, 28. doi:10.1007/978-3-642-12197-5_20.

Papageorgakis, C. (2017). *Patient specific conductivity models: Characterization of the skull bones*. Ph.D. thesis, Université Côte d'Azur. Available from: https://hal.inria.fr/tel-01662075v2.

Papanicolaou, A. C., Roberts, T. P. L., and Wheless, J. W. (Editors) (2020). *Fifty years of Magnetoencephalography: Beginnings, Technical Advances, and Applications*. New York: Oxford University Press. ISBN 9780190935719.

Parvizi, J. and Kastner, S. (2018). Promises and limitations of human intracranial electroencephalography. *Nature Neuroscience*, 21(4):474–483. doi:10.1038/s41593-018-0108-2.

Peterson, N. N., Schroeder, C. E., and Arezzo, J. C. (1995). Neural generators of early cortical somatosensory evoked potentials in the awake monkey. *Electroencephalography and Clinical Neurophysiology/Evoked Potentials Section*, 96(3):248–260. doi:10.1016/0168-5597(95)00006-E.

Piastra, M. C. (2019). *New Finite Element Methods for Solving the MEG and the Combined MEG/EEG Forward Problem*. Ph.D. thesis, Westfälische Wilhelms-Universität Münster. Available from: http://nbn-resolving.de/urn:nbn:de:hbz:6-53199662090.

Piastra, M. C., Nüßing, A., Vorwerk, J., Bornfleth, H., Oostenveld, R., Engwer, C., and Wolters, C. H. (2018). The discontinuous Galerkin finite element method for solving the MEG and the combined MEG/EEG forward problem. *Frontiers in Neuroscience*, 12:30. doi:10.3389/fnins.2018.00030.

Piastra, M. C., Nüßing, A., Vorwerk, J., Clerc, M., Engwer, C., and Wolters, C. H. (2021). A comprehensive study on electroencephalography and magnetoencephalography sensitivity to cortical and subcortical sources. *Human Brain Mapping*, 42(4):978–992. doi: 10.1002/hbm.25272.

Piastra, M. C., Schrader, S., Nüßing, A., Antonakakis, M., Medani, T., Wollbrink, A., Engwer, C., and Wolters, C. H. (2020). The WWU DUNEuro reference data set for combined EEG/MEG source analysis. doi:10.5281/zenodo.3888381.

Planitz, M. (1979). Inconsistent systems of linear equations. *The Mathematical Gazette*, 63(425):181–185. doi:10.2307/3617890.

Plonsey, R. and Heppner, D. B. (1967). Considerations of quasi-stationarity in electrophysiological systems. *The bulletin of mathematical biophysics*, 29:657–664. doi: 10.1007/BF02476917.

Pohlmeier, R., Buchner, H., Knoll, G., Rienäcker, A., Beckmann, R., and Pesch, J. (1997). The influence of skull-conductivity misspecification on inverse source localization in realistically shaped finite element head models. *Brain Topography*, 9(3):157–62. doi: 10.1007/BF01190384.

Press, W. H., Teukolsky, S. A., Vetterling, W. T., and Flannery, B. P. (2007). *Numerical Recipes 3rd Edition: The Art of Scientific Computing*. Cambridge: Cambridge University Press. ISBN 9780521880688.

Proudfoot, M., Woolrich, M. W., Nobre, A. C., and Turner, M. R. (2014). Magnetoencephalography. *Practical Neurology*, 14(5):336–343. doi:10.1136/practneurol-2013-000768.

Pruis, G. W., Gilding, B. H., and Peters, M. J. (1993). A comparison of different numerical methods for solving the forward problem in EEG and MEG. *Physiological Measurement*, 14(4A):A1–A9. doi:10.1088/0967-3334/14/4a/001.

Pursiainen, S., Lucka, F., and Wolters, C. H. (2012). Complete electrode model in EEG: relationship and differences to the point electrode model. *Physics in Medicine & Biology*, 57(4):999–1017. doi:10.1088/0031-9155/57/4/999.

Pursiainen, S., Sorrentino, A., Campi, C., and Piana, M. (2011). Forward simulation and inverse dipole localization with the lowest order Raviart-Thomas elements for electroencephalography. *Inverse Problems*, 27(4). doi:10.1088/0266-5611/27/4/045003.

Pursiainen, S., Vorwerk, J., and Wolter, C. H. (2016). Electroencephalography (EEG) forward modeling via H(div) finite element sources with focal interpolation. *Physics in Medicine & Biology*, 61(24). doi:10.1088/0031-9155/61/24/8502.

Ramon, C., Gargiulo, P., Fridgeirsson, E., and Haueisen, J. (2014). Changes in scalp potentials and spatial smoothing effects of inclusion of dura layer in human head models for EEG simulations. *Frontiers in Neuroengineering*, 7:32. doi:10.3389/fneng.2014.00032.

Ramon, C., Haueisen, J., and Schimpf, P. H. (2006). Influence of head models on neuromagnetic fields and inverse source localizations. *BioMedical Engineering Online*, 5(55). doi:10.1186/1475-925X-5-55.

Ramon, C., Schimpf, P. H., Haueisen, J., Holmes, M., and Ishimaru, A. (2004). Role of soft bone, CSF and gray matter in EEG simulations. *Brain Topography*, 16(4):245–8. doi:10.1023/B:BRAT.0000032859.68959.76.

Rampp, S. and Stefan, H. (2007). Magnetoencephalography in presurgical epilepsy diagnosis. *Expert Review of Medical Devices*, 4(3):335–347. doi:10.1586/17434440.4.3.335.

Rampp, S., Stefan, H., Wu, X., Kaltenhäuser, M., Maess, B., Schmitt, F. C., Wolters, C. H., Hamer, H., Kasper, B. S., Schwab, S., Doerfler, A., Blümcke, I., Rössler, K., and Buchfelder, M. (2019). Magnetoencephalography for epileptic focus localization in a series of 1000 cases. *Brain*, 142(10):3059–3071. doi:10.1093/brain/awz231.

Ratti, E., Waninger, S., Berka, C., Ruffini, G., and Verma, A. (2017). Comparison of medical and consumer wireless EEG systems for use in clinical trials. *Frontiers in Human Neuroscience*, 11:398. doi:10.3389/fnhum.2017.00398.

Rezaei, A., Antonakakis, M., Piastra, M. C., Wolters, C. H., and Pursiainen, S. (2020). Parametrizing the conditionally Gaussian prior model for source localization with reference to the P20/N20 component of median nerve SEP/SEF. *Brain Sciences*, 10(12):934. doi:10.3390/brainsci10120934.

Rice, J. K., Rorden, C., Little, J. S., and Parra, L. C. (2013). Subject position affects EEG magnitudes. *NeuroImage*, 64:476–484. doi:10.1016/j.neuroimage.2012.09.041.

Riera, J. J., Ogawa, T., Goto, T., Sumiyoshi, A., Nonaka, H., Evans, A., Miyakawa, H., and Kawashima, R. (2012). Pitfalls in the dipolar model for the neocortical EEG sources. *Journal of Neurophysiology*, 108(4):956–975. doi:10.1152/jn.00098.2011.

Roche-Labarbe, N., Aarabi, A., Kongolo, G., Gondry-Jouet, C., Dümpelmann, M., Grebe, R., and Wallois, F. (2008). High-resolution electroencephalography and source localization in neonates. *Human Brain Mapping*, 29(2):167–176. doi:10.1002/hbm.20376.

Rossini, P. M., Deuschl, G., Pizzella, V., Tecchio, F., Pasquarelli, A., Feifel, E., Romani, G. L., and Lücking, C. H. (1996). Topography and sources of electromagnetic cerebral responses to electrical and air-puff stimulation of the hand. *Electroencephalography and Clinical Neurophysiology/Evoked Potentials Section*, 100(3):229–239. doi:10.1016/0168-5597(95)00275-8.

Rullmann, M., Anwander, A., Dannhauer, M., Warfield, S. K., Duffy, F. H., and Wolters, C. H. (2009). EEG source analysis of epileptiform activity using a 1 mm anisotropic hexahedra finite element head model. *NeuroImage*, 44(2):399–410. doi:10.1016/j.neuroimage.2008.09.009.

Rush, S. and Driscoll, D. A. (1968). Current distribution in the brain from surface electrodes. *Anesthesia and Analgesia*, 47(6):717–23.

Ruthotto, L., Kugel, H., Olesch, J., Fischer, B., Modersitzki, J., Burger, M., and Wolters, C. H. (2012). Diffeomorphic susceptibility artifact correction of diffusion-weighted magnetic resonance images. *Physics in Medicine & Biology*, 57(18):5715–5731. doi:10.1088/0031-9155/57/18/5715.

Sadleir, R. J., Vannorsdall, T. D., Schretlen, D. J., and Gordon, B. (2012). Target optimization in transcranial direct current stimulation. *Frontiers in Psychiatry*, 3:90. doi:10.3389/fpsyt.2012.00090.

Sander, O. (2020). *DUNE — The Distributed and Unified Numerics Environment*. Lecture Notes in Computational Science and Engineering. Cham: Springer. ISBN 9783030597023.

Sarvas, J. (1987). Basic mathematical and electromagnetic concepts of the biomagnetic inverse problem. *Physics in Medicine & Biology*, 32(1):11–22. doi:10.1088/0031-9155/32/1/004.

Saturnino, G. B., Thielscher, A., Madsen, K. H., Knösche, T. R., and Weise, K. (2019). A principled approach to conductivity uncertainty analysis in electric field calculations. *NeuroImage*, 188:821–834. doi:10.1016/j.neuroimage.2018.12.053.

Schmidt, C., Wagner, S., Burger, M., Van Rienen, U., and Wolters, C. H. (2015). Impact of uncertain head tissue conductivity in the optimization of transcranial direct current stimulation for an auditory target. *Journal of Neural Engineering*, 12(4):046028. doi:10.1088/1741-2560/12/4/046028.

Schrader, S., Antonakakis, M., Rampp, S., Engwer, C., and Wolters, C. H. (2020). A novel method for calibrating head models to account for variability in conductivity and its evaluation in a sphere model. *Physics in Medicine & Biology*, 65(24):245043. doi:10.1088/1361-6560/abc5aa.

Schrader, S., Westhoff, A., Piastra, M. C., Miinalainen, T., Pursiainen, S., Vorwerk, J., Brinck, H., Wolters, C. H., and Engwer, C. (2021). DUNEuro – A software toolbox for forward modeling in bioelectromagnetism. *PLOS ONE*, 16(6):1–21. doi:10.1371/journal.pone.0252431.

Schubert, R., Ritter, P., Wüstenberg, T., Preuschhof, C., Curio, G., Sommer, W., and Villringer, A. (2008). Spatial attention related SEP amplitude modulations covary with BOLD signal in S1 – A simultaneous EEG-fMRI study. *Cerebral Cortex*, 18(11):2686–2700. doi:10.1093/cercor/bhn029.

Seran, E., Godefroy, M., Pili, E., Michielsen, N., and Bondiguel, S. (2017). What we can learn from measurements of air electric conductivity in 222Rn-rich atmosphere. *Earth and Space Science*, 4(2):91–106. doi:10.1002/2016EA000241.

Sharon, D., Hämäläinen, M. S., Tootell, R. B. H., Halgren, E., and Belliveau, J. W. (2007). The advantage of combining MEG and EEG: Comparison to fMRI in focally stimulated visual cortex. *NeuroImage*, 36(4):1225–1235. doi:10.1016/j.neuroimage.2007.03.066.

Shimony, J. S., McKinstry, R. C., Akbudak, E., Aronovitz, J. A., Snyder, A. Z., Lori, N. F., Cull, T. S., and Conturo, T. E. (1999). Quantitative diffusion-tensor anisotropy brain MR imaging: Normative human data and anatomic analysis. *Radiology*, 212(3):770–784. doi:10.1148/radiology.212.3.r99au51770.

Stefan, H., Hummel, C., Scheler, G., Genow, A., Druschky, K., Tilz, C., Kaltenhäuser, M., Hopfengärtner, R., Buchfelder, M., and Romstöck, J. (2003). Magnetic brain source imaging of focal epileptic activity: A synopsis of 455 cases. *Brain*, 126(11):2396–2405. doi:10.1093/brain/awg239.

Stefan, H. and Trinka, E. (2017). Magnetoencephalography (MEG): Past, current and future perspectives for improved differentiation and treatment of epilepsies. *Seizure*, 44:121–124. doi:10.1016/j.seizure.2016.10.028.

Stenroos, M. and Hauk, O. (2013). Minimum-norm cortical source estimation in layered head models is robust against skull conductivity error. *NeuroImage*, 81:265–272. doi: 10.1016/j.neuroimage.2013.04.086.

Stenroos, M., Hunold, A., and Haueisen, J. (2014). Comparison of three-shell and simplified volume conductor models in magnetoencephalography. *NeuroImage*, 94:337–348. doi: 10.1016/j.neuroimage.2014.01.006.

Stenroos, M. and Nummenmaa, A. (2016). Incorporating and compensating cerebrospinal fluid in surface-based forward models of magneto- and electroencephalography. *PLOS ONE*, 11(7):1–23. doi:10.1371/journal.pone.0159595.

Stenroos, M. and Sarvas, J. (2012). Bioelectromagnetic forward problem: isolated source approach revis(it)ed. *Physics in Medicine & Biology*, 57(11):3517–3535. doi:10.1088/0031-9155/57/11/3517.

Stinstra, J. G. and Peters, M. J. (1998). The volume conductor may act as a temporal filter on the ECG and EEG. *Medical and Biological Engineering and Computing*, 36(6):711–716. doi:10.1007/BF02518873.

Stubbemann, R. (2021). *Application of the mixed-FEM approach for the MEG-Problem*. Master's thesis, Westfälische Wilhelms-Universität Münster.

Stöhr, M., Dichgans, J., Büttner, U., and Hess, C. W. (2005). *Evozierte Potenziale – SEP - VEP - AEP - EKP - MEP*. Berlin: Springer-Verlag. ISBN 9783540266594.

Tadel, F., Baillet, S., Mosher, J. C., Pantazis, D., and Leahy, R. M. (2011). Brainstorm: A user-friendly application for MEG/EEG analysis. *Computational Intelligence and Neuroscience*, 2011:8. doi:10.1155/2011/879716.

Tamilia, E., Madsen, J. R., Grant, P. E., Pearl, P. L., and Papadelis, C. (2017). Current and emerging potential of magnetoencephalography in the detection and localization of high-frequency oscillations in epilepsy. *Frontiers in Neurology*, 8:14. doi:10.3389/fneur.2017.00014.

Tang, C., You, F., Cheng, G., Gao, D., Fu, F., and Dong, X. (2009). Modeling the frequency dependence of the electrical properties of the live human skull. *Physiological Measurement*, 30:1293–301. doi:10.1088/0967-3334/30/12/001.

Tang, C., You, F., Cheng, G., Gao, D., Fu, F., Yang, G., and Dong, X. (2008). Correlation between structure and resistivity variations of the live human skull. *IEEE Transactions on Biomedical Engineering*, 55(9):2286–2292. doi:10.1109/TBME.2008.923919.

Taylor, M. E. (2011). *Partial Differential Equations I – Basic Theory (2nd Ed.).* New York: Springer. ISBN 9781441970558.

Theiß, M., Wollbrink, A., Wolters, C. H., and Brinck, H. (2016). Impact of different registration methods in MEG source analysis. *Current Directions in Biomedical Engineering*, 2(1):463–466. doi:10.1515/cdbme-2016-0102.

Theodore, W. H., Spencer, S. S., Wiebe, S., Langfitt, J. T., Ali, A., Shafer, P. O., Berg, A. T., and Vickrey, B. G. (2006). Epilepsy in North America: A report prepared under the auspices of the global campaign against epilepsy, the International Bureau for Epilepsy, the International League Against Epilepsy, and the World Health Organization. *Epilepsia*, 47(10):1700–1722. doi:10.1111/j.1528-1167.2006.00633.x.

Theuvenet, P. J., Van Dijk, B. W., Peters, M. J., Van Ree, J. M., Lopes da Silva, F. L., and Chen, A. C. N. (2005). Whole-head MEG analysis of cortical spatial organization from unilateral stimulation of median nerve in both hands: No complete hemispheric homology. *NeuroImage*, 28(2):314–325. doi:10.1016/j.neuroimage.2005.06.010.

Tierney, T. M., Holmes, N., Mellor, S., López, J. D., Roberts, G., Hill, R. M., Boto, E., Leggett, J., Shah, V., Brookes, M. J., Bowtell, R., and Barnes, G. R. (2019). Optically pumped magnetometers: From quantum origins to multi-channel magnetoencephalography. *NeuroImage*, 199:598–608. doi:10.1016/j.neuroimage.2019.05.063.

Tierney, T. M., Mellor, S., O'Neill, G. C., Holmes, N., Boto, E. R., Gillian Hill, R. M., Leggett, J., Bowtell, R., Brookes, M. J., and Barnes, G. R. (2020). Pragmatic spatial sampling for wearable MEG arrays. *Scientific Reports*, 10(1):21609. doi:10.1038/s41598-020-77589-8.

Troebinger, L., López, J. D., Lutti, A., Bradbury, D., Bestmann, S., and Barnes, G. (2014). High precision anatomy for MEG. *NeuroImage*, 86:583–591. doi:10.1016/j.neuroimage.2013.07.065.

Tuch, D. S., Wedeen, V. J., Dale, A. M., George, J. S., and Belliveau, J. W. (2001). Conductivity tensor mapping of the human brain using diffusion tensor MRI. *Proceedings of the National Academy of Sciences*, 98(20):11697–11701. doi:10.1073/pnas.171473898.

Valdés-Hernández, P. A., Von Ellenrieder, N., Ojeda-Gonzalez, A., Kochen, S., Alemán-Gómez, Y., Muravchik, C., and Valdés-Sosa, P. A. (2009). Approximate average head models for EEG source imaging. *Journal of Neuroscience Methods*, 185(1):125–132. doi:10.1016/j.jneumeth.2009.09.005.

Vallaghé, S. and Clerc, M. (2009). A global sensitivity analysis of three- and four-layer EEG conductivity models. *IEEE Transactions on Biomedical Engineering*, 56(4):988–995. doi:10.1109/TBME.2008.2009315.

Vallaghé, S., Papadopoulo, T., and Clerc, M. (2008). The adjoint method for general EEG and MEG sensor-based lead field equations. *Physics in Medicine & Biology*, 54(1):135. doi:10.1007/978-3-642-12197-5_20.

Vatta, F., Meneghini, F., Esposito, F., Mininel, S., and Salle, F. (2009). Solving the forward problem in EEG source analysis by spherical and FDM head modeling: A comparative analysis. *Biomedical Sciences Instrumentation*, 45:382–8.

Vermaas, M., Piastra, M. C., Oostendorp, T. F., Ramsey, N. F., and Tiesinga, P. H. E. (2020). When to include ECoG electrode properties in volume conduction models. *Journal of Neural Engineering*, 17(5):056031. doi:10.1088/1741-2552/abb11d.

Von Ellenrieder, N., Muravchik, C. H., Wagner, M., and Nehorai, A. (2009). Effect of head shape variations among individuals on the EEG/MEG forward and inverse problems. *IEEE Transactions on Biomedical Engineering*, 56(3):587–597. doi:10.1109/TBME.2009.2008445.

Vorwerk, J. (2016). *New Finite Element Methods to Solve the EEG/MEG Forward Problem*. Ph.D. thesis, Westfälische Wilhelms-Universität Münster.

Vorwerk, J., Aydin, Ü., Wolters, C. H., and Butson, C. R. (2019a). Influence of head tissue conductivity uncertainties on EEG dipole reconstruction. *Frontiers in Neuroscience*, 13:531. doi:10.3389/fnins.2019.00531.

Vorwerk, J., Cho, J.-H., Rampp, S., Hamer, H., Knösche, T. R., and Wolters, C. H. (2014). A guideline for head volume conductor modeling in EEG and MEG. *NeuroImage*, 100:590–607. doi:10.1016/j.neuroimage.2014.06.040.

Vorwerk, J., Clerc, M., Burger, M., and Wolters, C. H. (2012). Comparison of boundary element and finite element approaches to the EEG forward problem. *Biomedical Engineering / Biomedizinische Technik*, 57(Suppl. 1):795–798. doi:10.1515/bmt-2012-4152.

Vorwerk, J., Hanrath, A., Wolters, C. H., and Grasedyck, L. (2019b). The multipole approach for EEG forward modeling using the finite element method. *NeuroImage*, 201:116039. doi:10.1016/j.neuroimage.2019.116039.

Vorwerk, J., Oostenveld, R., Piastra, M. C., Magyari, L., and Wolters, C. H. (2018). The FieldTrip-SimBio pipeline for EEG forward solutions. *BioMedical Engineering Online*, 17(1):37. doi:10.1186/s12938-018-0463-y.

Wagner, S., Burger, M., and Wolters, C. H. (2016). An optimization approach for well-targeted transcranial direct current stimulation. *SIAM Journal on Applied Mathematics*, 76(6):2154–2174. doi:10.1137/15M1026481.

Wendel, K. and Malmivuo, J. (2006). Correlation between live and post mortem skull conductivity measurements. In *2006 International Conference of the IEEE Engineering in Medicine and Biology Society*, pages 4285–4288. doi:10.1109/IEMBS.2006.259434.

Wendel, K., Narra, N. G., Hannula, M., Kauppinen, P., and Malmivuo, J. (2008). The influence of CSF on EEG sensitivity distributions of multilayered head models. *IEEE Transactions on Biomedical Engineering*, 55(4):1454–1456. doi:10.1109/TBME.2007.912427.

Wendel, K., Väisänen, J., Seemann, G., Hyttinen, J., and Malmivuo, J. (2010). The influence of age and skull conductivity on surface and subdermal bipolar EEG leads. *Computational Intelligence and Neuroscience*, 2010:397272. doi:10.1155/2010/397272.

Wendel, K., Väisänen, O., Malmivuo, J., Gencer, N. G., Vanrumste, B., Durka, P., Magjarević, R., Selma Supek, S., Pascu, M. L., Fontenelle, H., and De Peralta Menendez, R. G. (2009). EEG/MEG source imaging: Methods, challenges, and open issues. *Computational Intelligence and Neuroscience*, 2009(656092). doi:10.1155/2009/656092.

Werthmann, T. A., Wolters, C. H., and Grasedyck, L. (2020). Approximation of parameter-dependent leadfield matrices using tensor formats. In *Workshop Biosignalverarbeitung 2020, Gemeinsamer Workshop der Fachausschüsse 'Biosignale' und 'Magnetische Methoden in der Medizin' der DGBMT im VDE, Kiel (Germany).*

Whalen, C., Maclin, E. L., Fabiani, M., and Gratton, G. (2008). Validation of a method for coregistering scalp recording locations with 3D structural MR images. *Human Brain Mapping*, 29(11):1288–1301. doi:10.1002/hbm.20465.

Wolters, C. H. (2017). Mathematical methods in bioelectromagnetism and in the analysis of biosignals. Script from lectures given at the faculty of Mathematics/Computer Science and Medicine at the University of Münster, Germany.

Wolters, C. H., Anwander, A., Berti, G., and Hartmann, U. (2007a). Geometry-adapted hexahedral meshes improve accuracy of finite-element-method-based EEG source analysis. *IEEE Transactions on Biomedical Engineering*, 54(8):1446–1453. doi:10.1109/TBME.2007.890736.

Wolters, C. H., Anwander, A., Tricoche, X., Weinstein, D., Koch, M. A., and MacLeod, R. S. (2006). Influence of tissue conductivity anisotropy on EEG/MEG field and return current computation in a realistic head model: A simulation and visualization study using high-resolution finite element modeling. *NeuroImage*, 30(3):813–826. doi:10.1016/j.neuroimage.2005.10.014.

Wolters, C. H., Beckmann, R. F., Rienäcker, A., and Buchner, H. (1999). Comparing regularized and non-regularized nonlinear dipole fit methods: A study in a simulated sulcus structure. *Brain Topography*, 12(1):3–18. doi:10.1023/A:1022281005608.

Wolters, C. H., Grasedyck, L., and Hackbusch, W. (2004). Efficient computation of lead field bases and influence matrix for the FEM-based EEG and MEG inverse problem. *Inverse Problems*, 20(4):1099–1116. doi:10.1088/0266-5611/20/4/007.

Wolters, C. H., Kuhn, M., Anwander, A., and Reitzinger, S. (2002). A parallel algebraic multigrid solver for finite element method based source localization in the human brain. *Computing and Visualization in Science volume*, 5:165–177. doi:10.1007/s00791-002-0098-0.

Wolters, C. H., Köstler, H., Möller, C., Härdtlein, J., and Anwander, A. (2007b). Numerical approaches for dipole modeling in finite element method based source analysis. *International Congress Series*, 1300:189–192. doi:10.1016/j.ics.2007.02.014.

Wolters, C. H., Köstler, H., Möller, C., Härdtlein, J., Grasedyck, L., and Hackbusch, W. (2007c). Numerical mathematics of the subtraction method for the modeling of a current dipole in EEG source reconstruction using finite element head models. *SIAM Journal on Scientific Computing*, 30(1):24–45. doi:10.1137/060659053.

Wolters, C. H., Lew, S., MacLeod, R. S., and Hämäläinen, M. (2010). Combined EEG/MEG source analysis using calibrated finite element head models. In de Gruyter, W. (Editor), *Proc. of the 44th Annual Meeting, DGBMT 2010, Rostock-Warnemünde (Germany)*, pages 64–68.

Yang, J. and Lei, Z. (2019). Chapter 18 – Human head modeling and applications. In Scataglini, S. and Paul, G. (Editors), *DHM and Posturography*, pages 217–242. Academic Press. ISBN 9780128167137.

Zhang, Y., Van Drongelen, W., and He, B. (2006). Estimation of in vivo brain-to-skull conductivity ratio in humans. *Applied Physics Letters*, 89(22):223903. doi:10.1063/1.2398883.